Electromagnetic Tracking System for the Implantation of Deep Brain Stimulation Electrodes using Integrated Magnetometers

Inaugural dissertation

to
be awarded the degree of

Dr. sc. med.

presented at the Faculty of Medicine
of the University of Basel

&

PhD in Electronics, microelectronics, photonics

presented at the Doctoral School
"Mathématiques, Sciences de l'Information et de l'Ingénieur"
of the University of Strasbourg

by
Céline Vergne
from Vigeois, France

Basel, 2025

Approved by the Faculty of Medicine, University of Basel & the Doctoral School, University of Strasbourg
On application of:

Prof. Dr. med. Raphael Guzman, University of Basel – *primary advisor*
Prof. Dr. Morgan Madec, University of Strasbourg – *secondary advisor*
Prof. Dr. Pierre Jannin, University of Rennes – *external expert*
Prof. Dr. Olivier Romain, University of Cergy Paris – *external expert*
Prof. Dr. Simone Hemm-Ode, University of Applied Sciences and Arts Northwestern Switzerland – *further advisor*
Prof. Dr. Joris Pascal, University of Applied Sciences and Arts Northwestern Switzerland – *further advisor*

Basel, 23rd of April 2025

Prof. Dr. Eva Scheurer
Dean of the Faculty of Medecine, University of Basel

Prof. Dr. Thomas Noël
Director of the Doctoral School, University of Strasbourg

UNIVERSITÉ DE STRASBOURG

École doctorale 269 Mathématiques, Sciences de l'Information et de l'Ingénieur]

Laboratoire des sciences de l'ingénieur, de l'informatique et de l'imagerie (UMR 7357)

THÈSE présentée par :

Céline Vergne

soutenue le 23 avril 2025

pour obtenir le grade de **Docteur de l'Université de Strasbourg**
en Électronique, microélectronique, photonique

Electromagnetic Tracking System for the Implantation of Deep Brain Stimulation Electrodes using Integrated Magnetometers

THÈSE dirigée par :

GUZMAN Raphaël	Professeur, Universität Basel
MADEC Morgan	Professeur, Université de Strasbourg

RAPPORTEURS :

JANNIN Pierre	Professeur, Université de Rennes
ROMAIN Olivier	Professeur, Université de Cergy Paris

AUTRES MEMBRES DU JURY :

HEMM-ODE Simone	Professeur, University of Applied Sciences and Arts Northwestern Switzerland
PASCAL Joris	Professeur, University of Applied Sciences and Arts Northwestern Switzerland

---

INVITÉS :

TAUB Ethan	Docteur en neurochirurgie, University Hospital of Basel

To my better half

Acknowledgements

I wish to express my deepest gratitude to:

- ✧ Prof. Dr. med. Raphael Guzman for his invaluable support in the field of neurosurgery and for guiding me during my time at the University of Basel. His willingness to take the time to assist me, despite working in different locations, has been greatly appreciated.
- ✧ Prof. Dr. Morgan Madec for the opportunity to carry out a project across three institutions and for his continuous guidance throughout these years. Prof. Madec has been a mentor since my early university years, and I am grateful to have completed this journey under his supervision.
- ✧ Prof. Dr. Simone Hemm for her support and guidance. Beyond providing valuable feedback to enhance my work, her motivational spirit and enthusiasm have been truly inspiring. She played a crucial role in helping me navigate this interdisciplinary project and always did her best to keep me on track.
- ✧ Prof. Dr. Joris Pascal for sharing his expertise and for placing his trust in me during the development of this project. I greatly appreciated his open-mindedness and his willingness to see me grow and learn, even beyond this project.
- ✧ Dr. med. Ethan Taub and Dr. Birgit Westermann or welcoming me to the University Hospital Basel on multiple occasions, taking the time to explain, discuss, and provide valuable feedback.
- ✧ Dr. med. Jean-Jacques Lemaire and Dr. Jérôme Coste who gave me the opportunity to observe surgeries—an invaluable experience that allowed me to critically reflect on my own work.
- ✧ Prof. Dr. Karin Wardell and all the team from the Neuroengineering Lab at the University of Linkoping in Sweden. Meeting and engaging with them multiple times has been a great privilege, and I truly enjoyed our discussions on neuroengineering and knowledge-sharing.
- ✧ All my colleagues from the Institute of Medical informatics and Medical engineering (FHNW) with a special thanks to the Sensors's team:— Dr. Hugo Nicolas, Dr. Thomas Quirin, Corentin Féry, and Simon Lemoigne— for their tremendous help and feedback on electronics design and programming as well as the Neuroengineering's team: — Dr. Dorian Vogel, Frédéric Bourgeois, Marc Jermann, Vittoria Bucciarelli, and Eli Rickert— for their knowledge and contributions to the development of this project. A special mention goes to Hugo Nicolas, who embarked on his PhD journey at the same time as I did. His patience, knowledge, and countless shared discussions—both in the lab and at conferences around the world have been invaluable.

✧ My fellow PhD candidates of the department of Biomedical Engineering (DBE) thank you for welcoming me each time I visited Allschwil. A special thank you to Massimiliano Filipozzi and Oumeymah Cherkaoui, with whom I had the opportunity to collaborate. A heartfelt mention to Michaela Maintz, who also worked between FHNW and DBE—sharing this experience with her and exchanging valuable PhD life tips has been truly rewarding.

✧ The Bachelor or Master students, I had the pleasure of supervising or working with at the FHNW: Ismaël Mounime, Mathis Blais, José Inácio, Oliver Joss, Christophe Lepaumier, Eliot Saulnier, Ceyda Yildiz, Kurt Jethro Kuser, Sascha Müller and Alex Jensen Sasafuchi.

✧ The administrative team at both universities, including Mrs. Moira Lux, Dr. Sara Freud, Mrs. Natalie Kostmann, Mrs. Jenny Brehm, Mrs. Joelle Hube, Mr. Thomas Gerber, and Dr. Gabriela Oser, for their invaluable assistance.

✧ All the individuals I had the opportunity to meet and engage with during my PhD, who contributed to my growth as a researcher in a dynamic environment: Prof. Yuki Hayashida, Prof. Sebastien Saez, Prof. Jean-Baptiste Kammerer, Prof. Luc Hébrard, Prof. Urs Fischer, Prof. Naofumi Suematsu, Dr. Ahmet Demirörs, Dr. Josefin Kaufman, Dr. Dominique Neuhaus.

✧ My parents and my sister who never questioned my academic path, even when it took me far from home. Their unwavering support has meant the world to me.

✧ My partner, Vincent, for always being there for me and providing constant emotional support throughout the highs and lows of this journey. It goes without saying that I could not have done this without you.

Preface

The PhD project began as a collaborative research effort between the University of Applied Sciences and Arts Northwestern Switzerland (FHNW) and the University of Strasbourg. Early in the project, a grant application was submitted to the Swiss National Science Foundation. As a result, this doctoral thesis was developed under the framework of the Swiss National Science Foundation grant (204448), titled "Development of an Electromagnetic Tracking System for the Implantation of Deep Brain Stimulation Electrodes". The research was carried out at the Institute for Medical Engineering and Medical Informatics at the University of Applied Sciences and Arts Northwestern Switzerland (FHNW), in collaboration with the Department of Neurosurgery at the University Hospital Basel.
The awarding of the grant required my transfer from the University of Strasbourg to the University of Basel. To further strengthen the international dimension of the project, my supervisors and I initiated a cotutelle agreement to formally encompass the PhD project.

In this context, my PhD project was conducted in an international and multidisciplinary environment. This setting was highly rewarding, offering rich learning opportunities, but also presented challenges. I would like to express my gratitude to the funding organization and my supervisors for their support in fostering this unique environment, despite its complexities.

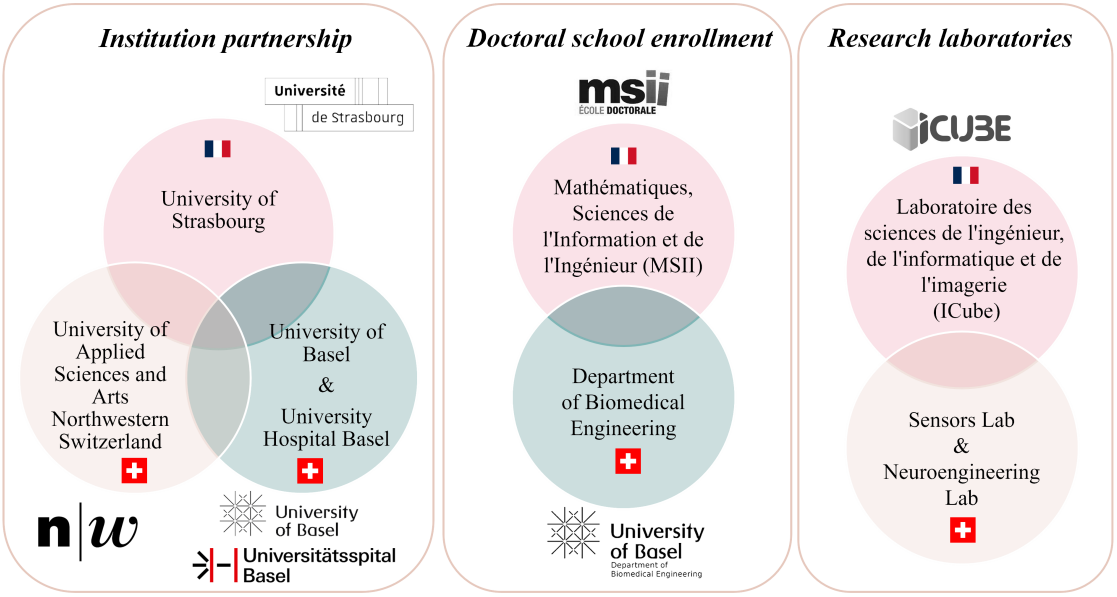

Figure 1: Framework of the thesis - Institution partnership and international collaboration.

Abstract

Deep Brain Stimulation (DBS) has become a pivotal treatment for neurological and psychiatric disorders, offering therapeutic benefits for conditions such as Parkinson's disease, essential tremor and dystonia. Despite its success, DBS surgery faces critical challenges, including the precise placement and orientation of electrodes and the optimization of the stimulation parameters. Traditional methods rely heavily on stereotactic imaging and intra-operative physiological recordings but lack real-time feedback during surgery. This limitation highlights the need for innovative solutions to enhance both surgical accuracy and therapeutic outcomes.

This thesis focuses on the development of an Electromagnetic Tracking (EMT) demonstrator to address the challenge of DBS localization. The proposed system combines quasi-static magnetic fields with integrated magnetic sensors, aiming to achieve spatial error and angular error of less than 1 mm and 1 degree, while integrating seamlessly into established surgical workflows.
A comprehensive assessment of the performance of the developed EMT system and its applicability to DBS surgery was conducted. Experimental results demonstrated its ability to provide reliable tracking performance with a spatial and angular error of 1.7 mm and 0.9° respectively. Additionally, the system proved to be robust when integrated with stereotactic systems, by eliminating errors caused by the associated distortions, outperforming commercial EMT systems based on the induction principle.
In addition to real-time localization, this research emphasizes the integration of the novel EMT system into DBS workflows. A novel registration-free method, using the same integrated magnetic sensors, has been developed to simplify the surgical process. This approach reduces the workload of the medical teams while ensuring accurate localization when visualizing the electrode positions in relation to the brain structures.

By addressing the technical and clinical challenges associated with DBS, this research represents a significant advance in neurosurgical technology. The findings underscore the potential of EMT systems to enhance surgical precision, reduce procedural risks, and at long-term improve patient outcomes, marking a step forward in the integration of cutting-edge technologies into neurosurgical practice.

Keywords: DBS, Stereotactic neurosurgery, EMT system, Magnetic sensor, Surgical workflow.

Zusammenfassung

Die tiefe Hirnstimulation (DBS) hat sich zu einer wichtigen Behandlungsmethode für neurologische und psychiatrische Erkrankungen entwickelt und bietet therapeutische Vorteile bei Krankheiten wie Parkinson, essentiellem Tremor und Dystonie. Trotz ihres Erfolgs steht die DBS-Chirurgie vor kritischen Herausforderungen, Dazu gehören die präzise Platzierung und Ausrichtung der Elektroden und die Optimierung der Stimulationsparameter. Herkömmliche Methoden stützen sich in hohem Maße auf stereotaktische Bildgebung und intraoperative physiologische Aufzeichnungen, aber es fehlt ein Echtzeit-Feedback während des Eingriffs. Diese Einschränkung unterstreicht den Bedarf an innovativen Lösungen, um sowohl die chirurgische Genauigkeit als auch die therapeutischen Ergebnisse zu verbessern.

Diese Arbeit konzentriert sich auf die Entwicklung eines Demonstrators für elektromagnetisches Tracking (EMT), um die Herausforderung der DBS-Lokalisierung anzugehen. Das vorgeschlagene System kombiniert quasi-statische Magnetfelder mit integrierten Magnetsensoren und zielt darauf ab, einen räumlichen Fehler und einen Winkelfehler von weniger als 1 mm und 1 Grad zu erreichen, während es sich nahtlos in etablierte chirurgische Arbeitsabläufe einfügt.
Es wurde eine umfassende Bewertung der Leistung des entwickelten EMT-Systems und seiner Anwendbarkeit für die DBS-Chirurgie durchgeführt. Die experimentellen Ergebnisse zeigten, dass das System eine zuverlässige Verfolgungsleistung mit einem räumlichen und winkligen Fehler von 1,7 mm bzw. 0,9° erbringen kann. Darüber hinaus erwies sich das System als robust, wenn es in stereotaktische Systeme integriert wurde, indem es die durch die damit verbundenen Verzerrungen verursachten Fehler eliminierte und den Goldstandard für das EMT-Prinzip übertraf.
Neben der Echtzeit-Lokalisierung steht bei dieser Forschung die Integration des neuartigen EMT-Systems in DBS-Arbeitsabläufe im Vordergrund. Zur Vereinfachung des chirurgischen Prozesses wurde eine neuartige registrierungsfreie Methode entwickelt, die dieselben integrierten Magnetsensoren verwendet. Dieser Ansatz reduziert die Arbeitsbelastung der medizinischen Teams und gewährleistet gleichzeitig eine genaue Lokalisierung bei der Visualisierung der Elektrodenpositionen in Bezug auf die Gehirnstrukturen.

Durch die Bewältigung der technischen und klinischen Herausforderungen, die mit der DBS verbunden sind, stellt diese Forschung einen bedeutenden Fortschritt in der neurochirurgischen Technologie dar. Die Ergebnisse unterstreichen das Potenzial von EMT-Systemen, die chirurgische Präzision zu erhöhen, die Verfahrensrisiken zu verringern und zur langfristigen Verbesserung der Patientenergebnisse, was einen Schritt nach vorn bei der Integration von Spitzentechnologien in die neurochirurgische Praxis darstellt.

Schlüsselwörter: THS, Stereotaktische Neurochirurgie, EMT-System, magnetischer Sensor, chirurgischer Arbeitsablauf.

Contents

List of Publications

Below is a list of publications produced during the PhD project and directly related to this thesis. The first four publications form the central core of the dissertation. Additional publications, not directly tied to the PhD project, are included at the end of the dissertation.

First author peer-reviewed publications in international scientific journals

1. **Vergne C**, Féry C, Quirin T, Nicolas H, Madec M, Hemm S and Pascal J. 'Low-Field Electromagnetic Tracking Using 3-D Magnetometer for Assisted Surgery'. IEEE Transactions on Magnetics, vol. 59, no. 2, pp. 1-5, Feb. 2023, Art no. 5400205. https://doi.org/10.1109/TMAG.2022.3204918
2. **Vergne C**, Madec M, Quirin T, Guzman R, Hemm. S and Pascal J. 'Electromagnetic tracking system for position and orientation detection of deep brain stimulation electrodes during surgery'. IEEE Trans Biomed Eng. 2025 Jan 14;PP. https://doi.org/10.1109/TBME.2025.3529716
3. **Vergne C**, Madec M, Guzman R, Pascal J, Taub E, Bourgeois F and Hemm S. 'In vitro assessment and comparison of a novel electromagnetic tracking system for stereotactic DBS surgery'. Ann Biomed Eng (2025). https://doi.org/10.1007/s10439-025-03728-9
4. **Vergne C**, Vogel D, Lemoigne S, Quirin T, Féry C, Madec M, Pascal J, Guzman R and Hemm S. 'Registration-free workflow for stereotactic neurosurgery guided by a new generation electromagnetic navigation system'. (accepted to IEEE EMBC conference 2025 as full-contributed paper)

Co-author peer-reviewed publications in international scientific journals

1. Quirin T, Féry C, Vogel D, **Vergne C**, Sarracanie M, Salameh N, Madec M, Hemm S, Hébrard L, Pascal J. 'Towards Tracking of Deep Brain Stimulation Electrodes Using an Integrated Magnetometer'. Sensors. 2021; 21(8):2670. https://doi.org/10.3390/s21082670

International peer-reviewed conferences; with or without proceedings

Oral presentation

1. **Vergne C**, Nicolas H, Madec M, Hemm S, Guzman R, and Pascal J. 'Experimental assessment of the performances of an anisotropic magnetoresistive sensor after exposure to strong magnetic fields'. 2023 IEEE International Magnetic Conference - Short Papers (INTERMAG Short Papers), Sendai, Japan, May 15-19, 2023, pp. 1-2. https://doi.org/10.1109/INTERMAGShortPapers58606.2023.10228508

   ⋆ *Selected as one of the five finalists for the IEEE Intermag 2023 Best Student Presentation Award*

2. **Vergne C**, Madec M, Raphael G, Pascal J, and Hemm S. 'Towards a new generation of electromagnetic navigation system for deep brain stimulation' in Barbarisi V. ESSFN Conference Proceedings, Stockholm, Sweden, September 27-30, 2023. Stereotactic and Functional Neurosurgery, 102 (Suppl 1:1-2), p 94-95.
https://doi.org/10.1159/000539983

Poster presentation

1. **Vergne C**, Madec M, Hemm S, Quirin T, Vogel D, Hébrard L and Pascal J. 'Tracking the Orientation of Deep Brain Stimulation Electrodes Using an Embedded Magnetic Sensor'. 10th IEEE EMBS Conference on Neural Engineering, online, May 4-6, 2021. (unpublished)
2. **Vergne C**, Madec M, Pascal J, and Hemm S. 'Orientation detection of deep brain stimulation electrodes based on neuronavigation with an embedded magnetic sensor' in Régis J, Gonçalves-Ferreira A. ESSFN Conference Proceedings, France, Marseille, September 8-11, 2021. Stereotactic and Functional Neurosurgery, 99(Suppl. 1), 35.
https://doi.org/10.1159/000520686
3. **Vergne C**, Pascal J, Madec M, Guzman R, Taub E, and Hemm S. 'Enhancing neurosurgical procedures with submillimeter magnetometers'. 2024 IEEE Sensors Conference, Young Professional Session, Kobe, Japan, October 20-23, 2024. (unpublished)
    ⋆ *IEEE Sensors 2024 Best Young Professional Poster Award*
4. **Vergne C**, Nicolas H, Lemoigne S, and Pascal J. 'Flexible coils localization using optically pumped magnetometers for biomedical applications'. 2024 IEEE Sensors Conference, Kobe, Japan, 2024.
https://doi.org/10.1109/SENSORS60989.2024.10784888

National conferences; refereed without associated proceedings

Poster presentation

1. **Vergne C**, Madec M, Pascal J and Hemm S. 'Orientation detection of deep brain stimulation electrode with an embedded magnetic sensor'. Swiss society of Biomedical engineering Conference 2021, Bern, Switzerland, August 26, 2021.
2. **Vergne C**, Féry C, Quirin T, Nicolas H, Madec M, Hemm S and Pascal J. 'Low-field electromagnetic tracking using 3D magnetometer for assisted surgery'. Colloque GDR SoC2 2022, Strasbourg, France, June 27-29, 2022.
3. **Vergne C**, Pascal J, Hemm S, Madec M, Taub E and Guzman R. 'Development and characterization of an electromagnetic tracking system: Application to deep brain stimulation surgery. Research Day DBE-UNIBAS 2022, Basel, Switzerland, August 30, 2022.
    ⋆ *Third place - Best Poster Award*
4. **Vergne C**. 'MPS: Magnetic Positioning System for Neurosurgery'. Tag der Forschung - School of Life Sciences FHNW, Brugg-Windisch, Switzerland, September 27, 2022.

5. **Vergne C**, Pascal J, Hemm S, Guzman R and Madec M. 'Towards a new generation of electromagnetic navigation system for deep brain stimulation surgery'. 10èmes Journées Scientifiques de la fédération de médecine translationnelle de Strasbourg, Strasbourg, France, June 21-22. 2023.
6. **Vergne C**, Pascal J, Hemm S, Madec M and Guzman R. 'Development of a robust electromagnetic navigation system for deep brain stimulation surgery'. Research Day DBE-UNIBAS 2023, Basel, Switzerland, August 29, 2023.
7. **Vergne C**, Madec M, Guzman R, Pascal J and Hemm S. 'A robust electromagnetic tracking system for deep brain stimulation surgery'. Swiss society of Biomedical engineering Conference 2023, Allschwil, Switzerland, September 13, 2023.
8. **Vergne C**, Pascal J, Madec M, Guzman R, Taub E and Hemm S. 'Electromagnetic navigation system for deep brain stimulation: How to?'. 10th Research Day DBE-UNIBAS 2024, Basel, Switzerland, August 21, 2024.
9. **Vergne C**, Madec M, Taub E, Guzman R, Pascal J and Hemm S. 'Towards a robust generation of electromagnetic navigation system for deep brain stimulation surgery'. Swiss society of Biomedical engineering Conference 2024, Winterthur, Switzerland, September 5, 2024.

Abbreviations

AMR Anisotropic Magneto-Resistance.

CE Conformité Européenne.

CT Computed Tomography.

DBS Deep Brain Stimulation.

EEG Electroencephalograpy.

EFS Electric Field Stereotaxis.

EMI Electromagnetic Interference.

EMT Electromagnetic Tracking.

ENS Electromagnetic Navigation System.

ET Essential Tremor.

ETRS Essential Tremor Rating scale.

FDA Food and Drug Administration.

FG Field Generator.

GMI Giant Magneto-Impedance.

GMR Giant Magneto-Resistance.

GPi Globus Pallidus internus.

iCT Intra-operative Computed Tomography.

iMRI Intra-operative Magnetic Resonance Imaging.

IPG Implanted Pulse Generator.

LFP Local Field Potential.

MEG Magnetoencephalography.

MEMS Micro-Electro-Mechanical Systems.

MER Micro-Electrode Recording.

MFC Magnetic Field Camera.

MRI Magnetic Resonance Imaging.

MV Measurement Volume.

NV Nitrogen-Vacancy.

OCD Obsessive-Compulsive Disorder.

OPM Optically Pumped Magnetometers.

PCB Printed Circuit Board.

PD Parkinson's Disease.

SQUID Superconducting Quantum Interference Device.

STN Subthalamic Nucleus.

TCS Transcranial Sonography.

TMR Tunnel Magneto-Resistance.

UPDRS Unified Parkinson Disease Rating Scale.

Vim Ventral intermediate nucleus.

List of Figures

List of Tables

CHAPTER 1

Introduction

Background

Deep Brain Stimulation (DBS) has emerged as a transformative neurosurgical intervention for managing movement disorders such as Parkinson's disease, essential tremor, and dystonia. By delivering electrical stimulation to targeted brain structures (Fig. 1.1), DBS effectively alleviates symptoms and improves quality of life for patients with treatment-resistant conditions.

The clinical success of DBS has led to its expanding indications, including psychiatric disorders and other neurological conditions [1]. Despite its established efficacy, several aspects of the procedure, particularly electrode placement and programming, present significant challenges requiring technological innovations [2, 3].

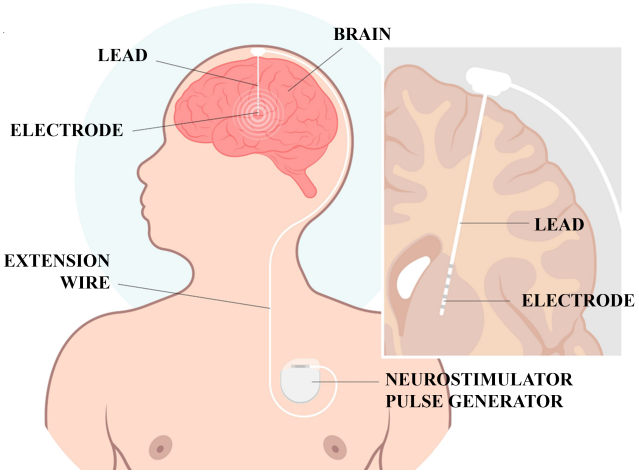

Figure 1.1: Overview of the DBS system. From stock.adobe.com, author: Pepermpron, N°:508895281.

One of the critical steps in DBS surgery is the accurate positioning of the electrode in relation to the anatomical and functional target. Traditionally, this is achieved using stereotactic systems guided by pre-operative imaging and intra-operative physiological recordings. However, these approaches lack real-time feedback on the position and orientation of the electrodes during implantation. This limitation has driven research into advanced tracking systems, some based on electroencephalography [4] or intracranial ultrasound [5], with the aim of improving surgical targeting and enhancing patient outcomes.

Motivation

Recent advancements in DBS technology have enabled the use of directional electrodes, which provide improved control over the brain regions being stimulated compared to full-ring electrodes. In this context, real-time monitoring of the electrode position and orientation relative to the brain anatomy is critical to ensure accurate targeting, optimize stimulation parameters, and avoid complications. However, current methods provide limited intra-operative feedback and often rely on pre- or post-implantation imaging for validation.
As the role of DBS continues to grow, there is an increasing need for a system that can be seamlessly integrated into different surgical workflows while remaining compatible with existing techniques. One potential solution is the development of complementary tracking systems, with the Electromagnetic Tracking (EMT) technique emerging as a promising option.
Despite advancements in EMT systems, existing solutions face challenges such as interferences from metallic objects in the operating room. Novel approaches combining quasi-static magnetic fields and miniaturized magnetic sensors show great potential in tackling these challenges. The development of a robust, real-time localization system could bridge existing gaps and improve the safety and efficacy of DBS surgery.

Objectives

This thesis proposes a novel EMT system and evaluates its performance and potential to provide real-time feedback on DBS electrode placement during surgery. The system aims to outperform existing EMT systems by:

- **Accurate Electrode Localization:** Achieving spatial and angular error below 1 mm and 1°, meeting or exceeding imaging-based standards.

- **Seamless Integration:** Ensuring compatibility with existing surgical workflows, including stereotactic techniques and intra-operative recording techniques.

- **Adaptability:** Developing a system adaptable to various surgical setups while addressing the constraints of the operating room and the challenges related to electromagnetic interferences.

By addressing these objectives, the proposed system paves the way to improve the precision of DBS procedures and assisting in the optimization of stimulation parameters. Additionally, this work contributes to the broader clinical adoption of advanced tracking technologies.

CHAPTER 2

Medical & Technical Background

This chapter outlines the key fundamentals of DBS and tracking systems essential for understanding this dissertation. The first section reviews the major challenges currently faced in DBS and discusses the importance of accurate electrode localization and orientation detection in addressing these issues. The following section examines the latest advancements in localization and navigation systems for DBS surgery, with a focus on electromagnetic localization techniques. Finally, the fundamentals of magnetic field sensing are explored, as magnetic field measurements and sensors constitute an important focus of this dissertation.

2.1 Deep brain stimulation (DBS)

2.1.1 History & Clinical indications

DBS is a modern neurosurgical procedure in which electrodes are implanted in specific regions of the brain. These electrodes deliver controlled electrical impulses to modulate abnormal neuronal activity in targeted brain areas that are associated with various neurological and psychiatric disorders. DBS is one of the most technologically advanced surgeries, resulting from the convergence of various contributors and innovations.

History

A historical overview can offer essential context for understanding the current status and challenges associated with this therapy [6, 7]. The development of DBS is closely tied to the introduction of the stereotactic method by Spiegel & Wycis in 1947 [8], originally used for ablative therapies such as thalamotomy. Thalamotomy is a surgical procedure involving the destruction of areas of the thalamus by using radiofrequency ablation. The area destroyed by this procedure is called a lesion. The stereotactic apparatus, a device fixed to the patient's skull during surgery, allowed surgeons to explore and ablate deeper regions of the brain by following a precise and straight trajectory. In the early 1960s, stereotactic thalamotomy was the treatment of choice for a wide range of movement disorders. This innovation led to the rise of a new neurosurgical field –stereotactic neurosurgery–where novel skills, tools, and knowledge were developed, eventually paving the way for the emergence of DBS as a therapeutic option.
The introduction of drugs for the management of movement disorder symptoms in the late 1960s [9, 10], particularly levodopa, significantly reduced the need for thalamotomies.

Levodopa quickly became the first-line treatment for Parkinson's Disease (PD). Compared to surgical interventions, levodopa offered an affordable, non-invasive, and highly effective means of symptom management. However, its use was associated with characteristic side effects, including nausea, vomiting, dyskinesia, on-off phenomena, postural hypotension, and a gradual decline in effectiveness with prolonged treatment [11, 12, 13]. By the mid-1970s, the rise of levodopa and a shifting political climate concerning the ethics of psychosurgery [7, 14] nearly led to the decline of stereotactic neurosurgery. At the same time, following the success of first cardiac pacemakers in the 1960s, neurostimulators began to be introduced across specialized centers in the U.S. and Europe for chronic pain [15, 16] and later for various conditions previously shown to respond to electrostimulation, such as motor disorders [17], mental disorders [18, 19] or epilepsy [20].
The approach of neurostimulation offered potential surgical solutions for a subset of PD patients who either could not tolerate levodopa or experienced diminished efficacy due to disease progression or the development of drug resistance [21]. The techniques and tools refined during the rapid advancement of stereotactic surgery seamlessly transitioned into the emerging field of DBS. The stereotactic apparatus, combined with imaging technologies, allowed precise targeting of brain regions for permanent electrode implantation, while intra-operative stimulation served to confirm the accuracy of the electrode placement within the intended brain area. Often, these areas were the same regions that had historically been ablated. Until the mid-1980s [22], DBS and other neurostimulation therapies showed promising clinical results. However, a lack of standardized objective measures to quantify improvements hindered the full recognition of the therapy's benefits. Combined with the evolving regulatory landscape under the Food and Drug Administration (FDA), this slowed the spread of neurostimulation treatments. The breakthrough came with the development of new clinical assessment tools, starting with the Unified Parkinson Disease Rating Scale (UPDRS), created in 1987 by the Movement Disorder Society [23]. This tool offered a comprehensive and standardized system to replace the various inconsistent scales used at different PD research centers, followed by the Essential Tremor Rating scale (ETRS) [24], clinical assessment tool for Essential Tremor (ET).
The modern narrative attributes the development of DBS to Benabid's groundbreaking work in 1987 [25] despite earlier exploratory and therapeutic advancements dating back to the 1950s. Benabid's team consolidated previous discoveries, yielding significant results. Indeed, these achievements culminated at the University Hospital Grenoble in France, where Benabid's team had been using ablative therapies to treat PD, dystonia, and psychiatric conditions unresponsive to medications. Grenoble was one of the few centers that retained stereotactic skills and tools and had also developed stimulation methods for chronic pain. At the same time, the accidental discovery of a neurotoxin [26, 27] led to the development of primate models for PD [28, 29]. These models helped confirm specific deep brain targets for DBS such as Ventral intermediate nucleus (Vim). With this confirmation and the availability of new clinical assessment tools, Benabid presented his findings to Medtronic in the early 1990s [30], leading to international clinical trials on DBS for PD. Finally in March 1997, UPDRS-derived data were presented to the FDA's Neurological Devices Panel Advisory Committee, leading to the approval of the "Medtronic Activa Tremor Control System for the suppression of tremor due to essential tremor or Parkinson's disease" [31].

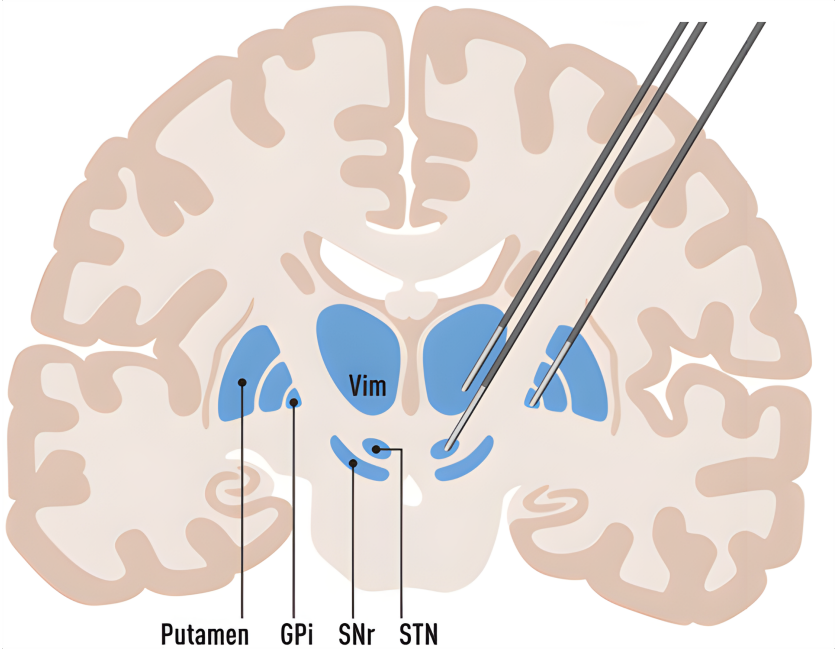

Figure 2.1: Coronal cut of the brain, highlighting structures of the basal ganglia such as the substantia nigra reticulata (SNr) and Putamen, with an exemplary depiction of DBS electrodes targeting the structures related to movement disorders: Subthalamic Nucleus (STN), Ventral intermediate nucleus (Vim) and Globus Pallidus internus (GPi).
Reproduced from [32], published under CC BY-NC-ND 4.0.

After years of research and technical advancements, DBS has been proven to greatly improve motor control and overall quality of life for individuals with movement disorders. For instance, DBS has been proven to be more effective in improving quality of life than drug-based treatments alone [33]. However, drug-based treatments like levodopa remain the first-line approach for motor disorder management, and the patient's responsiveness to the drug-based treatments became a prerequisite for DBS surgery. Current research explored DBS for early-stage PD patients, prior to the onset of motor fluctuations or dyskinesia. Patients who received early DBS showed significantly lower daily medication requirements and a reduced occurrence of resting tremors after five years [34].

Clinical indications

Since the initial studies on DBS, various manufacturers have obtained Conformité Européenne (CE) and FDA certifications for a range of pathologies. While DBS was initially approved for movement disorders like PD and ET, its indications have expanded to include conditions such as epilepsy and psychiatric disorders like Obsessive-Compulsive Disorder (OCD). Below are the most common clinical indications and brain structure targets (Fig. 2.1) [35, 36]:

❊ **Parkinson's Disease:** * *FDA-approved (1997)* and * *CE-approved (1998)*

Disease description: PD is a brain disorder that causes unintended or uncontrollable movements, such as shaking, stiffness, and difficulty with balance and coordination. Non-motor symptoms, such as cognitive changes, depression, sleep disturbances, and autonomic dysfunction, are also common. Symptoms usually begin gradually and worsen over time. As the disease progresses, people may have difficulty walking and talking.

DBS indications: Commonly used in patients with advanced PD who have motor fluctuations (e.g., "on-off" phenomena), dyskinesias (involuntary movements), or rigidity that is no longer well-controlled by medication.

Main target sites: STN, GPi

Effect: DBS can improve motor symptoms, reduce medication dosages, and alleviate adverse effects of long-term medication use.

❊ **Essential Tremor (ET):** * *FDA-approved (1997)* and * *CE-approved (1993)*

Disease description: ET is a neurological condition characterized by involuntary and rhythmic shaking, most commonly affecting the hands but sometimes involving the head, voice, or other body parts. Unlike Parkinson's disease, ET typically occurs during voluntary movements, such as eating or writing, rather than at rest. It is often hereditary and can range from mild to severe, significantly impacting daily activities.

DBS indications: For patients with disabling tremor that does not respond adequately to medications.

Main target site: Vim

Effect: DBS can significantly reduce tremor, improving quality of life and functional independence.

❊ **Dystonia:** * *FDA-approved under the category of Humanitarian Device Exemption (2003)* and * *CE-approved (2003)*

Disease description: Dystonia is a movement disorder characterized by involuntary, sustained, or repetitive muscle contractions that cause abnormal postures or twisting movements. It can affect a single body part (focal dystonia), multiple areas (segmental dystonia), or the entire body (generalized dystonia). Symptoms often worsen with voluntary movement and can be painful or disabling. While the exact cause varies, dystonia can be hereditary, associated with conditions like Parkinson's disease, or triggered by injury or medication.

DBS indications: For both generalized and focal dystonia, especially when refractory to pharmacological treatment.

Main target site: GPi

Effect: DBS can reduce abnormal muscle contractions and improve movement and posture over time, though therapeutic effects may take longer to appear than in other conditions.

❊ **Obsessive-Compulsive Disorder (OCD)):** * *FDA-approved under the category of Humanitarian Device Exemption (2009)* and * *CE-approved (2009)*

Disease description: OCD is a mental health condition characterized by recurring, unwanted thoughts (obsessions) and repetitive behaviors or mental acts (compulsions) performed to reduce distress or prevent feared outcomes. Common obsessions include fears of contamination, harm, or intrusive thoughts, while compulsions may involve excessive cleaning, checking, or arranging. OCD can interfere with daily functioning and cause significant distress.

DBS indications: For patients with severe, treatment-resistant OCD who have not responded to standard therapies, including medications and cognitive-behavioral therapy.

Main target sites: Anterior limb of the internal capsule or ventral striatum.

Effect: DBS can alleviate obsessive thoughts and compulsive behaviors, significantly improving daily functioning.

❊ **Epilepsy:** * *FDA-approved (2018)* and * *CE-approved (2010)*

Disease description: Epilepsy is a neurological disorder characterized by recurrent, unprovoked seizures resulting from abnormal electrical activity in the brain. Seizures can vary in type and severity, ranging from brief lapses in attention (absence seizures) to full-body convulsions (generalized tonic-clonic seizures). Epilepsy can affect people of all ages and significantly impact daily life.

DBS indications: For patients with drug-resistant epilepsy who are not suitable candidates for resective surgery.

Main target site: Anterior nucleus of the thalamus

Effect: DBS can reduce seizure frequency and severity in patients with refractory epilepsy.

❊ **Tourette Syndrome:** * *not FDA-approved* and * *not CE-approved*

Disease description: Tourette Syndrome is a neurological disorder characterized by repetitive, involuntary movements (motor tics) and sounds (vocal tics). These tics can range from simple, such as blinking or throat clearing, to complex, such as jumping or uttering phrases. The severity and frequency of tics vary between individuals, with symptoms typically appearing in childhood.

DBS indications: For severe cases of Tourette syndrome where tics are disabling and do not respond to behavioral therapy or medications.

Target Site: Centromedian nucleus of the thalamus

Effect: DBS can reduce the frequency and intensity of motor and vocal tics.

❊ **Emerging Indications:** * *not FDA-approved* and * *not CE-approved*

Major Depressive Disorder: Known as clinical depression, major depression disorder is a mood disorder characterized by persistent feelings of sadness, hopelessness, and a lack of interest or pleasure in activities once enjoyed. Other common symptoms include changes in appetite, sleep disturbances, fatigue, difficulty concentrating, and thoughts of death or suicide. Experimental use of DBS for treatment-resistant depression and ongoing studies focusing on the subgenual cingulate cortex and nucleus accumbens [37]. Abbott company launched a clinical study in September 2024, called TRANSCEND, aiming for the FDA-approval of DBS therapy for major depressive disorder.

Chronic Pain Syndromes: Characterized by persistent pain that lasts for months or even years, often beyond the expected recovery time from an injury or illness. Unlike acute pain, which typically resolves with healing, chronic pain can be debilitating, affecting daily activities, mood, and overall quality of life. DBS may be used in refractory cases of pain, targeting the periaqueductal gray matter, the anterior cingulate cortex or ventral posterior lateral nucleus of the thalamus [38].

Alzheimer's Disease: Progressive neurodegenerative disorder primarily affecting memory, thinking, and behavior. It is the most common cause of dementia, often beginning with mild memory loss and confusion and progressing to severe cognitive impairment, where individuals may struggle with daily tasks, communication, and recognizing loved ones. The application of DBS has been recently investigated, targeting regions such as the fornix to improve memory and cognitive decline [39, 3].

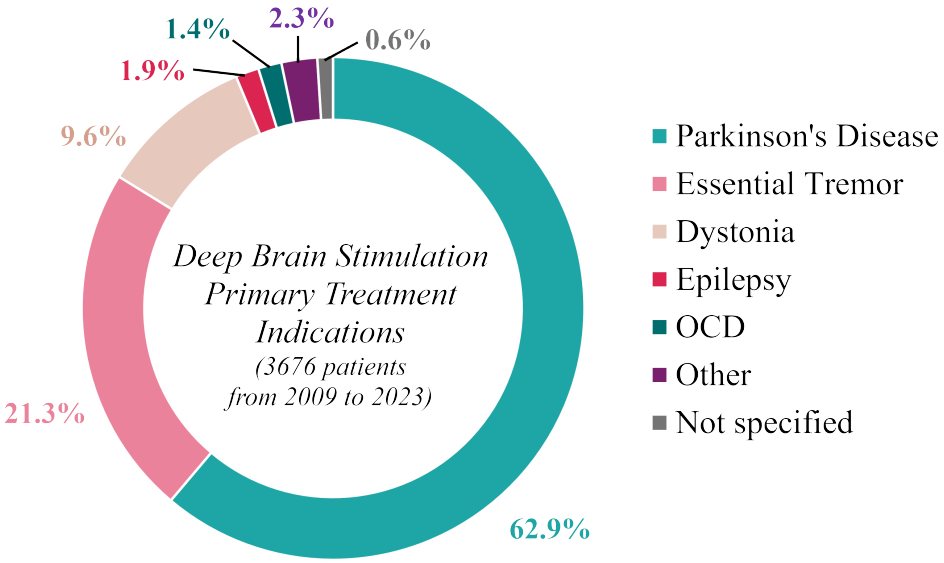

Figure 2.2: DBS primary treatment indications: Based on data collected from 2009 to 2023 within 64 centers partner of Medtronic, including 3676 patients with different treatment indications [40].

Although new clinical indications for DBS are being explored, most patients are treated for motor disorders, as illustrated in Figure 2.2. This data is derived from Medtronic Inc.'s Product Performance Report 2023 [40], which summarizes the primary indications for DBS implantation in 3676 patients across sixty-four centers worldwide from 2009 to 2023.

2.1.2 DBS Surgical Procedure

The surgical implantation of the DBS system is a highly complex procedure, with significant variation between centers regarding techniques, tools, and the time dedicated to each stage of the procedure [41, 42]. In this section, we outline the commonly used and widely adopted methods in clinical settings.

Frame-based and Frameless implantations

Since DBS involves implanting an electrode into millimeter-sized brain structures, accurately linking the patient's anatomy to the reference space used during surgery is essential. The stereotactic system serves this purpose by defining a 3D reference system and acting as a mechanical guide for precise targeting. The Leksell Stereotactic G System (Elekta AB, Sweden) has been the most widely used. In recent years, newer systems have been introduced, such as the Leksell Vantage system (released on 2017) from Elekta and the SUSy system (released on 2023) from Inomed (Inomed Medizintechnik GmbH, Germany). Before surgery, the stereotactic frame (Fig. 2.3(A)) is mounted on the patient's skull as part of the pre-operative process. Localizer plates, which contain contrast material arranged in an "N" shape (lead wire for Computed Tomography (CT) or copper sulfate solution for Magnetic Resonance Imaging (MRI)), are attached to the stereotactic frame (Fig. 2.3(B)). These plates generate hyper-intense voxels in the acquired images, enabling the creation of a 3D Cartesian coordinate system around the patient's anatomy. Once this reference space is established, the 3D coordinates for the electrode's trajectory can be determined, by defining the entry point (skull) and the target point (deep brain structures). These coordinates are used to determine the required settings for the stereotactic frame and arc, with (x, y, z) representing the target point, while the arc and ring angles are calculated from the trajectory path (Fig. 2.3(C)). After removing the localizer plates, the stereotactic arc is mounted onto the frame. The entire stereotactic system, including the frame and arc, is securely fixed to the operating table, which is immobilized to the floor to prevent any movement. The method described for the Leksell stereotactic system is similar to other stereotactic systems, with the primary difference being the shape of the localizer plates.

In the early 2000s, the frameless technique for DBS surgery began to gain interest as an alternative to the traditional stereotactic frame-based approach. This innovation sought to improve patient comfort while maintaining surgical precision [43]. Before pre-operative imaging, small fiducial markers, typically metallic screws, are attached to the patient's skull. The frameless approach links pre-operative imaging to the implantation procedure by using these markers as reference points, eliminating the need to attach a rigid frame with localizer plates. Examples of frameless systems include the NexFrame Stereotactic System (Medtronic Inc., USA), the Starfix Stereotactic Platform (FHC Inc., USA) and the SmartFrame OR

(ClearPoint Neuro Inc., USA). The NexFrame and SmartFrame system employs optical tracking to position the apparatus relative to the pre-operative fiducial markers, while the Starfix system uses a 3D-printed, patient-specific guiding apparatus attached in place of the markers. More recently, fiducial-less method has been introduced, implementing the Medtronic's O-arm (mobile Intra-operative Computed Tomography (iCT)) for the intra-operative placement of the Nexframe system [44, 45]. Despite improving patient comfort, these systems have notable drawbacks. Any angular inaccuracy at the entry point can lead to significant errors at the target deep within the brain because the center of rotation is at the skull surface—unlike arc-based methods where the rotation centers are aligned to the target area. This limitation was first recognized in the early 2010s [46, 47]. However, recent studies have shown no significant difference in placement accuracy between frame-based and frameless systems, largely due to advancements in commercial systems [48, 49].

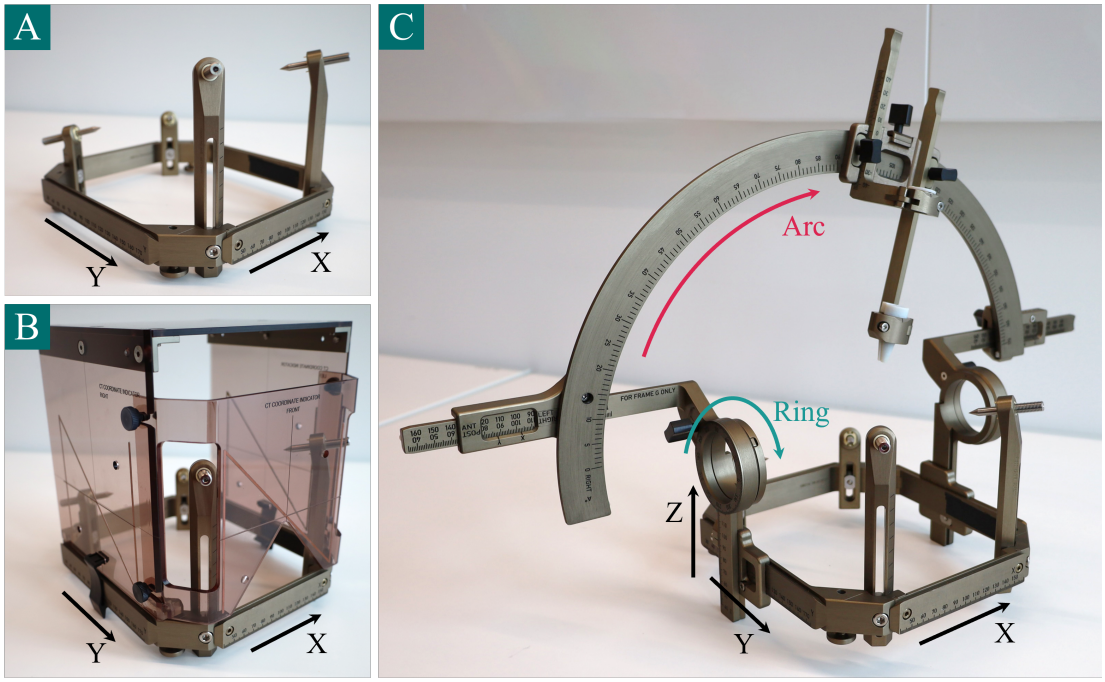

Figure 2.3: Example of stereotactic coordinate system (Elekta Leksell G system) (A) Stereotactic frame fixed to the patient's head. (B) The localizer plates mounted on the stereotactic frame enabling stereotactic imaging thanks to the lead wires in N-shape. (C) Stereotatic arc is later mounted on the frame. The ring and arc settings are respectively the rotations around X and Y.

Frameless and frame-based approaches are both established and reliable for DBS surgery. However, most centers continue to favor frame-based methods due to their extensive experience and proven reliability. Budget constraints often make transitioning to newer frameless systems less appealing, especially when the existing systems perform effectively. Additionally, the frameless procedure is more invasive, as it requires secure fixation to the skull with screws, whereas frame-based systems only involve surface-level fixation.

Surgical workflow

A simplified overview of the surgical workflow for DBS is illustrated in Figure 2.4. This proposed overview is based on the use of a stereotactic system and incorporates intra-operative testing. In the following section, we describe the pre-operative, intra-operative, and post-operative steps of the DBS surgical workflow, along with the available methods.

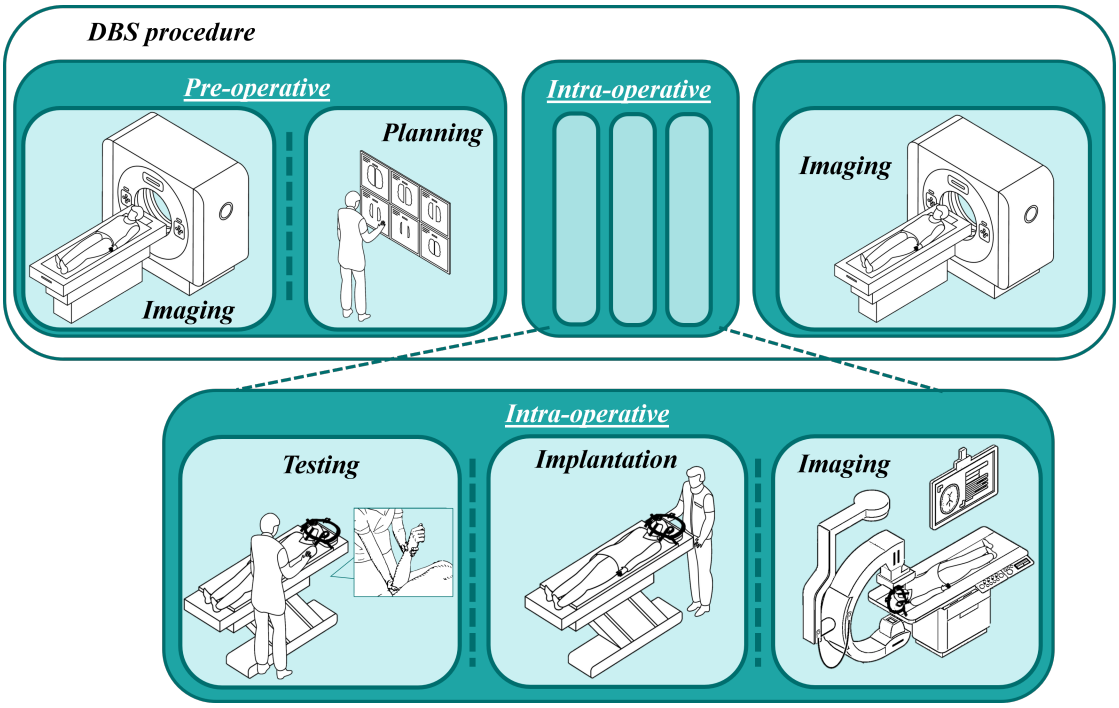

Figure 2.4: Simplify overview of the DBS surgical workflow, including the pre-operative, intra-operative, and post-operative steps.
Modified from stock.adobe.com, author: ylivdesign, N°: 527791548.

⁕ Pre-operative step: Imaging & Surgical planning

Prior to surgery, detailed brain imaging (typically MRI or CT scans) is performed to map the patient's brain, identify target areas for electrode placement, and locate markers for the stereotactic reference space. These target structures are very small, typically just a few millimeters in size, making them difficult to image and visualize. Therefore, different methods have been proposed to determine the position of the target areas.

Indirect targeting: As the traditional approach in surgical planning, indirect targeting typically refers to two primary methods. The first method involves aligning an anatomical atlas [50, 51] with the patient's brain by applying a linear spatial transformation. This alignment process is mainly performed semi-automatically [52]. The second method utilizes known anatomical landmarks, such as the anterior and posterior commissure points, to define coordinates relative

to these reference points. This technique, while simpler, relies solely on Euclidean geometry and does not involve image stretching [53].

Direct targeting: With the advances in MR imaging, direct targeting has become a viable solution for a growing number of targets. With this approach, the neurosurgeon can delineate the target anatomical structure in the patient's images themselves. Direct targeting is currently only limited to a few targets visible on standard MR sequences such as the STN [54]. For other structures, direct targeting can be achieved using modified traditional MR sequences [55], special sequences [56] or the combination of different MR sequences [57].

❊ **Intra-operative step: Testing, Implantation & Validation**

Given the challenges of accurately targeting deep brain structures during DBS implantation, intra-operative tests are commonly used to optimize electrode placement. Traditionally, DBS implantation surgeries were performed with the patient awake under local anesthesia, allowing intra-operative tests to optimize electrode placement based on immediate patient feedback. In this case, anesthetic is applied only to the scalp where the stereotactic frame is fixed and the burr holes are drilled, as the brain itself is not sensitive to pain. However, recent advancements in direct targeting techniques have enabled many centers to transition toward performing DBS surgeries under general anesthesia. The shift to "asleep" DBS surgeries aims to reduce psychological trauma and enhance patient comfort by eliminating the need for the patient to be awake during the procedure. Without intra-operative patient feedback, the electrode placement relies solely on meticulous pre-operative planning. Recent studies indicate no significant difference in the electrode implantation accuracy between awake and asleep surgeries, thanks to advancements in technology [58, 59].

Micro-Electrode Recording (MER): This method plays a crucial role in DBS procedure by capturing the neuronal activity along the electrode's path [60]. Based on characteristic spiking patterns, the electrode tip position is associated to specific anatomical structure. MER provides an additional check to ensure the electrode is passing through the expected structures, by recording local neuronal activity using the very fine tip of the MER electrode (25 µm in diameter, 100 µm in height) (Fig. 2.5(B)). This is especially important when certain targets are not clearly visible on pre-operative imaging. To address possible discrepancies between the planned and actual electrode trajectory, up to five parallel MER electrodes, arranged in a cross pattern with 2 mm spacing, can be implanted offering a broader "field of view". However, this method extend surgery time and increases the risk of complications, such as bleeding [61].

Local Field Potential (LFP): The macro contact of the MER electrode (550 µm in diameter, 1.4 mm in height) is used to record signal from a larger population of neurons. LFPs can also be recorded using the contacts from the DBS electrode (Fig. 2.5(A)). This approach is especially useful for STN implantation in Parkinson's disease patients, as the motor region of the STN shows increased beta-band activity

[62]. However, these measurements are used mainly post-operatively to optimize the stimulation programming [63].

Stimulation tests: Theses tests involve delivering electrical pulses at various amplitudes along different positions of the electrode's trajectory within the target region. A neurologist observes changes in the patient's symptoms and conducts specific tests to identify both beneficial effects and potential adverse effects. Stimulation testing during the surgery helps define the "therapeutic window", i.e. the range of stimulation amplitudes that produce the best clinical effects without causing adverse effects [64]. Based on these results, the optimal depth for final electrode placement is determined. These tests can be performed using the DBS electrode or the macro-contact of the MER electrode.

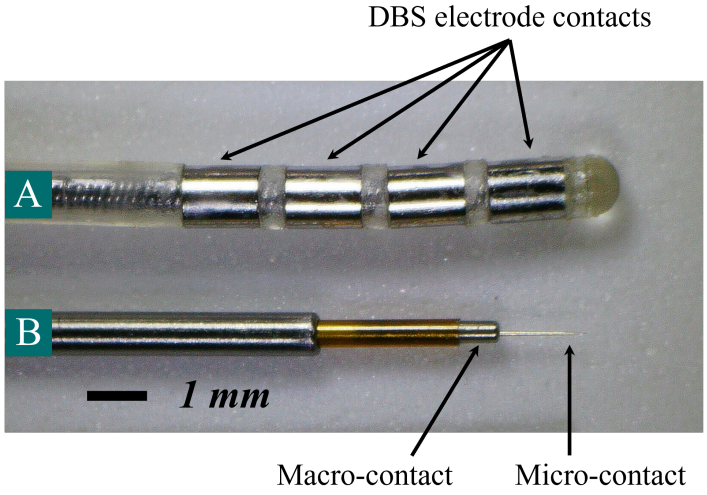

Figure 2.5: Picture of the DBS electrode contacts. (A) Medtronic 3389 DBS electrode (B) Medtronic LeadPoint MER electrode.

Once the final position of the DBS electrode has been defined considering the different intra-operative tests, imaging is performed to validate its position in relation to the pre-operative target. Depending on the clinical centers, different modalities such as 2D X-ray, fluoroscopy, Intra-operative Magnetic Resonance Imaging (iMRI) or iCT may be employed. This imaging step provides a first visual confirmation, with varying degrees of detail, of the electrode's position before it is anchored. After the DBS electrode anchoring to the patient's skull and suturing of the scalp, an additional 3D imaging is performed to obtain the 3D position and orientation of the electrode and verify the absence of hemorrhage.

⁕ Post-operative step: Imaging & Beyond

This last imaging step generally requires moving the patients to the imaging room as most operating rooms are not equipped with 3D imaging technology such as iCT or

iMRI. In contrast, hybrid operating rooms, i.e. equipped with imaging technologies, allow the procedure to be conducted in a single location. This setup greatly enhances patient comfort and reduces operating time, as it minimizes the need for patient transport between the operating and imaging facilities. In this context, the angular and spatial position of the electrode, as well as the absence of hemorrhage, can be confirmed before closing the skull and suturing the scalp. After the complete implantation of the DBS electrode, the IPG is generally placed subcutaneously, usually in the chest. This procedure is done under general anesthesia, either during the same surgery or the following day, depending on the surgical plan. The extension cable connecting the electrode to the IPG is tunneled along the patient's neck.

Long-term stimulation is not activated immediately after surgery, as the initial lesioning effect from electrode implantation can temporarily improve symptoms, potentially biasing early settings. This effect diminishes after a few weeks, allowing for the first set of stimulation parameters [65]. Between 3 to 6 months post-surgery, further adjustments are often necessary due to various factors. First, identifying the optimal stimulation parameters can take time, as changes in symptoms must be monitored before adjustments can be made. In response to the effectiveness of DBS, medication dosages also need to be altered. The adjusted settings represent a more stable, long-term balance between disease progression and the combined effects of medication and DBS. As a result, the programming task remains an arduous task for clinicians. Symptoms are continuously assessed, before surgery, after surgery, and throughout the programming phase, using tools previously mentioned such as UPDRS for PD patients or ETRS for ET patients.

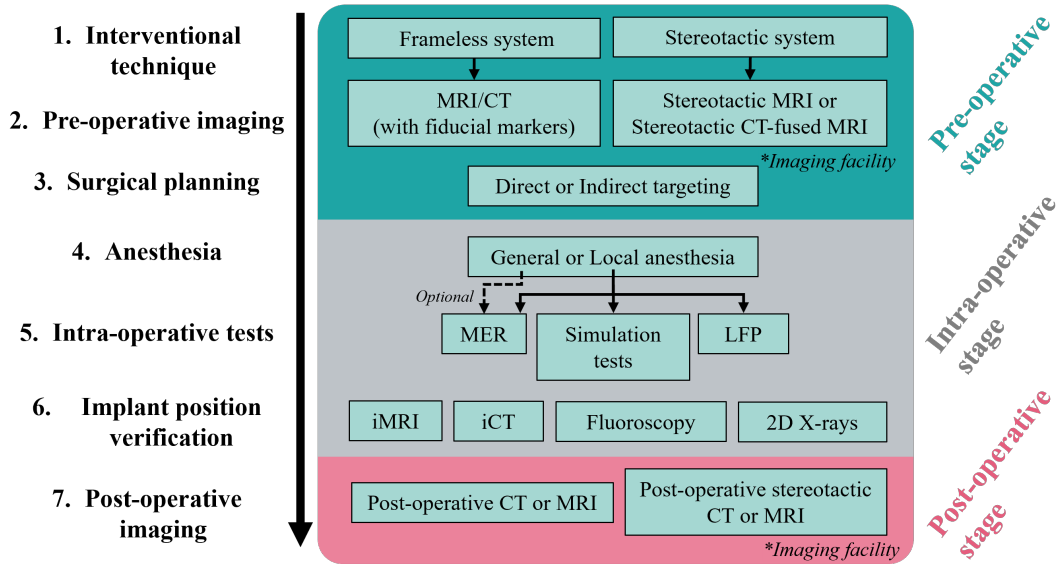

Figure 2.6: Detailed overview of the DBS surgical workflow with for each step, the different methods available.

A detailed overview of the different options in the surgical workflow are presented in Figure 2.6. Although DBS surgery is generally regarded as safe, it still carries risks such as infection, bleeding, or stroke during the implantation process, which may lead to neurological complications. There is also a limited risk of hardware-related issues, such as electrode migration or device malfunction. In the long term, hardware failures remain the main risk for patients. In addition, the neurostimulator, or IPG, typically needs to be replaced every 3 to 7 years due to battery depletion, depending on the specific device and the level of stimulation required [66]. Rechargeable models can last significantly longer, up to 9 to 15 years, with regular charging. The battery life varies based on factors such as stimulation settings and patient needs. When the battery is depleted, a surgical procedure is required to replace the IPG.

The DBS implantation procedure is highly individualized, with careful consideration given to the patient's specific neurological condition, brain anatomy, and response to stimulation during surgery. The surgical steps including the intra-operative tests and validation imaging are also highly dependent on the neurosurgeons' choices and equipment available.

2.1.3 Recent Technical Development

Intra-operative imaging techniques

DBS is constantly evolving and the 2010s has been a period of considerable progress, particularly in intra-operative imaging techniques. Traditionally, DBS surgeries were performed with the patient awake, relying on real-time feedback from the patient and external neurological assessments to guide electrode placement. However, with the introduction of advanced intra-operative imaging modalities such as iMRI and iCT [67], the surgical approach has shifted, aiming for greater accuracy, reduced operating time, and enhanced patient comfort. This shift, while promising, presents its own set of challenges, particularly in terms of equipment availability, clinical expertise, and adoption across different surgical centers.

In DBS surgeries, electrode placement accuracy is critical. Even one millimeter deviation can result in suboptimal stimulation, leading to reduced therapeutic efficacy or adverse effects [68]. By the early 2010s, the quest for minimizing such errors reached a threshold and few centers adopted intra-operative imaging to enhance the overall surgical workflow [69, 70]. Intra-operative imaging systems such as iMRI and iCT, enable the visualization of the electrode's trajectory and position relative to deep brain structures during the intra-operative stage. The advantage of iMRI over iCT is the visualization of brain structures and the possibility to consider some brain movements (brain shift) occurring intra-operatively with the opening of skull and dura, altering the position of the brain target with respect to the stereotactic frame [71, 72]. Recently, intra-operative functional MRI (ifMRI) has been introduced to assess the brain's real-time response to electrical stimulation [73]. It helps optimize electrode placement by targeting desired areas while avoiding regions critical for functions like speech or movement, offering deeper insights into both the patient's condition and DBS mechanisms.
Conventional surgeries often involve longer operating times due to the need for patient

interaction during electrode placement, as well as the potential shifts to the imaging and operating rooms. In contrast, intra-operative imaging reduces these logistical complications, simplifying the workflow and potentially shortening surgical times particularly in the case of iCT [74]. In addition, intra-operative imaging improves the comfort of the patient and clinicians, particularly when used in "asleep" DBS, where the patient is fully anesthetized [59]. The use of intra-operative imaging is expected to grow as more centers adopt this technology. However, its widespread adoption faces some limitations. First, the number of imaging acquisitions performed during the surgery is limited by either the duration of the imaging process or concerns about radiation exposure. Second, localizing the exact DBS position by visual inspection using iMRI and iCT during surgery is still a great challenge due to mentioned metal artifacts [75, 76]. In addition, a major factor influencing adoption is the availability of advanced imaging equipment. iCT is more commonly used than iMRI, as iMRI requires a dedicated MRI-compatible operating room, which limits its availability to larger, well-funded medical centers. Many smaller or less research-focused clinical settings still rely on 2D X-ray imaging. It is also important to note that many centers have been slow to adopt these new technologies due to the long-established expertise of their neurosurgical teams in both on surgical techniques and imaging technologies.
It is also important to note that intra-operative imaging approach is primarily compatible with frameless surgery setups, which are still not widely adopted. Stereotactic surgery, with its established reliability and accuracy, continues to be the gold standard in most centers. Recently, mobile iCT systems, such as Medtronic's O-arm, have gained interest due to their versatility [77, 78], easier integration into the operating space and compatibility with stereotactic systems. However, concerns about radiation exposure persist, which limits their use to the verification of the final electrode placement rather than for real-time monitoring during the procedure. Additionally, many studies assessing the effectiveness of intra-operative imaging tend to be single-center investigations, with results that are often highly dependent on the specific equipment and surgical protocols used. Introducing new imaging technologies or altering established surgical procedures entails risks and requires surgeons to undergo additional training, which can significantly hinder widespread adoption.

Innovations in DBS Device Design and Functionality

Conventional DBS electrodes feature four to eight cylindrical contacts spanning from the tip to ten of millimeters. These cylindrical contacts produce radial current flow, stimulating the surrounding tissues. Considering the irregular and non-spherical shape of some anatomical structures such as the STN, Vim, or GPi, achieving comprehensive coverage with a single electrode is challenging [79]. Due to its radial shape, the stimulation can activate unintended structures along with the target area.

Recent years have seen the introduction of new electrode designs that allow for shaping the electric field along the electrode axis. Directional DBS electrodes have been developed with the hope of reducing stimulation-induced adverse effects and optimizing clinical benefits by enabling more tailored stimulation to individual patients and compensating for suboptimal electrode placements. Those electrodes, from which a few examples are presented in Figure 2.7

use several contacts around the circumference of the electrode rather than the traditional ring design [80]. In 2015, the Vercise Cartesia directional electrode from Boston Scientific Corporation was the first directional lead to receive the CE mark for marketing in Europe, followed by FDA approval in 2017 [81]. Clinical studies involving these advanced electrodes have highlighted the innovative nature of this technology and its benefits [82, 83]. However, the increased number of electrode contacts and the more complex geometries significantly complicate the programming process. The already arduous task of manually testing various monopolar stimulation settings becomes a substantial and costly challenge for the neurologists and DBS nurses. In these cases, both the precise position of the electrode and the knowledge of its rotational orientation relative to the brain's anatomical structures are crucial for tailoring the current distribution and stimulation volume to the intended target area.
Another advancement in DBS devices is the integration of sensing capabilities into the electrode. These electrode contacts can be used to record LFPs, which provide valuable insights into neuronal activity. While this sensing function was initially used intra-operatively to record LFP signals, it is now available post-operatively. This functionality helps in optimizing the stimulation parameters [84] but also opens the door to adaptive DBS stimulation [85, 86], allowing the electrical stimulation to be adjusted according to the patient's needs and daily condition, offering a more personalized treatment approach. However, adaptive DBS is still in the research phase and has not yet been implemented in clinical practice.

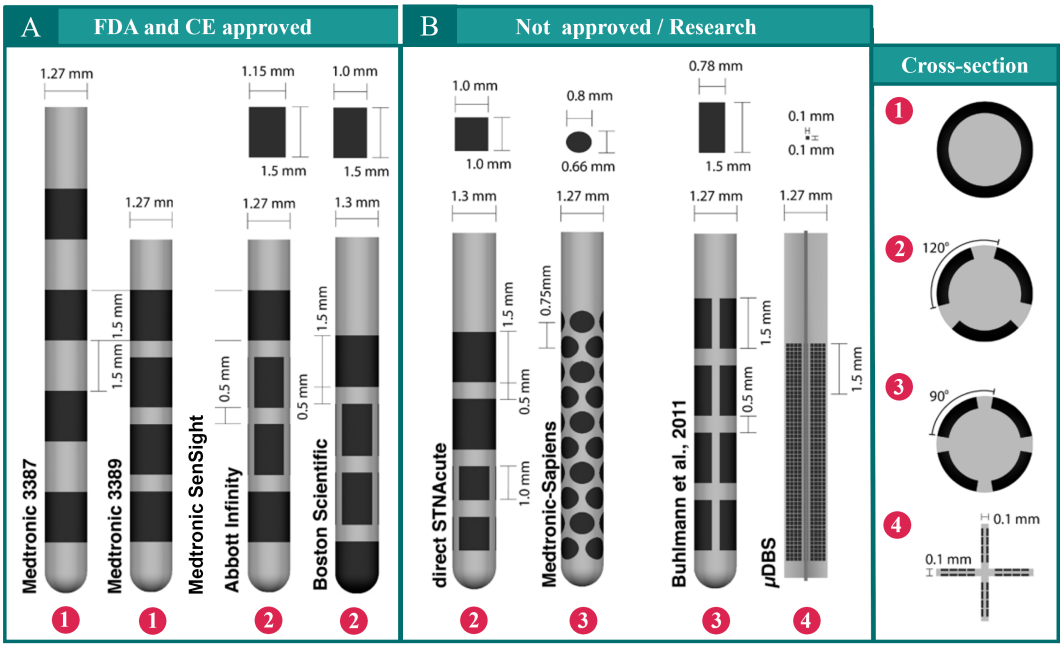

Figure 2.7: Examples of (A) commercial and (B) research-based DBS electrodes, including emerging directional DBS technology. Electrode designs from MedTech companies (Medtronic, Abbott, Boston scientific) and research-based design from Buhlmann [87] and the µDBS from Willsie [88]. The numbers links the electrode's side view to its cross-section.
Derived from [89], published under CC-BY-3.0.

2.1.4 Remaining Challenges

DBS has undergone significant advancements in recent years, particularly in terms of surgical techniques and electrode design. The following section examines the remaining challenges in DBS procedure.

Challenges in DBS Electrode Positioning

Intra-operative imaging enhances both patient comfort and surgical efficiency by reducing the need for patient displacement and streamlining procedural steps. However, it provides imaging only before and after the DBS electrode implantation process. This leaves neurosurgeons without real-time feedback on the electrode's position and orientation during the procedure. This feedback holds great importance as it could validate the implantation process, alert to trajectory deviations, and provide precise electrode positioning during LFP recordings. So far, only the information about the electrode implantation depth, i.e. the distance from the brain surface is provided using the manual or motor-guided implantation microdrive. This information is crucial for correlating neuronal activity with specific brain structures. Despite its potential, this challenge remains unmet, as no clinically available systems currently address it.

Challenges in DBS Stimulation Programming

Modern DBS programming predominantly relies on manual, trial-and-error methods where clinicians adjust settings based on patient responses [90]. This method is time-consuming and may expose patients to discomfort without guaranteeing optimized parameter settings. Patients require several visits to the programming center within the first six months after surgery [91].
The complexity of programming increases significantly with the number of potential parameter combinations. For a basic four-contact electrode, there are over 25,000 possible combinations when considering variables such as pulse width, frequency, amplitude, and 65 options for contact configurations [92]. In practice, the number of combinations tested is largely reduced thanks to the surgical feedback, neurologists' experience and insights from the scientific community. As the number of electrode contacts increases, the mathematical possibilities grow exponentially, making manual programming practically impossible for more complex electrode designs [89]. The introduction of assistance tools for programming aims to address these challenges by suggesting stimulation settings to clinicians, optimizing treatment efficacy while reducing the programming workload. It also offers the potential for remote programming, further easing the burden on both patients and healthcare providers [93, 94].
In this context, both academic and commercial programming assistance solutions [95] have emerged. These solutions enable visualization of anatomical structures alongside the predicted volume of activated tissue. However, the effectiveness of these tools relies on the precise knowledge of the electrode's position and orientation in relation to the brain. By precisely identifying the position of the electrode contacts relative to the target structures, the intensity and direction of stimulation can be fine-tuned to activate therapeutic sites while avoiding areas that could cause adverse effects, thereby optimizing patient outcomes.

The field of DBS is undergoing significant advancements. However, these developments also introduce new challenges, particularly in ensuring accurate surgical feedback and managing the complexity of post-operative programming. Overcoming these challenges requires the integration of advanced imaging, navigation, and programming technologies. Continued research and development in these areas are essential to fully realize the potential of DBS therapy and to overcome the remaining difficulties in its clinical application. This thesis addresses the challenge of real-time monitoring for DBS electrode placement during surgery, ensuring both the accuracy and safety of the implantation. Additionally, it can help refine stimulation parameters post-surgery for improved therapeutic outcomes based on the known electrode placement.
To meet this critical need, several key requirements must be fulfilled. First, the system must monitor both position and orientation, with high precision, achieving less than 1 mm spatial error and about 1° angular error —matching or exceeding imaging standards. Additionally, the localization of the electrode should be accurately referenced to anatomical brain structures. The proposed localization technique must integrate seamlessly into the existing surgical workflow and be adaptable to various methods used during implantation, such as MER or LFP recordings. These considerations are crucial for integrating a novel system into current DBS procedures and ensuring it provides substantial added value.

2.2 Localization and Navigation Systems for DBS

Over the past decade, researchers have focused on improving DBS surgery by either proposing new surgical tools and procedures or developing complementary tools to enhance the current workflow. The overarching goal of these advancements is to improve patient safety, optimize electrode placement, and potentially reduce the duration of surgery. This section explores the state-of-the-art exploratory methods proposed in the last decade for the localization of DBS electrodes mainly for the intra-operative stage.

2.2.1 Advances in Localization Techniques of DBS electrode

Novel surgical workflows based on non-standard systems have been proposed for DBS surgery. One notable line of research is the investigation of magnetically steered catheters for surgery. As part of this effort, Nelson's team at ETH Zurich first investigated this technique for cardiac ablations [96, 97]. The method was later adapted for potential use for the guidance of DBS electrodes [98]. This innovative approach involves using external magnetic fields to guide the electrode along non-linear trajectories. The method is combined with fluoroscopy to provide real-time feedback on electrode positioning. Unlike conventional procedure, this method does not integrate the stereotactic system. While this approach represents a radical departure from current DBS procedures, it introduces the potential for greater flexibility in electrode placement and may eventually offer a novel alternative to conventional techniques. However, given the drastic changes this method would require in DBS workflow, it is likely to take time before it reaches clinical practice.

From a different perspective, alternatives to MER for guiding and verifying the implanted brain structures have been explored. Although the current clinical trend leans towards using iMRI or iCT with limited reliance on MER, there is increasing interest in developing alternative methods for distinguishing brain structures. For example, optical fiber guidance has been tested on post-mortem brain tissue [99, 100]. This emerging technique aims to offer real-time feedback on electrode positioning within brain structures. While the principle has been demonstrated using a custom optical probe, it has yet to be integrated into a DBS electrode.

Several non-invasive technologies have also been investigated for their potential to localize DBS electrodes intra-operatively. These methods are described and their potential for DBS is discussed. Figure 2.8 summarizes the added value of each localization method in terms of accuracy, frequency, integrability, compatibility, degrees-of freedom and anatomical information provided.

- ❉ **Transcranial Sonography:** TCS estimates the DBS electrode position by measuring distances through the temporal bones using a transducer. The brain structures visible on TCS are not the primary surgical targets but rather hyper-echogenic landmarks, such as the substantia nigra [4, 101]. The position of the target structures is derived from these landmarks. Additionally, TCS provides positional information limited to a single plane parallel to the orbitomeatal line. These studies were conducted post-operatively, with some patients excluded due to inadequate bone window dimensions. Despite its promise, TCS has notable limitations for intra-operative use, including incomplete information on electrode position and orientation, and incompatibility with the stereotactic frame.

- ❉ **Electroencephalography:** EEG is typically used to investigate the mechanisms of DBS through scalp electrodes. During DBS, the electrical pulses generate artifacts in the EEG signal, which can be analyzed to estimate the location of the electrode [102]. However, intra-operative use of EEG is limited due to the need for a large number of electrodes and further improvements are needed to enhance its accuracy, which currently has a maximum error of 1.5 cm. Post-operative EEG-based localization has been recently proposed and proved to be a feasible alternative for the detection of the electrode orientation, with an error of about 1° [5].

- ❉ **Electric field stereotaxis:** EFS has also been explored as a non-invasive method for electrode localization. A recent study by Fang et al. [103] in 2024, introduced the concept of EFS, which involves measuring the electrical fields generated by a current injection electrode integrated into a surgical instrument. Scalp electrodes are used to measure signals and estimate the electrode position. This method showed promising results, with an average localization error of 3 mm and angular error of 2°. This study was conducted on an experimental bench and has not yet been introduced clinically. In the context of stereotactic neurosurgery, the use of scalp electrodes may limit the feasibility of applying EFS for DBS electrode monitoring. This technology is introduced as an extension of electric impedance tomography which was already assessed few years ago for the reconstruction of the tissue environment surrounding the MER electrode [104].

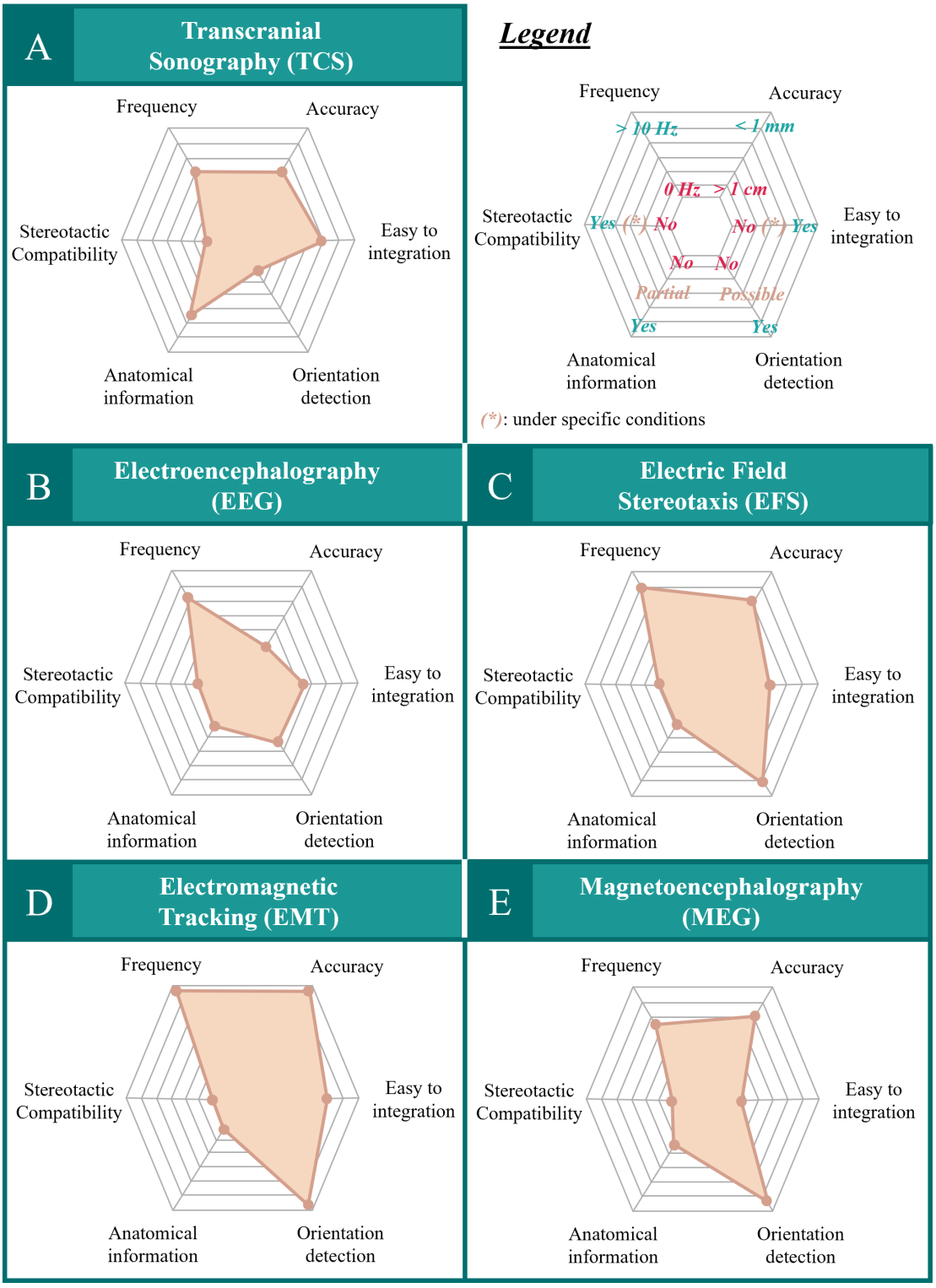

Figure 2.8: Potential localization systems eligible for DBS electrode tracking. The criteria are chosen to assess their interest and added value.

- **Magnetoencephalography:** Another non-invasive approach involves using Magnetoencephalography (MEG) for the localization of DBS electrode. Traditionally, MEG is used to measure the magnetic fields produced by neuronal activity. However, by measuring the magnetic fields generated by DBS electrode stimulation, Yalaz [105] demonstrated its possible localization with an accuracy of 2 mm and 4° in locating the DBS electrodes. This technique is currently limited to post-operative use, as it requires a large MEG machine housed in a shielded room to prevent magnetic field interference. While this method is not yet practical for intra-operative use, advancements in miniaturized on-scalp MEG sensor [106, 107] hold promise for enabling MEG-based electrode localization in free-environment like clinics and potentially during the surgery.

- **Electromagnetic tracking:** EMT technique involves generating a localized magnetic field around the patient's head and tracking the position of magnetic sensors embedded in the surgical tool relative to this field. This approach offers continuous feedback during the procedure, eliminating the need for intra-operative imaging while maintaining similar localization accuracy. Localization, in the context fo DBS, using an EMT system for surgical navigation has already been demonstrated clinically by Burchiel [108] in 2020. The study was performed using a frameless approach and achieved performance comparable to CT imaging. However, current EMT systems are highly sensitive to the presence of metallic or magnetic objects within the tracking volume, which limits their application in surgeries involving much equipment.

While these exploratory methods show great promise, most of them are not yet fully compatible with intra-operative use or the established stereotactic surgery workflows of DBS procedures. The challenge remains to develop a system that offers real-time, accurate feedback on electrode position and orientation while maintaining compatibility with stereotactic techniques. Electromagnetic tracking systems stand out as the most viable option, as they have already demonstrated clinical success. The next step would be to adapt EMT techniques for use with stereotactic frames, potentially making them a routine part of DBS surgery.

2.2.2 Existing Electromagnetic Tracking Systems and their Limitations

EMT systems in neurosurgical applications provide a highly precise and minimally invasive means of guiding instruments during brain surgery. These systems consist of electromagnetic sensors integrated into medical instruments and an external magnetic field generator. It allows for accurate localization without the need for continuous radiation, as seen in traditional imaging techniques like X-rays or CT scans. This technology is particularly valuable in procedures like DBS, where precise electrode placement is critical to the success of the treatment. This section describes the existing EMT technology available for clinical applications.

Description

EMT systems are traditionally used for surgical navigation in image-guided interventions when there is no line of sight to the target. EMT can also be used for surgical simulation. When combined with the visualization of the anatomical target based on the patient's imaging (CT or MRI), these systems are commonly referred to as Electromagnetic Navigation System (ENS). Current clinical applications leveraging EMT for instruments localization include bronchoscopy [109], neurosurgery [110] and ear, nose and throat surgery [111]. Few ENS or EMT systems are presented in Table 2.1.

Table 2.1: Example of commercial EMT systems and associated indications.

Clinical Indications	Systems
Bronchoscopy	Medtronic superDimension (Medtronic Inc., USA)[112] Veran SPiN (Easmed Pte Ltd, Singapore) [113]
Neurosurgery	Medtronic StealthStation AxiEM [114] Brainlab Kick EM (Brainlab AG, Germany) [115]
Ear, Nose and Throat (ENT) Craniomaxillofacial surgery	Fiagon EM (Fiagon GmbH, Germany)[116]
*Medical/Research purposes	NDI Aurora (Northern Digital Inc., Canada) [117] NDI Trakstar (formerly sold by Ascension Technologies) [118] Polhemus Fastrak (Polhemus Inc., USA) [119]

Generally, an EMT system consists of two primary components: a Field Generator (FG) that creates a spatially dependent magnetic field, and a magnetic sensor that measures this field to determine its relative position and orientation in relation to the FG. In this setup, one component remains fixed at a known location, while the other is mobile, with its position being unknown. Commercially available EMT systems typically use a fixed FG and sensors attached to the objects being tracked. In addition to the FG and the sensors, ENS or EMT systems include also a controller, a visualization computer and a registration system (Fig. 2.9) :

- **Electromagnetic Field Generator:** The core of the system is the FG, which creates a low-intensity ac magnetic field in the operating area, typically around the patient's head for neurosurgery. This field is generated by a set of coils positioned near the surgical area (Fig. 2.9(1)). The magnetic field is carefully shaped and calibrated to cover the operative space and allow precise spatial tracking.

- **Tracking Sensors:** The sensing technology is based on micro-coils or search coils. The tracking principle relies on the inductive principle. Small, varying voltages are induced in the micro-coil by the surrounding electromagnetic field. These voltages are translated into real-time positional data. Surgical instruments (such as probes, catheters, or electrodes) are equipped with these micro-coils usually embedded within or attached to the tool (Fig. 2.9(2)).

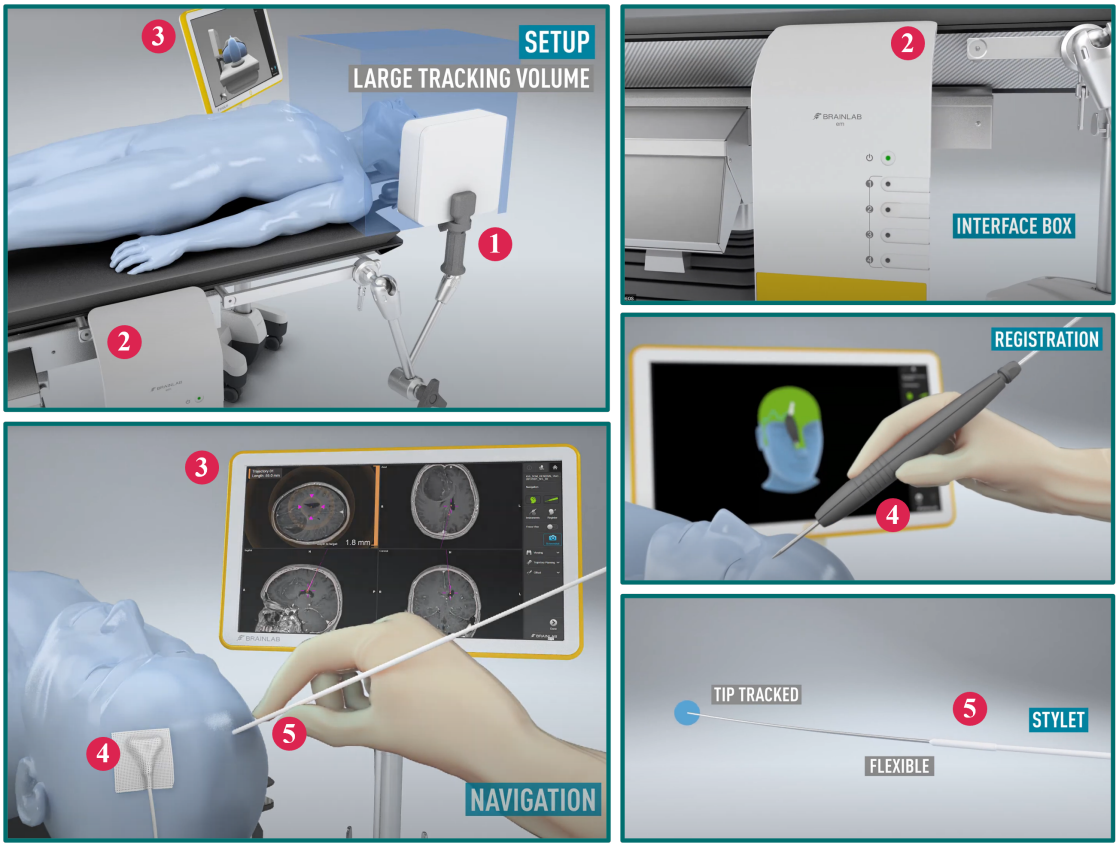

Figure 2.9: Overview of commercial EMT set-ups and components. (1) Electromagnetic Field Generator, (2) Interface box, (3) Visualization computer, (4) Patient registration system, and (5) Tracking Sensors or Stylet.
Courtesy from @Brainlab: Kick EM - Electromagnetic surgical navigation [120].

❉ **Interface box or controller:** The EMT system is connected to an interface that processes the signals from the tracking sensors and the generator. Advanced algorithms compute the exact position and orientation of the surgical instruments (Fig. 2.9(3)).

❉ **Visualization Computer:** The EMT interface box is connected to a visualization computer and provides positional information of the tracked instruments. This computer usually integrate pre-operative imaging data, such as MRI or CT scans, allowing the surgeon to visualize the instrument's real-time position overlaid on anatomical structures. In the case of EMT systems for neurosurgery, the tracked instrument position overlaid on the patient's brain images (Fig. 2.9(4)).

❉ **Patient Registration:** Before surgery, pre-operative imaging, such as CT or MRI, is acquired and uploaded into the visualization computer. In the case of neurosurgery, the patient's head is "registered" to align the pre-operative imaging with the real-time position. This registration process is typically achieved by referencing external markers

or anatomical landmarks that are visible in both the imaging data and during surgery. One method involves attaching fiducial markers to the patient's head, either by screwing them or sticking them to the skin. Alternatively, a second method continuously maps the patient's anatomical landmarks by using a stylet or probe equipped with sensors (Fig. 2.9(5)), which is moved across the patient's face. Both methods are manually performed and implies an additional step in the surgical workflow.

EMT systems are increasingly used for surgical guidance. EMT systems provide continuous localization without requiring intra-operative imaging, achieving submillimeter spatial error and an angular error inferior to 1°, under optimal conditions. However, their performance can be impacted by the presence of metallic or ferromagnetic objects in the surgical environment, which may distort the electromagnetic fields. The following section describes in more detail the limitations of existing EMT systems.

Limitations

While EMT systems offer several advantages, including radiation-free guidance and real-time instrument tracking with submillimeter spatial error, they still face technical challenges:

1. **Electromagnetic Interference (EMI)**:
   External electromagnetic fields induced by ferromagnetic materials or electronic devices interfere with the electromagnetic field generated by the FG. Since EMT systems rely on the known geometry of the generated electromagnetic field, their accuracy is highly impacted by field distortions. This phenomenon can be visualized as deviations in the magnetic field lines originally produced by the FG, as shown in Figure 2.10(A). Common sources of EMI in surgical environment include surgical tools made of ferromagnetic materials (such as iron, cobalt, and nickel) and electronic devices like screen monitors.
   The second category of EMI is known as conductive distortions. The ac electromagnetic fields from the FG induce Eddy currents within conductive materials. These currents generate a secondary field that interfere with the primary field (Fig. 2.10(B)). The secondary field is present only during FG activation and operates at the same frequency, making compensation particularly challenging. The magnitude of these conductive distortions depends on factors such as the size, composition, proximity, and shape of the distortion sources. Conductive distortions are a critical factor limiting the compatibility of current EMT systems with surgical environments.

2. **Field Strength Limitation**: The electromagnetic field generated is strongest near the FG, meaning that accuracy decreases as the distance from the generator increases. This poses a challenge in deep brain surgery, as precise targeting is critical and close proximity to the patient's head is limited by potential equipment and the sterile zone.

3. **Registration accuracy**: Patient movement, even slight, can result in misregistration. For this reason, the patient's head is often immobilized during the procedure. If fiducial markers are used, they must remain in the exact same position from pre-operative imaging to surgery. Shifting of markers, even slightly, can reduce the accuracy of registration, requiring re-registration or adjustments.

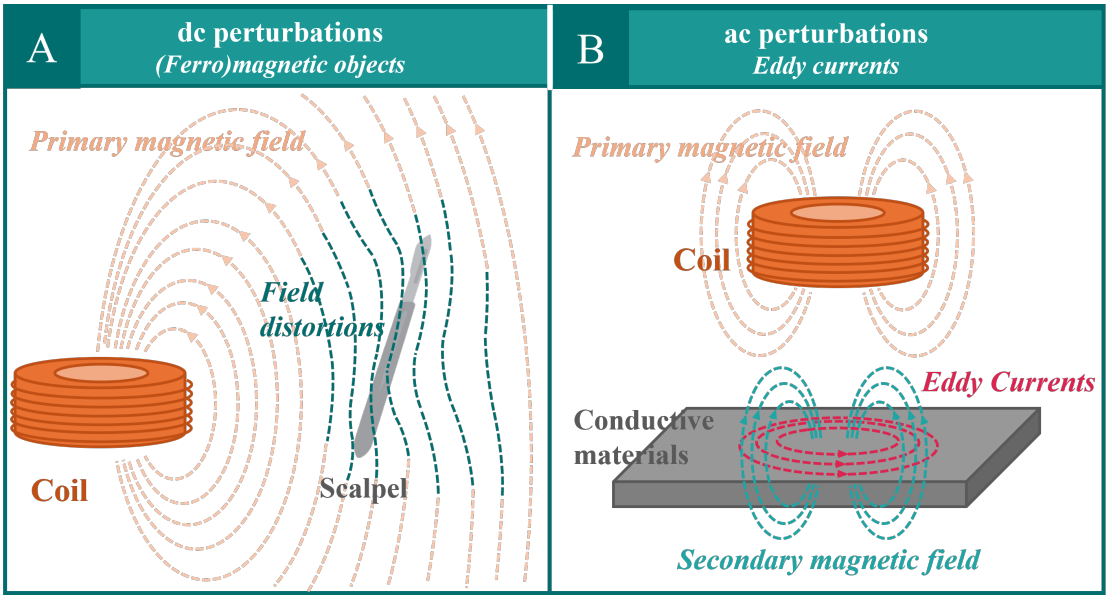

Figure 2.10: Examples of EMI: (A) dc perturbations generated from (ferro)magnetic objects and (B) ac perturbations induced by Eddy currents in conductive materials.

4. **Latency and Drift**: Over long periods, sensor drift or latency can reduce the system's accuracy, requiring recalibration of the system or re-registration during the procedure.

Overcoming these technical challenges is essential to ensure the accuracy and reliability of EMT systems in neurosurgery. However, several obstacles persist, including the vulnerability of these systems to interference from metallic objects such as stereotactic systems and imaging systems.

2.2.3 Novel Electromagnetic Tracking Systems

EMT systems have become a cornerstone for image-guided interventions, with applications ranging from neurosurgery to bronchoscopy and ear, nose, and throat surgery. Research in this field has largely focused on two main approaches: improving existing technologies and proposing novel EMT principles to overcome current limitations. This subsection explores these two directions, discussing the advancements in compensating for EMI and novel tracking principles.

One major research focus is improving existing EMT technology, particularly addressing the susceptibility of these systems to EMI. EMI remains a significant challenge for the precise localization of surgical tools, especially in environments with numerous metallic objects, such as operating rooms. Current compensation methods rely on the pre-mapping of the distorted electromagnetic field to account for variations in the surgical environment. These compensation techniques have been designed to mitigate known sources of interference, such as imaging systems [121, 122] or ultrasound probe [123], but compensating for unknown perturbations remains a more difficult task.

One significant advancement in this area comes from the work of Li [124], who proposed the use of ramp excitation as an alternative for traditional sinusoidal excitation. The induction principle based on sinusoidal waveform is presented in Figure 2.11(A). The excitation ramp approach was previously tested using a quadratic-rectangular excitation waveform [125]. EMT systems commonly based on sinusoidal waveform, operate by determining the sensor position from the amplitude of the voltage induced in the micro-coil. However, this amplitude is affected by conductive distortions, leading to position miscalculations. The induced voltage in the micro-coil varies due to direct and indirect induction, the last resulting from the double differentiation of the emitted signal when passing through conductive materials. By distinguishing signal components originating from the emitter versus those caused by distortions, the position can be estimate from the unaffected signal component. This separation is achievable using alternative waveforms such as quadratic-rectangular or ramp excitation. Preliminary studies showed that the proposed approach improved tracking accuracy [126], though a full evaluation is still needed. With modified waveforms, the output rate is slower than those of commercial systems.

Another noticeable development in EMT technology is the introduction of wireless tracking systems, as demonstrated by Philips Research [127] and represented in Figure 2.11(B). This method relies on ac magnetic fields but replace traditional micro-coils with miniature magneto-mechanical resonators (0.8 mm x 1.9 mm). While these systems still face some limitations in overcoming EMI, their wireless nature holds significant potential for seamless integration into surgical tools but also opens the door to new applications where wired systems would be impractical, such as implant monitoring. A key question arises regarding the compatibility of magneto-mechanical resonators with strong magnetic fields, such as those within an MRI environment. These resonators consist of two spherical NdFeB magnets (composed of neodymium, iron, and boron), one fixed to a cylindrical housing and the other suspended by a thin filament. These magnets interact with external magnetic fields, including those generated by an MRI. We estimates the magnetic torque and force were respectively of 220 μNm in 3T MRI and 220 μN at the entrance of the bore which exhibit gradient of 3 $T.m^{-1}$ equivalent to 0.15 kPa considering the dimension or the resonator. This might pose a risk, as the friction force in the brain is reported around 0.2 to 0.6 kPa [128]. Additionally, due to the design of the resonators, there is a high likelihood that the external magnetic field — being substantially stronger than the attractive force between the two magnets — could cause a realignment of the spherical magnets. This misalignment could lead to the rupture of the filament suspending the mobile magnet, ultimately rendering the resonators unusable as EMT sensors. Partial demagnetization of the spherical magnets is also a possibility.

While improvements to existing EMT technologies are crucial, researchers are also exploring novel tracking methods that rely on entirely different principles. Three main approaches have been proposed, each offering unique advantages and limitations.

- **Magnetic Field Camera (MFC)**:
  The first approach is the use of an array of integrated magnetic sensors, often referred to as a MFC (Figure 2.11(D)). In this system, a permanent magnet in the target device is

detected by the sensors of the MFC, allowing for precise localization. This method enables the use of extremely small magnets, ranging from micro to millimeter dimensions. The first demonstration of MFC for tracking purposes occurred in 2001, using Hall-effect sensors to monitor the position and orientation of a cylindrical permanent magnet measuring 6 mm by 7 mm within a 3D volume [129]. Several studies have explored different sensor array configurations [130] and sensing technologies [131] to achieve larger Measurement Volume (MV) or to reduce the dimension of the magnets used. For instance, Sebkhi et al. [132] implemented a magnet measuring 4.8 mm by 1.6 mm, achieving a position error of 1.8 mm within a MV of 4 x 6 x 7 cm^3. However, the magnet's dimension still poses limitations for integration into small medical devices, such as DBS electrodes. Moreover, as the magnet size decreases, the MV shrinks, limiting the effective measuring depth to only a few centimeters.

❉ **Ultra-low ac magnetic field**:

The second novel approach draws inspiration from the Global Positioning System (GPS) and applies it to the biomedical field. Previously impractical due to the lack of high-resolution magnetic sensors that could operate at room temperature, this method uses small coils to generate low-intensity and low-frequency ac magnetic fields (hundreds of nanoTeslas) (Figure 2.11(E)). These fields can be measured by high-resolution magnetometers such as optically pumped magnetometers or superconducting quantum interference devices (these sensing technologies are further described in section 2.3.1). The strength of the magnetic field varies with distance from the small coil, allowing a multilateration approach to determine the position of the coil. While this technique seems promising, it requires expensive and sensitive equipment, which may limit its widespread adoption in clinical settings.

❉ **Quasi-static magnetic fields**:

The third novel method involves the use of monolithic integrated magnetic sensors and quasi-static magnetic fields (Figure 2.11(C)). Monolithic on-chip 3D magnetic sensors have been widely used in automotive and consumer electronics for about 15 years. A new generation of miniaturized chips were introduced to the market a few years ago. These sensors are made using smaller packaging technologies with sub-millimeter dimensions and offer higher measuring and reliability performances [133]. This packaging technology was designed for harsh environments such as in automotive applications. Finally, the on-chip circuitry implements analogue to digital conversion, standard communication interface and sensor noise and offset reduction techniques [134]. This ensures signal integrity along the acquisition chain. In comparison, a micro-coil which is an analog, discrete and more bulky technology does not offer the advantages listed above which are specific to semiconductor devices.

In this last approach, the coils of the FG are activated sequentially to generate dc magnetic fields, which are then detected by the magnetometers embedded within the target device. This setup provides a unique spatial encoding system within the tracking volume, offering performance comparable to traditional methods. The key advantage of this technique lies in its robustness against EMI, particularly conductive distortions.

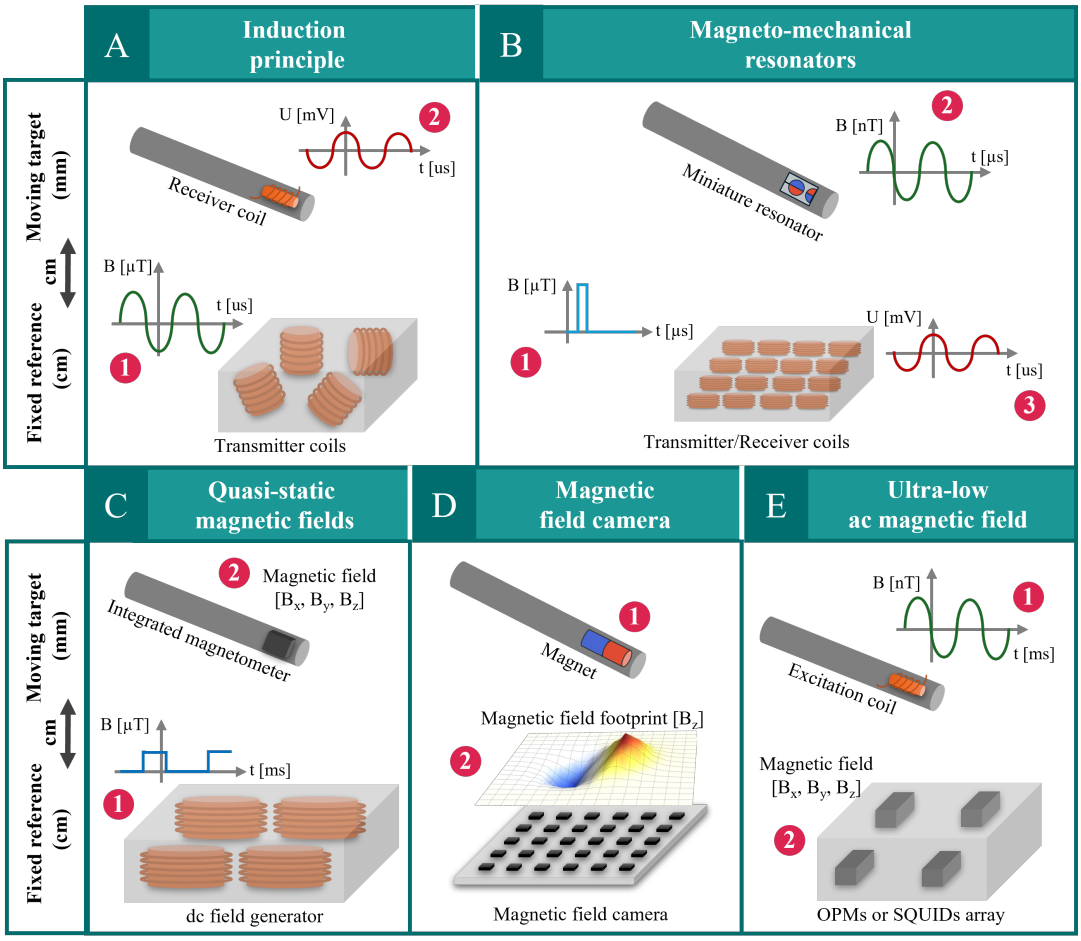

Figure 2.11: Schematic describing five different principles of electromagnetic tracking: (A) Induction principle on which most of the existing electromagnetic systems are based, (B) Novel principle based on Magneto-mechanical resonators presented by Philips Research [127], (C) Principle based on quasi-static magnetic fields, (D) Magnetic field camera principle and (E) Ultra-low ac magnetic field.
The numbers represent the step-by-step sequence of the EMT technique.

Early studies have shown that quasi-static EMT systems are compatible with certain surgical tools and medical equipment. In 2021, Sharma et al. [135] demonstrated a system based on three-axis Hall-effect magnetic sensors achieving tracking performance below 100 μm error. However, these systems face several challenges. One significant issue is the need for precise characterization of the magnetic field generated, as the field's accuracy directly impacts the tracking performance. Since each position within the MV is uniquely encoded by the magnetic field, high-precision characterization is essential for achieving accurate results. Another limitation is the rapid decay of the magnetic field with distance from the FG, typically following a cubic decay pattern. Increasing the

strength of the magnetic field and using high-resolution sensors help achieve a trade-off between adequate performance and minimization of the power consumption and coil heating. The last limitation is the slow sampling rate of the EMT system which is limited by the output rate of the magnetic sensors and ultimately by the ramp-up time of dc currents in the FG.

Despite the promising advancements in both existing and novel EMT systems, several challenges remain. A major obstacle is the susceptibility of existing EMT systems to interference, particularly from metallic objects commonly found in operating rooms. While compensation techniques for known disturbances have been developed, managing unpredictable EMI sources remains difficult. On the other hand, advancements in miniaturizing magnetic sensors and enhancing their sensitivity offer promising opportunities for novel EMT systems. Approaches based on MFC or quasi-static magnetic field take advantage of these innovations. In terms of MV dimension and integration within surgical tools or implants, systems based on quasi-static magnetic fields and integrated magnetic sensors demonstrated significant potential. EMT systems based on quasi-static fields may offer a viable solution for accurately localizing DBS electrodes while ensuring compatibility with stereotactic procedures.

2.3 Magnetic sensing technologies

Magnetic sensors are vital components in a wide range of applications, including automotive, industrial automation, robotics, medical devices, and consumer electronics [136]. These sensors detect the strength or variations in magnetic fields and convert them into electrical signals, enabling precise measurements. In recent years, there has been significant progress in magnetic sensor technology, driven by the demand for higher resolution, miniaturization, and improved performance in challenging environments. This section provides a comprehensive review of the different types of magnetic sensors, also highlighting recent technological advancements and emerging trends.

2.3.1 Existing technologies

Magnetic sensors can be broadly classified into several categories based on their operating principles. Each type of sensor has unique characteristics and is suited for different applications [137]. The different sensing technologies and their sensitivities are represented in Figure 2.12. Some of the technologies can be extended to propose the magnitude and direction of magnetic fields along all three spatial axes (X, Y, Z), classifying them as three-axis magnetic sensors. In contrast to single-axis magnetic sensors, which measure the magnetic field along one axis, three-axis sensors provide comprehensive field data (B_x, B_y, B_z). This capability is critical in applications like precise orientation tracking, 3D positioning, and advanced navigation systems.

- **Micro-coils:** Micro-coils, or search coils, operate based on the principle of electromagnetic induction as described by Faraday's law. They generate voltage in response to a time-varying magnetic field, ranging from the mHz to MHz frequency. A typical micro-coil consists of a copper winding with multiple turns and may either be air-cored or incorporate

a soft magnetic (ferrite) core. This technology is currently employed in commercial EMT systems. The micro-coils provide single-axis information. An arrangement of orthogonal coils can be used to provide three-axis information. The smallest commercially available micro-coils have a minimum diameter of 0.3 mm and a length of 2.5 mm [138]. However, they are particularly sensitive to mechanical stress, as it can alter the voltage induced in the coil windings. Research efforts are focused on miniaturization and circuit integration, but the overall dimensions remain relatively large (about 4 mm) due to the amplifiers and filters required for their operation [139].

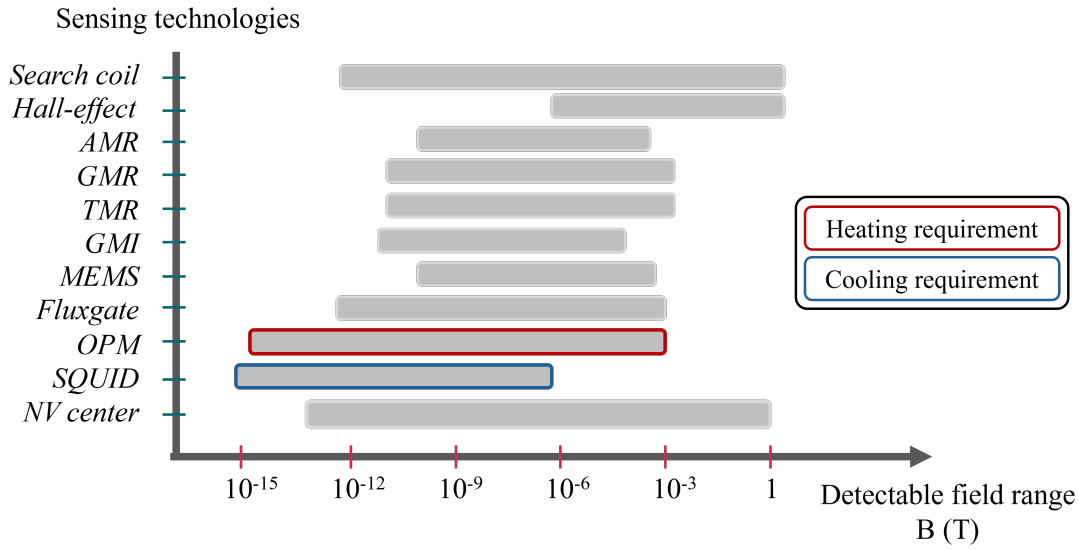

Figure 2.12: Different magnetic sensing technologies as a function of the measuring range and resolution. The figure shows both ac and dc sensing technologies, but only search coils are limited to ac magnetic fields detection.

❊ **Hall-effect Sensors:** Hall-effect sensors are one of the most widely used types of magnetic sensors. They operate on the principle that a current-carrying conductor placed in a magnetic field experiences a voltage (Hall voltage) perpendicular to the current and the magnetic field [140]. From this principle, a transducer converting the magnetic field into a proportional voltage can be built. Hall sensors are widely used in automotive and consumer electronics for position sensing, current measurement, and magnetic field detection. Hall-effect sensors are available in millimeter-size electronic chips providing three-axis information.

❊ **Magnetoresistive Sensors:** Magnetoresistive sensors rely on the change in electrical resistance of certain materials when exposed to magnetic fields. The two main types of magnetoresistive sensors are Anisotropic Magneto-Resistance (AMR) and Giant Magneto-Resistance (GMR) sensors. The phenomenon of AMR was first discovered by Lord Kelvin in 1856, who reported that ferromagnetic metals (Fe and Ni) exhibit higher

resistance, when magnetized parallel to the current, and minimum resistance, when the magnetization is perpendicular to the current [141]. Owing to its simple fabrication process, AMR sensors are used for many applications but mainly position detection. Its miniaturization is straight forward, and the robust structure allows its fabrication on a variety of substrates, including flexible and stretchable ones [142].
GMR sensors, discovered in the late 1980s [143, 144], offer higher sensitivity and have been largely employed in biosensing applications [145].
The most recent addition to the magnetoresistive family is Tunnel Magneto-Resistance (TMR), which offers even greater sensitivity and stability at room temperature. If the phenomenon was observed in 1975 by Julliere [146], Miyasaki proposed a first TMR in 1995 [147]. Biosensing applications are also targeted such as magnetocardiography and MEG [148, 149]. Magnetoresistive sensors are available in millimeter-size electronic chips providing three-axis information.

⁕ **Giant Magneto-Impedance (GMI):** In 1993, through large impedance change observed in amorphous wire by Panina [150] and Mohri [151], GMI was identified as a sensing effect for the first time and has since attracted strong interest due to its high magnetic sensitivity, achieved with simple fabrication process and relatively low cost. GMI refers to the effect of a significant change in the complex ac impedance of a conductor when exposed to a dc magnetic field. The performance and applications are similar to magnetoresistive sensors with the advantage of higher output frequency [152]. These sensors can also be found in millimeter-size electronic chips providing three-axis information.

⁕ **Micro-Electro-Mechanical Systems (MEMS):** MEMS have emerged as a powerful technology for magnetic sensing, offering compact, low-power, and cost-effective solutions for a variety of applications. MEMS-based magnetic sensors typically rely on piezoresistive, capacitive, or magnetoresistive effects to detect magnetic fields [153, 154]. However, most of the technology are company-based and therefore protected. MEMS magnetometers are available in millimeter-size electronic chips providing three-axis information.

⁕ **Fluxgate Sensors:** First fluxgate sensors have been developed in the beginning of the last century [155]. Fluxgate sensors are highly sensitive devices used to measure weak magnetic fields. Their operation is based on a core made of highly permeable material, surrounded by two coils [156]. The primary coil generates a magnetic field, while the secondary coil detects changes in the magnetic field. These sensors operate by measuring the voltage induced in the sensing coil, which results from the interaction between the controlled magnetic field generated by the primary coil and the external magnetic field. Fluxgate sensors are primarily used in geophysical surveys [157], spacecraft navigation, and defense applications. Recent advancements in fluxgate technology have focused on miniaturization, power efficiency, and improving signal-to-noise ratios [158, 159]. Fluxgate sensors can be found in rather small dimension, around few centimeters and providing three-axis information. An integrated version of a single-axis fluxgate is currently commercialized by Texas instruments (DRV425), with dimension of 4.15 x 4.15 x 0.8 mm^3.

⁕ **Superconducting Quantum Interference Device (SQUID):** SQUIDs are among the most sensitive magnetic sensors available, capable of detecting magnetic fields as weak as a few femtoteslas. They operate using superconducting loops and Josephson junctions, which respond to changes in magnetic field [160]. SQUIDs are used in applications requiring extremely high sensitivity, such as medical imaging (for instance MEG), fundamental physics research, and mineral exploration. However, their requirement for cryogenic cooling limits their widespread use. Recent research has focused on developing SQUIDs operating at higher temperatures, which could significantly broaden their applicability [161]. Due to their temperature requirements, SQUIDs are available as large devices only. These sensors measure the magnetic field vector but do not provide information about its direction. To obtain three-axis information, additional systems such as three orthogonal detection coils are required [162].

⁕ **Optically Pumped Magnetometers (OPM):** OPMs are a newer class of magnetic sensors that have gained attention for their high sensitivity and ability to operate at room temperature. Their principle relies on atoms (usually alkali metals like rubidium or cesium) optically pumped into a specific quantum state [163]. These atoms interacts with external magnetic fields, resulting in changes in their atomic states that can be detected using laser-based techniques. Depending on the type of atoms and sensitivity needs, the vapor cell housing the atoms may be heated to temperatures of up to 150°. OPMs are used in applications such as biomagnetic sensing, geophysical exploration, and brain activity monitoring. The key advantage of OPMs over SQUIDs is their operation without the need for cryogenic cooling, which makes them more practical for widespread use. Recent developments in OPM technology have focused on improving sensitivity, miniaturization, and the integration of OPMs into portable devices for medical diagnostics [164] and environmental monitoring [165]. OPMs are not available as integrated sensors but can be found in rather small dimensions, around a few centimeters. Similarly to SQUID technology, the three-axis information be obtained by integrating additional systems or increasing the number of lasers [166].

⁕ **Nitrogen-Vacancy (NV) Centers:** NV-based magnetometers rely on the quantum properties of nitrogen-vacancy defects in diamonds [167], where a nitrogen atom replaces a carbon atom in the diamond lattice, leaving a nearby vacancy. This defect in the diamond structure is sensitive to changes in the surrounding magnetic field, making NV centers a potential platform for high-sensitivity magnetometry. Similarly to OPM, these quantum states can be detected using lasers. However, NV-based magnetometers can operate at room temperature and have demonstrated a wide dynamic range, detecting both very weak and strong magnetic fields with impressive sensitivity [168]. Few NV-based magnetometers are available commercially, with typical dimensions in the tens of centimeters, including both the sensing elements and the control electronics. Recent research efforts have focused on miniaturizing the sensing elements [169], as optical components have inherent size limitations. One notable advancement is the proposed use of LEDs instead of lasers, which facilitates integration into more compact designs [170]. These sensors are also vector magnetic sensors and require additional systems [171].

In recent years, several key advancements have been made in magnetic sensor technology. One significant trend is the miniaturization of sensors, which has been driven by the demand for compact, wearable, and implantable devices. Another important development is the increasing sensitivity of magnetic sensors. This has unlocked new possibilities for their use in high-precision applications such as medical diagnostics, automotive systems, and magnetic navigation [136].

Despite these advancements, several challenges persist in the development of magnetic sensors. One major challenge is the trade-off between sensitivity and size. Miniaturization is crucial for many applications, but reducing the sensor dimension often results in increased noise. Ongoing progress in nanomaterials and innovative sensor designs is expected to address this issue, allowing for the creation of ultra-small, yet highly sensitive, magnetic sensors. Another challenge is ensuring the resilience of these sensors to strong magnetic fields. The sensing elements, often made from highly permeable materials, are susceptible to degradation when exposed to intense magnetic field exposure.

2.3.2 Monolithic on-chip magnetic sensors

From the sensing technologies presented, few of them are available as on-chip packages and providing three-axis information. As mentioned above, on-chip packaging offers many advantages in addition to miniaturization: high-reliability, high-robustness, and extended lifetime. Wafer-level chip scale packaging (WLCSP) is the smallest package currently available on the market, since the resulting package is practically of the same size as the die.

Table 2.2: Monolithic on-chip magnetic sensors

Technology	Reference	Sensitivity $[\mu T/LSB]$	rms noise $[\mu T]$	Range [mT]	Sampling rate [Hz]	Package dimension [mm^3]
Hall-effect [172]	AK09973D	1.1	5.5	$\pm$ 36	2000	1.18 × 0.78 × 0.55
MEMS & Hall-effect [173]	BMM150	0.3	0.6	$\pm$ 1.3	100	1.56 × 1.56 × 0.6
Hall-effect [174]	AK09919C	0.15	0.7	$\pm$ 4.9	100	0.76 × 0.76 × 0.5
AMR [175]	MMC5603NJ	0.00625	0.15	$\pm$ 3.6	75	0.8 × 0.8 × 0.4
MEMS [176]	LIS3MDLTR	0.015	0.4	$\pm$ 0.4	80	2 × 2 × 1
TMR [177]	AK09940A	0.01	0.4	$\pm$ 1.2	350	1.6 × 1.6 × 0.58
TMR [178]	BMM350	0.1	0.45	$\pm$ 2	100	1.28 × 1.28 × 0.5
GMI [179]	BM1422AGMV	0.042	0.130	$\pm$ 1.2	2000	2 × 2 × 1

In Table 2.2, a selection of different magnetic sensors available in WLCSP packaging is presented. This list highlights the potential sensors commercially available for biomedical applications more specifically to be used within an EMT system. The list focused on technologies available for 3D sensing, millimeter-size packaging and highest-resolution.
Monolithic on-chip magnetic sensors enable rapid prototyping due to their widespread availability, low cost, and reliable performance. These types of magnetometers are even more interesting for biomedical applications due to their compactness and integration capabilities. They typically consume less power, which is crucial for implantable biomedical devices that rely on battery life for long-term operation. Monolithic sensors can be easily integrated with wireless operation and data transmission, which reduces the need for wired connections during procedures, improving patient comfort and safety. The small size and integration capability make these magnetometers easier to encapsulate in biocompatible materials, ensuring safe long-term use in the human body. Therefore, monolithic on-chip magnetic sensors are good candidates for their combination within an EMT system based on quasi-static magnetic fields.

To conclude this chapter, the field of DBS is progressing rapidly, with advancements aimed at improving surgical precision and post-operative programming. However, these developments introduce challenges, including the need for accurate real-time feedback during electrode placement. Addressing these challenges necessitates the integration of advanced imaging, navigation, and programming technologies into DBS procedures. Among the localization methods, EMT systems show significant promise due to their demonstrated clinical success. However, current EMT systems face challenges with EMI from metallic objects in operating rooms. While some compensation methods exist, managing unpredictable EMI sources remains a challenge. Advancements in miniaturized and sensitive magnetic sensors, particularly monolithic on-chip designs, offer potential solutions. These sensors could be integrated into EMT systems using quasi-static magnetic fields, facilitating accurate electrode localization and compatibility with stereotactic procedures.

CHAPTER 3

Aims

This work focuses on developing an EMT system based on an innovative approach that combines quasi-static magnetic fields with integrated magnetic sensors. The primary objective of this thesis is to design and evaluate a first demonstrator based on this novel method for DBS applications. This research represents the first step toward achieving real-time localization of the DBS electrode's position and orientation during surgery, with the aim of enhancing current DBS practices and improving therapeutic outcomes in the long-term. To meet the necessary criteria, the system targets real-time monitoring with a spatial error of less than 1 mm and an angular error of approximately 1 degree. While the temporal resolution required for the system is less demanding than for other surgical applications, a resolution of 500 ms is considered sufficient for DBS surgery. Additionally, the system should incorporate a registration method enabling the visualization of the electrode localization in relation to anatomical brain structures. The overall system should be carefully designed to ensure compatibility with existing surgical workflows and tools.
This general intention was divided into specific goals addressed in the four publications that form the core of this thesis:

➥ Propose a new 3D localization method based on high-resolution monolithic magnetic sensors and quasi-static magnetic fields. Conclude about the FG requirements and the current best sensing technologies for the EMT system. (**Publication I**)

➥ Design of the EMT demonstrator for DBS surgery while taking into consideration the specifications of surgical environment. Extend the localization method to the orientation detection. (**Publication II**)

➥ Validate the suitability of the developed EMT system to the DBS surgery setting and more specifically to the stereotactic system. Compare the performance of the developed EMT system to existing systems for DBS surgery. (**Publication III**)

➥ Provide a registration method for the integration of the EMT system into the surgical procedure. (**Publication IV**)

CHAPTER 4

Publication I - Concept

Foreword and Overview

In this publication, the performance of an EMT system, previously developed at the FHNW-HLS Sensors Lab, for limb shape capture, was investigated. This EMT system was based on quasi-static magnetic field and two different sensing technologies were investigated. This publication highlights the important features of this EMT technique: the magnetic resolution of the sensors, the minimal magnetic gradient required to reach the spatial resolution expected as well as the localization method used. A Magnetic Field Camera (MFC) - arrays of magnetic sensors - was introduced for the quick assessment of the tracking performance.

Contribution: The candidate was overall responsible for the measurements, simulations and analysis. The EMT system and the MFC were technologies already developed by the research laboratory (Sensors lab, FHNW-HLS). The candidate was overall responsible for the writing of the manuscript. The supervisors and co-authors supported the process and reviewed the paper.

Abstract

This article describes an alternative to high-field electromagnetic tracking system, by using low consumption generator and high-performance magnetic sensors. Monotonically varying magnetic field over three positions are created to produce magnetic field gradients, which encode each spatial point uniquely. Millimetric size sensors capable of measuring their local magnetic field with high resolution are used to sense the gradient field. Such sensors can be embedded in surgical tools, such as catheters or brain electrodes. With low power consumption and low-field generator, the integrability of the electromagnetic system in a surgical theater is greatly enhanced. This system leads to unambiguous and orientation-independent spatial encoding with a mean absolute error of 3 mm at 42 cm from the field generator using the last generation three-axis magnetoresistive sensors. A calibration of the sensors was performed and leads to significant improvement in the localization over the Z-axis.

Introduction

EMT systems raise interest for surgical procedures and diagnostic techniques as a solution to overcome the limitations of current imaging techniques [180]. Indeed, this technique enables real-time tracking without line-of-sight of small objects. In contrast to X-rays, radio frequency, ultrasound, and visible light, static magnetic fields have negligible attenuation through the human body, no dependency on the tissue type, and no known harmful effects [181]. EMT systems are based on magnetic fields of known geometry to determine the position and orientation of sensors by measuring magnetic fields or magnetic fields gradients. The reference magnetic field is typically produced by permanent magnets or by coils. The implementation of this technique first emerged in the 1970s. Kuipers [182] and Raab [183] described the first tracking methods for positioning and orientation of a magnetic sensor.

Common EMT systems available on the market use micro-coils for the moving sensing elements. Micro-coils are dB/dt sensors, which measure the rate of change of the magnetic field. Thus, an alternating magnetic field is required for these sensors. Current EMT systems feature a magnetic field source, which generates magnetic fields typically varying up to 100 kHz [180]. Miniaturized micro-coils integrated within surgical tools can measure the signal necessary to determine the position of a catheter. For instance, the NDI Aurora system (Waterloo, ON, Canada) is a customizable EMT system based on miniaturized micro-coils for sub-millimeter applications [184].

However, most of the EMT systems are still very complex to apply, hindering a widespread clinical use. New systems based on integrated magnetometers, rather than micro-coils, are now investigated. The two main advantages of using micro-coils rather than encapsulated monolithic magnetometers were until recently 1) their smaller size and therefore better integrability into minimally invasive surgical tools and 2) their higher signal-to-noise ratio. Recent improvements in terms of miniaturization and sensitivity of monolithic integrated magnetometers permit to design various surgical tools instrumented with magnetometers [185]. These magnetometers are based on several physical principles, mainly the Hall effect and the

magnetoresistance. They are already used in the medical devices market, for instance, in cardiac implantable electronic devices. Besides, they mainly address the industrial, automotive, and consumer electronics markets.
These sensors now also raise interest in further medical applications, especially after a calibration step allowing to meet high-accuracy requirements [186]. Relying on magnetic sensors could permit the development of practical and simple tracking solutions that are applicable in clinical workflow, which is still considered as the main challenge in this area. A CMOS integrated 3D Hall magnetometer, which has been integrated inside a surgical tool model for tracking purpose, has already been investigated [135]. This study of Sharma et al. demonstrates the possibility to achieve sub-millimeter tracking precision using 3D Hall effect sensors in combination with 3D field gradients. The minimal required gradients were calculated according to the effective resolution of the sensors and the expected spatial resolution of the EMT system, which led to gradients of at least 30 mT/m.
However, this setup requires a bulky magnetic field generator with a large current consumption up to 30 A per coil. To reduce size and power consumption, we propose here a miniaturized system that can operate at low-field intensity for better integrability into a surgical theater. Previous published results demonstrated the capability of low-field EMT systems for localizing catheters or electrodes for cardiology or neurosurgery applications [187].

In this article, we present an alternative to high-field EMT system, by using low consumption generator and high-performance magnetic sensors. The system concept and overview are described in Section II. The performance of the system under different scenarios is described in Section III, and finally, Section IV discusses the limitations and outlook of this EMT system.

Materials & Methods

Experimental Setup

The magnetic generator consists of three air-core coils in a planar arrangement (3B Scientific GmbH, Germany) providing a large tracking volume of 40 cm × 40 cm × 35 cm. However, the performance assessment is done over a restricted volume, described further in this section. Fig. 4.1 illustrates the experimental setup of this study. A static current of 1 A leading to only 6 W power consumption is applied sequentially to the three coils. Each coil is made of 320 turns for a diameter of 138 mm and exhibits a dc resistance R of about 6.5 ohms. We developed two in-house MFCs, i.e., two sensor arrays (see Fig. 4.2). The first MFC implements 3D Hall effect sensors (TMAG5273A1, Texas Instruments, USA) with a resolution of 1.2 µT per Least-Significant Bit (LSB) and a maximal rms noise of 22 µT. The second MFC implements an array of 3D Anisotropic Magneto-Resistance (AMR) sensors (MMC5603NJ, MEMSIC Semiconductor Company, Ltd., China) with a resolution of 6.25 nT/LSB and a rms noise of 200 nT. These two sensors are the best-in-class for each technology.
In this study, the configuration chosen for the sensors provide the highest resolution at the expense of the output rate. Thus, the AMR sensor and the Hall effect sensor provide, respectively, a maximal output rate of 75 and 400 Hz, respectively. The two MFCs integrate

three microcontrollers. Two of them store the data, whereas the third one handles the communication tasks. It allows us to reach an output of 1.8 Hz for the AMR MFC and 20 Hz for the Hall effect MFC.

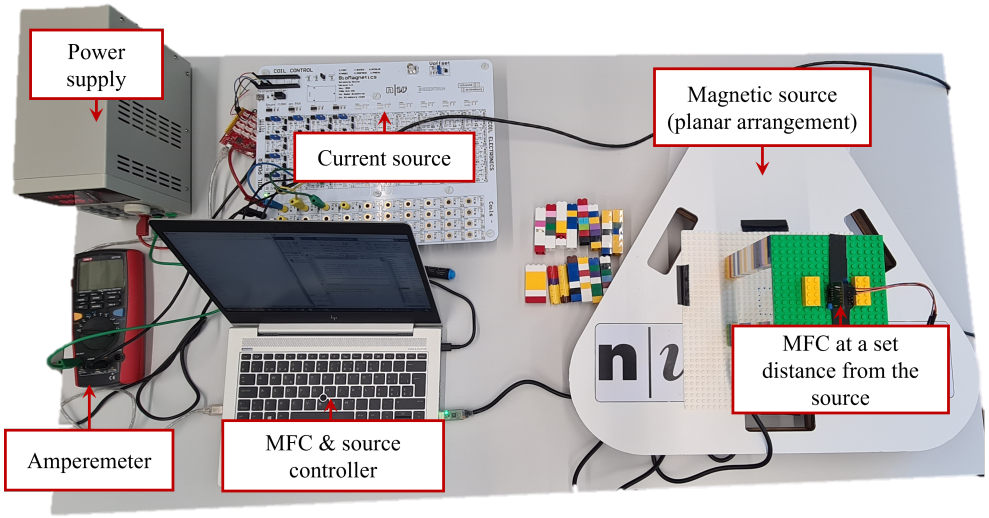

Figure 4.1: Photograph of the experimental setup with the Hall effect MFC placed above the three air-core coils source. Lego bricks are used to place the MFC with high precision.

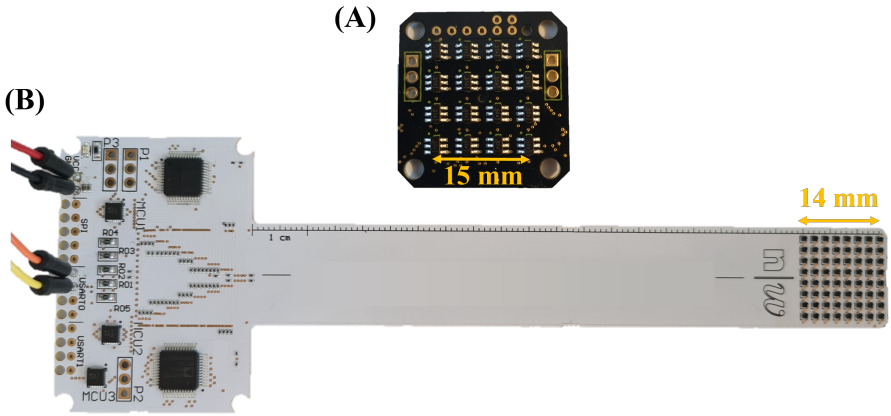

Figure 4.2: MFCs. (A) Hall effect-based MFC with a spacing of 5 mm in between sensor chips with a configuration of a 4 × 4 array. (B) Magnetoresistive-based MFC with a spacing of 2 mm in between sensor chips with a configuration of an 8 × 8 array.

The magnetic field maps of six parallel planes located above the three coils were measured with both MFC, depicted in Fig. 4.2, and for each activation of the three coils (Fig. 4.3(A)). The two MFCs were used to measure 64 different sensors positions at different horizontal planes located at 7, 14, 21, 28, 35, and 42 cm from the plane containing the generator (Fig. 4.3(B)). The 64 sensor positions were obtained with only one position of the array for the AMR MFC

and with four positions of the array for the Hall effect MFC, within each horizontal plane of 4 cm × 4 cm. It leads to an actual volume of 4 cm × 4 cm × 35 cm using the Hall effect MFC and a volume of 1.4 cm x 1.4 cm x 35 cm using the AMR MFC.

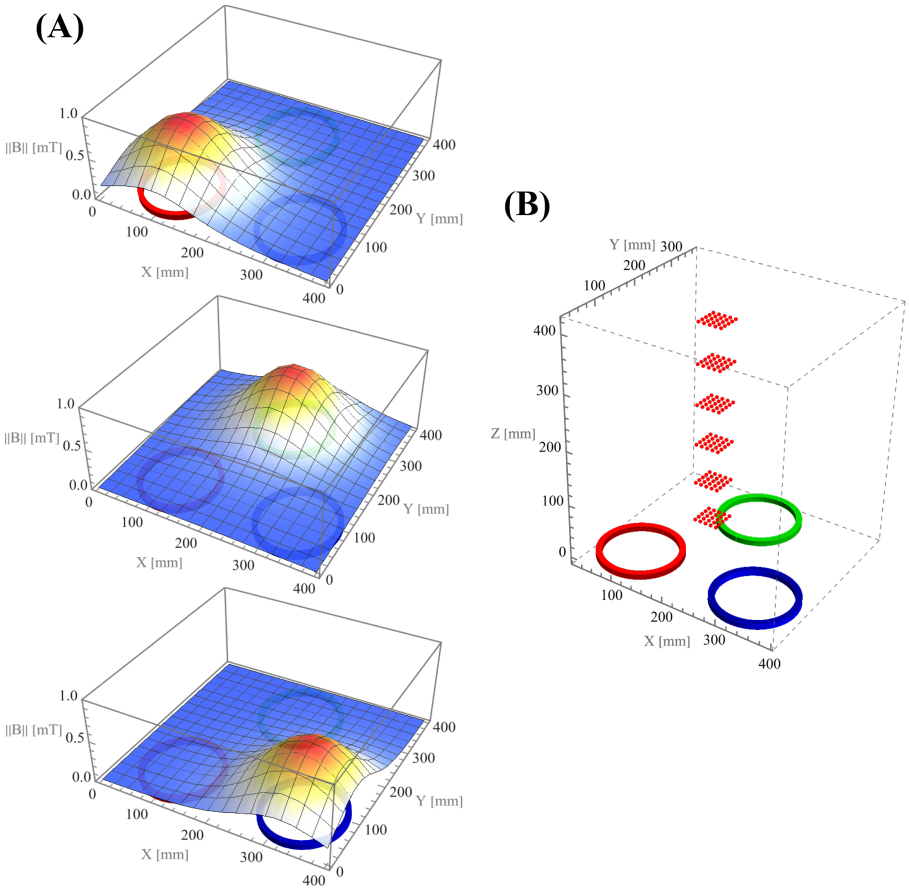

Figure 4.3: (A) Magnetic field maps at a horizontal plane located at 7 cm above the three air-core coils. Magnetic field gradients can be observed. (B) Visualization of the horizontal planes, where the MFC was placed above the coils. The red points indicate the restricted volume to be assessed.

A fourth acquisition with no current flowing through the coils was performed to measure the magnetic field generated by the environment. This fourth map is subtracted from the three coils' maps as an offset cancellation. In this manner the tracking system is immune to static disturbing magnetic fields, such as the Earth's magnetic field. The localization was solved using an error minimization between the measured magnetic norm and the theoretical norm which was obtained from magneto-static simulations (Mathematica 12.3, Wolfram Research, Inc). A volume of 9 cm x 9 cm x 43 cm was extracted from the simulation under the format of a grid with a specific pitch. Four pitches were tested: 10, 5, 2, and 0.5 mm. The minimization was performed on the grid, i.e., using a look-up table method or on the interpolated grid. Both

linear and tricubic interpolation were investigated. In the case of the look-up table method, the table was created by storing the pre-calculated simulated data. The minimization applied to the interpolated grid used the same method, i.e., the extended version of the Broyden–Fletcher–Goldfarb–Shannon algorithm known as L-BFGS-B algorithm, described in a previous study [187]. The resolution of the localization was programmed in Python 3.9 using the SciPy library.

Calibration Method

The MFC have been calibrated within a one-axis reference Helmholtz coil previously characterized. This characterization ensures that all the sensors of the MFC were exposed to the same magnetic field with a non-homogeneity of less than 0.5%. To calibrate independently the X, Y, and Z channels of the MFC, a low-frequency sinusoidal magnetic field has been applied. The misalignment of the MFC during the calibration of each sensors axis is detected and compensated through the measurement of the residual sinusoidal signals on the two other axis, which are quantified through a fast Fourier transform (FFT) analysis. Then, a static magnetic field of different intensities was applied to obtain the relationship between the known magnetic field and the magnetic field measured by the sensors. A linear regression provides the gain and offset correction coefficients for each axis of the sensors composing the MFC.

Results

The positions of the sensors on the magnetic cameras are known with an uncertainty of less than 0.1 mm due to the Printed Circuit Board (PCB) manufacturing process. The mean absolute error (MAE) of the distance between the known sensors positions and the tracked positions is then evaluated.

Magnetic field Gradient

Gradient values were investigated in Table I to relate them to the performances of the EMT system. The gradient was calculated over the tracking volume for the three coils. Gradients were obtained from simulations. Equation (4.1) describes, for instance, the gradient along the X-axis. The three coils exhibit similar gradient values:

$$X - gradient = \partial||B||/\partial x \tag{4.1}$$

In comparison, the maximal gradient values were ten times smaller than the gradient provided in the work of Sharma et al. [135]. Considering the experimental results detailed in Section III-B, a gradient of about 0.3 mT/m is large enough to provide a tracking precision of less than 1 mm while using best in class magnetoresistive sensor. The developed algorithm does not rely on gradient values. However, the study of the gradient provides valuable information to design future EMT systems.

Distance from the source	$X_{gradient}$ [mT/m]	$Y_{gradient}$ [mT/m]	$Z_{gradient}$ [mT/m]
7 cm	3.55	1.59	1.55
14 cm	1.06	0.58	0.93
21 cm	0.32	0.16	0.44
28 cm	0.11	0.06	0.21
35 cm	0.05	0.02	0.11
42 cm	0.02	0.01	0.06

Table 4.1: Typical gradient values for one coil

Impact of the Averaging

The magnetoresistive sensor provides steady performance with an MAE $\leq$ 0.7 mm up to 21 cm from the generator and an MAE $\leq$ 3 mm up to 42 cm (Fig. 4.4, top graph). In contrast, the Hall effect sensor shows similar performances (1 mm MAE) only at the closest distance from the generator, i.e., 7 cm (Fig. 4.4, bottom graph). The localization deteriorates with greater distance (5 mm MAE at 21 cm) due to the rms noise and limited sensitivity. After an averaging of 100 sensors values, the MAE is not reduced significantly for both technologies except in the far-field, i.e., 42 cm from the generator. Depending on the number of averaging, the time required to calculate the magnetic field norm for the 64 sensors of the AMR MFC is between 556 ms and 167 s. For the Hall effect MFC, the time required to calculate the magnetic field norm for the 16 sensors is between 50 ms and 15 s.
Therefore, this pitch was selected for presenting our results. The lookup table method was then arbitrarily chosen among the three methods.

Impact of the Grid Pitch and the Interpolation Method

Different grid pitches and different interpolation methods did not impact the performance of the tracking (Fig. 4.5). As expected, with a larger grid pitch, the error minimization method based on the lookup table exhibits degraded performance. Similar performances for all methods were observed with a grid based on a 0.5 mm pitch.

Impact of the Calibration

The influence of the calibration on the tracking performances was assessed on relative positions (Fig. 4.6(B)) as well as on absolute positions over the Z-axis (Fig. 4.6(B)). The relative positions are defined by their Euclidean distances in between the sensors over the array of the MFC. By subtracting the magnetic field measured without any coil activated, we cancel both the magnetic field of the environment and the internal offset of the sensors. It leads to good performances on the tracking of the relative positions even with non-calibrated sensors. After calibration, no significant improvement of the tracking performances on relative positions was observed. On the contrary, the absolute position of the sensors, especially over the Z-axis, shows a significant improvement after calibration. Prior to calibration, the error in the Z-position was more important with the magnetoresistive sensors than with the Hall effect sensors. It can be

explained by the less accurate intrinsic gain of the magnetoresistive sensors (mean value of 0.95) in comparison to the Hall effect sensors (mean value of 1.02) over the Z-axis.

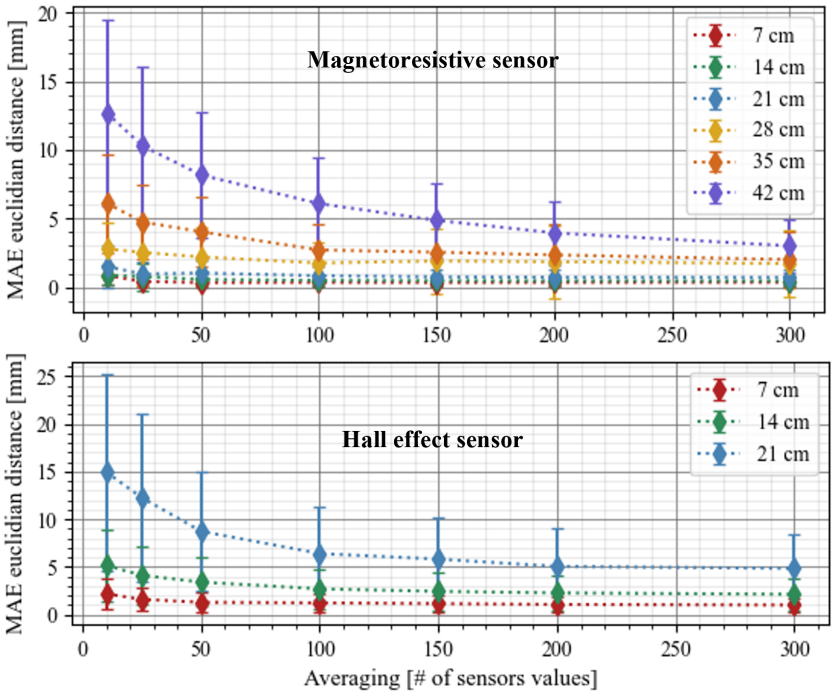

Figure 4.4: MAE of the Euclidean distance between the sensor positions as a function of the horizontal plane from the magnetic field generator. No calibration was applied here. A lookup table method based on 0.5 mm grid pitch was used.

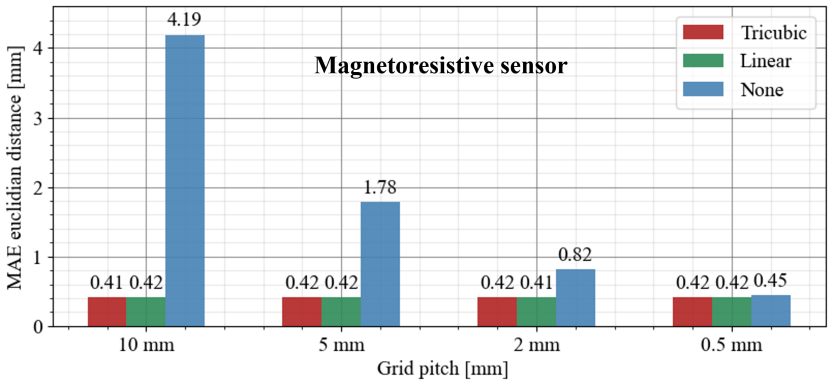

Figure 4.5: MAE of the Euclidean distance between the sensor positions as a function of the grid pitch and for different interpolation methods. No calibration was applied. The results were extracted from the plane at 14 cm to the field generator.

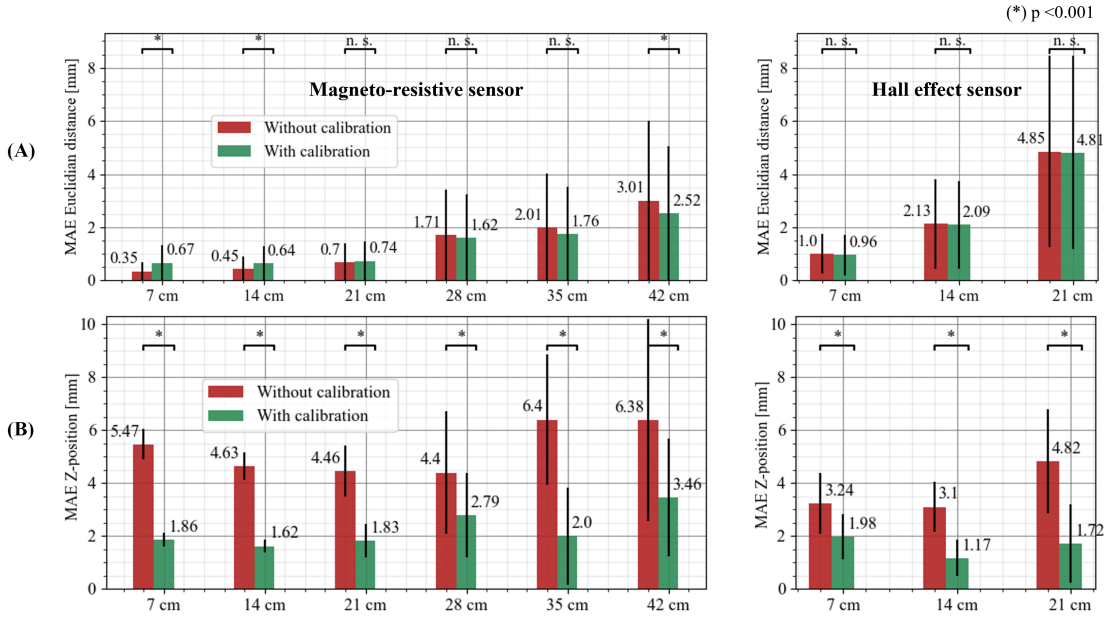

Figure 4.6: Performance of the tracking with/out applied calibration. (A) MAE between the true and detected relative positions after an averaging of 300 sensor values. (B) MAE on the absolute position over Z-axis after an averaging of 300 sensor values. A lookup table method based on 0.5 mm grid pitch was used. (: P-value > 0.001, n.s.: non-significant).*

Discussion

A low-field electromagnetic system combined with high-sensitivity magnetoresistive sensors widens the path to the tracking of surgical tools by providing a better integrability due to smaller field generators. New generation of millimetric or sub-millimetric chips such as the magnetoresistive sensor used in this study (0.8 mm × 0.8 mm × 0.4 mm) makes it possible to integrate a sensor for tracking purpose into surgical tools ranging from large endoscopic catheter to thin tube for brain shunt surgery.

A small tracking volume was investigated in this study, and this volume will be expanded in future work. Knowing the performances of the magnetoresistive sensor up to 42 cm along the Z-axis, the extension of the volume along the X-axis and Y-axis is not expected to significantly change the performance demonstrated here. The calibration showed a limited influence in the improvement of the localization of the relative positions. Indeed, one of the most important improvements in the measurement of the magnetic field is the removal of the intrinsic offset of the sensor. In this study, the subtraction of the magnetic field measured while no coil is activated acts as an auto-zero, where the system both cancels the sensors offset and the static magnetic field contribution of the environment. Moreover, the distribution of internal gain of the sensors was narrow distributed with a standard deviation inferior to 0.01.

However, the calibration greatly modified the absolute position along the Z-axis, even if the error was only partially removed. The residual error could be related to the differences between

the real magnetic field and the simulated magnetic field. To solve this issue, one could use high-resolution sensors such as the magnetoresistive sensor to map the entire tracking volume. This experimental mapping allows one to consider the imperfections of the coils, while avoiding adding the errors related to approximations in the simulation. Further investigations to validate possible improvement along the X-axis and Y-axis for the absolute positions still need to be carried out.
In a surgical theater, the stability of the magnetic field can be influenced by two types of perturbations from the environment. First, magnetic field sources such as current conductors or permanent magnets can disturb the magnetic field generated for the tracking. Second, the presence of ferromagnetic objects can cause distortions of the magnetic field and decrease the tracking accuracy. As explained, the presented setup includes a measurement phase with zero current flowing through the coils. During this phase, which is repeated for each localization sequence, the low-frequency varying magnetic fields produced by the environment are measured and then canceled by the tracking algorithm. This method cannot compensate for the distortions caused by soft ferromagnetic objects that could come near the tracked sensor. However, in surgical applications, the tracked sensor is located inside the body of the patient, which ensures a minimal distance to any objects from the environment. In further development, magnetic sensors will be placed around the tracking volume to continuously monitor the integrity of the magnetic field and to trigger a warning if the magnetic field is distorted by any external perturbation.
Concerning the minimization method applied either on a look-up table or on an interpolated grid, the non-significant differences observed on the performances did not permit us to conclude on a preferential way. Depending on the placement within the tracking volume, the magnetic field can be approximately considered linear, which explains the similar performances between tricubic and linear interpolation. A change in performances could have been expected in the case of a curvilinear magnetic field.

Conclusion

This article presented an EMT system using magnetic field gradients, which exhibits less than 1 mm localization error in 3D up to 21 cm from the surface of the generator. To achieve this performance while using simply a low-field generator, the system combined new high-resolution sensors and a dedicated calibration method. The demonstrated accurate and lightweight system meets the requirements for tracking minimally invasive surgical tools.

CHAPTER 5

Publication II - Technical Description & Performance

Foreword and Overview

Following **Publication I**, an EMT system called ManaDBS, especially designed for DBS surgery, was developed. **Publication II** described the technical aspects and performance of the ManaDBS system. It takes into account the results of the **Publication I** while extending the tracking method to include orientation detection. The intrinsic system performance is discussed as well as the performance in the context of DBS surgery. This publication also highlights in more detail the limitations of quasi-static EMT systems.

Contribution: The candidate was overall responsible for the design and prototyping of the EMT systems, which includes the FG, the controller (current source) and the electrode prototype. During this development, the candidate received technical support from members of the research laboratory (Sensors lab, FHNW-HLS) and used available technologies such as the MFC. The candidate performed the measurement and developed the programming including the tracking algorithm and analysis. The candidate was overall responsible for the writing of the manuscript. The supervisors and co-authors supported the process and reviewed the paper.

Abstract

This paper describes a 3D EMT system, based on quasi-static magnetic fields and a sub-millimetric 3D magnetometer, providing complete localization – both spatial and angular positions – during surgical procedures. By integrating miniaturized sensors into surgical tools, such as DBS electrodes, this tracking system offers complementary or alternative solutions for X-ray imaging. Each spatial position in the MV is uniquely encoded by a vector of four magnetic field amplitudes using the multilateration principle. The orientation is derived from the three orthogonal components associated with this vector. The FG was manufactured on printed circuit boards ensuring high reproducibility and accurate magnetic fields. Position localization was evaluated using a custom magnetic field camera placed at various positions in the MV while the orientation assessment employed a stereotactic system used in DBS surgery. Finally, DBS implantations were simulated to conclude on the validity of the tracking system for DBS surgery. The system achieved spatial and angular errors of 1.72 mm and 0.89° within a MV of 15 x 15 x 15 cm^3 located at 18 cm from the FG and an update rate of the position of 0.4 Hz. Better performances – mean spatial and angular errors of 0.87 mm and 0.52° – were achieved when simulating DBS implantations. With its large distance to the FG, this quasi-static EMT system is particularly well-suited for DBS surgery, offering regular feedback to neurosurgeons. The tracking system could also be adapted to other functional neurosurgeries.

Introduction

EMT or navigation systems offer alternative solutions to conventional imaging technologies, facilitating real-time tracking of devices within the patient's body [180]. Deployed in clinical settings for over two decades, ongoing research continues to focus on advancing the capabilities of existing current systems [188, 125, 122] while also introducing innovative systems to broaden the applicability of this technique to various surgical procedures [135, 189]. Functional neurosurgery emerges as one of the potential targets of novel navigation systems. To optimize surgical outcomes and safety, navigation systems must provide surgeons with accurate feedback regarding the relative position of tracked tools in specific brain regions. It is particularly expected in the context of DBS as it involves the implantation of stimulation electrodes into millimeter-size deep brain structures to modulate abnormal electrical activity. While DBS has demonstrated significant success in improving the quality of life for many patients with movement disorders and certain psychiatric conditions [190], the surgery remains challenging due to the dimensions of the structures targeted. The knowledge of the spatial and angular position of the DBS electrode is a critical point as it provides a starting point for the optimization of the stimulation parameters. With the introduction of the directional leads, greater clinical outcomes have been observed, albeit with added complexity in programming, placing an increased burden on neurologists [191, 192]. Unlike traditional DBS electrodes, directional leads feature segmented electrodes that allow for horizontal current steering, enabling precise adjustment of the stimulation volume relative to the targeted brain structure. This requires providing neurologists with accurate angular positioning of the DBS electrode to

enhance treatment effectiveness. The gold standard for DBS surgery involves frame-based procedure. Frame-based surgery uses a rigid stereotactic frame attached to the patient's skull to guide instruments and ensure accurate targeting of specific areas in the brain. It is commonly employed in procedures like DBS to minimize errors and enhance surgical outcomes. In the context of DBS, frame-based procedures are generally combined with 2D X-ray imaging for intra-operative validation [41] achieving a spatial position of about 1 to 2 mm [47]. In the past years, CT, particularly the Medtronic O-arm system for intra-operative imaging has been increasingly adopted in clinical centers [77, 193]. However, CT does not offer real-time or regular feedback and requires adjustments to the field of view based on the stereotactic systems and related artefacts. Currently, there are no commercial systems that provide real-time localization (both spatial and angular) of DBS electrodes compatible with frame-based surgery. Several technologies such as TCS [101], EEG [102] and EFS [103] have been explored, but none have met both criteria.

EMT system emerges as the most suitable technology in terms of safety, cost and intrinsic performance. Additionally, magnetic fields – up to few Teslas (T) – exhibit negligeable attenuation through the human body and are unaffected by tissue type [194]. Commercial EMT systems employ the induction principle, relying on micro-coils and alternating magnetic fields. While effective in frameless neurosurgery [108], [195],these systems are severely limited by electromagnetic (EM) distortions [196, 197], rendering them unsuitable for frame-based procedures.Current research follows two main directions. One focuses on improving the manufacturing and performance of micro-coils based on printed circuit boards (PCBs) [198] or CMOS technologies [139], enabling more robust and compact coil designs. Another focuses on developing compensation methods to mitigate EM distortions [122, 121]. In parallel, novel EMT systems are being developed based on integrated magnetometers [199] and quasi-static magnetic fields [135, 200, 187], which offer promising alternatives to overcome the limitations of commercial systems. These emerging technologies are paving the way for EMT systems that could be compatible with frame-based surgeries, addressing a long-standing challenge in this field. Preliminary investigations demonstrate the compatibility of these quasi-static EMT systems with some surgical tools and medical equipment [135, 201]. Nevertheless, quasi-static EMT system face limitations and challenges including the requirement for precise characterization of the induced magnetic field, a significant magnetic field decay with the distance to the magnetic FG and a limited update rate.

Accurate characterization of the generated magnetic fields is essential, as it serves as a truth map for the EMT system and therefore determines the performance achievable. Since the magnetic field uniquely encodes each position within the MV, achieving a thorough characterization of the induced field is crucial for high-precision outcomes. There are two main approaches to characterize the magnetic field: computational methods and experimental mappings of the MV. Computational methods are numerical simulations based on mathematical models of perfect components generating the magnetic field. While the computational method is advantageous in terms of characterization time – tens of minutes – and high-density of the mapping, it overlooks technical imperfections associated with the FG and uncertainties linked to electronic control, such as the current injected into the coils. In contrast, experimental mappings consider these aspects but are time-consuming, even automated, due to

the extensive measurement of the magnetic field across the MV. In this method, a single sensor typically acquires magnetic fields to recreate a discrete MV, a process that may span several days. Despite the lengthy process, it remains so far the preferred approach for achieving remarkable results [135, 189]. However, this process would be required for each EMT system before use. In this paper, the FG will consist of PCB coils which offer manufacturing tolerances in the range of micrometers and can be mass-produced with higher reproducibility compared to wired coils. Consequently, numerical simulations offer sufficient accuracy.
The second challenge for quasi-static electromagnetic tracking method is the rapid decay of the magnetic field at greater distances (cubic decay). Most of the quasi-static EMT system exhibited performance high enough for DBS surgery – about 1 mm – only at close distance to the FG, typically a few centimeters [135, 202]. Enhancing the magnetic field strength and using high-precision magnetic sensors can help achieving a balance by providing acceptable performance with minimal power consumption and limited coil heating.

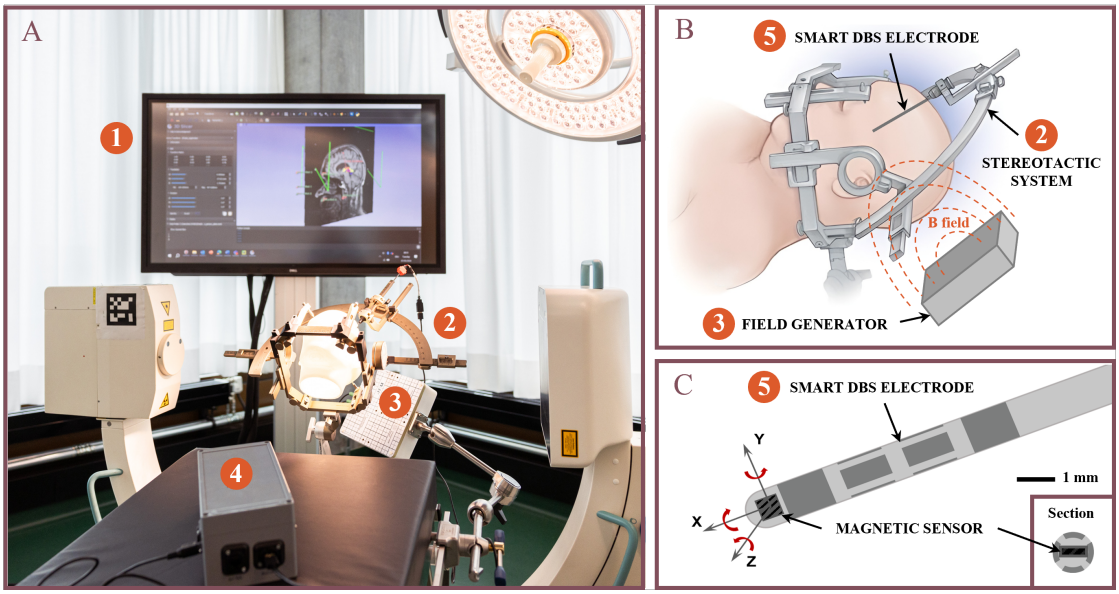

Figure 5.1: (A) Picture of the ManaDBS system and its integration into DBS surgical environment; 1) Visualization software showing the localization of the DBS electrode relative to the patient's imaging, 2) Stereotactic Leksell system fixed to the operating table, 3) Field generator fixed to the operating table and place near the patient's head, 4) System control unit connected to the user computer. (B) Concept image of the ManaDBS system and its placement relative to the stereotactic system. (C) Concept image of the 5) Smart DBS electrode integrating the magnetometer at its tip.

Given this context, we developed the ManaDBS system, a novel EMT system designed for DBS surgery. The ManaDBS is based on quasi-static magnetic fields and a high-precision integrated magnetometer to address the challenges in far-field detection as well as the orientation determination which is crucial for the DBS application. To the best of our knowledge, this is the first work presenting a quasi-static EMT system with orientation detection. Operating at an

18 cm distance from the field generator, ManaDBS provides six degrees-of-freedom (6DOF) information, including angular position. Section II outlines the system concept, while Section-III presents a performance assessment for both position and orientation detection. Section-IV evaluates the system in simulated DBS implantations using a stereotactic system. Section-V and VI discuss the results and conclude the paper.

System description

The system overview and its integration for the localization of the DBS electrode are shown in Fig. 5.1. During the DBS procedure, the patient's head will be fixed within the stereotactic system. Our system is designed such that a sub-millimetric sensor can be integrated into the DBS electrodes. The FG, consisting of four planar coils, is placed beneath the patient's head at approximately 20 cm. The FG produces monotonically varying magnetic fields, resulting in a known position and orientation of the DBS electrode. This enables regular feedback – update rate of the position and orientation of 0.4 Hz – on the localization of the DBS electrode without relying on 2D X-ray imaging.

Hardware overview

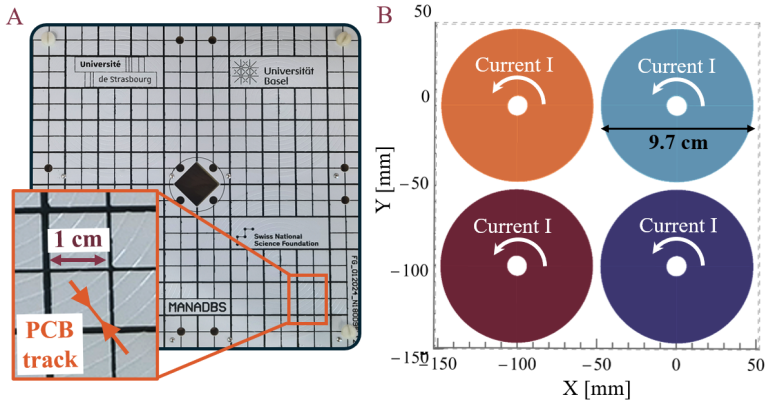

Figure 5.2: (A) Top view of the FG made from two stacked PCBs and a zoom on the bottom left, with a view of the PCB track of one of the four coils. (B) Four-coils arrangement and associated dc current.

The FG consists of four planar EM coils generating a 3D magnetic field within a MV of 15 x 15 x 15 cm^3 which approximates the dimensions of a human head. Table 5.1 lists the FG properties. The MV is located 18 cm from the surface of the FG. This offset distance was selected considering the requirements of the surgical environment. The four coils are integrated into a single electronic PCB (Fig. 5.2(A)). Due to the limited thickness of individual PCB, two PCBs were stacked to achieve the required parameters for the coils (Fig. 5.3(A)). Each coil consists of 360 turns, resulting in an inner diameter of 13 mm, an outer diameter of 97 mm,

and a thickness of 12 mm. The activation sequence of the coils follows five steps: the first four steps involve activating each coil individually, and the fifth step involves offset cancellation (Fig. 5.3(B)). All coils carry current in the same direction (Fig. 5.2(B)). In the offset cancellation step, the magnetic field from the environment (including the Earth's magnetic field) is measured with all coils deactivated. This environmental field measurement is then subtracted from each of the first four measurements, effectively eliminating any quasi-static perturbations.

Table 5.1: Field generator properties

Parameters	Values
Dimensions	20 cm x 20 cm x 3 cm
Coil diameter	9.7 cm
MV	15 x 15 x 15 cm^3
Offset distance	18 cm
dc current	5 A
Resistance	3.7 Ω
Inductance	4.6 mH

To optimize system performance, precise control of the dc current through the coil is essential, as deviations can lead to fluctuations in the generated magnetic fields. The system control unit consists of a current source, based on an N-channel MOSFET (IRFZ34) regulated by a reference voltage from a Digital-to-Analog converter (AD5683). This circuitry is engineered to maintain current fluctuations within 1% for a current supply of 5A.
A key factor affecting the precision of our system is the quantization error of the sensors. This quantization causes the sensor output to remain constant within regions of similar magnetic fields, rather than varying continuously throughout the MV. To mitigate this issue, the magnetic field gradient and sensor characteristics were selected to ensure that the maximum size of these quantization volumes does not exceed a voxel of 200 μm^3. The hardware design, which incorporates four planar coils, guarantees adequate field gradients across the MV, with at least three coils providing sufficient magnetic gradient at every location along each axis (Fig. 5.3(C)). The field gradients are determined based on the specifications of the MMC5603NJ magnetometer [175], an AMR sensor with a resolution of 6.25nT/LSB and a rms noise of 250 nT at a sampling rate of 50 Hz. To reduce the rms noise, the average of 20 sensor readings was performed. The minimal field gradient was introduced in a previous work [**Publication I**] and defined for this system as 0.3 µT/cm. Another advantage of this magnetometer lies in its compactness, measuring 0.8 x 0.8 x 0.4 mm^3, making it suitable for integration into small-diameter surgical tools, such as the DBS electrode (Fig. 5.1), which typically have a diameter of 1.2 to 1.4 mm.

Software overview

The outcomes of the five-step sequence is a matrix of 15 magnetic field components, reduced to 12 magnetic components after offset cancellation, $B\_(I\_meas)$, with $I = A, B, C, D$, representing the coil activated (Eq. (5.1)). The magnetic field notations employed in this study are outlined as follows:

$$\begin{bmatrix} B_{\text{A\_meas}} \\ B_{\text{B\_meas}} \\ B_{\text{C\_meas}} \\ B_{\text{D\_meas}} \end{bmatrix} = \begin{bmatrix} B_{\text{xA\_meas}} & B_{\text{yA\_meas}} & B_{\text{zA\_meas}} \\ B_{\text{xB\_meas}} & B_{\text{yB\_meas}} & B_{\text{zB\_meas}} \\ B_{\text{xC\_meas}} & B_{\text{yC\_meas}} & B_{\text{zC\_meas}} \\ B_{\text{xD\_meas}} & B_{\text{yD\_meas}} & B_{\text{zD\_meas}} \end{bmatrix} \tag{5.1}$$

From this matrix, the vector of the magnetic field amplitude is extracted (Eq. (5.3)).

$$||B_{\text{I\_meas}}|| = \sqrt{{B_{\text{xI\_meas}}}^2 + {B_{\text{yI\_meas}}}^2 + {B_{\text{zI\_meas}}}^2} \tag{5.2}$$

$$\begin{bmatrix} B_{\text{A\_norm}} \\ B_{\text{B\_norm}} \\ B_{\text{C\_norm}} \\ B_{\text{D\_norm}} \end{bmatrix} = \begin{bmatrix} ||B_{\text{A\_meas}}|| \\ ||B_{\text{B\_meas}}|| \\ ||B_{\text{C\_meas}}|| \\ ||B_{\text{D\_meas}}|| \end{bmatrix} \tag{5.3}$$

The FG is designed so that each point in the MV is uniquely encoded by a magnetic field amplitude vector (Fig. 5.3(D)). This unique encoding relies on the principle of multilateration. This localization technique determines the position of an object by measuring signals from different transmitters. The simplest form of multilateration, known as trilateration, involves three transmitters and is exemplified by the Global Positioning System (GPS) [203]. In the context of magnetic localization, multilateration is applied by using the magnetic field generated by the FG, which varies with the distance between the FG and the magnetic sensor. Consequently, each spatial point corresponds to the intersection of spheres, each representing a specific magnetic field amplitude from each emitter as depicted in Fig. 5.3(D). Accurate determination of these intersections requires precise knowledge of the magnetic fields $B\_(I\_theo)$ produced by the emitters. Spatial localization involves identifying the (x, y, z) coordinates where the difference between the measured $B\_(I\_meas)$ and theoretical amplitude vector $B\_(I\_theo)$ is minimized. The minimization function, F_min is defined in (Eq. (5.3)). The localization resolution was implemented in Python 3.8 using the SciPy library. The minimization method applied to the position determination is the extended version of the Broyden–Fletcher–Goldfarb–Shannon algorithm known as L-BFGS-B algorithm.

$$F_{\text{min}} = \sqrt{\sum_{I}^{[A,B,C,D]} (||B_{\text{I\_theo}}|| - ||B_{\text{I\_meas}}||)^2} \tag{5.4}$$

Given the good manufacturing tolerances of the PCBs, the theoretical magnetic field $B\_(I\_theo)$ was characterized through simulation. Static magnetic field simulations were conducted using the the magnetostatic library Radia available on Python 3.8. The methods for calculating the theoretical magnetic field are available online [204] and in the related publications of Radia library [205, 206]. To optimize simulation efficiency, each coil was approximated as a single conductor carrying a uniform current density. A discrete 3D volume of 25 x 25 x 25 cm^3 with a 5 mm pitch was extracted from the simulation, resulting in a 3D grid comprising approximately 130,000 points. This approximation allowed for a computation time of less than 5 minutes for the 3D grid extraction. The simulated discrete grid was interpolated using the tricubic spline interpolation function from the Python library Eqtools [207], enhancing the spatial resolution. The simulation of a sparse grid and its interpolation facilitates rapid characterization of the magnetic field. This approach was instrumental in designing the FG prior to manufacturing and optimizing the simulation parameters to improve tracking performance.

The orientation vector (Φ, Θ, Ψ), according to Cardan convention, is also determined through minimization. For each coil, $B\_(I\_theo)$ represents the three components of the magnetic field at the identified (x, y, z) position, assuming perfect alignment of the sensor with the FG. The measured field, $B\_(I\_meas)$, can be derived from $B\_(I\_theo)$ using a rotation matrix MR whose components depend on the three angles (Φ, Θ, Ψ), (Eq. (5.6)). The objective of the minimization process is to find the values of these three angles that minimize the error between $B\_(I\_meas)$ and $MR * B\_(I\_theo)$(Eq. (5.5)).

$$A_{\mathrm{I}} = \begin{bmatrix} B_{\mathrm{xI\_meas}} \\ B_{\mathrm{yI\_meas}} \\ B_{\mathrm{zI\_meas}} \end{bmatrix} = MR * \begin{bmatrix} B_{\mathrm{xI\_theo}} \\ B_{\mathrm{yI\_theo}} \\ B_{\mathrm{zI\_theo}} \end{bmatrix} \tag{5.5}$$

$$MR = R_{Z_\Psi} * R_{Y_\Theta} * R_{X_\Phi}, \quad with \tag{5.6}$$

$$R_{X_\Phi} = \begin{bmatrix} 1 & 0 & 0 \\ 0 & \cos\Phi & -\sin\Phi \\ 0 & \sin\Phi & \cos\Phi \end{bmatrix}, R_{Y_\Theta} = \begin{bmatrix} \cos\Theta & 0 & \sin\Theta \\ 0 & 1 & 0 \\ -\sin\Theta & 0 & \cos\Theta \end{bmatrix}, R_{Z_\Psi} = \begin{bmatrix} \cos\Psi & -\sin\Psi & 0 \\ \sin\Psi & \cos\Psi & 0 \\ 0 & 0 & 1 \end{bmatrix}$$

$$A_{\mathrm{I}} = \begin{bmatrix} c_\Theta c_\Psi B_{xI\_theo} - c_\Theta s_\Psi B_{yI\_theo} + s_\Theta B_{zI\_theo} \\ (c_\Phi s_\Psi + s_\Phi s_\Theta c_\Psi) B_{xI\_theo} + (c_\Phi c_\Psi - s_\Phi s_\Theta s_\Psi) B_{yI\_theo} - s_\Phi c_\Theta B_{zI\_theo} \\ (s_\Phi s_\Psi - c_\Phi s_\Theta c_\Psi) B_{xI\_theo} + (s\Phi c_\Psi + c_\Phi s_\Theta s_\Psi) B_{yI\_theo} + c_\Phi c_\Theta B_{zI\_theo} \end{bmatrix} \tag{5.7}$$

$$with \quad c_\Theta = \cos\Theta \quad or \quad s_\Phi = \sin\Phi$$

Due to the planar configuration of the FG, the MR and consequently the orientation vector (Φ, Θ, Ψ) is identical across all four coils. The orientation determination process is conducted in two steps. In the first step, the angles Ψ and Θ are calculated from the first two rows of the Eq. (5.7). In the second step, the angle is extracted from the third row of Eq. (5.7), using the previously determined angles Ψ and Θ. For the angle extraction, the minimization was based on the Powell method also from the Scipy library.

Performance assessment

Two distinct studies were conducted. The first study evaluated the performance of position localization in an environment free of electromagnetic perturbations. The second study focused on evaluating angular detection, using a stereotactic system as the reference.

Position assessment

A custom platform was built using 5 mm polymethyl methacrylate (PMMA) plates. In this platform, the FG was fixed at 18 cm from the MV (Fig. 5.4(A)). To evaluate the position localization performance, a custom magnetic field camera (MFC) consisting of an 8 x 8 sensor

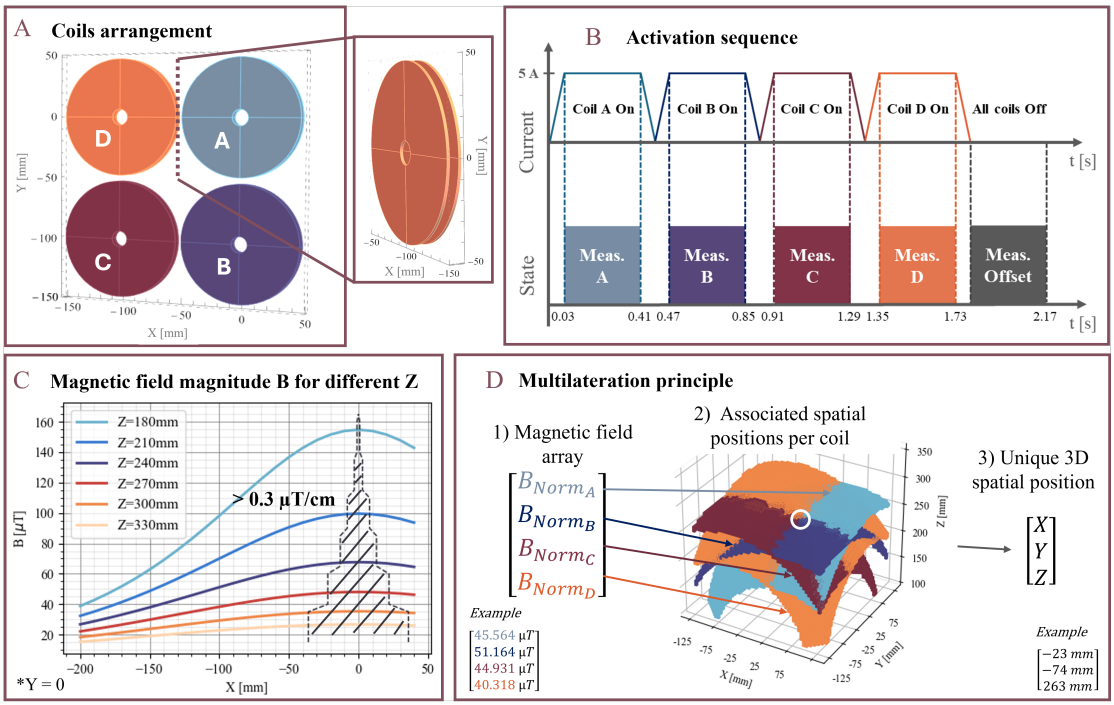

Figure 5.3: Overview of the ManaDBS system and localization methods: (A) Coil arrangement with on the side the representation of the two PCB layers stacked up. (B) Five-step activation sequence: Time diagram of the coil activation along with the field-measurement phases. (C) Plot of the magnetic field amplitude as a function of the distance to the FG. This field profile illustrated the activation of coil A. (D) Example for the multilateration principle leading to the determination of the 3D position for the magnetic field amplitude vector.

array was used to increase the number of positions acquired. The MFC was placed at 54 positions in the MV using a Lego board and mount (Fig. 5.4(A)). The MFC positions covered a volume of 15 x 15 x 15 cm^3, for a total of 3456 sensor positions (Fig. 5.4(C)). The sensors integrated on the MFC was the previously described sensor, the MMC5603NJ [175]. Due to the sensor response inhomogeneity and slight spatial or angular offsets between sensors on the MFC, a calibration method was implemented to correct the magnetic field output of the sensors. The MFC architecture as well as the calibration method was previously described in the literature [208, 209]. Due to the low sampling rate of the MFC, about 1.4 Hz, the system control unit couldn't be used. Instead, a laboratory power supply generator (EA-PS 3032-20 B, Elekto-Automatik Gmbh, Germany) was used to inject the 5A current for about 20 seconds allowing for the acquisition of 20 sensor values. These values were averaged as described in section II.A. The optical tracking system, NDI Optotrak Certus (Northern Digital Inc., Canada), reporting a localization error of 0.1 mm, was used as reference. Four optical markers were attached to the FG. Additionally, four further optical markers and the MFC were mounted on a PMMA plate (Fig. 5.4(B)). The MFC positions captured through optical tracking were transformed into the FG's coordinate system defined by the attached optical markers. This

transformation aligned the coordinate spaces of the optical and EMT tracking systems, enabling direct comparison of positions. The transformed positions served as 3D reference points and were compared to the corresponding 3D positions measured by the EMT system. Position error is calculated using the root mean squared error (RMSE), which represents the Euclidean distance between the measured 3D position and the reference 3D position. RMSE was computed for each MFC position – comprising 64 points – as well as the RMSE across all 3456 positions. Additionally, the mean absolute error (MAE) between the measured and reference positions along each axis was determined across all 3456 positions.
The RMSE at MFC positions ranged from 0.88 to 3.35 mm depending on the distance from the FG (Fig. 5.4(C)). Due to the significant magnetic field decay, performance at greater distances was more sensitive to the noise, particularly the sensor's noise. The RMSE – across all 3456 positions – is evaluated at 1.72 mm with a minimum error of 0.09 mm, a maximum error of 5.7 mm and a standard deviation of 0.97 mm. The MAE along each axis were inferior to 1 mm (Fig. 5.4(D)). The RMSE and MAE were not randomly distributed as the precision of tracking varies as a function of the distance and relative position of the sensors to the FG. Positions closer to the FG have higher localization precision due to a higher signal-to-noise ratio (SNR). Conversely, as the distance from the FG increases, the SNR decreases, resulting in reduced tracking precision. A similar effect occurs when comparing tracking precision at the center of the FG to its periphery.

Orientation assessment

To assess the orientation performance, the Lego board was replaced by the stereotactic Leksell system (Elekta, Sweden). The stereotactic system was secured using 3D-printed holders (Fig. 5.5(A)). For this study, a single magnetic field sensor was integrated at the tip of a 4 mm carbon tube mimicking the DBS electrode (Fig. 5.5(B)). To reduce the angular error caused by misalignment between the sensor axis and the carbon tube axis, the sensor was soldered onto a PCB board and partially inserted into the tube. This solution also helped minimize additional position localization errors. In contrast to the previous study, the sensor integrated in the prototype was not calibrated. Furthermore, the control system described in Section II.A was employed. The orientations obtained with the ManaDBS system were compared to the stereotactic Leksell system (Elekta, Sweden). Each rotational parameter was measured separately with distinct steps and ranges due to the dimensions of the stereotactic arc (Fig. 5.5(A)): arc angle (35° to 135° in 5° increments), ring angle (-50° to 40° in 5° increments), and electrode rotation (0° to 340° in 20° increments). A systematic offset correction was applied by subtracting the average of each angle's values. Following this correction, the angular error is defined as the MAE between the angles obtained from the two systems.
The MAE and standard deviation for the rotations around the arc, ring, and electrode were 0.18° ± 0.19°, 0.50° ± 0.32°, and 2.20° ± 0.92° respectively. The distribution of the angular errors is illustrated in Fig. 5.5(C). The observed variations in mean error and standard deviation between each angle are attributed to experimental uncertainties introduced by the system's graduation. The overall MAE – across all three angles - was determined to be 0.89°, with a minimum error of 0.01°, a maximum error of 3.83°, and a standard deviation of 1.03°.

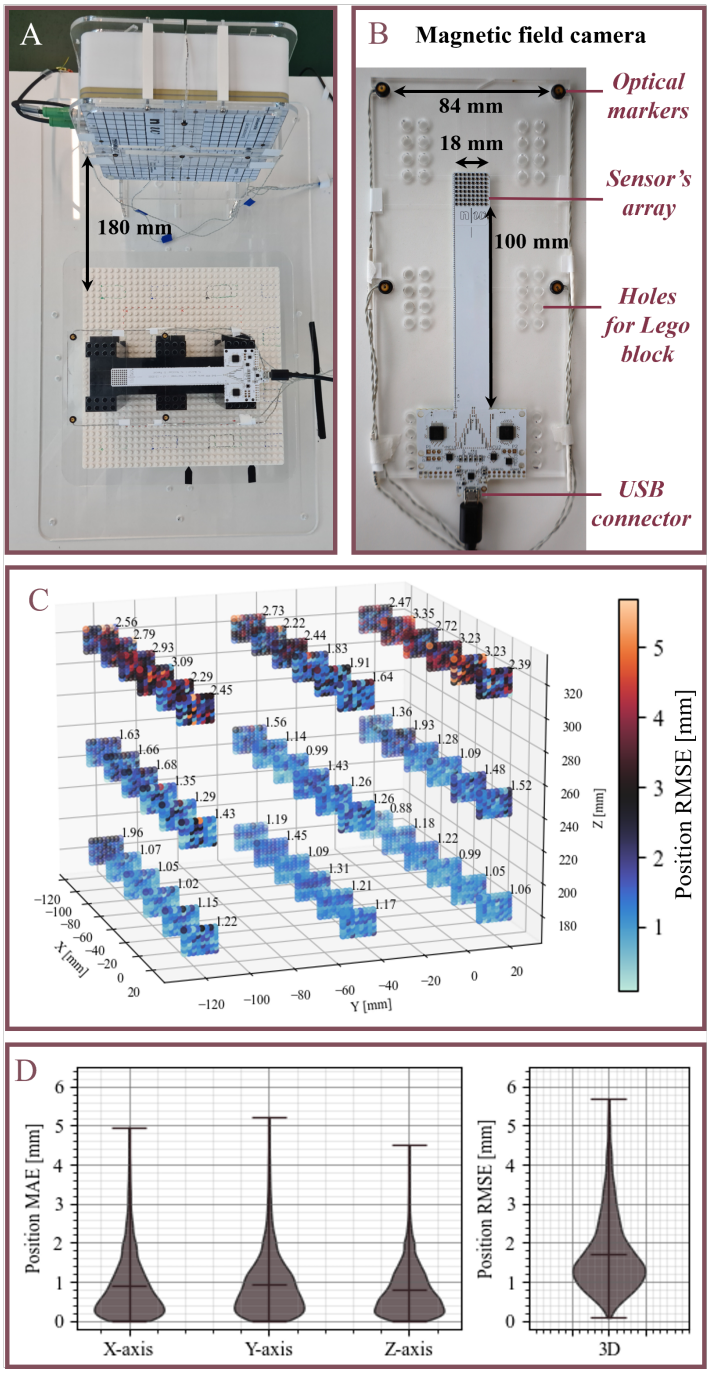

Figure 5.4: (A) Experimental setup including the FG fixed to the PMMA-plates and the MFC on a Lego board placed at 18 cm. (B) PMMA-plates integrating the optical markers and the MFC. (C) 3D Visualization of the RMSE per MFC positions in the MV. (D) Violin plot of the position MAE along each axis and the RMSE in 3D.

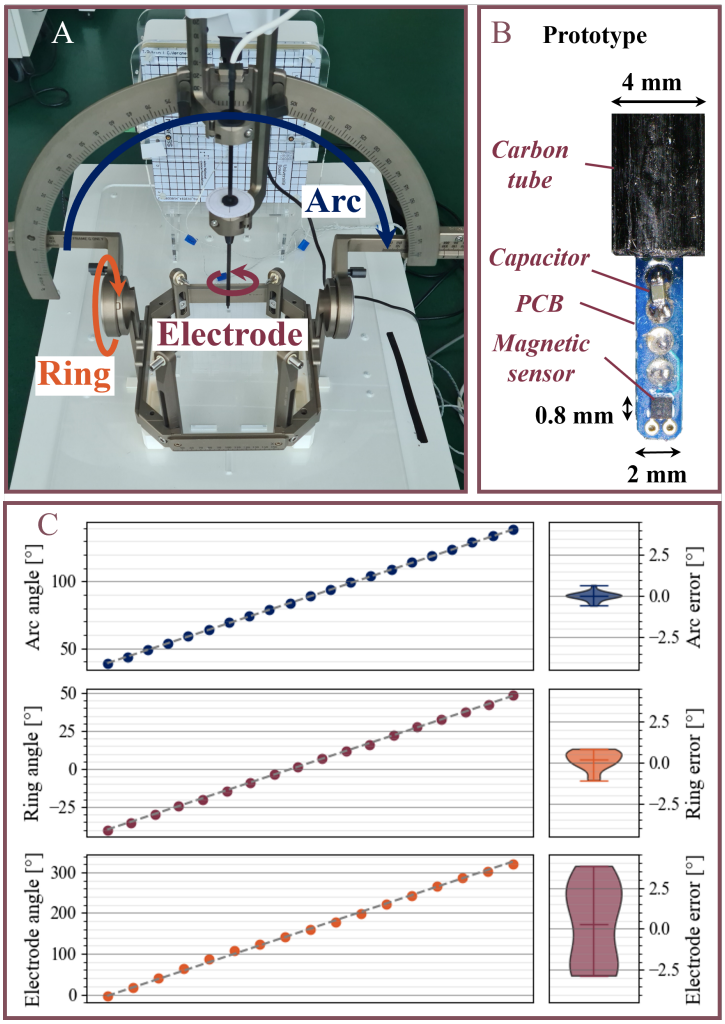

Figure 5.5: (A) Experimental setup including the FG fixed to the PMMA-plates and the stereotactic system with the three orientations defined. (B) Prototype of the DBS electrode consisting of a carbon tube with the magnetic field sensor at the tip. (C) Plot of the angular variations for each angle. The dot markers represent the angle obtained from ManaDBS, the dashed line the angles obtained from the optical tracking. On the right side, violin plots represent the error distributions for the three respective orientations.

DBS implantations

In a similar experimental setup, we evaluated the performance of the ManaDBS system by simulating DBS surgical implantations. A rigid body integrating four optical markers was placed on the DBS electrode prototype previously described (Fig. 5.6(A)) and served as a ground truth for the position variations. Due to the presence of the stereotactic system, the optical markers placed on the FG were inaccessible for optical tracking. Therefore, the positions from the optical system could not be accurately translated into the ManaDBS coordinate system. To address this issue, the rectilinear trajectories obtained from the optical tracking were manually aligned with the trajectories from the ManaDBS, using a simple 3D translation method. It is important to highlight that the position error in DBS implantations reflects relative positioning due to the manual alignment, whereas the position error discussed in Section III pertains to the system's absolute position error. Similarly to the study in Section III.B, the orientation was set by the stereotactic system. The arc and ring angles remained fixed throughout the implantation while only the electrode angle was changed. Variations of the electrode angle from the intended surgical orientation has been reported in the literature [210, 211], suggesting torsion of the electrode along its axis during implantation. We reproduced potential variations of the electrode angles in this study. The angle settings are detailed in Table 5.2. For each rectilinear implantation of 8 cm, ten positions were recorded. A total of six implantations were conducted (Fig. 5.6(B)) each with different values for the arc and ring angles. The position and orientation errors were defined as previously.

Table 5.2: Angles settings

Implantation	Arc angle [°]	Ring angle [°]	Electrode angle [°]
N°1	60°	20°	0, -5, -10, -15, -20, -25, -30, -25, -20, -15]
N°2	70°	10°	[10, 0, -5, 0, 5, 0, -5, 0, 5, 0]
N°3	85°	-5°	0
N°4	90°	0°	[0, 5, 10, 15, 10, 5, 0, 2, -3, -8]
N°5	105°	-15°	[5, 5, 5, 0, 0, 0, 0, -5, -5, -5]
N°6	110°	-20°	[-20, -10, 0, 10, 20, 30, 20, 10, 0, -10]

The RMSE is evaluated at 0.87 mm with a minimum error of 0.31 mm, a maximum error of 1.86 mm and a standard deviation of 0.35 mm. The MAE along each axis were below 0.5 mm (Fig. 5.6(C)). For the six implantations, the electrode angles varied from -30° to 30° as illustrated in Fig. 5.6(D). The MAE and standard deviation for the rotations around the arc, ring, and electrode were respectively 0.29° ± 0.38°, 0.72° ± 0.59°, 0.56 ± 0.5°. The overall mean orientation error was determined to be 0.52°, with a minimum error of 0.001°, a maximum error of 3.43°, and a standard deviation of 0.53°.

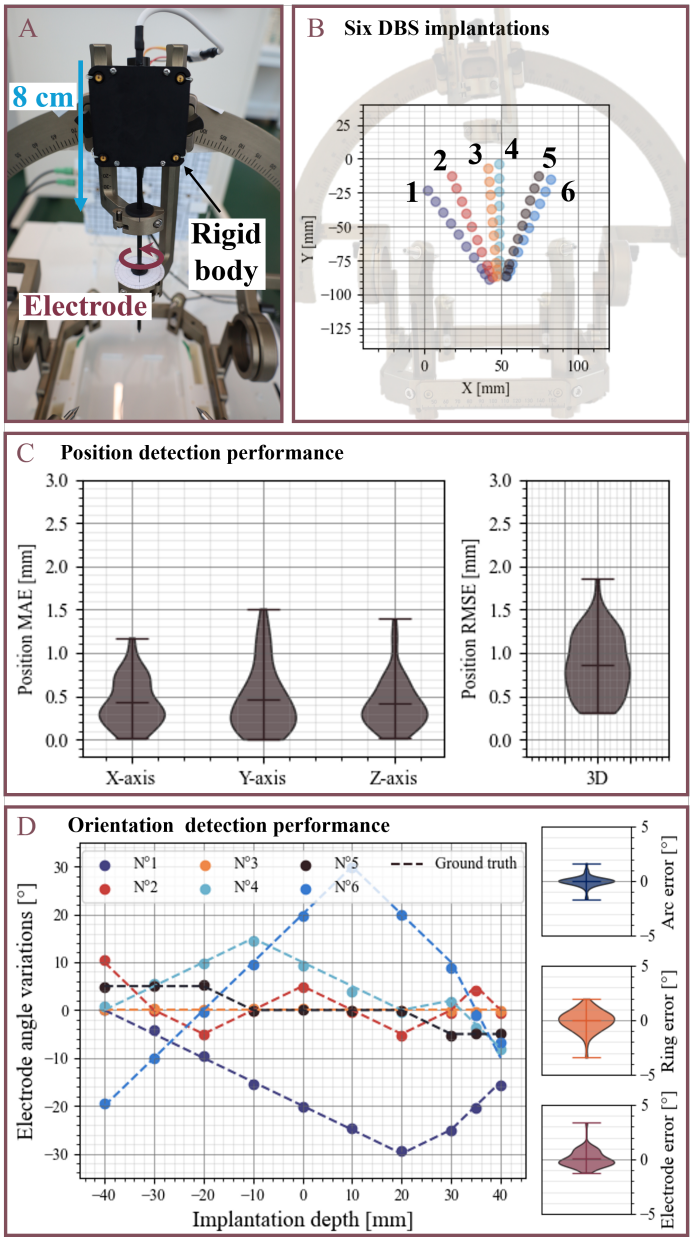

Figure 5.6: (A) Rigid body integrating the optical markers on the DBS electrode prototype. (B) 3D visualization of the six DBS implantations with the stereotactic frame in transparency. A stereotactic system picture was transparently added. (C) Violin plots of the position MAE error along each axis and the RMSE in 3D. (D) Electrode angle variations for each implantation. Dot markers indicate the angle obtained from ManaDBS; the dashed line represents the angles obtained from the optical tracking. The color scheme matches that of subfigure-(A). On the right, violin plots illustrate the angular error distribution for the three angles.

Discussion

In this study, we presented a detailed technical description of the ManaDBS system based on quasi-static magnetic field and high-resolution magnetometers. The ManaDBS system was specifically designed to address the unmet needs of DBS surgery which include the monitoring of the DBS electrode position and orientation during implantation. Traditional imaging technologies such as MRI, CT and 2D X-ray imaging are the current gold standard but remain limited by the number of acquisitions, environment compatibility and acquisition duration. The ManaDBS system is proposed as a complementary or alternative solution for DBS surgery, providing the orientation and position of the DBS electrode and mean error of 1.72 mm and 0.89° in the MV. Better performances – mean spatial and angular errors of 0.87 mm and 0.52° – were achieved when simulating DBS implantations.
This improvement can be attributed to the positioning of the DBS implantations at the center of the MV, where lower errors are reported. Additionally, position errors for the DBS implantations were calculated from relative positions, allowing for manual correction of potential offset errors, unlike in the first study which was based on absolute positions. While the reported update rate of 0.4 Hz is nearly 100 times lower than that of commercial EMT systems, it remains higher than the update rates of traditional imaging technologies and offers advantages in cost, safety, and integrability. The update rate could be increased up to a few Hz but will still be constrained by the ramp-up time of currents into the coil and the number of sensor values required to ensure tracking performance. The ManaDBS system offers spatial and angular resolutions similar to those of imaging technologies, without the need for lengthy acquisition times or radiation exposure. It is designed to aid neurosurgeons in decision-making by focusing on localization rather than actively guiding the electrode.

Currently, the system's accuracy is adequate for localizing the electrode relative to surrounding structures, which can be several millimeters in size. However, further improvements are necessary to achieve one-millimeter accuracy and higher precision throughout the entire volume of the MV. The dependency of the performance on the distance to the FG is a known limitation of the EMT technique based on quasi-static magnetic fields. Furthermore, the performance is affected by the relative placement of the sensors to the FG surface. Stronger gradients are generated at the center of the FG, which increases detection sensitivity. One potential improvement is to optimize the coil arrangement. Currently, four coils are used to ensure at least three significant gradients at any point within the MV. Increasing the number of coils would increase field data, and by weighting the contribution of each coil, depending on the region and associated gradient, position errors could be minimized. However, this may reduce the sampling frequency due to the activation of more coils. Enlarging the coils, while maintaining a similar MV, could also reduce regions with low gradients, although this modification is limited by the constraints of the surgical environment. Another method to increase the SNR involves increasing the current amplitude injected into the coils, thereby generating a stronger magnetic field. However, this approach would significantly increase power consumption and the heating of the coils during activation.
To reduce the system's dependency on strong magnetic fields while improving performance,

higher resolution magnetic sensors with lower RMS noise could be selected, reducing the need for extensive averaging. Tunnel Magneto-Resistance (TMR) sensors, such as those used in a recent pilot study [199] are great candidates. A newly released 3D TMR magnetometer for geomagnetic applications offers a resolution of 10 nT/LSB and an RMS noise of 40 nT [177]. However, we observed crosstalk issues between the sensors channels, making them in this state of research not adequate for our application [unpublished]. Another method to improve performance involves increasing the current amplitude injected into the coils, thereby generating a stronger magnetic field. However, this approach would significantly increase power consumption and the heating of the coils during activation. The balance between sensor resolution and magnetic field amplitude must be carefully considered, as both factors influence the sampling rate and tracking performance.
The ManaDBS system achieved significant penetration depth and MV while maintaining compact FG dimensions and low power consumption, without compromising performance.

Table 5.3: Comparison with existing EMT systems based on quasi-dc fields

System specification	This work	Sharma et al., 2021	Sharma et al., 2023
Target application	DBS surgery	Orthopedic surgery	Ingestible capsule
Localization dimension	6D	3D	3D
Mean spatial error	1.7 mm	0.1 mm	1.5 mm
Mean angular error	0.9°	N/A	N/A
MV	15 x 15 x 15 cm^3	20 x 20 x 20 cm^3	*40 x 40 x 40 cm^3
Offset distance	$^{\$}$18 cm	0 cm	0 cm
Penetration Depth	33 cm	10 cm	** 40 cm
Sampling Frequency	0.4 Hz	7 Hz	$^{£}$0.017 Hz
FG dimension	20 x 20 x 3 cm^3	30 x 30 x 1 cm^3	$^{\#}$60 x 60 x 2 cm^3
Maximal FG power consumption	92.5 W	N.R.	$^{\#}$800 W
FG weight	1.2 kg	N.R.	$^{\#}$18 kg

* *Requires two set of coils surrounding the MV*
** *For one set of coils, the penetration depth is reduced by half*
$^{\#}$ *For one set of coils*
$^{\$}$ *Tracking can be performed within the offset distance (down to 3.5 cm from the FG)*
$^{£}$ *Can be increased to 3.3 Hz, might require cooling system due to heating phenomena*
N.R.: *Not reported*
N/A: *Not applicable*

The compatibility and integrability of the ManaDBS within the DBS surgical environment were considered but not thoroughly assessed in this study. DBS implantations were simulated using a standard stereotactic system, and no additional or non-linear errors attributable to the stereotactic system were observed. Future research will involve a thorough evaluation of how the stereotactic system affects tracking performance. Additionally, surgical equipment related to DBS surgery, such as Microdrive systems or retractors, should be examined. The DBS

procedure involves several steps, from pre-operative imaging to the anchoring of electrode. The ManaDBS system is intended to be used during the electrode implantation phase, when no other equipment is being moved or imaging systems used in parallel. Since the measurement time is quite long (2.5 seconds), moving magnetic bodies could compromise tracking performance. Therefore, the ManaDBS system is well-suited for DBS surgical procedures that require the gradual insertion of DBS electrodes into the patient's brain. However, its application to other surgeries would be limited, highlighting the need to further improve the sampling frequency.
Regarding medical safety, relevant standards should be verified, such as the IEEE C95 Standards (C95.6-2002 for 0 Hz to 3 kHz) [212] from the International Committee on Electromagnetic Safety (ICES). For quasi-static magnetic fields (< 8 Hz), ICES recommends a maximum magnetic flux amplitude of 18.1/*f* (T) (f being the frequency in Hz) for head exposure. In our case, the maximum magnetic amplitude is set at 45 mT, which is about 300 times greater than the amplitude generated by the FG within the MV and 1.5 times greater than that at its immediate surface. Furthermore, peripheral nerve stimulation (PNS) can be triggered by coil switching. The PNS threshold is commonly defined as the peak $d|B|/dt$ and reported in the range of 43-57 T/s in [213]. The peak value of the ManaDBS was calculated as 0.005 T/s ($B \leq 160\mu T$ and 30 ms rise-time) which is significantly below the threshold for PNS. In addition to these precautions, the system is compatible with potential patients with programmable ventriculoperitoneal shunts as well as cardiac implantable electronic devices. Indeed, the maximum amplitude of the magnetic field in the MV is about 160 µT and the maximal gradient is about 8 µT/cm in contrast to the reference threshold given by manufacturer of 140 mT/cm gradient for programmable ventriculoperitoneal shunts [214] and 1 mT maximum field exposure for cardiac implantable electronic devices [215]. At the direct surface of the FG, the maximal amplitude is about 30 mT with a gradient of 8 mT/cm which still comply with the guidelines but could carry a risk for patients with cardiac implantable electronic devices. Therefore, the system is set to be used with a minimum distance of 10 cm from the FG. A further magnetization of the surrounding magnetic or ferromagnetic objects is not expected due to the low magnetic fields generated within the MV (<160 µT). However, this could occur with objects placed directly on the FG (30 mT at the surface). While additional dc noise may arise in this scenario, the magnetic objects would remain at least 20 cm away from the tracked DBS electrode, leading to negligible impact on tracking performance. This issue can also be mitigated by enclosing FG in a packaging that restricts access.

Conclusion

This paper introduces the ManaDBS, a novel EMT system designed for monitoring the position and orientation of DBS electrodes during implantation surgery. The system achieves a 3D localization error of 1.72 mm and 0.89° within a 15 x 15 x 15 cm^3 volume, utilizing safe quasi-static magnetic fields. This level of performance is achieved at an offset distance of 18 cm, making it suitable for neurosurgical applications. By integrating a 3D magnetic sensor at the tip of a DBS electrode, the ManaDBS proposes a realistic solution for regular monitoring of the DBS electrodes eliminating the need for potentially harmful X-Ray imaging.

CHAPTER 6

Publication III - EMT compatibility to DBS Surgical environment

Foreword and Overview

Following the development of the ManaDBS system, its suitability to the DBS surgical environment was further investigated. This investigation included mainly the impact of the stereotactic system on tracking performance. This evaluation was also performed using a commercial EMT system to compare the compatibility of these two EMT techniques to DBS surgery. The commercial EMT system relies on alternating magnetic fields and micro-coil technology, which is known to be incompatible with stereotactic systems.

Contribution: The candidate was overall responsible for the design of the study. The candidate received technical support from members of the research laboratory (Neuroengineering Lab, FHNW-HLS) concerning the development of a 3D assessment setup. The candidate performed the measurement and analysis. The candidate was overall responsible for the writing of the manuscript. The supervisors and co-authors supported the process and reviewed the paper.

Abstract

Real-time guidance of the implantation of DBS electrodes in the context of stereotactic neurosurgery is essential but is currently unavailable. EMT systems offer high-accuracy localization of tools in restricted volumes but face compatibility issues with standard DBS procedures due to electromagnetic distortions. This paper aims to evaluate and compare the localization performance (position and orientation) of a novel EMT system, the ManaDBS, specifically designed for stereotactic surgical environments, against the NDI Aurora, a commercially available EMT system. Two studies were conducted to assess the suitability of each EMT system for DBS surgery. The first study evaluated performance accuracy within the measurement volume in the presence of two different stereotactic systems (Frame G and Vantage system, Elekta). The second study simulated a DBS surgical theatre, performing implantation procedures with each EMT system and evaluating the position accuracy of the EMT sensor. The localization errors of Aurora (0.66 mm and 0.89°) were slightly lower to those of ManaDBS (1.57 mm and 1.01°). However, in the presence of a stereotactic system, Aurora exhibited notable degradation (2.34 mm and 1.03°), whereas ManaDBS remained unaffected. This pattern persisted during simulated implantation in a DBS surgical environment, where nonlinear trajectories with significant error fluctuations along the implantation path were observed with Aurora. The significant electromagnetic-field distortions of Aurora render it incompatible for DBS surgery. However, the ManaDBS system exhibited no impact from these distortions, suggesting its potential suitability for DBS surgery and other potential applications in stereotactic neurosurgery.

Introduction

DBS surgery involves implanting electrodes into deep brain structures to alleviate motor disorders such as Parkinson's disease or essential tremor. Typically performed with a stereotactic system under local anaesthesia, the procedure is complemented by MER of the neuronal activity and/or through stimulation tests to verify the target location [41]. Intra-operative validation of the electrode implantation position can be achieved using 2D X-rays or 3D CT. However, challenges remain, such as the angular localization of new directional DBS leads or real-time navigation during implantation. A promising technique for addressing these challenges is EMT) [216, 217], which has been explored as a complementary or alternative imaging method to X-rays. EMT systems provide regular feedback on the position and orientation of DBS electrodes, offering advantages like reduced radiation exposure and precise 3D localization relative to brain structures. A comprehensive review by Frank in 2014 [180] presented the commercial market and typical EMT technology used. The state-of-the-art EM systems approved for neurosurgery include the AxiEM (Medtronic Inc., Minneapolis, USA) and the Kick EM (Brainlab, Munich, Germany). These systems are integrated into surgical platforms that also incorporate optical tracking and image-guided software, such as Medtronic's StealthStation. Table 6.1 summarizes the known characteristics of the two systems. In the context for DBS electrode, a study by Burchiel [108] showed comparable performance between EMT and CT guidance. However, due to compatibility issues, frameless stereotactic surgery was performed instead of the standard

stereotactic procedure.

Despite its potential, EMT technology has limitations that affect its clinical application. One inherent limitation is the minimum practical sizes of the sensors and field generators necessary for the optimal functioning of EMT systems. Another significant constraint arises from the technology's sensitivity to electromagnetic (EM) distortions caused by the proximity of medical diagnostic devices like CT or MRI scanners [218], as well as ferromagnetic objects [219]. These issues accentuate the need for ongoing advancements to enhance EMT's robustness and adaptability in clinical settings. Commercial EMT systems comprise a FG that produces an alternating magnetic field and specialized magnetic sensors known as micro-coils. However, operating with alternating magnetic fields at frequencies in the hundreds of kilohertz introduces additional EM distortions. Beyond the primary sources of distortions, including ferromagnetic materials and electronic devices, conductive distortions must also be considered. These distortions arise from Eddy currents induced by alternating magnetic fields in conductive materials, which generate secondary EM fields that interfere with the primary magnetic field. This secondary EM field is present only during FG activation and operates at the same frequency, making it particularly challenging to compensate for. The magnitude of conductive distortions depends on many factors such as the size, composition, proximity, and shape of the distortion sources. Nixon et al. [220] proposed an initial theoretical model that correlates tracking errors with distortion sources. This model is based on experimental observations and is therefore tailored to the specific setup used. Given the unique nature of each surgical environment, translating performance assessments and compensation strategies [221, 222] across different setups remains challenging.

Table 6.1: Description of the two EMT systems available on the market for neurosurgery: Medtronic AxiEM and the Brainlab Kick EM [223, 224].

EMT system	Medtronic AxiEM	Brainlab Kick EM (Model: NDI Aurora V3)
Emitter type	Flat and Side-mount	Side-mount
FG dimension	Side-mount: 13.5 x 13.5 x 8.5 cm Flat: 50 x 35 x 3.5 cm	20 x 20 x 7 cm
Magnetic field	FG emits low intensity and varying electromagnetic fields which induce small currents in the sensors embedded in the instrument.	
Volume of tracking	Side-mount: 46 x 46 x 31 cm Flat: 40 x 40 x 37.5 cm	50 x 50 x 40 cm
Sensors	Micro-coils	
Datasheet warning	Metallic and conductive objects such as the surgical table. Recommended distance from the metal of 5 cm for the flat emitter and 25 cm for the side-mount emitter.	System accuracy may be affected by the setup (monitor, base station...). Some metal objects and radio frequency communication equipment may cause interference.

Concurrently with these advancements, there is a growing interest in EMT systems based on quasi-static magnetic fields. Over the past decade, progress in miniaturized integrated magnetic sensors has enabled the design of functionalized catheters with millimeter dimensions, offering enhanced mechanical robustness in contrast to miniaturized coils. The primary benefit of an EMT technique based on integrated magnetic sensors and quasi-static magnetic fields lies in its inherent resistance to distortion and ability to maintain a high level of precision [135, 189]. Nevertheless, this EMT technology suffers from another limitation: its reduced update rate ranging from 1 to 10 Hz, which defines the number of localization outputs provided per second. This limited update rate restricts this EMT technology's suitability to certain surgical procedures such as DBS surgery, as it involves slowly inserting electrodes along tens of centimeters into the patient's brain. Knowing that many clinical centers heavily rely on stereotactic systems, the introduction of a compatible EMT system could enhance safety and reduce surgery duration. To this end, we developed a quasi-static EMT system, named ManaDBS, for intra-operative localization of DBS electrodes [225, 201].

This paper provides a comprehensive evaluation of the performance and a comparative analysis between the NDI Aurora V2 system and the ManaDBS system. The two studies focuses on the integration of each EMT system within a DBS surgical environment including a stereotactic system. The commercial system from NDI is a well-known electromagnetic tracking system. The V3 version of the NDI Aurora system is notably marketed by Brainlab under the product name Kick EM, as indicated in the FDA's 510(k) premarket notification [226]. While the system used in this paper is an earlier version, the underlying technological principles remain the same. Through two distinct studies, we aimed to provide valuable insights on the applicability of EMT systems in the context of stereotactic DBS surgery.

Electromagnetic tracking systems

- **NDI Aurora:** The commercial EMT system considered in this paper is the Aurora V2 Planar FG from NDI, depicted in Fig. 6.1. The FG, with dimensions of 20 × 20 × 7 cm, generates an alternating magnetic field within a tracking volume of 50 × 50 × 50 cm^3. NDI reports localization errors of 0.5 mm and 0.3° at the centre of the tracking volume with an update rate of 40 Hz. A flextube of 1.3 mm diameter, containing a standard six degrees-of-freedom (DOF) sensor (610060 from NDI) was used as the tracking tool in the two evaluative studies. All tracking data (positions and orientations) were recorded and managed via the NDI ToolBox software.

- **ManaDBS:** The technological principle of the ManaDBS system relies on quasi-dc magnetic field measured by monolithic magnetic sensors. The FG consists of four planar coils which sequentially generate static magnetic field with a maximum strength of 160 μT. To ensure consistency with the Aurora system and avoid introducing additional errors in the comparative study, the dimensions of the FG were made identical to those of the Aurora, allowing the two FGs to be swapped in the experimental setup. The activation sequence of the coils follows five steps: the first four steps involve activating each coil individually, and

the fifth step involves offset cancellation. During offset cancellation, the environmental magnetic field, including the Earth's magnetic field, is measured with all coils turned off. This environmental field data is subtracted from the first four measurements to eliminate any static perturbations. The outcome of the five-step sequence is a matrix of 15 magnetic field components, reduced to 12 magnetic components after offset cancellation. The FG is designed to uniquely encode each point in the MV) with a magnetic field amplitude vector. This unique encoding is based on the principle of multilateration, where an object's position is determined by measuring signals from multiple transmitters. In the case of electromagnetic localization, multilateration uses the magnetic fields generated by the FG, which vary with the distance between the FG and the magnetic sensor. The update rate of ManaDBS is 0.3 Hz. To ensure high tracking accuracy, precise knowledge of the magnetic fields is required. Static magnetic field simulations were conducted using the Radia magnetostatic library in Python 3.8 [206]. Additionally, the current supply to the coils is regulated to ensure fluctuations remain within 1% at a supply current of 5A. The detailed principle of the ManaDBS system and its characterization were presented in a previous publication [**Publication II**], which reported localization errors of 1.72 mm and 0.89° within a tracking volume of 15 × 15 × 30 cm^3. For this study, a customized flextube with a diameter of 1.8 mm was developed. The flextube contains an three-axis anisotropic magnetoresistive sensor (MMC5603NJ, Memsic Semiconductor Co.) placed at its tip (Fig. 6.1).

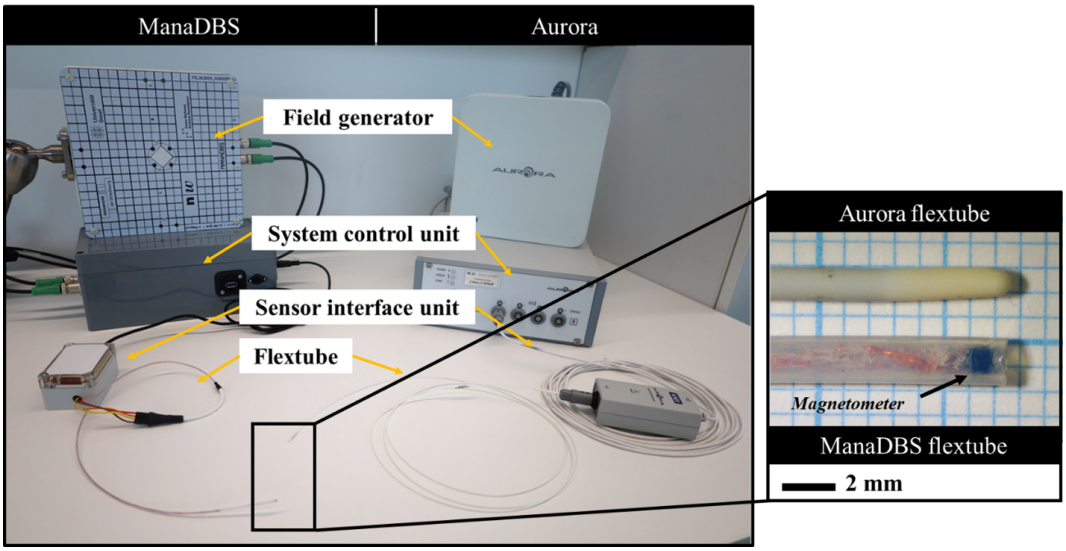

Figure 6.1: The two tracking systems: Aurora (right) and our developed system ManaDBS (left), both with a field generator of 20 × 20 × 7 cm and the associated flextubes with diameters of 1.3 mm and 1.8 mm, respectively.

Assessment methods

Study 1: Tracking performance in the presence of a stereotactic system

Study 1 evaluated the performance of both EMT systems within the measurement volume using a high-precision setup to accurately replicate experimental conditions. Three distinct settings were examined. Initially, we established a baseline environment free of any EM perturbations. Subsequently, we conducted two additional experiments introducing two different stereotactic systems: the Leksell Stereotactic G System (Elekta AB, Stockholm, Sweden), which has been a reference for functional neurosurgery and particularly for DBS surgery for over two decades, and the recently released Leksell Vantage Stereotactic System (Elekta AB). These three settings are referred to as the baseline, Gframe, and Vantage setups, respectively.

❉ **3D assessment setup:** Setups for assessing the performance of EMT systems are commonly made from Lego [227] or Polymethyl methacrylate (PMMA) arrangements [228, 229] to avoid additional EM distortions. A custom-made fixed-size 3D system was built using 5 mm PMMA plates (Fig. 6.2). Four 2D platforms of varying heights were sequentially positioned at 18 cm from the FG. Each platform included 25 positions. A 3D-printed piece holding the flextube was manually placed at each position. A total of 100 positions were acquired, covering a volume of $11.25 \times 11.25 \times 11.25$ cm^3, as depicted in Fig. 6.2. At each position, 25 measurements were acquired for each flextube. The stereotactic systems (frame and arc) were positioned around the platforms and secured using 3D-printed holders.

❉ **Setup calibration:** To validate the placement of the flextube within the assessment setup, we established reference positions using the NDI Optotrak Certus optical tracking system (Northern Digital Inc., Waterloo, Canada). This calibration step was essential to correct any errors introduced during the manufacturing of the 3D assessment setup. The NDI Optotrak Certus system provides a reported localization accuracy of 0.1 mm. Four LED markers were fixed on the FG, while four embedded markers were integrated into the flextube holder. These optical markers were employed to capture the 100 positions within the 3D assessment setup, which were then transformed into the coordinate system of the FG. Subsequently, the reference positions were aligned with the measured positions of the baseline setup using the iterative closest point (ICP) algorithm simpleICP [230]. The ICP algorithm accounted for any misalignment or errors arising from the placement of LED markers on the FG and flextube holder. Once the ICP registration was completed, the corrected reference positions were saved and used as the ground truth for evaluating localization performance.

❉ **Data Analysis:** The measured positions and orientations were averaged over the 25 measurements per location. Position errors were defined as the Euclidean distance between the measured position and the ground-truth position. The orientation error was also defined as the Euclidean distance (in the angular space) between the measured orientation and the true orientation. The latter was defined to be the average orientation

measured over 100 positions in the baseline setup. The jitter for both position and orientation, was calculated as the standard deviation of all 25 measurements per location. Statistical analysis was performed using Python 3.9 and the library Scipy.stats. A Kruskal–Wallis one-way ANOVA test with Bonferroni correction was used to compare the three setups described above. A $p < 0.001$ was considered a statistically significant difference.

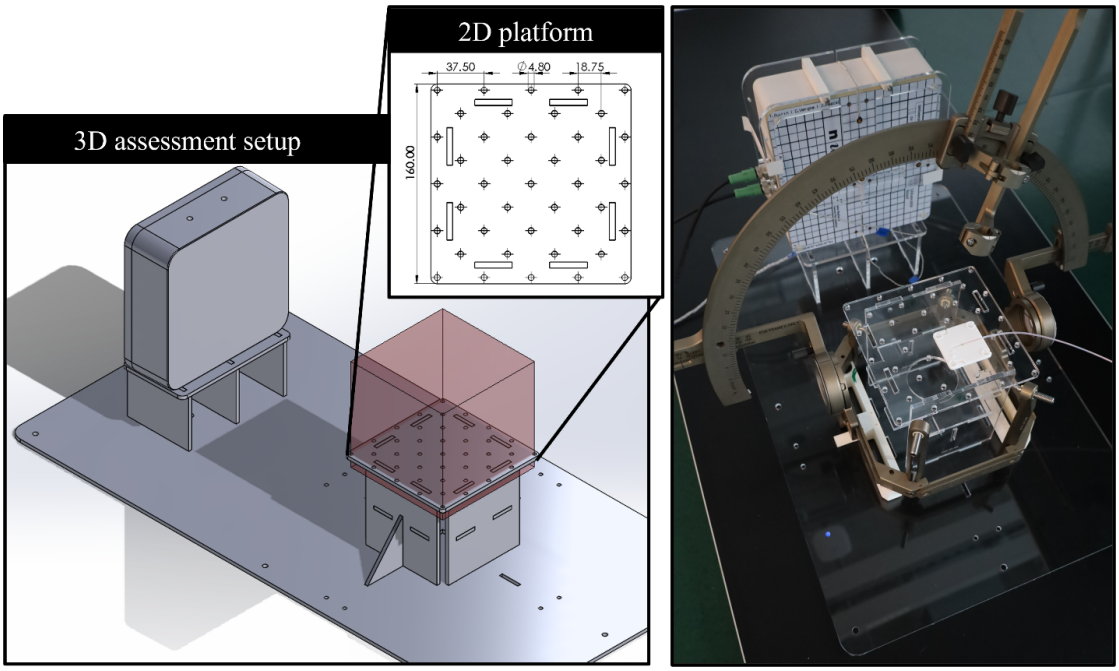

Figure 6.2: On the left, a rendering of the 3D assessment setup, constructed with 5 mm-thick PMMA. The measurement volume (15 × 15 × 15 cm^3) is represented in red. On the right, a picture of the Gframe setup, including the Stereotactic G system (frame and arc) and the ManaDBS system.

Study 2: DBS electrode implantation

Study 2 assessed the suitability of both EMT systems for the DBS operating room. A DBS surgical theater was created to mimic as faithfully as possible the EM disturbances associated with this environment. During the implantation process, the flextube was used in place of the DBS electrode. Straight implantations were performed for both EMT systems and registered using the Optotrak system.

❋ **Surgical environment:** The simulated operating-theater environment included an operating table along with its requisite accessories: a surgical bed (Maquet Betaclassic, Getinge AB, Gothenburg, Sweden), fixtures for the stereotactic frame comprising a connection bracket (1130.54B0, Getinge AB) and an adjustable base unit (1005.50A0, Getinge AB),

two stereotactic systems with their respective interfaces for the operating table (Leksell Stereotactic System Clamp and Vantage Starburst 3/8", Elekta AB), and fixations for each EMT system to be attached to the right side rail of the operating table (Fig. 6.3). In contrast to study 1, the FG was placed at the bottom left side of the stereotactic system. A 3D-printed head phantom was positioned within the stereotactic frame. Subsequently, a C-arm (Ziehm Vision FD Vario 3D, Ziehm Imaging GmbH, Nuremberg, Germany) was positioned on either side of the stereotactic arc.

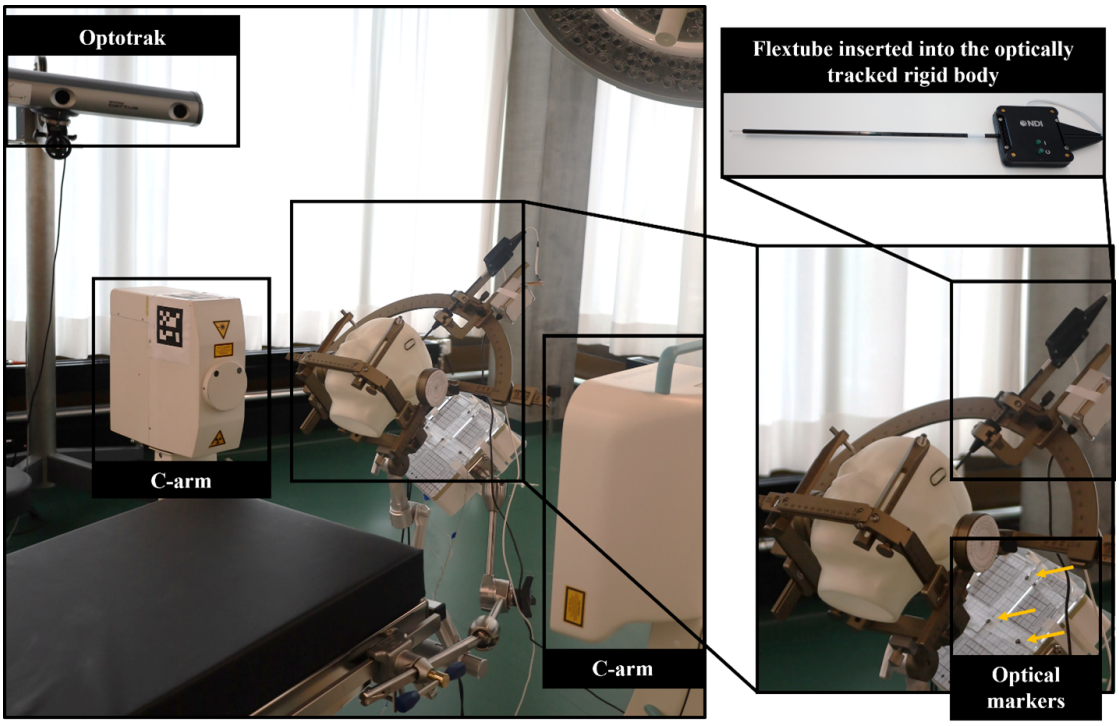

Figure 6.3: DBS surgical theater: On the left, a picture of the fixation of the EMT system (ManaDBS) and the stereotactic system (G system) to the operating table in the presence of the Optotrak system and the C-arm system. On the bottom right, the zoom on the stereotactic system with at its bottom left, the ManaDBS FG and the associated optical markers. On the top right, a picture of the rigid body integrating the ManaDBS flextube.

❊ **Reference system:** The Optotrak tracking system was again used as the reference system. Four LED markers were fixed to the FG, while a rigid body integrating four embedded LED markers (S-type 4-marker Probe, 8700311, NDI) and the flextube (Fig. 6.3) was used to capture the ground-truth positions and orientations. Subsequently, spatial information was translated into the coordinate system of the FGs.

❊ **Data Analysis:** Two rectilinear trajectories (one per hemisphere) of 10 cm were defined according to the stereotactic parameters in Table 6.2. The implantation started from the surface of the phantom head – i.e., the closest of the stereotactic frame – and went down

to a depth of 10 cm, further from the stereotactic arc. These two trajectories were reproduced five times for a total of ten trajectories per EMT system and per stereotactic system. Along each trajectory, ten positions were recorded, and for each position 25 measurements were made. In study 2, the systematic error was removed by fitting the two rectilinear trajectories from the optical reference to the two trajectories obtained with the EMT system. An automatic fitting could not be performed with the ICP algorithm as no baseline was available. Therefore, a 3D linear transformation was manually applied. This process eliminated systematic error, leaving only the error associated with trajectory nonlinearity. In image-guided procedures employing EMT or optical tracking, systematic error is typically addressed during the registration step. This step is performed at the beginning of the procedure and involves identifying patient-specific fiducials — such as anatomical landmarks — using both the patient's imaging and the tracking system. From these fiducials, the spatial transformation between the tracking coordinate space and the patient's coordinate space is established. To simulate the outcome of this registration step, we manually corrected the systematic error in our study. In this study, the position error was defined as the Euclidean distance between the measured position and the fitted optical reference. Jitter error for each position was defined as previously introduced. Statistical analysis was performed as stated above. The orientation was not investigated due to the missing reference.

Table 6.2: Parameters chosen for the Leksell Frame G and Vantage Frame. These parameters are possible parameters for patients suffering from Parkinson's disease or Essential tremor.

Side	x	y	z	Ring	Arc
Left	110	98	116	78°	112°
Right	88	98	116	78°	65°

Results

Study 1: Tracking performance in the presence of a stereotactic system

On average, for the ManaDBS system, there was no significant difference in the position and orientation errors between the baseline and the stereotactic setups ($p > 0.2$) (Fig. 6.4). The median position errors (Q1–Q3) of the ManaDBS system were about 1.57 mm (1.3–1.9 mm) for all the setups. A nonsignificant difference ($p = 0.07$) in the orientation was observed between the baseline and the Gframe setup. The median orientation errors (Q1–Q3) were about 1.01° (0.65–1.4°) for all the setups. Although there also was not a significant difference in the orientations between the baseline and stereotactic setups for the Aurora system ($p > 0.6$), a significant difference in the positions between the baseline and each stereotactic setup was observed ($p < 0.001$). The median position errors (Q1–Q3) increased from 0.66 mm (0.13–0.89 mm) at baseline to 2.1 mm (1.37–3.24 mm) in the Gframe setup and 2.34 mm (1.67–2.84 mm) in the Vantage setup. The median orientation errors (Q1–Q3) of the Aurora system were about 0.94° (0.5–1.6°) for all the setups.

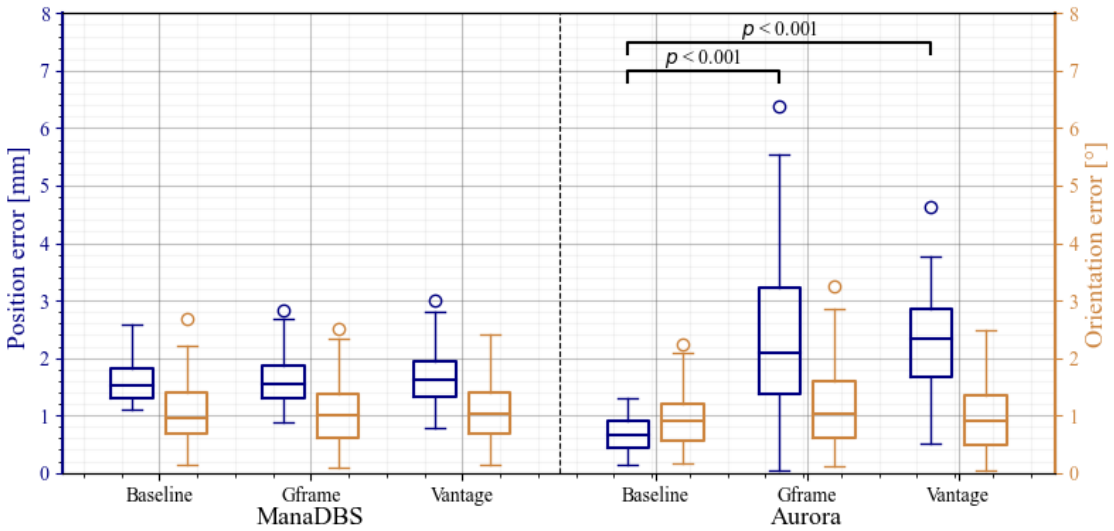

Figure 6.4: Boxplots of the position (blue boxes on the left) and orientation (yellow boxes on the right) error per setup, calculated from the 100 measurements in the 3D assessment setup. Significant differences are indicated at the top of the boxplots.

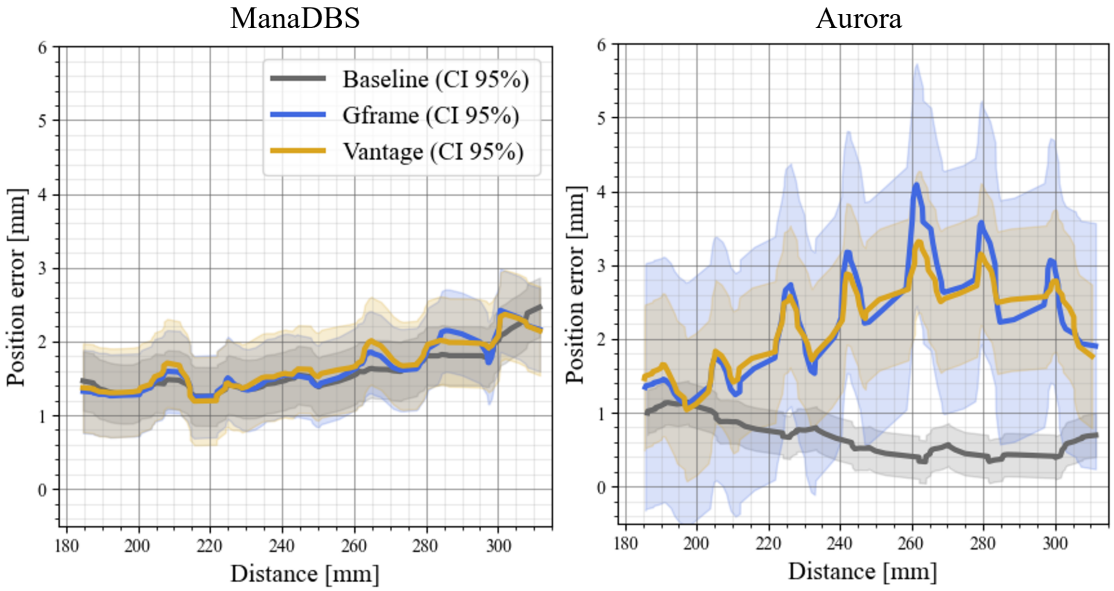

Figure 6.5: Position error for the ManaDBS system (left) and the Aurora system (right) with 95% confidence intervals as a function of the distance to the FG for the two EMT systems. Data from the three different setups are presented: baseline (grey), Gframe (blue), and Vantage (yellow).

There were not any significant differences between the setups for the position jitter (all <0.8 mm and all <0.08 mm) and the orientation jitter (all <0.35° and all <0.3°) for the ManaDBS and Aurora systems, respectively. The jitter was ten times higher for ManaDBS than Aurora. Additionally, both the position error and the jitter increased at greater distances from the FG, particularly for ManaDBS. These observations can be attributed to the high RMS noise of the sensor used in the ManaDBS system.
The position error as a function of the distance of the EMT sensor from the FG for both systems is shown in Fig. 6.5. For ManaDBS, the position error increased by 0.8 mm at greater distances from the FG, but it remained consistent across all the setups. In contrast, the Aurora system exhibited a specific error pattern for the stereotactic setup, with large peak errors at greater distances. These peaks occurred near large metallic parts of the stereotactic systems.

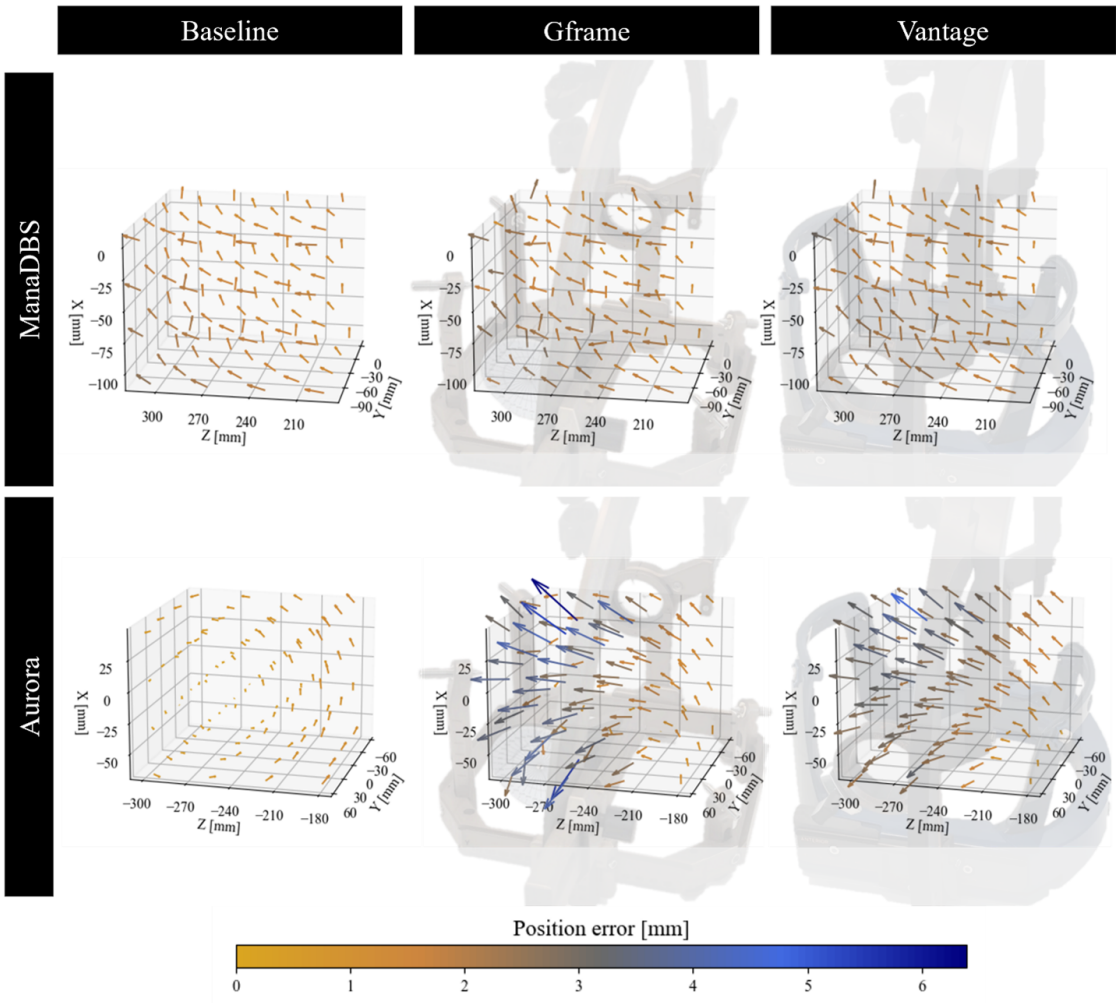

Figure 6.6: Position error distribution of the ManaDBS (top) and Aurora (bottom) systems for the three setups: baseline (left), Gframe (middle), and Vantage (right). Stereotactic system pictures were transparently added.

Fig. 6.6 shows the distribution of position errors in 3D space relative to the placement of the stereotactic systems. The arrow indicates the direction of the error, pointing from the ground-truth position to the measured position. The color of the arrow represents the magnitude of the error. To enhance the visibility of the small error values, the arrow length has been scaled by a factor of 10.

Study 2: DBS electrode implantation

In Study 2, the position error reflected the nonlinearity of the trajectories, as the systematic errors were removed. Differences were observed based on the implantation side, as shown in the boxplot in Fig. 6.7. For ManaDBS, the median position errors (Q1–Q3) were about 0.55 mm (0.4–0.9 mm) for all the setups. No significant differences between the stereotactic setups were observed regarding the position errors. However, there was a significant difference between the implantation sides for the Vantage setup. Similarly, significant differences between the two implantation sides were observed for the Aurora system. On the left side, the median position errors (Q1–Q3) were 2.3 mm (1.5–2.7 mm) in the Gframe setup and 1.2 mm (0.9–1.7 mm) for the Vantage setup. On the right side, the median position errors (Q1–Q3) increased to 2.8 mm (2.5–3.2 mm) for the Gframe setup and remained about 1.2 mm (1.0–1.7 mm) for the Vantage setup.
There were no significant differences between ManaDBS and Aurora for the position jitter (all <0.4 mm and <0.2 mm, respectively) for both the Gframe and Vantage setups.

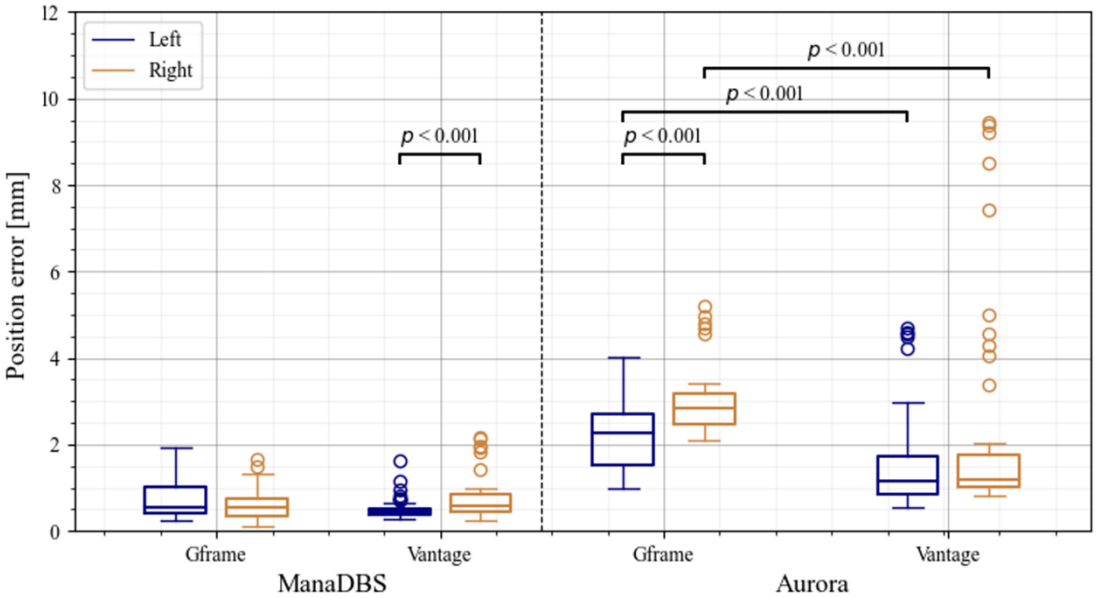

Figure 6.7: Boxplots of the position errors for the trajectories implanted on the left side (blue boxes on the left) and right side (yellow boxes on the right) per setup. Significant differences are indicated at the top of the boxplots.

Fig. 6.8 illustrates the position errors relative to the implantation depths of the EMT sensors. The graph also depicts the distance to the FG as a function of implantation depth. The implantations for both EMT systems were performed at similar distances from the FG, ranging from 24 cm to 30 cm. For ManaDBS, the position errors remained low and consistent across different stereotactic setups. In contrast, the Aurora system exhibited high nonlinear behavior, with errors between 0.6 mm and 10 mm. The largest errors were observed at the start of the implantations near the stereotactic arc. In the Vantage setup, the position errors decreased with implantation depth. However, in the Gframe setup, the errors initially decreased but subsequently increased.

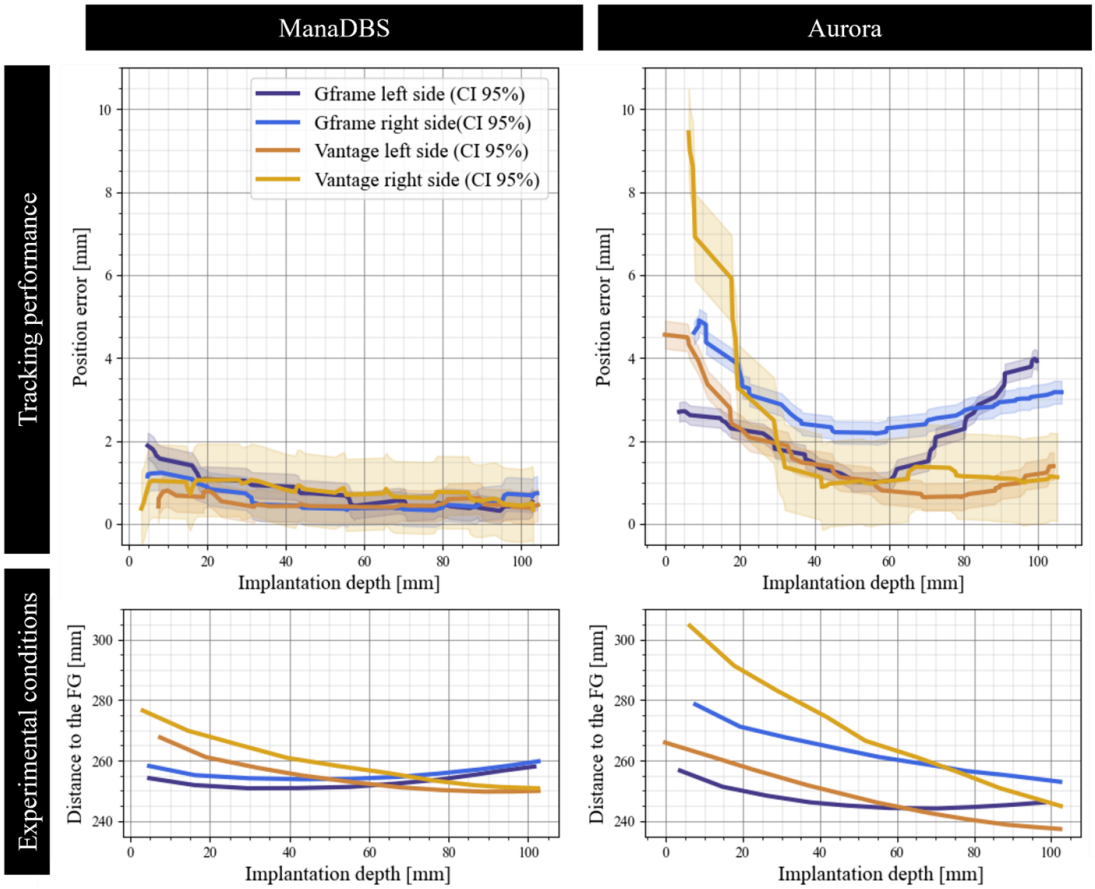

Figure 6.8: At the top, position errors with 95% confidence intervals as a function of the implantation depth for the ManaDBS system (left) and the Aurora system, (right). Data from the two different stereotactic setups and implantation sides: Gframe left side (dark blue), Gframe right side (light blue), Vantage left side (orange), and Vantage right side (yellow). At the bottom, implantation depth as a function of the distance to the FG.

Discussion

The DBS surgical theater is a challenging environment that includes many devices such as the operating table, imaging technologies, and stereotactic systems. Providing regular and high-accuracy navigation for the implantation of the DBS lead has not yet been achieved. When considering factors such as cost, safety, and integration into the surgical environment, electromagnetic navigation emerges as the most suitable technology. However, electromagnetic tracking has only been investigated in frameless settings, which are not the gold standard in DBS surgery [108].
This paper compared the performance of a commercial system and a novel EMT system currently under development. The results indicated that ManaDBS is well-suited for the DBS surgical environment. Study 1 revealed increased localization errors for the Aurora system when a stereotactic system was introduced, whereas ManaDBS maintained consistent localization performance. In study 2, the Aurora system exhibited high nonlinear errors on rectilinear trajectories, with localization errors of up to several millimeters near the stereotactic systems. In contrast, the ManaDBS tracking performance was unaffected, even in a simulated DBS surgical theatre. Due to the asymmetry of the experimental setup, differences in performance between the two hemispheres were expected. For the Aurora system, this difference can be partially explained by a greater distance to the FG for the Vantage setup (Fig. 6.8). However, the distance to the FG is not considered the primary cause of this variability; rather, the proximity to the stereotactic system likely contributed to a greater extent. Indeed, the largest errors occurred near the stereotactic arc at the beginning of the implantations. Additionally, in the Gframe setup, increased errors were noted at greater implantation depths. This may be due to the proximity to the stereotactic frame at the end of implantation. The Vantage frame is made from resin, while the Frame G is made from metal, resulting in increased EM perturbations from the Gframe setup. These results confirm the expected performance degradation observed in the Aurora system, which is primarily due to conductive distortions induced by the high-frequency alternating magnetic fields within the stereotactic systems. In contrast, the ManaDBS system generates a quasi-static magnetic field at low frequencies, effectively eliminating these conductive distortions. While the results are promising, further validation is required, as the ManaDBS system has not yet been tested in clinical environments.

This study considers only the effects of non-magnetic metallic tools, such as stereotactic systems, but does not address performance degradation caused by static magnetic distortions from magnetic sources or tools made from ferromagnetic materials. While the offset cancellation step accounts for stray magnetic fields during the activation sequence, it does not mitigate distortions introduced by ferromagnetic objects, which can impact tracking performance. To evaluate the integrity of tracking performance, we tested both EMT systems by positioning various surgical tools (scalpel, retractor, needle holder, and MER electrode…) at distances ranging from 80 mm to 2 mm from the magnetic sensors (data not presented). Overall, the Aurora system demonstrated better resilience to ferromagnetic tools in position localization (maximal error < 0.3 mm) but showed significant degradation in orientation

tracking (ranging from a few degrees at 20 mm to 30 degrees at 2 mm). In contrast, the ManaDBS system was less resilient, with notable impacts on both position and orientation tracking performance (ranging from a few degrees and 0.2 mm at 20 mm to 30 degrees and 1.3 mm at 2 mm). These preliminary results indicate that both systems experienced performance degradation when larger magnetic instruments, such as the retractor and needle holder made of steel, were used. Therefore, a minimum distance of 20 mm from these magnetic tools should be maintained. However, larger tools like retractors and needle holders are typically positioned farther from the DBS electrode in practice. Conversely, the MER electrode, being the closest tool, had no impact on tracking performance in our tests. Currently, commercial systems can detect significant EM perturbations and disable tracking feedback when near distortion sources. A similar approach could be implemented in the ManaDBS system. Further research and development are necessary to better address EM perturbations caused by magnetic sources.

The ManaDBS system is particularly well-suited for DBS procedures, as they involve the gradual insertion of electrodes over several centimeters into the patient's brain. However, the system's low update rate should ideally be increased to 2 Hz for better integration and expanded applicability. To address this issue, several improvements can be considered. Using a sensor with lower rms noise and higher frequency would reduce the activation time required for each coil during measurement, enabling an increase in frequency. Alternatively, increasing the magnetic field strength could mitigate the sensor noise, reducing the number of sensor readings needed to maintain tracking performance and thereby increasing the frequency. However, the frequency would still be constrained by the ramp-up time of currents into the coil. Furthermore, the observed spatial position error remained slightly worse than expected for DBS when compared to the performance based on imaging methods (approximately 1–2 mm) [108]. The performance of the ManaDBS system is influenced by the magnetic field strength and the accuracy of current control through the coils that generate the magnetic field. The system's ability to differentiate between two spatial positions relies on detectable differences in their magnetic fields, which necessitates sufficient sensitivity in the magnetic sensors. In this study, the system's performance is mainly limited by the rms noise of the sensor, approximately 250 nT, with a resolution of 6.25 nT/LSB. The performance should be enhanced using a sensor with a higher resolution and lower rms noise but also an improved control of the current injected through the FG, and a characterized magnetic field associated with the unique FG magnetic field. The ManaDBS system had not been fully optimized, limiting its actual tracking performance. However, the aim of this study was to compare the compatibility of two EMT systems within a DBS environment.

In addition, the feedback on the position and orientation of the DBS electrode can be coupled with visualization software such as 3D Slicer [231], providing surgeons with visualization of the electrode displacement according to the anatomical brain structures of the patient. Another advantage is the potential mechanical compatibility of the sub-millimeter magnetic sensor with the DBS electrode. In contrast to the micro-coils used in the commercial system, which typically have a length of 10 mm, rendering them impossible to integrate permanently into the

DBS electrode, the magnetic sensor chosen with a robust package of $0.8 \times 0.8 \times 0.4$ mm^3 should alter the rigidity of the DBS electrode only locally at its tip. The overall length of the DBS electrode should not be affected, allowing the elastic modulus of the DBS electrode to remain close to the brain reducing tissue damage. Providing electrode orientation feedback to the neurosurgeon offers significant advantages, enabling optimized positioning and programming of chronic stimulation. The position and orientation can be transferred to the neurologist to speed up the programming process of the directional DBS electrode. While the directional DBS electrode offers substantial benefits by steering the stimulation and expanding the therapeutic stimulation by avoiding adverse effects, it also increases the possible stimulation settings. The ManaDBS system demonstrated an orientation error of 1° across 100 tested positions, which is adequate for DBS application. However, on study 1, only a limited range of orientations was evaluated, further orientations should be tested to cover all possible orientations.

Conclusion

To our knowledge, this paper is the first to quantify the impact of stereotactic systems on the accuracy of an EMT system within a 3D-tracking volume relevant to DBS surgery. Our findings demonstrate that when using Aurora with two different stereotactic systems (Frame G and Vantage, Elekta), there were localization errors of up to 10 mm in position and 1.0° in orientation. In contrast, the ManaDBS system exhibited better compatibility with the DBS environment, achieving an accuracy of approximately 1.7 mm in position and 1.0° in orientation within the clinical working volume. System adaptations are expected to further improve this performance. The results of our studies suggest that navigating DBS electrodes may be feasible using this new generation of EMT system.

CHAPTER 7

Publication IV - Integration into DBS surgical procedure

Foreword and Overview

After developing and demonstrating the compatibility of the ManaDBS system within the DBS surgical environment, its integration into the surgical workflow was explored in **Publication IV**. The integration of EMT systems into surgical procedures is often overlooked during the development of localization methods. However, implementing an appropriate registration method is critical for ensuring localization accuracy and system acceptance, as it may impact established surgical workflows.
To minimize the burden on the medical team, registration-free methods have been explored. Building on our EMT system, we developed a registration-free approach based on markers which can be automatically detected on pre-operative stereotactic CT imaging, simplifying integration and enhancing procedural efficiency.

Contribution: The candidate was overall responsible for the design of the study. The candidate received technical support from members of the research laboratory (Sensors lab, FHNW-HLS) concerning the development of flexible PCBs and the segmentation algorithm (Neuroengineering Lab, FHNW-HLS). The candidate performed the measurement and analysis. The candidate was overall responsible for the writing of the manuscript. The supervisors and co-authors supported the process and reviewed the paper.

Abstract

Electromagnetic Navigation System (ENS) provide a promising solution for tracking electrode positioning during Deep Brain Stimulation (DBS) surgery, enhancing precision and potentially improving clinical outcomes. Recent studies suggest that novel ENS based on quasi-static magnetic fields may be compatible with the DBS surgical environment, particularly with stereotactic systems — the gold standard for electrode implantation. However, a key challenge persists: ensuring seamless integration into the surgical workflow requires an efficient and reliable patient-to-image registration system. In this study, we present a novel registration system tailored for stereotactic procedures. The system employs flexible markers attached to the stereotactic frame, incorporating magnetic sensors and wireless communication to enable seamless interaction with the surgical environment. These markers are visible on pre-operative Computed Tomography (CT) scans, eliminating the need for additional intra-operative imaging. The registration method demonstrated robust performance with automatic segmentation of the markers on CT images, achieving an average point matching error of 1.51 mm. During implantation tests, the system localized the ENS sensors with a target registration error of 2.54 ± 0.92 mm. This innovative navigation approach ensures precise localization, reducing reliance on repeated CT imaging for verification, thus streamlining the surgical workflow.

Introduction

Deep Brain Stimulation (DBS) is a well-established therapeutic intervention for movement disorders and other neurological conditions, offering significant symptom relief when drug-based treatments are insufficient. Accurate placement and orientation of DBS electrodes are critical for achieving optimal clinical outcomes. Electromagnetic Navigation System (ENS) designed for localization (without actuation) have emerged as a promising tool, offering the potential for real-time monitoring of electrode positioning and orientation during DBS surgical procedures. Such capabilities are particularly advantageous for fine-tuning precision during intra-operative stimulation tests and provide a quick and accurate method for final electrode localization [108]. Although widely employed in neuronavigation [232, 233], commercial ENS systems are not compatible with stereotactic systems [234], which remain the gold standard for DBS surgery. Recent advancements in electromagnetic tracking techniques have been explored to address these limitations. These novels ENS rely on quasi-static magnetic field, unlike the alternating magnetic fields used in commercial systems. When combined with integrated magnetometers, these advanced ENS demonstrate inherent robustness to non-magnetic metallic objects, such as stereotactic systems [**Publication II and III**] or knee implant [135]. However, for seamless integration into the DBS surgical workflow, a reliable and efficient patient-to-image registration system is essential.

The registration process establishes a connection between the patient space (physical space) and the image space. The accuracy of the registration directly influences how closely the virtual position of the tracked instruments in the image space matches their actual physical position on the patient.

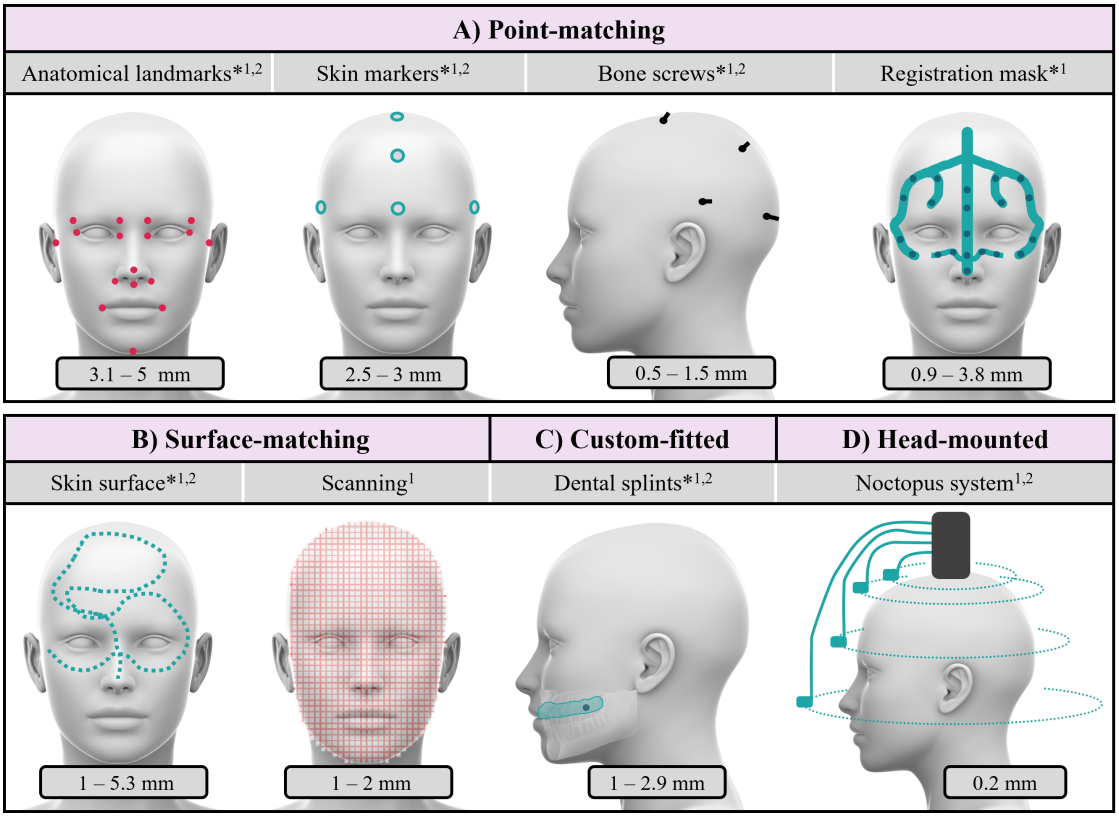

Figure 7.1: Different registration methods commercially available (*) or developed clinically: (A) Point-matching methods based on the acquisition of known fiducials including anatomical landmarks, adhesive skin markers, bone screws or registration mask. (B) Surface-matching methods are based on the accumulation of larger number of fiducials with a navigation probe moving over the patient face or using optical portable scanner. (C) Custom-fitted method using dental splint integrating markers. (D) Head-mounted systems such as the Noctopus system. Registration methods compatible with optical navigation[1] or electromagnetic navigation[2]. Numbers represent the TRE (min-max) reported in the literature.

An overview of the registration methods available for cranio-maxillofacial surgery or neurosurgery are presented in Figure 7.1 as well as the associated target registration error (TRE) reported in the literature (min-max TRE). Traditional registration methods, such as point-matching using anatomical landmarks [235, 236, 237, 238, 239] (3.1-5 mm), are limited by their sparse distribution and difficulty in accurate digitization. Artificial markers offer an alternative, including adhesive skin markers [238, 240, 241] (2.5-3 mm), bone screws [235, 239, 242, 243] (0.5-1.5 mm) and dental splints [244, 245, 246, 247] (1.0-2.9 mm), require additional imaging, invasive procedures or additional equipment such as 3D-printers. Advanced techniques include registration mask equipped with LEDs visible to infrared cameras [248, 249, 250] (0.9–3.8 mm). This mask enables automatic surface registration by leveraging unique anatomical landmarks on the face, reducing user dependency. While effective, their

setup is not compatible with stereotactic systems due to light blocking, and their accuracy also depends on adherence throughout the procedure. To reduce the TRE, which strongly depends on the number and distribution of points across the skull, surface-matching techniques have been developed. Surface-matching uses digitized scalp points fitted to pre-operative imaging. The accumulation of landmarks for surface-matching can be done with a navigation probe [238, 239, 240, 251] (1-5.3 mm) or laser pointer [241, 252, 253] (1.8–2.9 mm) moving over the patient face or portable optical scanner [254, 255] (1–2 mm). Although less invasive, its accuracy is lower than point-matching methods using bone screw fiducials and is further affected by high TRE at greater distances from the matched region. The Noctopus system, a head-mounted frameless stereotactic device [256] (0.2 mm TRE), offers a modern solution by optimizing marker configuration to minimize registration error. Anchored to the parietal bone, its movable arms detectable in imaging can integrate optical or electromagnetic markers, providing reliable registration and dynamic tracking throughout surgery. However, the Noctopus system, while innovative, cannot be integrated with DBS stereotactic systems.
Integrating an ENS into the DBS surgical workflow requires a registration system that fulfills several key criteria: it must be non-invasive, quick to implement, logistically simple, and automated to minimize user dependency. The system should be universally applicable to all patients, avoid additional radiation exposure, and, most importantly, deliver high accuracy to ensure reliable navigation data. Current registration methods, primarily developed for frameless procedures, are not suitable for frame-based surgeries like DBS and fail to meet these requirements [257]. DBS surgery demands precise image-guided intervention, requiring registration markers to be accurately identified and marked both in the virtual imaging dataset and on the patient. Emerging research is shifting toward registration-free approaches that limit user interaction and enable automated registration, addressing many current limitations [258, 259, 260]. Expanding on this concept, we developed a novel registration system tailored specifically for ENS use in stereotactic DBS. This system employs flexible markers attached to the stereotactic frame, using magnetic sensors and wireless communication for seamless integration. These markers can be identified on preoperative CT scans, enabling accurate registration without requiring additional imaging during surgery. This registration method is designed to complement the ManaDBS, an innovative research-driven electromagnetic tracking system previously developed [**Publication II and III**]. ManaDBS represents the first proposed electromagnetic tracking system for DBS surgery, providing position and orientation tracking while demonstrating robustness in presence of the stereotactic system. The associated registration method aims to maintain navigation performance while ensuring a streamlined, non-invasive workflow optimized for frame-based procedures.

In this study, we describe the development, implementation, and performance evaluation of this method. The goal is to enable ENS for stereotactic procedures and deliver a registration-free workflow. Consequently, the primary focus was on evaluating the positional registration error. Although the ManaDBS system also provides orientation data, this aspect was not investigated in this study. Through this proof of concept, we addressed the demands of usability, and integration into the stereotactic surgical workflow knowing that the performance of the systems can be further improved.

Methods

Preparations

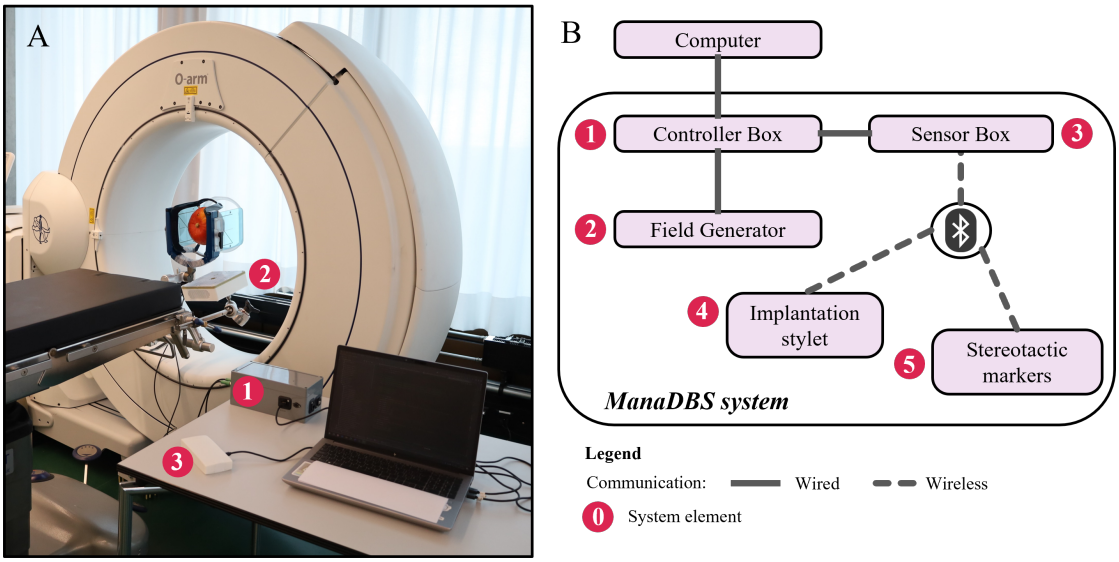

Figure 7.2: (A) Experimental environment: Picture of the placement of the ENS (ManaDBS) and the stereotactic system (Vantage stereotactic system) and associated CT box within the O-arm imaging system. (B) Overview of the ManaDBS system, comprising the system elements (1-Controller box, 2-FG, 3-Sensor Box, 4-DBS electrode and 5-Stereotactic ENS Markers) as well as the communication type between elements.

An experimental environment was created to mimic as faithfully as possible the pre-operative phase of a stereotactic DBS procedure. The simulated pre-operative theatre is depicted in Figure 7.2(A).This environment included an operating table along with its requisite accessories: a surgical bed (Maquet Betaclassic, Getinge AB, Gothenburg, Sweden), fixtures for the stereotactic frame comprising a connection bracket (1130.54B0, Getinge AB) and an adjustable base unit (1005.50A0, Getinge AB), the Leksell Vantage Stereotactic System (Elekta AB) with the respective interface for the operating table (Vantage Starburst 3/8", Elekta AB), and fixation for the ENS (ManaDBS) to be attached to the right side rail of the operating table. A red kuri squash was positioned within the stereotactic frame and the associated CT Fiducial box used in the case of surgical planning. The stereotactic arc was not utilized in this study, as it focuses on the pre-operative phase of surgery where the stereotactic arc is not present. Subsequently, the operating table was positioned with the mobile CT: O-arm (Medtronic, Minneapolis, USA).

Electromagnetic navigation system – ManaDBS

The different elements of the ManaDBS system and the communication methods are depicted in Figure 7.2(B). The ENS consists of a Field Generator (FG) with a dimension of 20 × 20 × 7 cm, integrating four identical coils. Each coil generated static magnetic fields. The

coil activation sequence includes five steps: four individual coil activations and one offset cancellation step. During offset cancellation, the ambient magnetic field, including Earth's magnetic field, is measured with all coils off, and this data is subtracted from the prior measurements to remove static perturbations. The offset cancellation helps eliminate potential sources of distortion, such as medical equipment or surgical instruments, that could affect tracking performance. This method has already shown its robustness to the presence of the stereotactic system [**Publication II and III**]. Using multilateration principles, each point in the measurement volume is encoded with a unique magnetic field amplitude vector derived from the activation sequence. Previous research on the ManaDBS system [**Publication II**], reported localization errors of 1.72 mm and 0.89° within a tracking volume of 15 × 15 × 30 cm³. Position and orientation data are extracted at an update rate of 0.4 Hz. In this study, the update rate was adjusted to 0.15 Hz due to the simultaneous activation of a greater number of sensors and the resulting technological limitations. Consequently, the registration step will require 7 seconds, while the intra-operative phase will benefit from an improved ManaDBS refresh rate of 2.5 seconds. The sensing elements include an implantation stylet and three stereotactic ENS markers, described in the next section. A sensor box manages the sensing element measurements and receives the corresponding data via Bluetooth. The sensor box is connected to a controller box, which synchronizes the field generator activation with sensing element data acquisition.

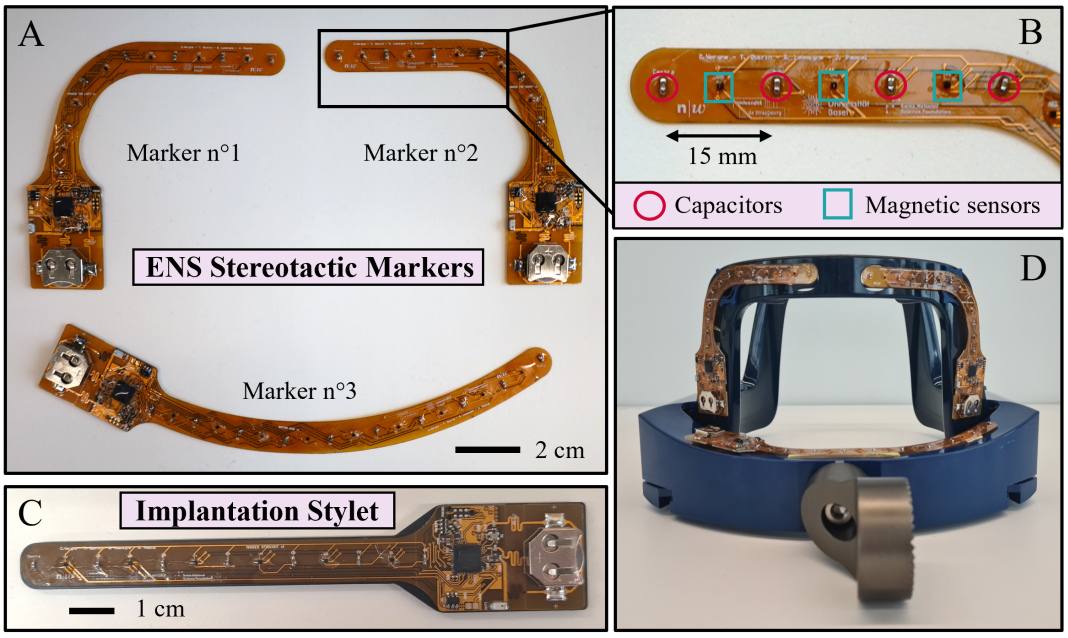

Figure 7.3: Sensing elements of the ManaDBS system: (A) Stereotactic ENS markers: Three different designs for a better conformation to the stereotactic frame shape for a total of 21 magnetic sensors. (B) Zoom-in on the marker n°2 with the magnetic sensors and capacitors. (C) Implantation stylet integrated six magnetic sensors. (D) Placement of the three ENS markers on the stereotactic frame.

Stereotactic ENS markers & Implantation Stylet

The stereotactic ENS markers consists of three flexible electronic PCBs (Fig. 7.3(A)). Each PCB was designed according to the shape of the stereotactic frame. A total of 21 magnetic sensors (anisotropic magnetoresistive three-axis sensors, MMC5603NJ, Memsic Semiconductor Co.) are present on the PCBs. Each sensor is placed half-way capacitors necessary for sensors integrity and separated by 15 mm (Fig. 7.3(B)). Microcontrollers were programmed to handle the commands and data communication between the sensor box and the sensors elements (nRF52832, Nordic Semiconductor, Trondheim, Norway). The stereotactic ENS markers are placed on the posterior part of the stereotactic frame and fixed using Parafilm. They are expected to remain attached to the stereotactic frame throughout the entire surgical procedure. The implantation stylet is a straight variant of the same flexible electronic PCB, incorporating six sensors (Fig. 7.3(C)). The stylet is mounted on a rigid holder and used to simulate electrode trajectories. This parallel measurement approach minimizes the need for multiple CT scans and ENS acquisitions, which would otherwise be required to evaluate registration performance if a single sensor were embedded in a catheter or DBS electrode.

Registration-free method

X-ray imaging obtained from the O-arm system (Metronic O-arm, 0.77mm x 0.77mm x 0.83mm) were saved in DICOM format and visualized using 3D Slicer [231]. The position of the magnetic sensors on the ENS stereotactic markers was determined relative to the position of the capacitors (Fig. 7.4(A)) as the capacitors are larger, causing identifiable hyper-intensities (Fig. 7.4(B)). The capacitors were segmented using an intensity threshold optimized in each image set. The optimization routine increased the threshold value, excluding objects smaller than 1 mm^3 and larger than 10 mm^3 and calculated pairwise distances between centroids of the segmented objects. The stopping criteria is the detection of 24 objects (Marker 1&2: 7 capacitors, Marker 3: 10 capacitors) with pairwise distances with any other object included between 14 and 16 mm (capacitors spacing of 15 mm). The resulting objects were then clustered using Scikit-learn's agglomerative clustering with a distance threshold of 17 mm. The three largest clusters were kept, and capacitors were numbered based on their maximal pairwise distance to other capacitors in the cluster, which allows for the identification of the capacitors at each extremity of the markers. Finally, the positions of the magnetic sensors were calculated as the midpoint between each pair of capacitors. The final segmentation results were checked visually.
After completing the segmentation, the positions of the magnetic field sensors extracted from the CT images were registered to the positions obtained from the ENS using a point-matching method, available in the SlicerIGT module "Fiducial Registration Wizard" [261]. The point-matching method was evaluated on 25 stereotactic CT images paired with corresponding ENS acquisitions. The magnetic field positions derived from the ENS were imported into 3D Slicer, and the associated root mean squared (RMS) error of the matching process was calculated and reported. The resulting spatial transformation from the point-matching method was stored and applied to the ENS positions of the implantation stylet. The registered positions of each magnetic sensor on the implantation stylet were compared to the positions of the magnetic sensors on the CT imaging after manual assignment. The TRE was quantified as the Euclidean distance

between these two positions. The implantation stylet was positioned within the squash at five distinct locations (Fig. 7.5(B)), generating five rectilinear trajectories. Each trajectory provided six positions corresponding to the six sensors on the implantation stylet (Fig. 7.5(C)). For each position, ENS measurements were repeated 11 times, resulting in 55 ENS acquisitions and 5 CT acquisitions. A total of 30 positions were manually defined from the CT images and used as ground truth for comparison against the 330 positions derived from the ENS. All processes, from segmentation to the visualization and transformation, were implemented within 3D Slicer, ensuring an integrated workflow for data analysis and evaluation.

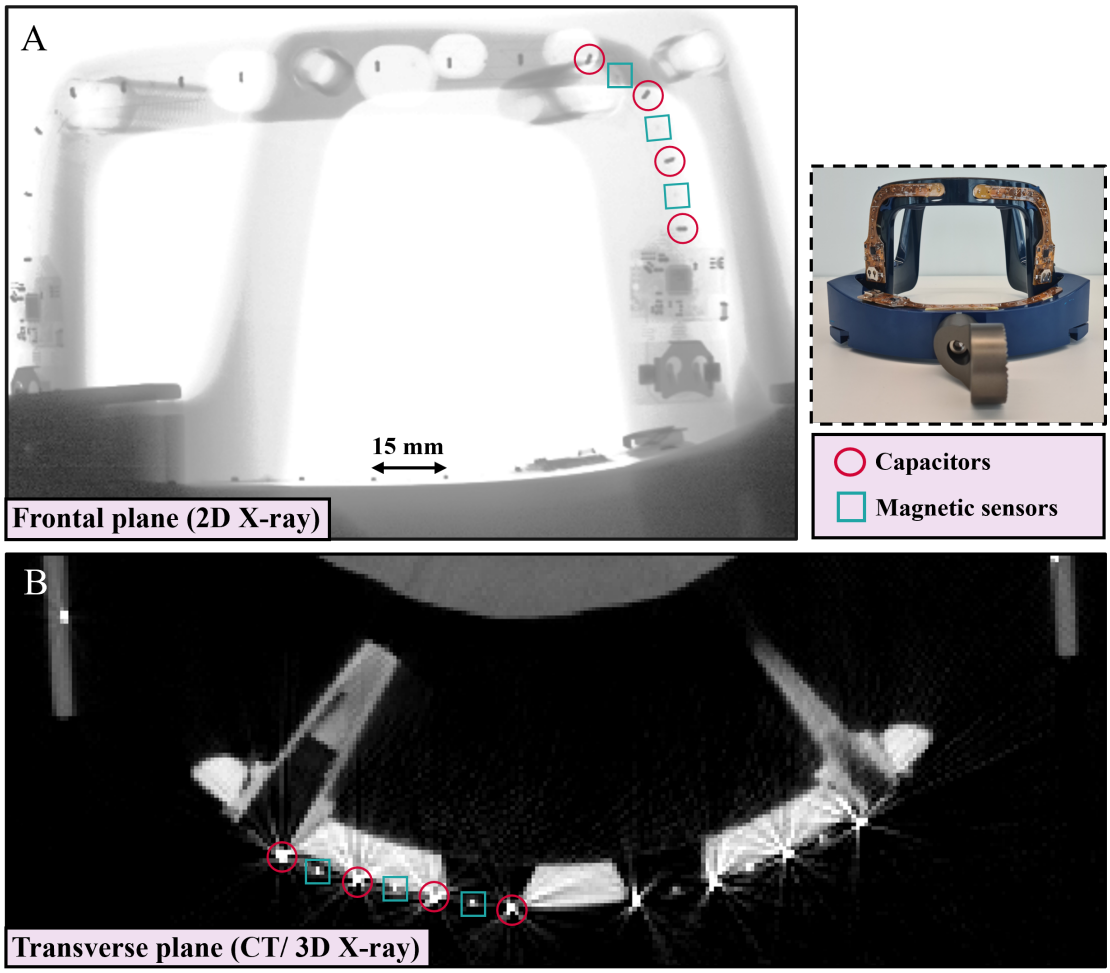

Figure 7.4: CT images visualized in the 3D Slicer environment: (A) Frontal plane of a 2D X-ray of the stereotactic frame and the associated ENS stereotactic markers. (B) Transverse plane of a 3D X-ray of the stereotactic frame and the associated ENS stereotactic markers.
The capacitors appear as clusters of high-intensity voxels, with in between one or two high-intensity voxels corresponding to the magnetic sensors.

Experimental methods

In practice, the ENS markers were attached to the posterior section of the stereotactic frame. Once the stereotactic frame was secured to the operating table, a red kuri squash was positioned within it and fixed using associated screws. The operating table was then aligned with the aperture of the O-arm imaging system to ensure proper centering for imaging. Holes were drilled in the squash to accommodate the implantation stylet. CT scans were performed to capture the following elements: the red kuri squash with the implantation stylet, the stereotactic frame with its associated CT box, and the stereotactic markers. This setup effectively mimicked the pre-operative stereotactic CT configuration, apart from the implantation stylet being present. Between each CT scan, an ENS measurement was performed. For this, the FG was added to the operating table, and the arm fixation was maintained in the same configuration, restricting variations in the FG's position to only a few millimeters. During our experiments, a systematic error was observed between the sensor positions from the implantation stylet detected by ManaDBS and the ground truth. This error varied across implantations and was influenced by the orientation of the sensors. Upon preliminary investigation, this error was attributed to the transverse sensitivities of the sensors. Transverse sensitivity, or cross-sensitivity, refers to additional magnetic fields reported on perpendicular axes when a sensor measures along the main axis. The anisotropic magnetoresistive sensors used in this study exhibited cross-sensitivities between 2–5%, explaining the observed discrepancies. Cross-sensitivity is particularly challenging to characterize and compensate for. Acknowledging this technical limitation, we conducted our measurements aware of this issue. The implantation trajectories were carefully selected to ensure that the sensor's orientation achieved optimal alignment with the FG surface. While localization performance is affected by systematic error, this impact is reduced through the experimental setup. Technological solutions to address this issue are presented in the Discussion part.

Results

Figure 7.5(A) presents the automatic segmentation results, visualizing the capacitors and the corresponding positions of the magnetic sensors. Segmentation errors for the capacitors were estimated to be below 200 m on CT images. The figure also illustrates the outcomes of the point-matching method, including the registered positions of the magnetic sensors from the ENS. Across the 25 tests, the mean ± standard deviation (minimum, maximum) of the RMS error from the point-matching method, were 1.51 mm ± 0.05 mm (1.42 mm, 1.61 mm) respectively.

Across all positions of the implantation stylet, the TRE was calculated resulting in a mean ± standard deviation (minimum-maximum) of 2.54 mm ± 0.92 mm (0.36 mm-4.96 mm) respectively. To evaluate noise effects on the TRE, sensor values at each position were extracted 11 times, resulting in an average standard deviation of 0.3 mm for these repeated measurements. As expected, the TRE increases with greater distances from the FG (Fig. 7.6(B)). This behavior is typical of ENS systems, where the tracking accuracy depends on the strength of the magnetic field, which strongly decreases as the distance from the FG increases.

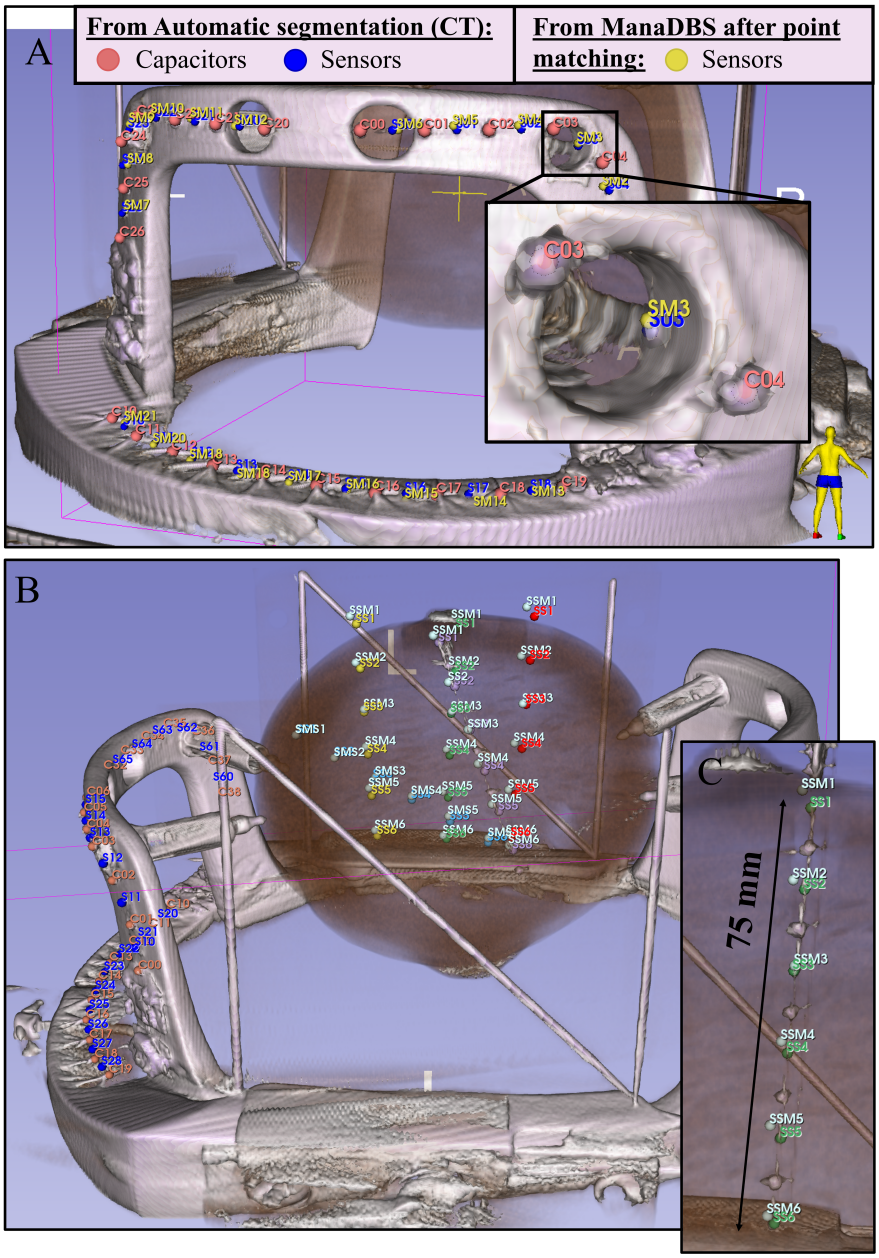

Figure 7.5: (A) Volume rendering view obtained in 3D Slicer: Visualization of the posterior part of the stereotactic frame with the segmented capacitors (in pink: C00:26) and resulting sensors positions (in blue: S00:20) obtained from the CT imaging and the sensors positions (in yellow: SM1:21) obtained from the ManaDBS after point matching. (B) Volume rendering view from the 3D Slicer CT, showing the five implantation locations. (C) Close-up of one implantation site, displaying the positions manually extracted from the CT (in green, SS1 to SS6) alongside the ENS positions after registration (in white, SSM1 to SSM6).

Discussion

Current registration methods face challenges in meeting the requirements for DBS surgeries and frame-based procedures. To address these limitations, we developed a novel registration system tailored for use with ENS in DBS procedures. This system utilizes flexible markers fixed to the stereotactic frame, which remain securely in place throughout the surgery. The markers integrate magnetic sensors and wireless communication for seamless tracking, and their positions can be automatically detected on preoperative CT imaging using a tuned segmentation algorithm. This automation reduces user-dependent errors and significantly improves efficiency, generating the spatial transformation matrix within seconds. The markers enable continuous tracking, enhance safety and ensure precise placement throughout the procedure. If the ManaDBS lacks robustness against patient movement due to a slow refresh rate, the registration can be repeated intra-operatively to account for any changes.

The point-matching method used to register the ENS stereotactic markers demonstrated an average RMS error of 1.51 mm with a standard deviation of 0.05 mm. The observed RMS error of 1.51 mm is likely due to small deviations (±5%) between the actual magnetic field and the measured field, caused by manufacturing imperfections. The low standard deviation can be attributed to the proximity (<10 cm) of the ENS markers to the field generator, where the magnetic field is strongest. In this region, strong magnetic gradients reduce the impact of sensor measurement noise, unlike the sensors on the implantation stylet. This is also likely why the magnetic sensors on the stereotactic markers showed minimal error related to the cross-sensitivities of the sensors.

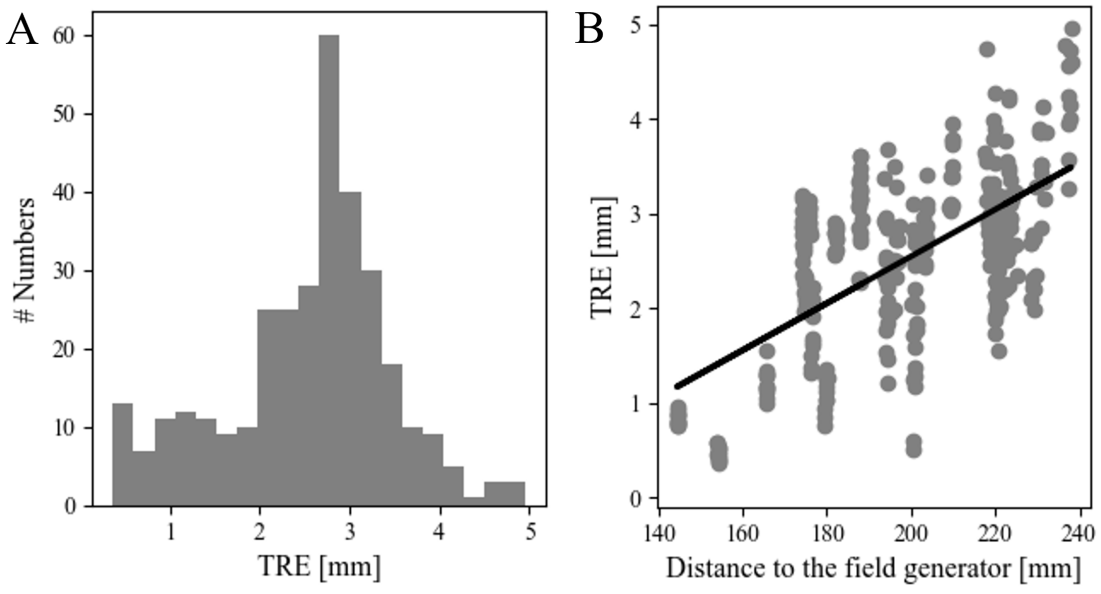

Figure 7.6: (A) Histogram of the TRE and (B) Plot of the TRE as a function of the distance between the positions and FG, with in black a regression line.

The reported TRE reflects the combined effects of registration and tracking accuracy in the ManaDBS system. Both sources of error should be further investigated to identify potential areas for system improvement. For instance, a small angular registration error on the stereotactic markers can have a significant impact on positional accuracy at greater distances, such as those on the implantation stylet. Although this type of error was not observed in our experiment, adding a stereotactic marker to the anterior part of the stereotactic frame could help mitigate potential angular errors. Despite its strengths, the current registration method has limitations. The segmentation of the capacitors instead of magnetic sensors may introduce additional errors. The positions of the magnetic field sensors, determined through automatic segmentation, were observed on the highest hyper-intensity voxel. Therefore, the segmentation error should be within the resolution of the O-arm imaging, with a voxel dimension of 0.77 x 0.77 x 0.83 mm^3. To reduce even further this variable, a larger magnetic sensor could be used for direct segmentation. This approach would eliminate errors associated with calculating sensor positions as midpoints between capacitors. Additionally, a redesign of the ENS stereotactic markers, addressing the current obstructions of the posterior screws, and the optimization of the number and placement of magnetic sensors could further reduce the TRE.
The spatial error of the ManaDBS was reported at 1.72 mm in previous studies [**Publication II and III**]. However, the TRE observed in this study is higher. A common challenge in ENS systems is the impact of distance on tracking performance. The ManaDBS was developed for tracking up to a distance of 33 cm, which is greater than the distances reported in our study (Fig. 7.6(B)). Therefore, variation in distance from the field generator is unlikely to explain the spatial error discrepancies between the studies. As outlined in the Methods section, the increased error was linked to the cross-sensitivity of the magnetic sensors. This effect causes fluctuations of approximately 1 T in the measured magnetic field, resulting in potential spatial errors of 1 to 3 mm. One possible solution is to increase the current, thereby amplifying the generated magnetic field, given that ManaDBS currently operates at 5A, producing 160 T within the tracking volume. This approach would enhance the signal-to-noise ratio and mitigate cross-sensitivity effects. However, this may not be practical, as higher power consumption could lead to overheating of the field generator. A second solution is to characterize the cross-sensitivity of the sensor and apply a calibration method correcting its effect. Another solution could involve using sensors with lower cross-sensitivity ($< 0.5\%$), such as Hall Effect sensors. However, the resolution of the sensors is crucial for tracking performance. To maintain accurate tracking, the sensor resolution must remain in the nanotesla range for compatibility with the current version of the ManaDBS. Alternative sensing technologies will be investigated in future studies to improve the performance of the ManaDBS.

The system's performance was evaluated based on position error, while orientation was not further investigated. However, the relative orientation among the six sensors on the implantation stylet is expected to remain consistent, as the sensors are soldered onto the PCBs with the same alignment. The deviation between the detected orientation and the overall average orientation of the six sensors for each implantation was calculated. The resulting orientation error had an average of 1.05° and a standard deviation of 0.7° along each axis.

This registration method is optimized for pre-operative stereotactic CT imaging. Extending it to pre-operative stereotactic MRI is theoretically feasible, as the magnetic sensors retain their sensitivity even after exposure to strong magnetic fields [209]. However, the larger voxel dimension in MRI poses challenges for detecting the capacitors, requiring further validation. Additionally, this method has potential applications in frameless procedures, as the flexible markers could be placed directly on the patient's skin or head. While optical navigation systems already employ this concept [248, 249, 250], it has not been feasible for electromagnetic navigation due to reliance on analog magnetic field detection requiring extensive electronics. Our approach, using digital magnetic field sensors and wireless communication, simplifies complexity and enables registration-free techniques, promising future advancements. The process can be fully automated within planning and navigation software like 3D Slicer, requiring no specialized operator.

Conclusion

This study presented a registration-free workflow for electromagnetic navigation during stereotactic DBS surgery. This approach provides a non-invasive, user-independent alternative to traditional registration methods, potentially enhancing intra-operative time efficiency. The method's accuracy was assessed using a custom implantation stylet implanted in a red kuri squash model under conditions simulating a stereotactic pre-operative CT. The preliminary results demonstrated promising performance, achieving a mean target registration error of 2.54 ± 0.92 mm.

CHAPTER 8

Discussion & Outlook

Key findings

The four publications presented in this work collectively address the primary objectives of this thesis. The objectives center on developing an initial prototype of an EMT using quasi-static fields and integrated magnetometers. Every component of the tracking system — including the field generator, sensors, and tracking algorithm — was designed, developed or evaluated for its intended application: real-time monitoring of electrodes positioning during stereotactic DBS surgery. The complete system also incorporates a registration method, enabling visualization of the sensor's position within the DBS electrode relative to the patient's anatomy.

Publication I introduces a novel technique for localizing DBS electrodes using a quasi-static magnetic field and integrated magnetic sensors. Within this work, the requirements concerning the sensitivity of the magnetic sensor as well as the gradients of the magnetic field generated by the FG was investigated and discussed. Both aspects constitute the main features of this novel EMT technique. By targeting low-field magnetic field generation and accounting for the minimal magnetic field gradient within the measurement volume, AMR sensors were selected for their exceptional high resolution and comparatively low rms noise.
Publication II extends this first study by proposing an enhanced version capable of determining the sensor's orientation and evaluating the system's performance within the scope of DBS surgery. This version features an optimized field generator designed to ensure adequate magnetic field gradients within the measurement volume while maintaining dimensions compatible with the DBS surgical setup. The number of coils in the field generator increased to four for enhanced performance. Using the same activation sequence, the tracking algorithm was expanded to determine orientation using the three magnetic field components, while position is derived from the magnetic field vector. This underscores the necessity of three-axis magnetic field sensors. Results demonstrate the system's efficacy, achieving an average localization error of 1.72 mm and an angular error of 0.89°, with potential for further improvement.
Rather than optimizing the system, the thesis focuses on its suitability for surgical applications, a critical objective. **Publication III** highlights the system's robustness when integrated with stereotactic equipment, outperforming commercial systems by limiting additional errors from

conductive distortions. Subsequently, **Publication IV** introduces a custom registration method tailored for stereotactic neurosurgery, prioritizing automation, minimal user dependency, and non-invasiveness. This registration method is based on the same magnetic field sensors, integrated onto flexible PCBs that serve as markers detectable in pre-operative stereotactic CT scans. Developed as an extension of the ManaDBS system, this approach achieved a localization error of 2.54 mm, though orientation validation has not yet been confirmed.

Overall, this thesis proposes a navigation system for stereotactic DBS surgery, offering regular position and orientation localization of the DBS electrode. This thesis bridges the technical development of the system with its practical integration into surgical workflows.

Suitability of the ManaDBS navigation system

Tracking technique

The localization technique used in this work is based on multilateration, a method that determines the position of an object by analyzing signals emitted by multiple transmitters. Multilateration works by calculating the distances between the receiver and the transmitters, enabling the creation of spheroids centered on each transmitter. The object's position is mathematically determined by identifying the intersection of these spheroids.
In the context of electromagnetic fields, the emitters are field generators, represented here by four coils, while the receiver is a sensor integrated within the DBS electrode. The signals used are the magnetic field components generated by each coil. This technique is advantageous due to its simplicity in both generating and detecting magnetic fields. However, its effectiveness relies heavily on the accuracy of the magnetic field generation and detection processes. A significant limitation is the cubic decay of magnetic field strength with distance from the emitters, a challenge inherent to any electromagnetic localization method.
Optimally, the emitters should surround the tracking volume to enhance detection accuracy. However, this configuration is impractical in an operating room environment. As a solution, a planar arrangement of emitters was adopted, offering compactness but introducing new challenges. One significant challenge is the uneven localization performance. The performance is notably better at the center of the planar arrangement, while it diminishes toward the periphery. This phenomenon was demonstrated in **Publication I**, where submillimetric tracking accuracy was achieved at the center of the planar emitter arrangement. **Publication II** further confirmed this observation during a comprehensive evaluation of the entire MV, highlighting the disparity in resolution between the center (about 1 mm position error) and peripheral regions (about 3 mm position error). Since the orientation is derived from the magnetic field components measured and the calculated position, any increase in position detection error will negatively impact the accuracy of orientation determination.

Enhancing such a system requires addressing these limitations by either redesigning the emitters to optimize their placement and numbers or enhancing the magnetic field strength and sensor resolution. These improvements are essential for achieving more reliable localization

performance. In this context, the effect of the number of emitters on tracking performance was analyzed in Appendix A. Simulations were conducted with arrangements ranging from three to nine emitters, and the corresponding tracking performance was evaluated. The findings highlight a significant improvement in tracking performance when increasing the number of coils from three to four. Additionally, a multilateration algorithm based on various machine learning approaches was explored. Among these, the XG-Boost method demonstrated the best performance, yielding promising results. While the study focused on position localization, the approach could be extended to include orientation determination in future work.

System's performance

The system performance presented in **Publication II** demonstrated a localization error of 1.72 mm and an angular error of 0.89°. This performance was achieved within a MV of 15 x 15 x 15 cm^3, with an offset distance of 18 cm from the FG. Better performance was observed in simulations of DBS implantation in **Publications II and III**, attributed to the positioning of the DBS implants near the center of the MV and closer proximity to the FG. However, the system's update rate is relatively low at 0.4 Hz. While this rate could potentially be increased to a few Hz, it remains limited by the ramp-up time of currents in the coils and the number of sensor measurements required to maintain tracking accuracy. The DBS system is intended to be used during the electrode implantation phase, when no other equipment is being moved or imaging systems used in parallel. Since the measurement time is quite long, moving magnetic bodies could compromise tracking performance. However, as DBS involves the slow and gradual insertion of electrodes into the patient's brain, the ManaDBS update rate is sufficient for this procedure, especially when compared to the temporal resolution of imaging systems.
The ManaDBS system provides spatial and angular resolutions comparable to imaging technologies but avoids lengthy acquisition times and radiation exposure. Designed to assist neurosurgeons in decision-making, it focuses on localization rather than actively guiding the electrode. Compared to existing EMT systems, the ManaDBS demonstrates slightly lower performance and a smaller MV. However, it remains well-suited and valuable for DBS applications. Performance improvements could be realized by increasing the system's signal-to-noise ratio. This would involve generating stronger magnetic fields or using sensors with lower noise, as presented in the previous section. For example, transitioning to TMR sensors might enhance accuracy and precision due to their greater sensitivity and lower rms noise.

It's worth noting that the system's performance was primarily assessed with sensors placed throughout the volume, all maintaining a consistent orientation. This limitation arose from the experimental setup, which required precise knowledge of sensor placement, either through an MFC system [**Publication I and II**] or an assessment setup [**Publication III**]. In **Publication IV**, system performance was evaluated using CT imaging, allowing for greater flexibility in sensor placement and orientation. During this experiment, a systematic error ranging from 1 mm to 6 mm was observed, depending on the sensor's orientation and proximity to the FG. Preliminary analysis indicated that sensor cross-sensitivity were likely the primary source of this error. According to the datasheet of the AMR sensors used in this research, for a magnetic

field of 100 μT along the X-axis, up to 5 μT of additional magnetic field can appear along the Y- and Z-axis. This phenomenon can be mitigated by characterizing and compensating for sensor cross-sensitivities. Alternatively, generating stronger magnetic gradients could reduce the impact of cross-sensitivity, or adopting different sensing technologies might provide a more robust solution. This thesis, as proof of concept, establishes the requirements for magnetic field generation and sensor units. While various sensors are currently available and new models are frequently introduced, a promising immediate solution could involve using Hall-effect sensors, such as the AK09919C [174], which share similar dimensions with the sensors used in this research. Hall-effect sensors inherently exhibit lower cross-sensitivities, making them a compelling option for future system iterations.

Ultimately, the system's performance reflects a balance between sensing capabilities, FG dimensions and power consumption. The challenge addressed in this thesis was designing a system tailored to the specific spatial and performance requirements of DBS procedures. In this regard, the aim was validated with the ManaDBS system.

Integrability

The DBS procedure encompasses several stages, from pre-operative imaging to anchoring the electrode. The ManaDBS system is specifically designed for use during the electrode implantation phase, making it an intra-operative navigation tool. The system's development was guided by the requirements of the operating room. These requirements were discussed with neurosurgeons collaborating on the project. The primary design goals were compactness and seamless integration with existing DBS procedures across different clinical centers.

The compactness of the system, as discussed earlier, is critical to its performance and usability. The components of the ManaDBS system were arranged for optimal integration within the operating room of the University Hospital of Basel but remain flexible to different surgical theaters. Integrating a navigation system into a surgical workflow inevitably introduces additional steps. To minimize this, a registration system was developed based on wireless, flexible electronic markers fixed to the stereotactic frame during the pre-operative phase. These markers are automatically segmented on pre-operative CT images and saved as fiducials.
During surgery, the FG of the ManaDBS system is positioned behind the patient's head and secured to the operating table's side rail. The electromagnetic navigation system then acquires the stereotactic marker positions, registering them to the CT-based positions. This enables the calculation of a transformation matrix, which is subsequently applied to the following EMT positions, providing the visualization of the DBS electrode in relation to the patient's brain from the pre-operative imaging. This registration method, presented as proof of concept in **Publication IV**, shows promise due to its user-independent and fully automated nature. However, its current localization error of approximately 3 mm is insufficient for DBS surgery and requires improvement. For instance, improvements can be achieved by optimizing the design and placement of the markers on the stereotactic frame.
The system's integration into the operating room and surgical workflow was successfully

achieved. However, verifying its compatibility with this environment was critical, as outlined in **Publication III**. While compatibility with the stereotactic system was confirmed, smaller surgical instruments, such as microdrives, retractors, or MER electrodes, were not fully evaluated. These instruments may introduce localized and static distortions affecting the field generated, which serves as the reference for tracking. This sensitivity was explored in Appendix B, highlighting that the ManaDBS system is vulnerable to large ferromagnetic instruments, such as a steel retractor or needle holder. These distortions result in tracking errors, with positional inaccuracies of a few millimeters and orientation deviations of tens of degrees when the instruments were within 2 cm of the sensor. Existing EMT exhibited degradations only on the angular components of about tens of degrees when the same instruments were within 2 cm of the sensor. However, in practical scenarios, the needle holder and retractor are not expecting at close proximity of the DBS electrode integrating the magnetic sensors. In contrast, the instruments positioned a few millimeters away from the DBS electrode, such as the MER electrode, did not affect tracking performance. Future advancements should focus on developing compensation methods to address this issue.
Even if effective compensation methods are implemented, it remains critical to verify whether the metrological performance of the sensors is preserved after being exposed to the magnetic fields of surgical tools or to strong MRI fields. Magnetic sensing technologies, such as TMR and AMR, are composed of highly permeable materials that are sensitive to magnetic fields. As a result, they may become unintentionally magnetized or demagnetized when exposed to strong magnetic fields, which could potentially impair their performance. The AMR sensors used in this study are rated to withstand magnetic fields up to 1 T, as specified in the manufacturer's datasheet. This robustness is attributed to an integrated micro-coil at the wafer level, which reinitializes the permalloy material of the AMR through a peak current pulse. The resilience of these sensors was experimentally verified under exposure to fields as strong as 7 T, with detailed results provided in Appendix C. Furthermore, sensor calibration could theoretically be carried out over the course of the patient's lifetime, using procedures that are both quick and safe. However, this approach may ultimately prove to be impractical.

Overall, while the ManaDBS system addresses many challenges of the DBS surgical environment, further refinements are essential to improve its accuracy and robustness, paving the way for safe clinical trials.

Manufacturing & Miniaturization

The design of each ManaDBS system component was guided by the defined requirements and a focus on enhancing performance. Initially, the system was based on traditional copper coils, but the imperfections in the wiring and the resulting inhomogeneities in the magnetic fields led to the decision to integrate the coils onto a PCB. The PCB manufacturing process, with its micrometer-level precision and ability for mass production with improved reproducibility, was beneficial for enhancing system performance, robustness, and future industrial scalability. Similarly, the stereotactic markers used for the registration can be mass-produced at a low cost, which further supports the system's practical implementation.
On the other hand, the DBS electrode presented the greatest challenge. To maintain the same

dimensions as traditional DBS electrodes (about 1.2 mm), sensors with submillimetric packaging were preferred. The first prototype incorporated a small PCB onto which the AMR magnetic sensor was soldered. We progressively reduced the size of the PCB and ultimately removed it to integrate the sensors directly into the DBS electrode. The wires were soldered directly onto the sensor pads and encased in resin at the tip of the electrode. Although this method proved to be functional, it is not practical for mass production. Moreover, the AMR sensor chosen requires an external capacitor for optimal functionality. To guarantee optimal performance, the maximum allowed resistance between the sensors and the capacitor is 0.2 ohms. This may require its close integration within the DBS electrode rather than being placed further away. The close integration of the capacitor was possible into the first prototypes but not within a real DBS electrode.
As a result, technical solutions need to be developed to integrate the sensors, potential capacitors, and associated wiring while ensuring proper alignment with the electrode axis. These solutions remain unexplored and present an open challenge for future development.

Outlook and perspectives

Towards Clinical trials

Several considerations must be addressed before deploying the ManaDBS system for clinical trials in an operating room setting with human participants. The primary concern is safety, which was initially assessed in **Publication II**. The study indicated that the system is unlikely to induce peripheral nerve stimulation from the coils under standard operation. However, further evaluations are necessary to ensure compliance with established safety standards. Future investigations should follow guidelines such as the International Commission on Non-Ionizing Radiation Protection's recommendations for limiting exposure to time-varying electric and magnetic fields (1 Hz to 100 kHz) and the IEEE C95 Standards (C95.6-2002) for the 0 Hz to 3 kHz range, established by the International Committee on Electromagnetic Safety. Meeting these standards may require modifications to the system, particularly in the coil activation sequence. For instance, implementing a ramped activation and deactivation sequence for the coils can reduce the amplitude of signal harmonics, enhancing safety and compliance. These adjustments on system performance are detailed in Appendix D.
Another critical safety consideration is addressing potential events throughout the patient's lifetime. Patients may require imaging procedures, such as X-rays or MRI scans, either as part of routine medical care or for post-operative follow-ups. While the integration of sensors within the DBS electrode poses no known risks for X-ray imaging, MRI safety presents a more complex challenge. In recent years, manufacturers have made significant advancements in developing "MRI-compatible" devices for 1.5T to 3T systems. To ensure widespread clinical acceptance, DBS electrodes, even those incorporating non-active sensors, must align with these developments and prioritize MRI compatibility. However, from the patient's perspective, the MRI compatibility of the system must be thoroughly assessed to ensure safety.

The success of medical device research ultimately depends on its ability to transition from the laboratory to practical use in the operating room, providing advantages for both surgeons and patients. In this case, the work has not yet reached this critical stage. To advance further, a preliminary evaluation using cadavers could be conducted, enabling a complete simulation of the DBS surgical procedure while integrating the ManaDBS system.
Such a study would serve as a foundational milestone, demonstrating the practical feasibility of the system and its implications in a realistic surgical context. This step could also facilitate partnerships with industry stakeholders, paving the way for discussions on the translational potential and value of the system within the medical device market.

Post-operative use of the ManaDBS system

This thesis primarily addresses the development of a navigation system for DBS surgery, but the system could also have potential applications for post-operative DBS electrode tracking. Since the sensor is integrated into the DBS electrode, it remains implanted within the patient, allowing for post-surgical localization of the electrode. The ability to detect DBS electrode positions post-operatively offers the advantage of verifying electrode placement without exposing the patient to additional radiation. This can be particularly valuable during the stimulation programming, as electrode positions and orientations have been observed to shift in some cases within the first months or year following implantation [262, 263, 264]. Additionally, the accurate knowledge of the electrode's position enables clinicians to track changes in symptoms and link them to disease progression or the positioning of the DBS electrode. This can help identify when stimulation adjustments are needed, optimizing therapeutic outcomes and improving the long-term management of the condition.
However, implementing this capability would require significant modifications to current DBS systems, particularly in designing a neurostimulator capable of providing power and communication to the sensor. For the sensors used in this work, additional wiring would be necessary: four extra lines (ground, power supply voltage, and two communication buses). With the increasing complexity of DBS electrodes driven by the adoption of directional designs, the addition of wires has already been demonstrated as feasible. However, the integration of a sensor remains largely unexplored, and the potential regulatory and approval costs associated with redesigning a neurostimulator should not be underestimated.
Furthermore, to employ the ManaDBS system as a post-operative localization tool, a method for registering the ManaDBS coordinate space with the patient's anatomical space must be developed. One potential solution could involve integrating magnetic sensors into the burr hole cover device. This device is employed to seal the hole drilled into the skull and to anchor the DBS electrode. By embedding sensors within the burr hole, a stable reference point for the ManaDBS system could be established.

From the system's perspective, localization can be efficiently performed. The sensors used in this work were tested for resilience after exposure to strong MRI fields, demonstrating their ability to withstand such conditions, suggesting their potential for use even after MRI imaging (see Appendix C).

The potential post-operative application of the ManaDBS system should be carefully evaluated and discussed with neurosurgeons and neurologists to gain their practical insights and determine its clinical value.

Proposition of a novel electromagnetic tracking technique

In this thesis, we proposed an electromagnetic tracking technique based on quasi-static magnetic fields measured by AMR sensors. While this approach demonstrates significant promise, it is not the sole option. Advances in magnetic sensing technologies led to highly sensitive commercial sensors, such as OPMs. In Appendix E, we explore an alternative multilateration-based technique that utilizes a single emitter, a compact and flexible coil, paired with multiple OPM acting as receivers. This concept envisions integrating these small flexible coils into catheters, endoscopic capsules, or DBS electrodes, enabling detection using external OPMs. This example also highlights the emerging capabilities of advanced sensing technologies and their expansive potential applications in the medical fields.

CHAPTER 9

Conclusion

This work has contributed to the field of neurosurgery by addressing challenges in the development of an EMT system designed to improve real-time localization and orientation feedback during stereotactic DBS procedures.
A novel concept combining quasi-static magnetic fields with integrated magnetic sensors, was introduced. A first demonstrator based on this concept was developed and the system's requirements for generating the quasi-static magnetic field along with the specifications for the sensing units were thoroughly examined. The developed system has shown promising results in position and orientation localization. Additionally, the system demonstrates robustness in handling the challenges of the surgical environment, including compatibility with stereotactic systems. Ensuring seamless integration into surgical workflows was also a key focus, leading to the development of an innovative registration method. Further development is necessary, particularly to achieve submillimetric spatial accuracy.

Although the system's primary focus was DBS procedures, the developed concept is adaptable to other interventions requiring precise electrode placement and tracking. For DBS, the system was validated through replicated surgical setups, showing compatibility with stereotactic systems and the potential for integration into standard surgical workflows. However, certain challenges remain, including the impact of EMI caused by ferromagnetic surgical tools.
The EMT system was evaluated under simplified conditions, with results indicating that the concept is promising. However, the system's performance when integrated into a complete surgical workflow depends heavily on its compatibility with various other systems, such as electronic devices or intra-operative imaging, as well as the constraints of the DBS device. These additional components may impose new constraints or influence the EMT system's initial design, necessitating further iterations.

The successful integration of the EMT system into DBS workflows is an iterative process where new insights into surgical requirements and environmental limitations will refine the system's design and performance. The current system represents a first iteration that addresses key challenges in DBS surgery, providing a foundation for further development.

Bibliography

[1] I. E. Harmsen, F. Wolff Fernandes, J. K. Krauss, and A. M. Lozano, "Where are we with deep brain stimulation? a review of scientific publications and ongoing research," *Stereotact. Funct. Neurosurg.*, vol. 100, no. 3, pp. 184–197, Feb. 2022, https://doi.org/10.1159/000521372.

[2] J. K. Krauss, N. Lipsman, T. Aziz, A. Boutet, P. Brown, J. W. Chang, B. Davidson, W. M. Grill, M. I. Hariz, A. Horn, M. Schulder, A. Mammis, P. A. Tass, J. Volkmann, and A. M. Lozano, "Technology of deep brain stimulation: current status and future directions," *Nat. Rev. Neurol.*, vol. 17, no. 2, pp. 75–87, Feb. 2021, https://doi.org/10.1038/s41582-020-00426-z.

[3] V. Vedam-Mai, K. Deisseroth, J. Giordano, G. Lazaro-Munoz, W. Chiong, N. Suthana, J.-P. Langevin, J. Gill, W. Goodman, N. R. Provenza, C. H. Halpern, R. S. Shivacharan, T. N. Cunningham, S. A. Sheth, N. Pouratian, K. W. Scangos, H. S. Mayberg, A. Horn, K. A. Johnson, C. R. Butson, R. Gilron, C. de Hemptinne, R. Wilt, M. Yaroshinsky, S. Little, P. Starr, G. Worrell, P. Shirvalkar, E. Chang, J. Volkmann, M. Muthuraman, S. Groppa, A. A. Kühn, L. Li, M. Johnson, K. J. Otto, R. Raike, S. Goetz, C. Wu, P. Silburn, B. Cheeran, Y. J. Pathak, M. Malekmohammadi, A. Gunduz, J. K. Wong, S. Cernera, W. Hu, A. Wagle Shukla, A. Ramirez-Zamora, W. Deeb, A. Patterson, K. D. Foote, and M. S. Okun, "Proceedings of the eighth annual deep brain stimulation think tank: Advances in optogenetics, ethical issues affecting DBS research, neuromodulatory approaches for depression, adaptive neurostimulation, and emerging DBS technologies," *Front. Hum. Neurosci.*, vol. 15, p. 644593, Apr. 2021, https://doi.org/10.3389/fnhum.2021.765150.

[4] U. Walter, M. Kirsch, M. Wittstock, J.-U. Müller, R. Benecke, and A. Wolters, "Transcranial sonographic localization of deep brain stimulation electrodes is safe, reliable and predicts clinical outcome," *Ultrasound Med. Biol.*, vol. 37, no. 9, pp. 1382–1391, Sep. 2011, https://doi.org/10.1016/j.ultrasmedbio.2011.05.017.

[5] A. B. Jacob, M. T. Krueger, H. Akram, K. Aristovich, and V. Litvak, "Measuring the orientation of segmented deep brain stimulation leads using electroencephalography," *bioRxiv*, Mar. 2024, https://doi.org/10.1101/2024.02.27.582287.

[6] J. Gardner, "A history of deep brain stimulation: Technological innovation and the role of clinical assessment tools," *Soc. Stud. Sci.*, vol. 43, no. 5, pp. 707–728, Oct. 2013, https://doi.org/10.1177/0306312713483678.

[7] M. I. Hariz, P. Blomstedt, and L. Zrinzo, "Deep brain stimulation between 1947 and 1987: the untold story," *Neurosurg. Focus*, vol. 29, no. 2, p. E1, Aug. 2010, https://doi.org/10.3171/2010.4.FOCUS10106.

[8] E. A. Spiegel, H. T. Wycis, M. Marks, and A. J. Lee, "Stereotaxic apparatus for operations on the human brain," *Science*, vol. 106, no. 2754, pp. 349–350, Oct. 1947, https://doi.org/10.1126/science.106.2754.349.

[9] W. Birkmayer and O. Hornykiewicz, "Der L-Dioxyphenylalanin (=L-DOPA)-Effekt beim Parkinson-Syndrom des menschen: Zur pathogenese und behandlung der Parkinson-Akinese," *Archiv fur Psychiatrie und Zeitschrift f. d. ges. Neurologie*, vol. 203, no. 5, pp. 560–574, 1962, https://doi.org/10.1007/BF00343235.

[10] G. C. Cotzias, P. S. Papavasiliou, and R. Gellene, "Modification of parkinsonism–chronic treatment with l-dopa," *N. Engl. J. Med.*, vol. 280, no. 7, pp. 337–345, Feb. 1969, https://doi.org/10.1056/NEJM196902132800701.

[11] W. Birkmayer and E. Neumayer, "Die moderne medikamentöse behandlung des parkinsonismus," *Z. Neurol.*, vol. 202, no. 4, pp. 257–280, 1972, https://doi.org/10.1007/BF00316175.

[12] C. H. Markham, L. J. Treciokas, and S. G. Diamond, "Parkinson's disease and levodopa. a five-year follow-up and review," *West. J. Med.*, vol. 121, no. 3, pp. 188–206, Sep. 1974. [Online]. Available: https://pmc.ncbi.nlm.nih.gov/articles/PMC1129565/

[13] A. Barbeau, "Editorial: Long-term assessment of levodopa therapy in parkinson's disease," *Can. Med. Assoc. J.*, vol. 112, no. 12, pp. 1379–1380, Jun. 1975. [Online]. Available: https://pmc.ncbi.nlm.nih.gov/articles/PMC1956240/

[14] P. Breggin, "The return of lobotomy and psychosurgery," *Congressional Record, Washington, DC:United States Government Printing Office*, 1972. [Online]. Available: https://breggin.com/admin/fm/source/6905_breggin/ect-resources/Breggin_return_of_psychosurgerry_1982_with_cite_.pdf

[15] C. N. Shealy, J. T. Mortimer, and J. B. Reswick, "Electrical inhibition of pain by stimulation of the dorsal columns: preliminary clinical report," *Anesth. Analg.*, vol. 46, no. 4, pp. 489–491, Jul. 1967. [Online]. Available: https://journals.lww.com/anesthesia-analgesia/citation/1967/07000/electrical_inhibition_of_pain_by_stimulation_of.25.aspx

[16] Y. Hosobuchi, J. E. Adams, and B. Rutkin, "Chronic thalamic and internal capsule stimulation for the control of central pain," *Surg. Neurol.*, vol. 4, no. 1, pp. 91–92, Jul. 1975, https://doi.org/10.1016/0304-3959(76)90065-8.

[17] N. P. Bekhtereva, A. N. Bondarchuk, V. M. Smirnov, and L. A. Meliucheva, "Therapeutic electric stimulation of deep brain structures," *Vopr. Neirokhir.*, vol. 36, no. 1, pp. 7–12, Jan. 1972.

[18] C. W. Sem-Jacobsen, "Depth-electrographic observations in psychotic patients," *Acta Psychiatr. Scand.*, vol. 34, no. s136, pp. 412–416, Sep. 1959, https://doi.org/10.1111/j.1600-0447.1959.tb07829.x.

[19] L. V. Laitinen, "Emotional responses to subcortical electrical stimulation in psychiatric patients," *Clin. Neurol. Neurosurg.*, vol. 81, no. 3, https://doi.org/10.1016/0303-8467(79)90002-7.

[20] F. Escobedo, A. Fernandez-Guardiola, and G. Solis, "Chronic stimulation of the cingulum in humans with behaviour disorders," *Surgical approaches in psychiatry*, pp. 65–68, 1973.

[21] J. Nonnekes, M. H. M. Timmer, N. M. de Vries, O. Rascol, R. C. Helmich, and B. R. Bloem, "Unmasking levodopa resistance in parkinson's disease," *Mov. Disord.*, vol. 31, no. 11, pp. 1602–1609, Nov. 2016, https://doi.org/10.1002/mds.26712.

[22] I. S. Cooper, A. R. M. Upton, and I. Amin, "Reversibility of chronic neurologic deficits. some effects of electrical stimulation of the thalamus and internal capsule in man," *Stereotact. Funct. Neurosurg.*, vol. 43, no. 3-5, pp. 244–258, 1980, https://doi.org/10.1159/000102263.

[23] S. Fahn and R. L. Elton, "Unified parkinson's disease rating scale," in *Recent developments in Parkinson's disease*, S. Fahn, C. D. Marsden, and M. Goldstein, Eds. Macmillian, pp. 153–163.

[24] S. Fahn, E. Tolosa, and C. Marín, "Clinical rating scale for tremor," in *Jankovik J and Tolosa E. Parkinson's disease and movement disorders*. Baltimore Munich:Urban ¬Schwarzenberg, vol. 2, pp. 225–34.

[25] A. L. Benabid, P. Pollak, A. Louveau, S. Henry, and J. de Rougemont, "Combined (thalamotomy and stimulation) stereotactic surgery of the VIM thalamic nucleus for bilateral parkinson disease," *Stereotact. Funct. Neurosurg.*, vol. 50, no. 1-6, pp. 344–346, 1987, https://doi.org/10.1159/000100803.

[26] G. C. Davis, A. C. Williams, S. P. Markey, M. H. Ebert, E. D. Caine, C. M. Reichert, and I. J. Kopin, "Chronic parkinsonism secondary to intravenous injection of meperidine analogues," *Psychiatry Res.*, vol. 1, no. 3, pp. 249–254, Dec. 1979, https://doi.org/10.1016/0165-1781(79)90006-4.

[27] J. W. Langston, P. Ballard, J. W. Tetrud, and I. Irwin, "Chronic parkinsonism in humans due to a product of meperidine-analog synthesis," *Science*, vol. 219, no. 4587, pp. 979–980, Feb. 1983, https://doi.org/10.1126/science.6823561.

[28] R. S. Burns, C. C. Chiueh, S. P. Markey, M. H. Ebert, D. M. Jacobowitz, and I. J. Kopin, "A primate model of parkinsonism: selective destruction of dopaminergic neurons in the pars compacta of the substantia nigra by n-methyl-4-phenyl-1,2,3,6-tetrahydropyridine," *Proc. Natl. Acad. Sci. U. S. A.*, vol. 80, no. 14, pp. 4546–4550, Jul. 1983, https://doi.org/10.1073/pnas.80.14.4546.

[29] M. R. DeLong, "Primate models of movement disorders of basal ganglia origin," *Trends Neurosci.*, vol. 13, no. 7, pp. 281–285, Jul. 1990, https://doi.org/10.1016/0166-2236(90)90110-v.

[30] A. L. Benabid, P. Pollak, C. Gervason, D. Hoffmann, D. M. Gao, M. Hommel, J. E. Perret, and J. de Rougemont, "Long-term suppression of tremor by chronic stimulation of the ventral intermediate thalamic nucleus," *Lancet*, vol. 337, no. 8738, pp. 403–406, Feb. 1991, https://doi.org/10.1016/0140-6736(91)91175-t.

[31] Food and Drugs Administration - Department of Health and Human services, "p960009 premarket approval: Implantable deep brain stimulation for the treatment of tremor due to parkinson's disease and essential tremor," 1997. [Online]. Available: https://www.accessdata.fda.gov/cdrh_docs/pdf/p960009.pdf

[32] M. Hariz and P. Blomstedt, "Deep brain stimulation for parkinson's disease," *J. Intern. Med.*, vol. 292, no. 5, pp. 764–778, Nov. 2022, https://doi.org/10.1111/joim.13541.

[33] C. A. Artusi, L. Lopiano, and F. Morgante, "Deep brain stimulation selection criteria for parkinson's disease: Time to go beyond CAPSIT-PD," *J. Clin. Med.*, vol. 9, no. 12, p. 3931, Dec. 2020, https://doi.org/10.3390/jcm9123931.

[34] M. L. Hacker, M. Turchan, L. E. Heusinkveld, A. D. Currie, S. H. Millan, A. L. Molinari, P. E. Konrad, T. L. Davis, F. T. Phibbs, P. Hedera, K. R. Cannard, L. Wang, and D. Charles, "Deep brain stimulation in early-stage parkinson disease: Five-year outcomes," *Neurology*, vol. 95, no. 4, pp. e393–e401, Jul. 2020, https://doi.org/10.1212/WNL.0000000000009946.

[35] A. Merola, J. Singh, K. Reeves, B. Changizi, S. Goetz, L. Rossi, S. Pallavaram, S. Carcieri, N. Harel, A. Shaikhouni, F. Sammartino, V. Krishna, L. Verhagen, and B. Dalm, "New frontiers for deep brain stimulation: Directionality, sensing technologies, remote programming, robotic stereotactic assistance, asleep procedures, and connectomics," *Front. Neurol.*, vol. 12, p. 694747, Jul. 2021, https://doi.org/10.3389/fneur.2021.694747.

[36] N. Shaheen and O. Flouty, "Unlocking the future of deep brain stimulation: innovations, challenges, and promising horizons," *Int. J. Surg.*, vol. 110, no. 6, pp. 3146–3148, Jun. 2024, https://doi.org/10.1097/JS9.0000000000001279.

[37] K. A. Johnson, M. S. Okun, K. W. Scangos, H. S. Mayberg, and C. de Hemptinne, "Deep brain stimulation for refractory major depressive disorder: a comprehensive review," *Mol. Psychiatry*, vol. 29, no. 4, pp. 1075–1087, Apr. 2024, https://doi.org/10.1038/s41380-023-02394-4.

[38] N. Shaheen, A. Shaheen, A. Elgendy, Y. B. Bezchlibnyk, T. Zesiewicz, B. Dalm, J. Jain, A. L. Green, T. Z. Aziz, and O. Flouty, "Deep brain stimulation for chronic pain: a systematic review and meta-analysis," *Front. Hum. Neurosci.*, vol. 17, p. 1297894, Nov. 2023, https://doi.org/10.3389/fnhum.2023.1297894.

[39] B. Picton, J. Wong, A. M. Lopez, S. S. Solomon, S. Andalib, N. J. Brown, R. R. Dutta, M. R. Paff, F. P. Hsu, and M. Y. Oh, "Deep brain stimulation as an emerging therapy for cognitive decline in alzheimer disease: Systematic review of evidence and current targets," *World Neurosurg.*, vol. 184, pp. 253–266.e2, Apr. 2024, https://doi.org/10.1016/j.wneu.2023.12.083.

[40] Medtronic Inc., "PRODUCT PERFORMANCE REPORT - Summary of Data from the Medtronic Post-market Registry 2023- v.1.0 Apr2023," Accessed: 29-01-2025. [Online]. Available: https://www.medtronic.com/content/dam/medtronic-wide/public/united-states/products/neurological/product-performance-report-deep-brain-stimulation.pdf

[41] S. Hemm and K. Wårdell, "Stereotactic implantation of deep brain stimulation electrodes: a review of technical systems, methods and emerging tools," *Med. Biol. Eng. Comput.*, vol. 48, no. 7, pp. 611–624, Jul. 2010, https://doi.org/10.1007/s11517-010-0633-y.

[42] A. Abosch, L. Timmermann, S. Bartley, H. G. Rietkerk, D. Whiting, P. J. Connolly, D. Lanctin, and M. I. Hariz, "An international survey of deep brain stimulation procedural steps," *Stereotact. Funct. Neurosurg.*, vol. 91, no. 1, pp. 1–11, 2013, https://doi.org/10.1159/000343207.

[43] V. Palys and K. L. Holloway, "Frameless functional stereotactic approaches," *Prog. Neurol. Surg.*, vol. 33, pp. 168–186, Jan. 2018, https://doi.org/10.1159/000481102.

[44] C. P. Picciano, P. Mantovani, V. Rosetti, G. Giannini, M. Pegoli, C. A. Castioni, I. Cani, L. Baldelli, P. Cortelli, and A. Conti, "How accurate is frameless fiducial-free deep brain stimulation?" *Oper. Neurosurg. (Hagerstown)*, vol. 27, no. 4, pp. 431–439, Oct. 2024, https://doi.org/10.1227/ons.0000000000001151.

[45] M. Abolfotoh, K. Tavanaipour, and D. Tavanaipour, "Frameless and fiducial-less, o-arm assisted navigation for deep brain stimulation placement using the nexframe®. a technical note," *Deep Brain Stimulation*, vol. 4, pp. 9–12, Jun. 2024, https://doi.org/10.1016/j.jdbs.2023.11.003.

[46] L. Zrinzo, "Pitfalls in precision stereotactic surgery," *Surg. Neurol. Int.*, vol. 3, no. Suppl 1, pp. S53–61, Jan. 2012, https://doi.org/10.4103/2152-7806.91612.

[47] H. Bjartmarz and S. Rehncrona, "Comparison of accuracy and precision between frame-based and frameless stereotactic navigation for deep brain stimulation electrode implantation," *Stereotact. Funct. Neurosurg.*, vol. 85, no. 5, pp. 235–242, May 2007, https://doi.org/10.1159/000103262.

[48] A. Roth, S. S. Buttrick, I. Cajigas, J. R. Jagid, and M. E. Ivan, "Accuracy of frame-based and frameless systems for deep brain stimulation: A meta-analysis," *J. Clin. Neurosci.*, vol. 57, pp. 1–5, Nov. 2018, https://doi.org/10.1016/j.jocn.2018.08.039.

[49] R. Eleopra, S. Rinaldo, G. Devigili, M. Mondani, S. D'Auria, C. Lettieri, T. Ius, and M. Skrap, "Frameless deep brain stimulation surgery: A single-center experience and retrospective analysis of placement accuracy of 220 electrodes in a series of 110 patients," *Stereotact. Funct. Neurosurg.*, vol. 97, no. 5-6, pp. 337–346, 2019, https://doi.org/10.1159/000503335.

[50] A. Morel, *Stereotactic atlas of the human thalamus and basal ganglia*. Boca Raton, FL: CRC Press, Mar. 2007, https://doi.org/10.3109/9781420016796.

[51] J. Talairach and P. Tournoux, *Co-planar stereotaxic atlas of the human brain: 3-Dimensional proportional system: An approach to cerebral imaging*. New York: Thieme Medical Publishers, Inc, 1988. [Online]. Available: https://api.semanticscholar.org/CorpusID:264653382

[52] P.-H. Tu, Z.-H. Liu, C. C. Chen, W. Y. Lin, A. L. Bowes, C. S. Lu, and S.-T. Lee, "Indirect targeting of subthalamic deep brain stimulation guided by stereotactic computed tomography and microelectrode recordings in patients with parkinson's disease," *Front. Hum. Neurosci.*, vol. 12, p. 470, Dec. 2018, https://doi.org/10.3389/fnhum.2018.00470.

[53] L. Houshmand, K. S. Cummings, K. L. Chou, and P. G. Patil, "Evaluating indirect subthalamic nucleus targeting with validated 3-tesla magnetic resonance imaging," *Stereotact. Funct. Neurosurg.*, vol. 92, no. 6, pp. 337–345, Oct. 2014, https://doi.org/10.1159/000366286.

[54] K. Ashkan, P. Blomstedt, L. Zrinzo, S. Tisch, T. Yousry, P. Limousin-Dowsey, and M. I. Hariz, "Variability of the subthalamic nucleus: the case for direct MRI guided targeting," *Br. J. Neurosurg.*, vol. 21, no. 2, pp. 197–200, Apr. 2007, https://doi.org/10.1080/02688690701272240.

[55] L. Buentjen, K. Kopitzki, F. C. Schmitt, J. Voges, C. Tempelmann, J. Kaufmann, and M. Kanowski, "Direct targeting of the thalamic anteroventral nucleus for deep brain stimulation by t1-weighted magnetic resonance imaging at 3 T," *Stereotact. Funct. Neurosurg.*, vol. 92, no. 1, pp. 25–30, 2014, https://doi.org/10.1159/000351525.

[56] F. Vassal, J. Coste, P. Derost, V. Mendes, J. Gabrillargues, C. Nuti, F. Durif, and J.-J. Lemaire, "Direct stereotactic targeting of the ventrointermediate nucleus of the thalamus based on anatomic 1.5-t MRI mapping with a white matter attenuated inversion recovery (WAIR) sequence," *Brain Stimul.*, vol. 5, no. 4, pp. 625–633, Oct. 2012, https://doi.org/10.1016/j.brs.2011.10.007.

[57] E. J. Ebani, M. G. Kaplitt, Y. Wang, T. D. Nguyen, G. Askin, and J. L. Chazen, "Improved targeting of the globus pallidus interna using quantitative susceptibility mapping prior to MR-guided focused ultrasound ablation in parkinson's disease," *Clin. Imaging*, vol. 68, pp. 94–98, Dec. 2020, https://doi.org/10.1016/j.clinimag.2020.06.017.

[58] J. Wang, F. A. Ponce, J. Tao, H.-M. Yu, J.-Y. Liu, Y.-J. Wang, G.-M. Luan, and S.-W. Ou, "Comparison of awake and asleep deep brain stimulation for parkinson's disease: A detailed analysis through literature review," *Neuromodulation*, vol. 23, no. 4, pp. 444–450, Jun. 2020, https://doi.org/10.1111/ner.13061.

[59] M. L. Lim, A. B. B. Zhan, S. J. Liu, S. E. Saffari, W. Li, M. M. Teo, T. G.-L. Wong, W. H. Ng, and K. R. Wan, "Awake versus asleep anesthesia in deep brain stimulation surgery for parkinson's disease: A systematic review and meta-analysis," *Stereotact. Funct. Neurosurg.*, vol. 102, no. 3, pp. 141–155, Apr. 2024, https://doi.org/10.1159/000536310.

[60] B. Kundu, A. A. Brock, J. A. Thompson, and J. D. Rolston, "Microelectrode recording in neurosurgical patients," in *Stereotactic and Functional Neurosurgery*. Cham: Springer International Publishing, 2020, pp. 93–106, https://doi.org/10.1007/978-3-030-34906-6_8.

[61] L. Zrinzo, T. Foltynie, P. Limousin, and M. I. Hariz, "Reducing hemorrhagic complications in functional neurosurgery: a large case series and systematic literature review," *J. Neurosurg.*, vol. 116, no. 1, pp. 84–94, Jan. 2012, https://doi.org/10.3171/2011.8.JNS101407.

[62] C. C. Chen, A. Pogosyan, L. U. Zrinzo, S. Tisch, P. Limousin, K. Ashkan, T. Yousry, M. I. Hariz, and P. Brown, "Intra-operative recordings of local field potentials can help localize the subthalamic nucleus in parkinson's disease surgery," *Exp. Neurol.*, vol. 198, no. 1, pp. 214–221, Mar. 2006, https://doi.org/10.1016/j.expneurol.2005.11.019.

[63] R. Kolb, A. Abosch, G. Felsen, and J. A. Thompson, "Use of intraoperative local field potential spectral analysis to differentiate basal ganglia structures in parkinson's disease patients," *Physiol. Rep.*, vol. 5, no. 12, p. e13322, Jun. 2017, https://doi.org/10.14814/phy2.13322.

[64] V. J. Geraedts, R. A. P. van Ham, J. Marinus, J. J. van Hilten, A. Mosch, C. F. E. Hoffmann, N. A. van der Gaag, and M. F. Contarino, "Intraoperative test stimulation of the subthalamic nucleus aids postoperative programming of chronic stimulation settings in parkinson's disease," *Parkinsonism Relat. Disord.*, vol. 65, pp. 62–66, Aug. 2019, https://doi.org/10.1016/j.parkreldis.2019.05.017.

[65] N. Göransson, J. D. Johansson, K. Wårdell, and P. Zsigmond, "Postoperative lead movement after deep brain stimulation surgery and the change of stimulation volume," *Stereotact. Funct. Neurosurg.*, vol. 99, no. 3, pp. 221–229, 2021, https://doi.org/10.1159/000511406.

[66] E. de Schlichting, G. Coll, J. F. Zaldivar-Jolissaint, J. Coste, A. R. Marques, A. Mulliez, F. Durif, and J.-J. Lemaire, "Pulse generator battery life in deep brain stimulation: out with the old… in with the less durable?" *Acta Neurochir. (Wien)*, vol. 161, no. 10, pp. 2043–2046, Oct. 2019, https://doi.org/10.1007/s00701-019-04043-8.

[67] D. Dormont, D. Seidenwurm, D. Galanaud, P. Cornu, J. Yelnik, and E. Bardinet, "Neuroimaging and deep brain stimulation," *AJNR Am. J. Neuroradiol.*, vol. 31, no. 1, pp. 15–23, Jan. 2010, https://doi.org/10.3174/ajnr.A1644.

[68] F. Zhang, F. Wang, W. Li, N. Wang, C. Han, S. Fan, P. Li, L. Xu, J. Zhang, and F. Meng, "Relationship between electrode position of deep brain stimulation and motor symptoms of parkinson's disease," *BMC Neurol.*, vol. 21, no. 1, p. 122, Mar. 2021, https://doi.org/10.1186/s12883-021-02148-1.

[69] T. Fiegele, G. Feuchtner, F. Sohm, R. Bauer, J. V. Anton, T. Gotwald, K. Twerdy, and W. Eisner, "Accuracy of stereotactic electrode placement in deep brain stimulation by intraoperative computed tomography," *Parkinsonism Relat. Disord.*, vol. 14, no. 8, pp. 595–599, Dec. 2008, https://doi.org/10.1016/j.parkreldis.2008.01.008.

[70] P. A. Starr, A. J. Martin, and P. S. Larson, "Implantation of deep brain stimulator electrodes using interventional MRI," *Neurosurg. Clin. N. Am.*, vol. 20, no. 2, pp. 193–203, Apr. 2009, https://doi.org/10.1016/j.nec.2009.04.010.

[71] C. H. Halpern, S. F. Danish, G. H. Baltuch, and J. L. Jaggi, "Brain shift during deep brain stimulation surgery for parkinson's disease," *Stereotact. Funct. Neurosurg.*, vol. 86, no. 1, pp. 37–43, 2008, https://doi.org/10.1159/000108587.

[72] Y. Miyagi, F. Shima, and T. Sasaki, "Brain shift: an error factor during implantation of deep brain stimulation electrodes," *J. Neurosurg.*, vol. 107, no. 5, pp. 989–997, Nov. 2007, https://doi.org/10.3171/JNS-07/11/0989.

[73] A. Loh, D. Gwun, C. T. Chow, A. Boutet, J. Tasserie, J. Germann, B. Santyr, G. Elias, K. Yamamoto, C. Sarica, A. Vetkas, A. Zemmar, R. Madhavan, A. Fasano, and A. M. Lozano, "Probing responses to deep brain stimulation with functional magnetic resonance imaging," *Brain Stimul.*, vol. 15, no. 3, pp. 683–694, May 2022, https://doi.org/10.1016/j.brs.2022.03.009.

[74] B. Carl, M. Bopp, M. Gjorgjevski, C. Oehrn, L. Timmermann, and C. Nimsky, "Implementation of intraoperative computed tomography for deep brain stimulation: Pitfalls and optimization of workflow, accuracy, and radiation exposure," *World Neurosurg.*, vol. 124, pp. e252–e265, Dec. 2018, https://doi.org/10.1016/j.wneu.2018.12.079.

[75] A. Boutet, T. Rashid, I. Hancu, G. J. B. Elias, R. M. Gramer, J. Germann, M. Dimarzio, B. Li, V. Paramanandam, S. Prasad, M. Ranjan, A. Coblentz, D. Gwun, C. T. Chow, R. Maciel, D. Soh, E. Fiveland, M. Hodaie, S. K. Kalia, A. Fasano, W. Kucharczyk, J. Pilitsis, and A. M. Lozano, "Functional MRI safety and artifacts during deep brain

stimulation: Experience in 102 patients," *Radiology*, vol. 293, no. 1, pp. 174–183, Oct. 2019, https://doi.org/10.1148/radiol.2019190546.

[76] Y. Nagayama, S. Tanoue, S. Oda, D. Sakabe, T. Emoto, M. Kidoh, H. Uetani, A. Sasao, T. Nakaura, O. Ikeda, K. Yamada, and Y. Yamashita, "Metal artifact reduction in head CT performed for patients with deep brain stimulation devices: Effectiveness of a single-energy metal artifact reduction algorithm," *AJNR Am. J. Neuroradiol.*, vol. 41, no. 2, pp. 231–237, Feb. 2020, https://doi.org/10.3174/ajnr.A6375.

[77] L. Furlanetti, H. Hasegawa, A. Oviedova, A. Raslan, M. Samuel, R. Selway, and K. Ashkan, "O-arm stereotactic imaging in deep brain stimulation surgery workflow: A utility and cost-effectiveness analysis," *Stereotact. Funct. Neurosurg.*, vol. 99, no. 2, pp. 93–106, 2021, https://doi.org/10.1159/000510344.

[78] M. J. Katati, V. A. Jover, V. B. Iañez, P. M. J. Navarro, S. J. de la Cruz, O. G. García, S. F. Escamilla, and C. A. Mínguez, "An initial experience with intraoperative O-Arm for deep brain stimulation surgery: can it replace post-operative MRI?" *Acta Neurol. Belg.*, vol. 120, no. 2, pp. 295–301, Apr. 2020, https://doi.org/10.1007/s13760-018-1037-2.

[79] A. Horn, W.-J. Neumann, K. Degen, G.-H. Schneider, and A. A. Kühn, "Toward an electrophysiological "sweet spot" for deep brain stimulation in the subthalamic nucleus," *Hum. Brain Mapp.*, vol. 38, no. 7, pp. 3377–3390, Jul. 2017, https://doi.org/10.1002/hbm.23594.

[80] F. Steigerwald, C. Matthies, and J. Volkmann, "Directional deep brain stimulation," *Neurotherapeutics*, vol. 16, no. 1, pp. 100–104, Jan. 2019, https://doi.org/10.1007/s13311-018-0667-7.

[81] Food and Drugs Administration, "P150031a premarket approval: Versice dbs system in the treatment of patients with moderate to advanced levodopa-responsive parkinsons disease (pd)," 2017. [Online]. Available: https://www.accessdata.fda.gov/scripts/cdrh/cfdocs/cfpma/pma.cfm?id=P150031

[82] T. A. Dembek, P. Reker, V. Visser-Vandewalle, J. Wirths, H. Treuer, M. Klehr, J. Roediger, H. S. Dafsari, M. T. Barbe, and L. Timmermann, "Directional DBS increases side-effect thresholds—a prospective, double-blind trial," *Mov. Disord.*, vol. 32, no. 10, pp. 1380–1388, Oct. 2017, https://doi.org/10.1016/j.parkreldis.2019.08.017.

[83] P. Rebelo, A. L. Green, T. Z. Aziz, A. Kent, D. Schafer, L. Venkatesan, and B. Cheeran, "Thalamic directional deep brain stimulation for tremor: Spend less, get more," *Brain Stimul.*, vol. 11, no. 3, pp. 600–606, May 2018, https://doi.org/10.1016/j.brs.2017.12.015.

[84] J. L. Busch, J. Kaplan, B. H. Bahners, J. Roediger, K. Faust, G.-H. Schneider, E. Florin, A. Schnitzler, P. Krause, and A. A. Kühn, "Local field potentials predict motor performance in deep brain stimulation for parkinson's disease," *Mov. Disord.*, vol. 38, no. 12, pp. 2185–2196, Dec. 2023, https://doi.org/10.1002/mds.29626.

[85] C. R. Oehrn, S. Cernera, L. H. Hammer, M. Shcherbakova, J. Yao, A. Hahn, S. Wang, J. L. Ostrem, S. Little, and P. A. Starr, "Chronic adaptive deep brain stimulation versus conventional stimulation in parkinson's disease: a blinded randomized feasibility trial," *Nat. Med.*, Aug. 2024, https://doi.org/10.1038/s41591-024-03196-z.

[86] A. Priori, N. Maiorana, M. Dini, M. Guidetti, S. Marceglia, and R. Ferrucci, "Adaptive deep brain stimulation (aDBS)," in *International Review of Neurobiology*, ser. International review of neurobiology. Elsevier, 2021, pp. 111–127, https://doi.org/10.1016/bs.irn.2021.06.006.

[87] J. Buhlmann, L. Hofmann, P. A. Tass, and C. Hauptmann, "Modeling of a segmented electrode for desynchronizing deep brain stimulation," *Front. Neuroeng.*, vol. 4, p. 15, Dec. 2011, https://doi.org/10.3389/fneng.2011.00015.

[88] A. Willsie and A. Dorval, "Fabrication and initial testing of the μDBS: a novel deep brain stimulation electrode with thousands of individually controllable contacts," *Biomed. Microdevices*, vol. 17, no. 3, p. 9961, 2015, https://doi.org/10.1007/s10544-015-9961-x.

[89] D. N. Anderson, B. Osting, J. Vorwerk, A. D. Dorval, and C. R. Butson, "Optimized programming algorithm for cylindrical and directional deep brain stimulation electrodes," *J. Neural Eng.*, vol. 15, no. 2, p. 026005, Apr. 2018, https://doi.org/10.1088/1741-2552/aaa14b.

[90] K. Hunka, O. Suchowersky, S. Wood, L. Derwent, and Z. H. T. Kiss, "Nursing time to program and assess deep brain stimulators in movement disorder patients," *J. Neurosci. Nurs.*, vol. 37, no. 4, pp. 204–210, Aug. 2005, https://doi.org/10.1097/01376517-200508000-00006.

[91] G. Duffley, B. J. Lutz, A. Szabo, A. Wright, C. W. Hess, A. Ramirez-Zamora, P. Zeilman, S. Chiu, K. D. Foote, M. S. Okun, and C. R. Butson, "Home health management of parkinson disease deep brain stimulation: A randomized clinical trial," *JAMA Neurol.*, vol. 78, no. 8, pp. 972–981, Aug. 2021, https://doi.org/10.1001/jamaneurol.2021.1910.

[92] A. M. Kuncel and W. M. Grill, "Selection of stimulus parameters for deep brain stimulation," *Clin. Neurophysiol.*, vol. 115, no. 11, pp. 2431–2441, Nov. 2004, https://doi.org/10.1016/j.clinph.2004.05.031.

[93] A. Wagle Shukla, P. Zeilman, H. Fernandez, J. A. Bajwa, and R. Mehanna, "DBS programming: An evolving approach for patients with parkinson's disease," *Parkinsons Dis.*, vol. 2017, pp. 1–11, 2017, https://doi.org/10.1155/2017/8492619.

[94] Y. Değirmenci, "Current DBS programming," *Deep Brain Stimulation*, vol. 4, pp. 29–31, Jun. 2024, https://doi.org/10.1016/j.jdbs.2023.12.002.

[95] J. D. Johansson and P. Zsigmond, "Comparison between patient-specific deep brain stimulation simulations and commercial system SureTune3," *Biomed. Phys. Eng. Express*, vol. 7, no. 5, p. 055001, Jul. 2021, https://doi.org/10.1088/2057-1976/ac0dcd.

[96] J. Hwang, S. Jeon, B. Kim, J.-Y. Kim, C. Jin, A. Yeon, B.-J. Yi, C.-H. Yoon, H.-J. Park, S. Pané, B. J. Nelson, and H. Choi, "An electromagnetically controllable microrobotic interventional system for targeted, real-time cardiovascular intervention," *Adv. Healthc. Mater.*, vol. 11, no. 11, p. e2102529, Jun. 2022, https://doi.org/10.1002/adhm.202102529.

[97] C. Chautems, S. Lyttle, Q. Boehler, and B. J. Nelson, "Design and evaluation of a steerable magnetic sheath for cardiac ablations," *IEEE Robot. Autom. Lett.*, vol. 3, no. 3, pp. 2123–2128, Jul. 2018, https://doi.org/10.1109/LRA.2018.2809546.

[98] A. Hong, A. J. Petruska, A. Zemmar, and B. J. Nelson, "Magnetic control of a flexible needle in neurosurgery," *IEEE Trans. Biomed. Eng.*, vol. 68, no. 2, pp. 616–627, Feb. 2021, https://doi.org/10.1109/TBME.2020.3009693.

[99] D. DePaoli, L. Goetz, D. Gagnon, G. Maranon, M. Prud'homme, L. Cantin, M. Parent, and D. C. Côté, "Intraoperative fiber optic guidance during chronic electrode implantation in deep brain stimulation neurosurgery: proof of concept in primates," *J. Neurosurg.*, vol. 132, no. 6, pp. 1810–1819, Jun. 2020, https://doi.org/10.3171/2019.1.JNS182600.

[100] S. Jerczynski, M. Quémener, V. P. Noël, A. Rousseau, E. Parham, A. Bédard, S. Masoumi, T. Charland, A. Drouin, J. Roussel, V. Dionne, T. Shooner, A. Parrot, M. A. Takech, É. Philippe, D. DePaoli, L. Cantin, M. Parent, and D. C. Côté, "Human brain tissue identification using coherent anti-stokes raman scattering spectroscopy and diffuse reflectance spectroscopy for deep brain stimulation surgery," *Neurophotonics*, vol. 11, no. 2, p. 025006, Apr. 2024, https://doi.org/10.1117/1.NPh.11.2.025006.

[101] L. Ispierto, J. Muñoz, J. M. Cladellas, P. Cuadras, J. Capellades, P. Latorre, A. Dávalos, T. Vancamp, and R. Álvarez, "Post-operative localization of deep brain stimulation electrodes in the subthalamus using transcranial sonography," *Neuromodulation*, vol. 21, no. 6, pp. 574–581, Aug. 2018, https://doi.org/10.1111/ner.12733.

[102] M. I. Iacono, S. R. Atefi, L. Mainardi, H. C. Walker, L. M. Angelone, and G. Bonmassar, "A study on the feasibility of the deep brain stimulation (DBS) electrode localization based on scalp electric potential recordings," *Front. Physiol.*, vol. 9, p. 1788, 2018, https://doi.org/10.3389/fphys.2018.01788.

[103] Y. Fang, F. Yang, L. Tan, W. He, P. Wang, and X. Ding, "An electric field stereotaxis method for surgical localization and navigation of solid organs," *IEEE Sens. J.*, vol. 24, no. 12, pp. 19 736–19 744, Jun. 2024, https://doi.org/10.1109/JSEN.2024.3393857.

[104] S. Martin, "A post-processing tool and feasibility study for three-dimensional imaging with electrical impedance tomography during deep brain stimulation surgery," *arXiv*, 2022, https://doi.org/10.48550/arXiv.2204.05201.

[105] M. Yalaz, N. Maling, G. Deuschl, L. M. Juárez-Paz, M. Butz, A. Schnitzler, A.-K. Helmers, and M. Höft, "MaDoPO: Magnetic detection of positions and orientations of segmented deep brain stimulation electrodes: A radiation-free method based on magnetoencephalography," *Brain Sci.*, vol. 12, no. 1, p. 86, Jan. 2022, https://doi.org/10.3390/brainsci12010086.

[106] B. Riaz, C. Pfeiffer, and J. F. Schneiderman, "Evaluation of realistic layouts for next generation on-scalp MEG: spatial information density maps," *Sci. Rep.*, vol. 7, no. 1, p. 6974, Aug. 2017, https://doi.org/10.1038/s41598-017-07046-6.

[107] M. Pedersen, D. F. Abbott, and G. D. Jackson, "Wearable OPM-MEG: A changing landscape for epilepsy," *Epilepsia*, vol. 63, no. 11, pp. 2745–2753, Nov. 2022, https://doi.org/10.1111/epi.17368.

[108] K. J. Burchiel, M. Kinsman, K. Mansfield, and A. Mitchell, "Verification of the deep brain stimulation electrode position using intraoperative electromagnetic localization," *Stereotact. Funct. Neurosurg.*, vol. 98, no. 1, pp. 37–42, Feb. 2020, https://doi.org/10.1159/000505494.

[109] K. A. Khan, P. Nardelli, A. Jaeger, C. O'Shea, P. Cantillon-Murphy, and M. P. Kennedy, "Navigational bronchoscopy for early lung cancer: A road to therapy," *Adv. Ther.*, vol. 33, no. 4, pp. 580–596, Apr. 2016, https://doi.org/10.1007/s12325-016-0319-4.

[110] E. J. Hermann, H.-H. Capelle, C. A. Tschan, and J. K. Krauss, "Electromagnetic-guided neuronavigation for safe placement of intraventricular catheters in pediatric neurosurgery," *J. Neurosurg. Pediatr.*, vol. 10, no. 4, pp. 327–333, Oct. 2012, https://doi.org/10.3171/2012.7.PEDS11369.

[111] F. Kral, E. J. Puschban, H. Riechelmann, F. Pedross, and W. Freysinger, "Optical and electromagnetic tracking for navigated surgery of the sinuses and frontal skull base," *Rhinology*, vol. 49, no. 3, pp. 364–368, Aug. 2011, https://doi.org/10.4193/Rhino10.177.

[112] J. A. Akulian, D. Molena, M. M. Wahidi, A. Chen, D. Yu, F. Maldonado, H. Lee, A. Vachani, L. Yarmus, and Interventional Pulmonary Outcomes Group (IPOG), "A direct comparative study of bronchoscopic navigation planning platforms for peripheral lung navigation: The ATLAS study," *J. Bronchology Interv. Pulmonol.*, vol. 29, no. 3, pp. 171–178, Jul. 2022, https://doi.org/10.1097/LBR.0000000000000806.

[113] E. J. Trimble, K. Stewart, and J. M. Reinersman, "Early comparison robotic bronchoscopy versus electromagnetic navigational bronchoscopy for biopsy of pulmonary nodules in a thoracic surgery practice," *J. Robot. Surg.*, vol. 18, no. 1, p. 149, Apr. 2024, https://doi.org/10.1007/s11701-024-01898-7.

[114] H. Keeble, J. P. Lavrador, N. Pereira, K. Lente, C. Brogna, R. Gullan, R. Bhangoo, F. Vergani, and K. Ashkan, "Electromagnetic navigation systems and intraoperative neuromonitoring: Reliability and feasibility study," *Oper. Neurosurg. (Hagerstown)*, vol. 20, no. 4, pp. 373–382, Mar. 2021, https://doi.org/10.1093/ons/opaa407.

[115] E. Harwick, I. Singhal, B. Conway, W. Mueller, R. Treffy, and M. O. Krucoff, "Pinless electromagnetic neuronavigation during awake craniotomies: Technical pearls, pitfalls, and nuances," *World Neurosurg.*, vol. 175, pp. e159–e166, Jul. 2023, https://doi.org/10.1016/j.wneu.2023.03.045.

[116] P. Schilke, S. Anderssohn, K. Tziridis, K. Mantsopoulos, S. Mueller, M. Sievert, A.-O. Gostian, H. Iro, C. Bohr, and M. Traxdorf, "Phantom-based prospective analysis of the accuracy of photo registration technology in electromagnetic navigation of the frontal skull base," *Eur. Rev. Med. Pharmacol. Sci.*, vol. 26, no. 5, pp. 1674–1682, Mar. 2022, https://doi.org/10.26355/eurrev_202203_28236.

[117] D. Tho, M.-C. Lavallée, and L. Beaulieu, "Performance of an enhanced afterloader with electromagnetic tracking capabilities for channel reconstruction and error detection," *Med. Phys.*, vol. 48, no. 8, pp. 4402–4410, Aug. 2021, https://doi.org/10.1002/mp.14877.

[118] E. Lugez, H. Sadjadi, C. P. Joshi, S. G. Akl, and G. Fichtinger, "Improved electromagnetic tracking for catheter path reconstruction with application in high-dose-rate brachytherapy," *Int. J. Comput. Assist. Radiol. Surg.*, vol. 12, no. 4, pp. 681–689, Apr. 2017, https://doi.org/10.1007/s11548-017-1534-4.

[119] A. Jaiswal, J. Nenonen, and L. Parkkonen, "On electromagnetic head digitization in MEG and EEG," *Sci. Rep.*, vol. 13, no. 1, p. 3801, Mar. 2023, https://doi.org/10.1038/s41598-023-30223-9.

[120] "Kick EM Electromagnetic surgical navigation system," Accessed : 09-12-2024. [Online]. Available: https://www.brainlab.com/surgery-products/overview-platform-products/kick-em/

[121] M. Cavaliere and P. Cantillon-Murphy, "Intraoperative compensation of magnetic field distortions for fluoroscopic and electromagnetic hybrid navigation," *Int. J. Comput. Assist. Radiol. Surg.*, vol. 17, no. 9, pp. 1717–1721, Sep. 2022, https://doi.org/10.1007/s11548-022-02663-7.

[122] H. Krumb, D. Das, R. Chadda, and A. Mukhopadhyay, "CycleGAN for interpretable online EMT compensation," *Int. J. Comput. Assist. Radiol. Surg.*, vol. 16, no. 5, pp. 757–765, May 2021, https://doi.org/10.1007/s11548-021-02324-1.

[123] E. Lugez, H. Sadjadi, C. P. Joshi, K. Hashtrudi-Zaad, S. G. Akl, and G. Fichtinger, "Field distortion compensation for electromagnetic tracking of ultrasound probes with application in high-dose-rate prostate brachytherapy," *Biomed. Phys. Eng. Express*, vol. 5, no. 3, p. 035026, Apr. 2019, https://doi.org/10.1088/2057-1976/ab12b6.

[124] M. Li, C. Hansen, and G. Rose, "A software solution to dynamically reduce metallic distortions of electromagnetic tracking systems for image-guided surgery," *Int. J. Comput. Assist. Radiol. Surg.*, vol. 12, no. 9, pp. 1621–1633, Sep. 2017, https://doi.org/10.1007/s11548-017-1546-0.

[125] T. Bien, M. Li, Z. Salah, and G. Rose, "Electromagnetic tracking system with reduced distortion using quadratic excitation," *Int. J. Comput. Assist. Radiol. Surg.*, vol. 9, no. 2, pp. 323–332, Mar. 2014, https://doi.org/10.1007/s11548-013-0925-4.

[126] M. Li, C. Hansen, and G. Rose, "A Robust Electromagnetic Tracking System for Clinical Applications," in *Proceedings of the Annual Meeting of the German Society of Computer- and Robot-Assisted Surgery*, Bremen, 2015, pp. 31–36. [Online]. Available: https://www.var.ovgu.de/pub/Li_2015_CURAC.pdf

[127] B. Gleich, I. Schmale, T. Nielsen, and J. Rahmer, "Miniature magneto-mechanical resonators for wireless tracking and sensing," *Science*, vol. 380, no. 6648, pp. 966–971, Jun. 2023, https://doi.org/10.1126/science.adf5451.

[128] F. Casanova, P. R. Carney, and M. Sarntinoranont, "In vivo evaluation of needle force and friction stress during insertion at varying insertion speed into the brain," *J. Neurosci. Methods*, vol. 237, pp. 79–89, Nov. 2014, https://doi.org/10.1016/j.jneumeth.2014.08.012.

[129] V. Schlageter, P.-A. Besse, R. S. Popovic, and P. Kucera, "Tracking system with five degrees of freedom using a 2d-array of hall sensors and a permanent magnet," *Sens. Actuators A Phys.*, vol. 92, no. 1-3, pp. 37–42, Aug. 2001, https://doi.org/10.1016/S0924-4247(01)00537-4.

[130] H. Dai, W. Yang, X. Xia, S. Su, and K. Ma, "A three-axis magnetic sensor array system for permanent magnet tracking," in *2016 IEEE International Conference on Multisensor Fusion and Integration for Intelligent Systems (MFI)*. IEEE, Sep. 2016, https://doi.org/10.1109/MFI.2016.7849533.

[131] S. Song, X. Qiu, J. Wang, and M. Q.-H. Meng, "Design and optimization strategy of sensor array layout for magnetic localization system," *IEEE Sens. J.*, vol. 17, no. 6, pp. 1849–1857, Mar. 2017, https://doi.org/10.1109/JSEN.2017.2652470.

[132] N. Sebkhi, N. Sahadat, S. Hersek, A. Bhavsar, S. Siahpoushan, M. Ghoovanloo, and O. T. Inan, "A deep neural network-based permanent magnet localization for tongue tracking," *IEEE Sens. J.*, vol. 19, no. 20, pp. 9324–9331, Oct. 2019, https://doi.org/10.1109/JSEN.2019.2923585.

[133] B. Brajon, E. Gasparin, and G. Close, "A benchmark of integrated magnetometers and magnetic gradiometers," *IEEE Access*, vol. 11, pp. 115 635–115 643, 2023, https://doi.org/10.1109/ACCESS.2023.3325035.

[134] R. S. Popovic, "High resolution hall magnetic sensors," in *2014 29th International Conference on Microelectronics Proceedings - MIEL 2014*. IEEE, May 2014, https://doi.org/10.1109/MIEL.2014.6842087.

[135] S. Sharma, A. Telikicherla, G. Ding, F. Aghlmand, A. H. Talkhooncheh, M. G. Shapiro, and A. Emami, "Wireless 3D surgical navigation and tracking system with 100μm accuracy using magnetic-field gradient-based localization," *IEEE Trans. Med. Imaging*, vol. 40, no. 8, pp. 2066–2079, Aug. 2021, https://doi.org/10.1109/TMI.2021.3071120.

[136] M. A. Khan, J. Sun, B. Li, A. Przybysz, and J. Kosel, "Magnetic sensors-a review and recent technologies," *Eng. Res. Express*, vol. 3, no. 2, p. 022005, Jun. 2021, https://doi.org/10.1088/2631-8695/ac0838.

[137] J. Lenz and S. Edelstein, "Magnetic sensors and their applications," *IEEE Sens. J.*, vol. 6, no. 3, pp. 631–649, Jun. 2006, https://doi.org/10.1109/JSEN.2006.874493.

[138] Northern Digital Inc., "Aurora 5DOF 0.3x2.5 Sensor (P/N 10002320)," Accessed : 27-01-2025. [Online]. Available: https://www.ndigital.com/wp-content/uploads/2022/09/DOC-10008368-Rev001-Small-Sensors.pdf

[139] S. Sharma, H. Melton, L. Edmonds, O. Addington, M. Shapiro, and A. Emami, "A monolithic 3D magnetic sensor in 65nm CMOS with <10μT_{rms} noise and 14.8μW power," pp. 1–2, Apr. 2023, https://doi.org/10.1109/CICC57935.2023.10121313.

[140] R. S. Popovic, *Hall effect devices, second edition*, 2nd ed., ser. Series in Sensors. Boca Raton, FL: CRC Press, Dec. 2004, https://doi.org/10.1016/0250-6874(89)80063-0.

[141] W. Thomson, "XIX. on the electro-dynamic qualities of metals:—effects of magnetization on the electric conductivity of nickel and of iron," *Proc. R. Soc. Lond.*, vol. 8, no. 0, pp. 546–550, Dec. 1857, https://doi.org/10.1098/rspl.1856.0144.

[142] E. S. Oliveros Mata, G. S. Cañón Bermúdez, M. Ha, T. Kosub, Y. Zabila, J. Fassbender, and D. Makarov, "Printable anisotropic magnetoresistance sensors for highly compliant electronics," *Appl. Phys. A Mater. Sci. Process.*, vol. 127, no. 4, Apr. 2021, https://doi.org/10.1007/s00339-021-04411-1.

[143] M. N. Baibich, J. M. Broto, A. Fert, Nguyen Van Dau F, F. Petroff, P. Etienne, G. Creuzet, A. Friederich, and J. Chazelas, "Giant magnetoresistance of (001)Fe/(001)Cr magnetic superlattices," *Phys. Rev. Lett.*, vol. 61, no. 21, pp. 2472–2475, Nov. 1988, https://doi.org/10.1103/PhysRevLett.61.2472.

[144] G. Binasch, P. Grünberg, F. Saurenbach, and W. Zinn, "Enhanced magnetoresistance in layered magnetic structures with antiferromagnetic interlayer exchange," *Phys. Rev. B Condens. Matter*, vol. 39, no. 7, pp. 4828–4830, Mar. 1989, https://doi.org/10.1103/PhysRevB.39.4828.

[145] K. Wu, D. Tonini, S. Liang, R. Saha, V. K. Chugh, and J.-P. Wang, "Giant magnetoresistance biosensors in biomedical applications," *ACS Appl. Mater. Interfaces*, vol. 14, no. 8, pp. 9945–9969, Mar. 2022, https://doi.org/10.1021/acsami.1c20141.

[146] M. Julliere, "Tunneling between ferromagnetic films," *Phys. Lett. A*, vol. 54, no. 3, pp. 225–226, Sep. 1975, https://doi.org/10.1016/0375-9601(75)90174-7.

[147] T. Miyazaki and N. Tezuka, "Giant magnetic tunneling effect in Fe/Al2O3/Fe junction," *J. Magn. Magn. Mater.*, vol. 139, no. 3, pp. L231–L234, Jan. 1995, https://doi.org/10.1016/0304-8853(95)90001-2.

[148] A. Kanno, N. Nakasato, M. Oogane, K. Fujiwara, T. Nakano, T. Arimoto, H. Matsuzaki, and Y. Ando, "Scalp attached tangential magnetoencephalography using tunnel magnetoresistive sensors," *Sci. Rep.*, vol. 12, no. 1, p. 6106, Apr. 2022, https://doi.org/10.1038/s41598-022-10155-6.

[149] K. Kurashima, M. Kataoka, T. Nakano, K. Fujiwara, S. Kato, T. Nakamura, M. Yuzawa, M. Masuda, K. Ichimura, S. Okatake, Y. Moriyasu, K. Sugiyama, M. Oogane, Y. Ando, S. Kumagai, H. Matsuzaki, and H. Mochizuki, "Development of magnetocardiograph without magnetically shielded room using high-detectivity TMR sensors," *Sensors (Basel)*, vol. 23, no. 2, p. 646, Jan. 2023, https://doi.org/10.3390/s23020646.

[150] L. V. Panina and K. Mohri, "Effect of magnetic structure on giant magneto-impedance in co-rich amorphous alloys," *J. Magn. Magn. Mater.*, vol. 157-158, pp. 137–140, May 1996, https://doi.org/10.1016/0304-8853(95)01173-0.

[151] K. Mohri, T. Uchiyama, and L. V. Panina, "Recent advances of micro magnetic sensors and sensing application," *Sens. Actuators A Phys.*, vol. 59, no. 1-3, pp. 1–8, Apr. 1997, https://doi.org/10.1016/S0924-4247(97)80141-0.

[152] A. Zhukov, M. Ipatov, and V. Zhukova, "Advances in giant magnetoimpedance of materials," in *Handbook of Magnetic Materials*, ser. Handbook of magnetic materials. Elsevier, 2015, pp. 139–236, https://doi.org/10.1016/bs.hmm.2015.09.001.

[153] J. Javor, A. Stange, C. Pollock, N. Fuhr, and D. J. Bishop, "100 pt/cm single-point MEMS magnetic gradiometer from a commercial accelerometer," *Microsyst. Nanoeng.*, vol. 6, no. 1, p. 71, Aug. 2020, https://doi.org/10.1038/s41378-020-0173-z.

[154] S. B. Mbarek, N. Alcheikh, H. M. Ouakad, and M. I. Younis, "Highly sensitive low field lorentz-force MEMS magnetometer," *Sci. Rep.*, vol. 11, no. 1, p. 21634, Nov. 2021, https://doi.org/10.1038/s41598-021-01171-z.

[155] P. Ripka, "Review of fluxgate sensors," *Sens. Actuators A Phys.*, vol. 33, no. 3, pp. 129–141, Jun. 1992, https://doi.org/10.1016/0924-4247(92)80159-Z.

[156] ——, "Advances in fluxgate sensors," *Sens. Actuators A Phys.*, vol. 106, no. 1-3, pp. 8–14, Sep. 2003, https://doi.org/10.1016/s0924-4247(03)00094-3.

[157] S. Wei, X. Liao, H. Zhang, J. Pang, and Y. Zhou, "Recent progress of fluxgate magnetic sensors: Basic research and application," *Sensors (Basel)*, vol. 21, no. 4, p. 1500, Feb. 2021, https://doi.org/10.3390/s21041500.

[158] D. Hrakova, P. Ripka, and T. Kmječ, "Enhancing performance of fluxgate sensors using annealed nanocrystalline core," *IEEE Trans. Magn.*, vol. 59, no. 9, pp. 1–9, Sep. 2023, https://doi.org/10.1109/TMAG.2023.3296205.

[159] S. Angelopoulos, P. Priftis, A. Anastasopoulos, A. Ktena, and E. Hristoforou, "Design and development of a high-sensitivity, portable, and low-cost fluxgate magnetometer," *IEEE Trans. Magn.*, vol. 59, no. 2, pp. 1–8, Feb. 2023, https://doi.org/10.1109/TMAG.2022.3212585.

[160] J. Clarke and A. I. Braginski, *The SQUID handbook: Fundamentals and technology of SQUIDs and SQUID systems v. 1*, J. Clarke and A. I. Braginski, Eds. Weinheim, Germany: Wiley-VCH Verlag, Jun. 2004, https://doi.org/10.1002/9783527609956.

[161] M. I. Faley, J. Dammers, Y. V. Maslennikov, J. F. Schneiderman, D. Winkler, V. P. Koshelets, N. J. Shah, and R. E. Dunin-Borkowski, "High-T_cSQUID biomagnetometers," *Supercond. Sci. Technol.*, vol. 30, no. 8, p. 083001, Aug. 2017, https://doi.org/10.1088/1361-6668/aa73ad.

[162] The Dang Vu, T. H. Ho, S. Miyajima, M. Toji, Y. Ninomiya, H. Shishido, M. Maezawa, M. Hidaka, M. Hayashi, S. Kawamata, and T. Ishida, "SQUID microscopy for mapping vector magnetic fields," *Supercond. Sci. Technol.*, vol. 32, no. 11, p. 115006, Nov. 2019, https://doi.org/10.1088/1361-6668/ab3945.

[163] D. Budker and M. Romalis, "Optical magnetometry," *Nat. Phys.*, vol. 3, no. 4, pp. 227–234, Apr. 2007, https://doi.org/10.1038/nphys566.

[164] B. Zhao, L. Li, Y. Zhang, J. Tang, Y. Liu, and Y. Zhai, "Optically pumped magnetometers recent advances and applications in biomagnetism: A review," *IEEE Sensors Journal*, vol. 23, no. 17, pp. 18 949–18 962, 2023, https://doi.org/10.1109/JSEN.2023.3297109.

[165] S. Tanaka, T. Ohtani, and K. Hayashi, "Comparison of the performance of metal contaminant detection using an optically pumped magnetometer with an hts squid," *IEEE Transactions on Applied Superconductivity*, pp. 1–5, 2024, https://doi.org/10.1109/TASC.2024.3507748.

[166] S. Li, B. Xing, X. Fang, K. Wang, Y. Gao, Q. Wei, and B. Han, "Three-axis magnetic field measurement based on dual-pump polarization with high sensitivity and orthogonality," *Results Phys.*, vol. 49, no. 106546, p. 106546, Jun. 2023, https://doi.org/10.1016/j.rinp.2023.106546.

[167] J. M. Taylor, P. Cappellaro, L. Childress, L. Jiang, D. Budker, P. R. Hemmer, A. Yacoby, R. Walsworth, and M. D. Lukin, "High-sensitivity diamond magnetometer with nanoscale resolution," *Nat. Phys.*, vol. 4, no. 10, pp. 810–816, Oct. 2008, https://doi.org/10.1038/nphys1075.

[168] L. Rondin, J.-P. Tetienne, T. Hingant, J.-F. Roch, P. Maletinsky, and V. Jacques, "Magnetometry with nitrogen-vacancy defects in diamond," *Rep. Prog. Phys.*, vol. 77, no. 5, p. 056503, May 2014, https://doi.org/10.1088/0034-4885/77/5/056503.

[169] R. Katsumi, M. Sekino, and T. Yatsui, "Design of an ultra-sensitive and miniaturized diamond NV magnetometer based on a nanocavity structure," *Jpn. J. Appl. Phys. (2008)*, vol. 61, no. 8, p. 082004, Aug. 2022, https://doi.org/10.35848/1347-4065/ac7e10.

[170] F. M. Sturner, A. Brenneis, J. Kassel, U. Wostradowski, R. Rölver, T. Fuchs, K. Nakamura, H. Sumiya, S. Onoda, J. Isoya, and F. Jelezko, "Compact integrated magnetometer based on nitrogen-vacancy centres in diamond," *Diam. Relat. Mater.*, vol. 93, pp. 59–65, Mar. 2019, https://doi.org/10.1016/j.diamond.2019.01.008.

[171] B. Zhao, H. Guo, R. Zhao, F. Du, Z. Li, L. Wang, D. Wu, Y. Chen, J. Tang, and J. Liu, "High-sensitivity three-axis vector magnetometry using electron spin ensembles in single-crystal diamond," *IEEE Magn. Lett.*, vol. 10, pp. 1–4, 2019, https://doi.org/10.1109/LMAG.2019.2891616.

[172] AKM Semiconductor, Inc.,, "3D Magnetic Smart Switch Sensor, AK09973D, [200900045-E-00] datasheet, September. 2020." Accessed : 09-12-2024.

[173] Bosch Sensortec GmbH, "Geomagnetic sensor, BMM150, [BST-BMM150-DS001-05] datasheet, April. 2020." Accessed : 09-12-2024.

[174] AKM Semiconductor, Inc.,, "3-axis Electronic Compass, AK09919C, [200300034-E-00] datasheet, March. 2020." Accessed : 09-12-2024.

[175] MEMSIC Semiconductor Co., Ltd., "MMC5603NJ ±30 Gauss, Monolithic, High Performance, Low Cost 3-axis Magnetic Sensor, [MEMSIC MMC5603NJ Rev.B] datasheet, January. 2022." Accessed : 09-12-2024.

[176] STMicroelectronics NV, "Digital output magnetic sensor: ultra-low-power, high-performance 3-axis magnetometer, LIS3MDLTR, [DocID024204 Rev 6] datasheet, May. 2017." Accessed : 09-12-2024.

[177] AKM Semiconductor, Inc.,, "Ultrahigh precision 3-axis Electronic Magnetometer, AK09940A", [221000042-E-01] datasheet, February. 2023." Accessed : 09-12-2024.

[178] Bosch Sensortec GmbH, "3-axis magnetic sensor with high data rate, BMM350, [BST-BMM350-DS001-26] datasheet, November. 2024." Accessed : 09-12-2024.

[179] ROHM Co., Ltd., "3-Axis Digital Magnetometer IC, BM1422AGMV, [TSZ02201-0M2M0F916070-1-2] datasheet, October. 2016." Accessed : 09-12-2024.

[180] A. M. Franz, T. Haidegger, W. Birkfellner, K. Cleary, T. M. Peters, and L. Maier-Hein, "Electromagnetic tracking in medicine–a review of technology, validation, and applications," *IEEE Trans. Med. Imaging*, vol. 33, no. 8, pp. 1702–1725, Aug. 2014, https://doi.org/10.1109/TMI.2014.2321777.

[181] V. P. B. Grover, J. M. Tognarelli, M. M. E. Crossey, I. J. Cox, S. D. Taylor-Robinson, and M. J. W. McPhail, "Magnetic resonance imaging: Principles and techniques: Lessons for clinicians," *J. Clin. Exp. Hepatol.*, vol. 5, no. 3, pp. 246–255, Sep. 2015, https://doi.org/10.1016/j.jceh.2015.08.001.

[182] J. B. Kuipers, "SPASYN-an electromagnetic relative position and orientation tracking system," *IEEE Trans. Instrum. Meas.*, vol. 29, no. 4, pp. 462–466, Dec. 1980, https://doi.org/10.1109/TIM.1980.4314980.

[183] F. Raab, E. Blood, T. Steiner, and H. Jones, "Magnetic position and orientation tracking system," *IEEE Trans. Aerosp. Electron. Syst.*, vol. AES-15, no. 5, pp. 709–718, Sep. 1979, https://doi.org/10.1109/TAES.1979.308860.

[184] Northern Digital Inc., "Medical aurora-medical," Accessed: 2022-06-09. [Online]. Available: https://www.ndigital.com/electromagnetic-tracking-technology/aurora/

[185] H. Heidari and V. Nabaei, *Magnetic sensors for biomedical applications*, ser. IEEE Press Series on Sensors. New York, NY: Wiley-IEEE Press, Feb. 2020, https://doi.org/10.1002/9781119552215.

[186] https://doi.org/10.3390/s19081850.

[187] T. Quirin, C. Féry, D. Vogel, C. Vergne, M. Sarracanie, N. Salameh, M. Madec, S. Hemm, L. Hébrard, and J. Pascal, "Towards tracking of deep brain stimulation electrodes using an integrated magnetometer," *Sensors (Basel)*, vol. 21, no. 8, p. 2670, Apr. 2021, https://doi.org/10.3390/s21082670.

[188] M. Cavaliere and P. Cantillon-Murphy, "Enhancing electromagnetic tracking accuracy in medical applications using pre-trained witness sensor distortion models," *Int. J. Comput. Assist. Radiol. Surg.*, vol. 19, no. 1, pp. 27–31, Jan. 2024, https://doi.org/10.1007/s11548-023-02994-z.

[189] J. Lu, L. Zhang, and R. Maeda, "Real-time tracking of organ-shape and vessel-locations for surgical navigation using MEMS tri-axis magnetic sensors," *Med. Eng. Phys.*, vol. 93, pp. 42–48, Jul. 2021, https://doi.org/10.1016/j.medengphy.2021.05.020.

[190] T. Aziz and A. L. Green, *Deep Brain Stimulation (DBS) Applications*. MDPI, https://doi.org/10.3390/books978-3-03842-539-7.

[191] A. Macerollo, L. Zrinzo, H. Akram, T. Foltynie, and P. Limousin, "Subthalamic nucleus deep brain stimulation for parkinson's disease: current trends and future directions," *Expert Rev. Med. Devices*, vol. 17, no. 10, pp. 1063–1074, Oct. 2020, https://doi.org/10.1080/17434440.2020.1747433.

[192] M. H. Pourfar and A. Y. Mogilner, "Lead angle matters: Side effects of deep brain stimulation improved with adjustment of lead angle," *Neuromodulation*, vol. 19, no. 8, pp. 877–881, Dec. 2016, https://doi.org/10.1111/ner.12476.

[193] R. A. Holewijn, M. Bot, P. van den Munckhof, and P. R. Schuurman, "Implementation of intraoperative cone-beam computed tomography (o-arm) for stereotactic imaging during deep brain stimulation procedures," *Oper. Neurosurg. (Hagerstown)*, vol. 19, no. 3, pp. E224–E229, Sep. 2020, https://doi.org/10.1093/ons/opaa110.

[194] J. F. Schenck, "Physical interactions of static magnetic fields with living tissues," *Prog. Biophys. Mol. Biol.*, vol. 87, no. 2-3, pp. 185–204, Feb. 2005, https://doi.org/10.1016/j.pbiomolbio.2004.08.009.

[195] P. Veiceschi, D. Locatelli, A. Dario, and G. Agresta, "Frameless neuronavigation-assisted brain biopsy with electromagnetic tracking: how I do it?" *Acta Neurochir. (Wien)*, vol. 164, no. 12, pp. 3317–3322, Dec. 2022, https://doi.org/10.1007/s00701-022-05252-4.

[196] S. Boutaleb, E. Racine, O. Fillion, A. Bonillas, G. Hautvast, D. Binnekamp, and L. Beaulieu, "Performance and suitability assessment of a real-time 3D electromagnetic

needle tracking system for interstitial brachytherapy," *J. Contemp. Brachytherapy*, vol. 7, no. 4, pp. 280–289, Aug. 2015, https://doi.org/10.5114/jcb.2015.54062.

[197] E. Lugez, H. Sadjadi, D. R. Pichora, R. E. Ellis, S. G. Akl, and G. Fichtinger, "Electromagnetic tracking in surgical and interventional environments: usability study," *Int. J. Comput. Assist. Radiol. Surg.*, vol. 10, no. 3, pp. 253–262, Mar. 2015, https://doi.org/10.1007/s11548-014-1110-0.

[198] M. Cavaliere, O. McVeigh, H. A. Jaeger, S. Hinds, K. O'Donoghue, and P. Cantillon-Murphy, "Inductive sensor design for electromagnetic tracking in image guided interventions," *IEEE Sens. J.*, vol. 20, no. 15, pp. 8623–8630, Aug. 2020, https://doi.org/10.1109/JSEN.2020.2984323.

[199] R. Nagano, K. Hara, E. Kobayashi, T. Ohya, and I. Sakuma, "A pilot study on an electromagnetic tracking system using tunneling magnetoresistance (TMR) sensors applicable to a 4F catheter (1.4 mm in diameter)," *Int. J. Comput. Assist. Radiol. Surg.*, vol. 18, no. 1, pp. 17–27, Jan. 2023, https://doi.org/10.1007/s11548-022-02746-5.

[200] C. Vergne, C. Fery, T. Quirin, H. Nicolas, M. Madec, S. Hemm, and J. Pascal, "Low-field electromagnetic tracking using 3-D magnetometer for assisted surgery," *IEEE Trans. Magn.*, vol. 59, no. 2, pp. 1–5, Feb. 2023, https://doi.org/10.1109/TMAG.2022.3204918.

[201] C. Vergne, M. Morgan, G. Raphael, P. Joris, and H. Simone, "Towards a new generation of electromagnetic navigation system for deep brain stimulation," *Stereotact. Funct. Neurosurg.*, vol. 102 Suppl 1, no. Suppl. 1, pp. 94–95, Aug. 2024, https://doi.org/10.1159/000539983.

[202] T. Quirin, C. Féry, C. Vergne, M. Madec, L. Hébrard, and J. Pascal, "A magnetic tracking system featuring calibrated three-axis AMR sensors," in *Eurosensors 2023*. MDPI, p. 31, https://doi.org/10.3390/proceedings2024097031.

[203] G. Blewitt, *Basics of the GPS technique: Observation equations*, geod. appl. GPS ed., no. 10. [Online]. Available: https://nbmg.unr.edu/staff/pdfs/blewitt%20basics%20of%20gps.pdf

[204] O. Chubar, "Radia - 3D Magnetostatics Computer Code," Accessed : 09-12-2024. [Online]. Available: https://github.com/ochubar/Radia.git

[205] P. Elleaume, O. Chubar, and J. Chavanne, "Computing 3D magnetic fields from insertion devices," in *Proceedings of the 1997 Particle Accelerator Conference (Cat. No.97CH36167)*. IEEE, 2002, https://doi.org/10.1109/PAC.1997.753258.

[206] O. Chubar, P. Elleaume, and J. Chavanne, "A three-dimensional magnetostatics computer code for insertion devices," *J. Synchrotron Radiat.*, vol. 5, no. Pt 3, pp. 481–484, May 1998, https://doi.org/10.1107/S0909049597013502.

[207] M. A. Chilenski, I. C. Faust, and J. R. Walk, "eqtools: Modular, extensible, open-source, cross-machine python tools for working with magnetic equilibria," *Comput. Phys. Commun.*, vol. 210, pp. 155–162, Jan. 2017, https://doi.org/10.1016/j.cpc.2016.09.011.

[208] C. Vergne, J. Inácio, T. Quirin, D. Sargent, M. Madec, and J. Pascal, "Tracking of a magnetically navigated millirobot with a magnetic-field camera," *IEEE Sens. J.*, vol. 24, no. 6, pp. 7336–7344, Mar. 2024, https://doi.org/10.1109/JSEN.2023.3264496.

[209] C. Vergne, H. Nicolas, M. Madec, S. Hemm, R. Guzman, and J. Pascal, "Experimental assessment of the performances of an anisotropic magnetoresistive sensor after exposure to strong magnetic fields," in *2023 IEEE International Magnetic Conference - Short Papers (INTERMAG Short Papers)*. IEEE, pp. 1–2, https://doi.org/10.1109/INTERMAGShortPapers58606.2023.10228508.

[210] J. M. Schmidt, L. Buentjen, J. Kaufmann, D. Gruber, H. Treuer, A. Haghikia, and J. Voges, "Deviation of the orientation angle of directional deep brain stimulation leads quantified by intraoperative stereotactic x-ray imaging," *Neurosurg. Rev.*, vol. 45, no. 4, pp. 2975–2982, Aug. 2022, https://doi.org/10.1007/s10143-022-01801-8.

[211] K. R. Henry, M. M. Miulli, N. B. Nuzov, M. J. Nolt, J. M. Rosenow, B. Elahi, J. Pilitsis, and L. Golestanirad, "Variations in determining actual orientations of segmented deep brain stimulation leads using the DiODe algorithm: A retrospective study across different lead designs and medical institutions," *Stereotact. Funct. Neurosurg.*, vol. 101, no. 5, pp. 338–347, Sep. 2023, https://doi.org/10.1159/000531644.

[212] "IEEE Standard for Safety Levels With Respect to Human Exposure to Electromagnetic Fields, 0-3 kHz," *IEEE Std C95.6-2002*, pp. 1–64, 2002, https://doi.org/10.1109/IEEESTD.2002.94143.

[213] C. L. Ham, J. M. Engels, G. T. van de Wiel, and A. Machielsen, "Peripheral nerve stimulation during MRI: effects of high gradient amplitudes and switching rates," *J. Magn. Reson. Imaging*, vol. 7, no. 5, pp. 933–937, Sep. 1997, https://doi.org/10.1002/jmri.1880070524.

[214] Miethke, ProGAV 2.0, "proGAV 2.0 - MRI SAFETY INFORMATION," Accessed: 09-12-2024.

[215] K. Jongnarangsin, J. P. Thaker, and R. K. Thakur, "Pacemakers and magnets: an arranged marriage," *Heart Rhythm*, vol. 6, no. 10, pp. 1437–1438, Oct. 2009, https://doi.org/10.1016/j.hrthm.2009.07.032.

[216] M. Baszyński, Z. Moroń, and N. Tewel, "Electromagnetic navigation in medicine – basic issues, advantages and shortcomings, prospects of improvement," *J. Phys. Conf. Ser.*, vol. 238, p. 012056, Jul. 2010, https://doi.org/10.1088/1742-6596/238/1/012056.

[217] T. M. Peters and K. R. Cleary, *Image-Guided Interventions*, T. Peters and K. Cleary, Eds. New York, NY: Springer, Dec. 2008, https://doi.org/10.1007/978-0-387-73858-1.

[218] Z. Yaniv, E. Wilson, D. Lindisch, and K. Cleary, "Electromagnetic tracking in the clinical environment," *Med. Phys.*, vol. 36, no. 3, pp. 876–892, Mar. 2009, https://doi.org/10.1118/1.3075829.

[219] F. Poulin and L.-P. Amiot, "Interference during the use of an electromagnetic tracking system under OR conditions," *J. Biomech.*, vol. 35, no. 6, pp. 733–737, Jun. 2002, https://doi.org/10.1016/S0021-9290(02)00036-2.

[220] M. A. Nixon, B. C. McCallum, W. R. Fright, and N. B. Price, "The effects of metals and interfering fields on electromagnetic trackers," *Presence (Camb.)*, vol. 7, no. 2, pp. 204–218, Apr. 1998, https://doi.org/10.1162/105474698565587.

[221] H. Sadjadi, K. Hashtrudi-Zaad, and G. Fichtinger, "Simultaneous electromagnetic tracking and calibration for dynamic field distortion compensation," *IEEE Trans. Biomed.*

Eng., vol. 63, no. 8, pp. 1771–1781, Aug. 2016, https://doi.org/10.1109/TBME.2015.2502138.

[222] Y. Zhang, K. Wang, J. Jiang, and Q. Tan, "Research on intraoperative organ motion tracking method based on fusion of inertial and electromagnetic navigation," *IEEE Access*, vol. 9, pp. 49 069–49 081, 2021, https://doi.org/10.1109/ACCESS.2021.3068741.

[223] Brainlab AG., "ENT EM Software User Guide - Revision 1.6." Accessed : 06-01-2025. [Online]. Available: https://userguides.brainlab.com/wp-content/uploads/userguides/5839/ENT-EM-version.1.2-revision.1.6-en.pdf

[224] Medtronic Inc., "StealthStation FlexENT System Quick Reference Guide - M334577Z001DOC1 Revision C," Accessed : 06-01-2025. [Online]. Available: https://www.medtronic.com/content/dam/emanuals/st/M334577Z001DOC1_C_9736192EUSW_FlexENT_SYS_QRG_COLOR.pdf

[225] C. Vergne, M. Madec, T. Quirin, R. Guzman, S. Hemm, and J. Pascal, "Electromagnetic tracking system for position and orientation detection of deep brain stimulation electrodes during surgery," *IEEE Trans. Biomed. Eng.*, pp. 1–10, 2025, https://doi.org/10.1109/TBME.2025.3529716.

[226] Food and Drugs Administration - Department of Health and Human services, "510(k) Premarket notification - k213989 - Cranial EM System," Accessed : 06-01-2025. [Online]. Available: https://www.accessdata.fda.gov/cdrh_docs/pdf21/K213989.pdf

[227] D. Kügler, H. Krumb, J. Bredemann, I. Stenin, J. Kristin, T. Klenzner, J. Schipper, R. Schmitt, G. Sakas, and A. Mukhopadhyay, "High-precision evaluation of electromagnetic tracking," *Int. J. Comput. Assist. Radiol. Surg.*, vol. 14, no. 7, pp. 1127–1135, Jul. 2019, https://doi.org/10.1007/s11548-019-01959-5.

[228] J. Hummel, M. Figl, W. Birkfellner, M. R. Bax, R. Shahidi, C. R. Maurer, Jr, and H. Bergmann, "Evaluation of a new electromagnetic tracking system using a standardized assessment protocol," *Phys. Med. Biol.*, vol. 51, no. 10, pp. N205–10, May 2006, https://doi.org/10.1088/0031-9155/51/10/N01.

[229] B. Sirokai, M. Kiss, L. Kovács, B. Benyó, Z. Benyó, and T. Haidegger, "Best practices in electromagnetic tracking system assessment." [Online]. Available: http://hdl.handle.net/10890/4783

[230] P. Glira, N. Pfeifer, C. Briese, and C. Ressl, "A correspondence framework for als strip adjustments based on variants of the icp algorithm," pp. 275–289, Aug. 2015, https://doi.org/10.1127/pfg/2015/0270.

[231] A. Fedorov, R. Beichel, J. Kalpathy-Cramer, J. Finet, J.-C. Fillion-Robin, S. Pujol, C. Bauer, D. Jennings, F. Fennessy, M. Sonka, J. Buatti, S. Aylward, J. V. Miller, S. Pieper, and R. Kikinis, "3D slicer as an image computing platform for the quantitative imaging network," *Magn Reson Imaging*, vol. 30, no. 9, pp. 1323–1341, Jul. 2012, https://doi.org/10.1016/j.mri.2012.05.001.

[232] C. Hayhurst, P. Byrne, P. R. Eldridge, and C. L. Mallucci, "Application of electromagnetic technology to neuronavigation: a revolution in image-guided neurosurgery," *J.*

Neurosurg., vol. 111, no. 6, pp. 1179–1184, Dec. 2009, https://doi.org/10.3171/2008.12.JNS08628.

[233] A. Giamouriadis, D. Perera, A. Safdar, F. Vergani, R. Bhangoo, R. Gullan, and K. Ashkan, "Safety and accuracy of frameless electromagnetic-navigated (AXIEMTM)-guided brain lesion biopsies: a large single-unit study," *Acta Neurochir. (Wien)*, vol. 161, no. 12, pp. 2587–2593, Dec. 2019, https://doi.org/10.1007/s00701-019-04093-y.

[234] T. Takenaka, S. Toyota, H. Kuroda, M. Kobayashi, T. Kumagai, K. Mori, and T. Taki, "Freehand technique of an electromagnetic navigation system emitter to avoid interference caused by metal neurosurgical instruments," *World Neurosurg.*, vol. 118, pp. 143–147, Oct. 2018, https://doi.org/10.1016/j.wneu.2018.07.071.

[235] M. C. Metzger, A. Rafii, B. Holhweg-Majert, A. M. Pham, and B. Strong, "Comparison of 4 registration strategies for computer-aided maxillofacial surgery," *Otolaryngol. Head Neck Surg.*, vol. 137, no. 1, pp. 93–99, Jul. 2007, https://doi.org/10.1016/j.otohns.2007.02.015.

[236] S. Wolfsberger, K. Rössler, R. Regatschnig, and K. Ungersböck, "Anatomical landmarks for image registration in frameless stereotactic neuronavigation," *Neurosurg. Rev.*, vol. 25, no. 1-2, pp. 68–72, Mar. 2002, https://doi.org/10.1007/s10143-001-0201-x.

[237] R. R. Shamir, L. Joskowicz, S. Spektor, and Y. Shoshan, "Localization and registration accuracy in image guided neurosurgery: a clinical study," *Int. J. Comput. Assist. Radiol. Surg.*, vol. 4, no. 1, pp. 45–52, Jan. 2009, https://doi.org/10.1007/s11548-008-0268-8.

[238] P. A. Woerdeman, P. W. A. Willems, H. J. Noordmans, C. A. F. Tulleken, and J. W. B. van der Sprenkel, "Application accuracy in frameless image-guided neurosurgery: a comparison study of three patient-to-image registration methods," *J. Neurosurg.*, vol. 106, no. 6, pp. 1012–1016, Jun. 2007, https://doi.org/10.3171/jns.2007.106.6.1012.

[239] S. M. Hardy, C. Melroy, D. R. White, M. Dubin, and B. Senior, "A comparison of computer-aided surgery registration methods for endoscopic sinus surgery," *Am. J. Rhinol.*, vol. 20, no. 1, pp. 48–52, Jan. 2006, https://doi.org/10.1177/194589240602000110.

[240] M. A. Mongen and P. W. A. Willems, "Current accuracy of surface matching compared to adhesive markers in patient-to-image registration," *Acta Neurochir. (Wien)*, vol. 161, no. 5, pp. 865–870, May 2019, https://doi.org/10.1007/s00701-019-03867-8.

[241] P. Ballesteros-Zebadúa, O. A. García-Garduño, O. O. Galván de la Cruz, A. Arellano-Reynoso, J. M. Lárraga-Gutiérrez, and M. A. Celis, "Assessment of an image-guided neurosurgery system using a head phantom," *Br. J. Neurosurg.*, vol. 30, no. 6, pp. 606–610, Dec. 2016, https://doi.org/10.3109/02688697.2016.1173188.

[242] C. Wang, J. Hong, Z. Mao, W. Chen, B. Chen, W. Chen, X. Ye, C. Zhang, Y. Lu, Q. Liu, and J. Xu, "Frameless robot-assisted asleep centromedian thalamic nucleus deep brain stimulation surgery in patients with drug-resistant epilepsy: Technical description and short-term clinical results," *Neurol. Ther.*, vol. 12, no. 3, pp. 977–993, Jun. 2023, https://doi.org/10.1007/s40120-023-00451-2.

[243] T. D. Grauvogel, C. Becker, F. Hassepass, S. Arndt, R. Laszig, and W. Maier, "Comparison of 3D c-arm-based registration to conventional pair-point registration

regarding navigation accuracy in ENT surgery," *Otolaryngol. Head Neck Surg.*, vol. 152, no. 2, pp. 266–271, Feb. 2015, https://doi.org/10.1177/0194599814561175.

[244] L. Lin, Y. Gao, G. Chai, H. Xu, and L. Xie, "Electromagnetic navigation in craniofacial surgery based on automatic registration of dental splints," *J. Craniofac. Surg.*, vol. 31, no. 2, pp. 393–396, 2020, https://doi.org/10.1097/SCS.0000000000006038.

[245] N. Panchal, L. Mahmood, A. Retana, and R. Emery, 3rd, "Dynamic navigation for dental implant surgery," *Oral Maxillofac. Surg. Clin. North Am.*, vol. 31, no. 4, pp. 539–547, Nov. 2019, https://doi.org/10.1016/j.coms.2019.08.001.

[246] D. Venosta, Y. Sun, F. Matthews, A. L. Kruse, M. Lanzer, T. Gander, K. W. Grätz, and H.-T. Lübbers, "Evaluation of two dental registration-splint techniques for surgical navigation in cranio-maxillofacial surgery," *J. Craniomaxillofac. Surg.*, vol. 42, no. 5, pp. 448–453, Jul. 2014, https://doi.org/10.1016/j.jcms.2013.05.040.

[247] M. Hofer, E. Dittrich, C. Baumberger, M. Strauss, A. Dietz, T. Lüth, and G. Strauss, "The influence of various registration procedures upon surgical accuracy during navigated controlled petrous bone surgery," *Otolaryngol. Head Neck Surg.*, vol. 143, no. 2, pp. 258–262, Aug. 2010, https://doi.org/10.1016/j.otohns.2010.04.021.

[248] C. Y. Wu and A. Kahana, "Stereotactic navigation with a registration mask in orbital decompression surgery," *Ophthal. Plast. Reconstr. Surg.*, vol. 31, no. 6, pp. 440–444, Nov. 2015, https://doi.org/10.1097/IOP.0000000000000369.

[249] T. D. Grauvogel, P. Engelskirchen, W. Semper-Hogg, J. Grauvogel, and R. Laszig, "Navigation accuracy after automatic- and hybrid-surface registration in sinus and skull base surgery," *PLoS One*, vol. 12, no. 7, p. e0180975, Jul. 2017, https://doi.org/10.1371/journal.pone.0180975.

[250] O. Makiese, P. Pillai, A. Salma, S. Sammet, and M. Ammirati, "Accuracy validation in a cadaver model of cranial neuronavigation using a surface autoregistration mask," *Neurosurgery*, vol. 67, no. 3 Suppl Operative, pp. ons85–90; discussion ons90, Sep. 2010, https://doi.org/10.1227/01.NEU.0000383751.63835.2F.

[251] S. Sukegawa, T. Kanno, and Y. Furuki, "Application of computer-assisted navigation systems in oral and maxillofacial surgery," *Jpn. Dent. Sci. Rev.*, vol. 54, no. 3, pp. 139–149, Aug. 2018, https://doi.org/10.1016/j.jdsr.2018.03.005.

[252] A. Raabe, R. Krishnan, R. Wolff, E. Hermann, M. Zimmermann, and V. Seifert, "Laser surface scanning for patient registration in intracranial image-guided surgery," *Neurosurgery*, vol. 50, no. 4, pp. 797–801; discussion 802–3, Apr. 2002, https://doi.org/10.1097/00006123-200204000-00021.

[253] J. Schlaier, J. Warnat, and A. Brawanski, "Registration accuracy and practicability of laser-directed surface matching," *Comput. Aided Surg.*, vol. 7, no. 5, pp. 284–290, Jan. 2002, https://doi.org/10.1002/igs.10053.

[254] Y. Fan, D. Jiang, M. Wang, and Z. Song, "A new markerless patient-to-image registration method using a portable 3D scanner," *Med. Phys.*, vol. 41, no. 10, p. 101910, Oct. 2014, https://doi.org/10.1118/1.4895847.

[255] Y. Fan, X. Yao, T. Hu, and X. Xu, "An automatic spatial registration method for image-guided neurosurgery system," *J. Craniofac. Surg.*, vol. 30, no. 4, pp. e344–e350, Jun. 2019, https://doi.org/10.1097/SCS.0000000000005330.

[256] Y. Özbek, Z. Bárdosi, and W. Freysinger, "Noctopus: a novel device and method for patient registration and navigation in image-guided cranial surgery," *Int. J. Comput. Assist. Radiol. Surg.*, vol. 19, no. 12, pp. 2371–2380, Dec. 2024, https://doi.org/10.1007/s11548-024-03135-w.

[257] A. F. de Geer, S. G. Brouwer de Koning, M. J. A. van Alphen, S. van der Mierden, C. L. Zuur, F. W. B. van Leeuwen, A. J. Loeve, R. L. P. van Veen, and M. B. Karakullukcu, "Registration methods for surgical navigation of the mandible: a systematic review," *Int. J. Oral Maxillofac. Surg.*, vol. 51, no. 10, pp. 1318–1329, Oct. 2022, https://doi.org/10.1016/j.ijom.2022.01.017.

[258] R. Schreurs, F. Baan, C. Klop, L. Dubois, L. F. M. Beenen, P. E. M. H. Habets, A. G. Becking, and T. J. J. Maal, "Registration-free workflow for electromagnetic and optical navigation in orbital and craniofacial surgery," *Sci. Rep.*, vol. 11, no. 1, p. 18080, Sep. 2021, https://doi.org/10.1038/s41598-021-97706-5.

[259] D. G. E. Thiem, L. Seifert, J. Graef, B. Al-Nawas, M. Gielisch, and P. W. Kämmerer, "Marker-free registration for intraoperative navigation using the transverse palatal rugae," *Int. J. Med. Robot.*, vol. 18, no. 3, p. e2362, Jun. 2022, https://doi.org/10.1002/rcs.2362.

[260] S.-W. Bang, Y.-J. Lee, H. Kee, and S. Park, "Registration-free minimally invasive surgery without preoperative phase," *Int. J. Control Autom. Syst.*, vol. 21, no. 10, pp. 3313–3323, Oct. 2023, https://doi.org/10.1007/s12555-022-0916-8.

[261] J. Tokuda, G. S. Fischer, X. Papademetris, Z. Yaniv, L. Ibanez, P. Cheng, H. Liu, J. Blevins, J. Arata, A. J. Golby, T. Kapur, S. Pieper, E. C. Burdette, G. Fichtinger, C. M. Tempany, and N. Hata, "OpenIGTLink: an open network protocol for image-guided therapy environment," *Int. J. Med. Robot.*, vol. 5, no. 4, pp. 423–434, Dec. 2009, https://doi.org/10.1002/rcs.274.

[262] T. Morishita, J. D. Hilliard, M. S. Okun, D. Neal, K. A. Nestor, D. Peace, A. A. Hozouri, M. R. Davidson, F. J. Bova, J. M. Sporrer, G. Oyama, and K. D. Foote, "Postoperative lead migration in deep brain stimulation surgery: Incidence, risk factors, and clinical impact," *PLoS One*, vol. 12, no. 9, p. e0183711, Sep. 2017, https://doi.org/10.1371/journal.pone.0183711.

[263] T. A. Dembek, M. Hoevels, A. Hellerbach, A. Horn, J. N. Petry-Schmelzer, J. Borggrefe, J. Wirths, H. S. Dafsari, M. T. Barbe, V. Visser-Vandewalle, and H. Treuer, "Directional DBS leads show large deviations from their intended implantation orientation," *Parkinsonism Relat. Disord.*, vol. 67, pp. 117–121, Oct. 2019, https://doi.org/10.1002/mds.27093.

[264] M. Kim, N. Y. Jung, and J. W. Chang, "Image analysis of the intracranial lead bending phenomenon during deep brain stimulation," *PLoS One*, vol. 15, no. 8, p. e0237537, Aug. 2020, https://doi.org/10.1371/journal.pone.0237537.

[265] D. F. He and M. Shiwa, "An anisotropic magneto resistive sensor with set/reset field," *Rev. Sci. Instrum.*, vol. 82, no. 9, p. 094703, Sep. 2011, https://doi.org/10.1063/1.3640412.

[266] International Commission on Non-Ionizing Radiation Protection (ICNIRP), "Guidelines for limiting exposure to time-varying electric and magnetic fields (1 hz to 100 khz)," *Health Phys.*, vol. 99, no. 6, pp. 818–836, Dec. 2010, https://doi.org/10.1097/HP.0b013e3181f06c86.

[267] J. Patrick Reilly, "Human exposure standards in the frequency range 1 hz to 100 khz," *Health Phys.*, vol. 107, no. 4, pp. 343–350, Oct. 2014, https://doi.org/10.1097/HP.0000000000000112.

[268] H. Nicolas, T. Quirin, and J. Pascal, "FPGA-based magnetic field camera for dynamic magnetic field mapping," *IEEE Sens. Lett.*, vol. 8, no. 5, pp. 1–4, May 2024, https://doi.org/10.1109/LSENS.2024.3389099.

[269] M. A. Ragolia, G. Andria, F. Attivissimo, A. D. Nisio, A. Maria Lucia Lanzolla, M. Spadavecchia, P. Larizza, and G. Brunetti, "Performance analysis of an electromagnetic tracking system for surgical navigation," in *2019 IEEE International Symposium on Medical Measurements and Applications (MeMeA)*. IEEE, Jun. 2019, https://doi.org/10.1109/MeMeA.2019.8802220.

[270] J. C. Allred, R. N. Lyman, T. W. Kornack, and M. V. Romalis, "High-sensitivity atomic magnetometer unaffected by spin-exchange relaxation," *Phys. Rev. Lett.*, vol. 89, no. 13, p. 130801, Sep. 2002, https://doi.org/10.1103/PhysRevLett.89.130801.

[271] J. R. Corea, A. M. Flynn, B. Lechêne, G. Scott, G. D. Reed, P. J. Shin, M. Lustig, and A. C. Arias, "Screen-printed flexible MRI receive coils," *Nat. Commun.*, vol. 7, no. 1, p. 10839, Mar. 2016, https://doi.org/10.1038/ncomms10839.

[272] QuSpin, Inc., "QTFM gen-2 operation," Accessed : 09-12-2024. [Online]. Available: https://quspin.com/qtfm-gen-2-operation/

[273] V. Schultze, T. Scholtes, G. Oelsner, F. Wittkaemper, T. Wieduwilt, and R. Stolz, "An optically pumped magnetometer with omnidirectional magnetic field sensitivity," *Sensors (Basel)*, vol. 23, no. 15, p. 6866, Aug. 2023, https://doi.org/10.3390/s23156866.

APPENDIX A

Investigation on the coils arrangement and tracking performance based on machine learning approaches

Foreword and Overview

This appendix examines how the number of coils comprising the FG affects the tracking performance. Additionally, machine learning techniques such as K-Nearest Neighbor, Random Forest, and Gradient Boosting Regression were evaluated for position determination within the MV. However, the full
exploration of these methods is not comprehensively detailed in this appendix. Conducted prior to **Publication II**, this study contributed to the design choices of the ManaDBS FG.

Contribution: The candidate was responsible for simulating the magnetic fields. Based on these simulations, Prof. Madec and members of the Gaia platform at the University of Strasbourg proposed machine learning approaches for position determination. The results were generated by Prof. Madec and discussed collaboratively with the candidate. The candidate was responsible for the measurement leading to the experimental dataset the magnetic fields.

Introduction

To enhance both the accuracy and precision of a quasi-static electromagnetic tracking system like ManaDBS, further improvements are essential. One key limitation of quasi-static EMT systems is the performance dependency on the distance to the FG. Additionally, tracking performance is influenced by the relative placement of sensors with respect to the FG surface. Stronger field gradients are generated near the center of the FG, resulting in better performances. In contrast, the peripheral regions of the MV exhibit weaker gradients, leading to reduced performance. This inhomogeneity in performance is primarily linked to the coil arrangement.
Optimizing the coil arrangement offers a potential solution. The current ManaDBS FG design includes four coils to ensure the presence of at least three significant gradients at any point within the MV. Increasing the number of coils could provide additional field data and, by weighting each coil's contribution based on the region and associated gradients, minimize positional errors. However, this could also reduce the system's sampling frequency due to the need for sequential activation of more coils.
Alternatively, enlarging the coils while maintaining a similar MV could reduce regions with low gradients. However, this modification is constrained by the spatial limitations of the surgical environment. Another approach to improve signal-to-noise ratio is to increase the current amplitude injected into the coils, thereby generating stronger magnetic fields. However, this method would significantly raise power consumption and cause greater coil heating during activation, which may introduce additional challenges.

Methods

This study explores among others the influence of the number of coils in the FG on tracking performance. The coil model used in this analysis corresponds to the three-coil arrangement of the FG described in **Publication I**.
Simulations were conducted for arrangements ranging from three to nine coils (Fig. A.1), with the resulting static magnetic fields computed using the magnetostatic library Radia, developed for Wolfram Mathematica 12.3 [206]. A volume of 400 mm × 400 mm × 320 mm, discretized with a 16 mm × 16 mm × 18 mm pitch, was analyzed for each coil configuration. This produced a dataset of 10,816 points, with corresponding magnetic field values (26 points along the X- and Y-axis and 16 points along the Z-axis), which were saved in a CSV file for further analysis.

The following investigations were performed using this dataset:

- ❉ **Machine learning approaches:** Three algorithms were selected and evaluated using simulated data for a three-coil arrangement: K-Nearest Neighbor (KNN), Random Forest (RF), and Gradient Boosting Regression (GB). The associated hyperparameters for each were also analyzed.

- ❉ **Impact of the numbers of coils on the algorithm performance:** Based on the optimal

parameters, the dataset for different coil arrangements were trained and tested to simulate the tracking performance of the EMT system.

❉ **Impact of the noise on the algorithm performance:** The noise of the measuring sensor should be considered to get closer to the real tracking performance.

❉ **Impact of the data reduction in the algorithm performance:** Reduction of the numbers of dataset points used to train the machine learning algorithm.

❉ **Validation on experimental data:** Validation of the machine learning methods was performed on the experimental dataset, based on the approaches explored for the simulated dataset. The number of dataset points used to train the machine learning algorithm was reduced.

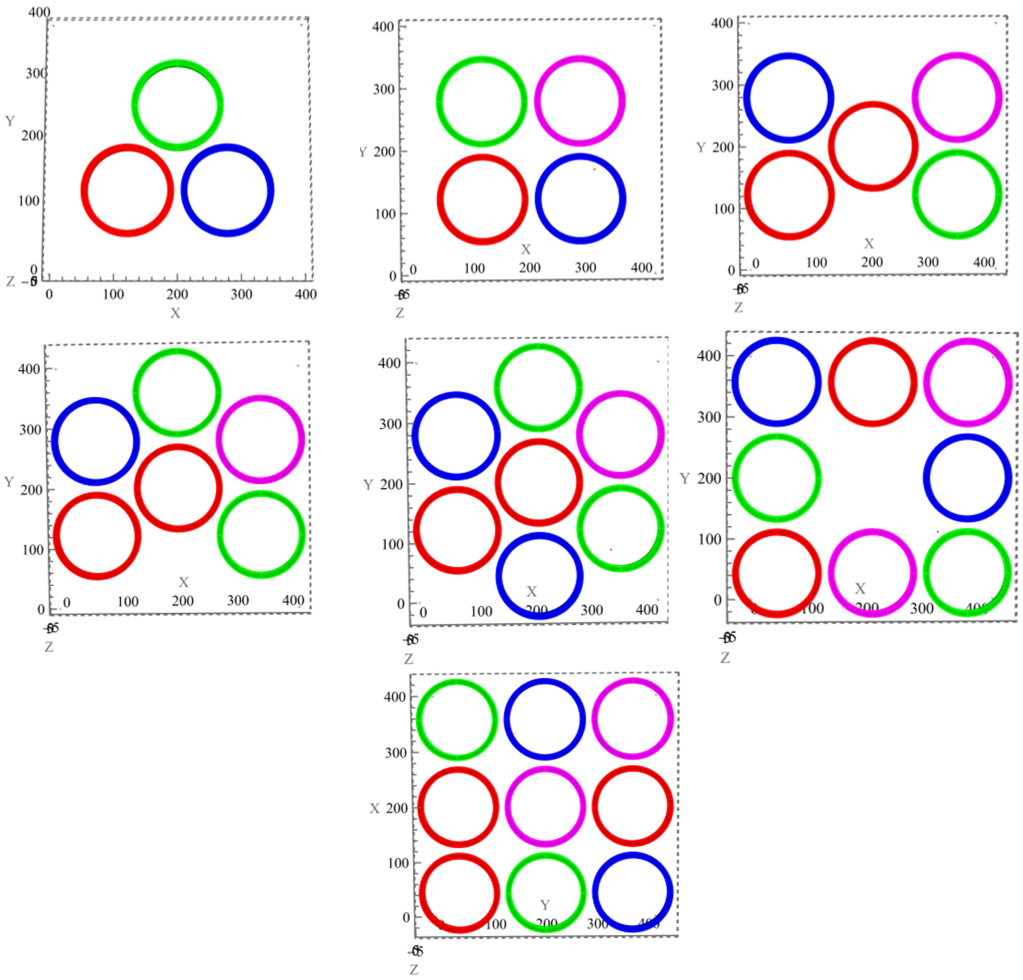

Figure A.1: Different coil arrangements from three to nine coils.

Results

Machine learning approaches

In machine learning, metaparameters (commonly referred to as hyperparameters) are predefined configuration settings that determine the behavior, structure, or training process of a machine learning model. Unlike model parameters (such as weights and biases in neural networks) that are learned and updated during the training process, hyperparameters remain fixed throughout training and are set prior to the start of the learning process. Hyperparameters play a crucial role in shaping the performance and efficiency of a model. They can be broadly categorized into two types:

❉ **Model-Specific Hyperparameters:** These define the architecture or structure of the model. Examples include the number of layers and neurons in a neural network, the kernel type in a support vector machine, or the maximum depth of a decision tree.

❉ **Training Process Hyperparameters:** This influence how the model is trained, such as the learning rate, batch size or number of training epochs.

Choosing appropriate hyperparameter values is critical, as they significantly impact the model's ability to generalize and avoid overfitting or underfitting. optimization or genetic algorithms. The following hyperparameters were investigated:

❉ **KNN:** [3, 5, 9] neighbors (N)

❉ **RF:** [50, 500] estimators (NE) and [1, 3, 5, 15] minimum number of sample per leaf (MSL)

❉ **GB:** [5000, 50000] estimators (NE), [5, 15] MSL and [0.1, 0.3] learning rate (LR)

To compare the results, we used three key metrics: the Root Mean Square Error (RMSE), the Mean Absolute Error (MAE), and the Maximal Error (ME). These metrics were calculated separately for each coordinate and applied to both the training dataset and the test (or verification) dataset. The RMSE provides a measure of the average magnitude of the prediction errors, giving more weight to larger errors. The MAE represents the average absolute difference between predicted and actual values. The ME indicates the largest deviation observed, highlighting the worst-case performance of the model. By comparing these metrics across the training and validation datasets, we can assess the degree of overfitting induced by the chosen hyperparameters. Overfitting occurs when the model performs significantly better on the training data than on the validation data. A smaller discrepancy between the metrics for the two datasets suggests that the model generalizes well, while a larger discrepancy indicates potential overfitting. Ensuring that RMSE, MAE, and ME values are closely aligned for both datasets is a key indicator of a robust and well-regularized model.
Tables A.1, A.2 and A.3 presents the results after training of the three machine learning methods with unoptimized parameters. This investigation was performed only using the three-coil configuration.

Table A.1: Results obtained on the three-coil configuration with KNN method for N=3.

Metrics	$X_{training}$	$Y_{training}$	$Z_{training}$	X_{test}	Y_{test}	Z_{test}
RMSE [mm]	8.6	8.0	10.5	12.4	11.1	15.4
MAE [mm]	6.0	5.3	5.9	9.0	7.9	9.2
ME [mm]	48	42	78	58	64	102

Table A.2: Results obtained on the three-coil configuration with RF method for NE=50 and MSL=15.

Metrics	$X_{training}$	$Y_{training}$	$Z_{training}$	X_{test}	Y_{test}	Z_{test}
RMSE [mm]	3.9	4.1	5.6	6.2	6.2	8.8
MAE [mm]	2.9	3.0	3.8	4.2	4.3	5.9
ME [mm]	51	83	40	145	148	58

Table A.3: Results obtained on the three-coil configuration with GB method for NE=50000, MSL=15 and a LR=0.1.

Metrics	$X_{training}$	$Y_{training}$	$Z_{training}$	X_{test}	Y_{test}	Z_{test}
RMSE [mm]	1.0	0.8	0.9	3.4	3.4	4.6
MAE [mm]	0.6	0.5	0.6	2.2	2.3	3.2
ME [mm]	10	7	13	42	61	34

For the KNN method, increasing of the number of neighbors did not affect the results.
For the RF method, increasing the number of estimators (NE) beyond 50 shows no additional improvement. The accuracy gain between 10 and 50 estimators is approximately 25%. Reducing the MSL improves accuracy but also increases the risk of overfitting.
Overall, the GB method outperformed both RF and KNN methods. Increasing the NE improved performance, with 500 estimators being the minimum required for acceptable results. To mitigate overfitting, the MSL was initially increased to 15, and the LR was reduced to 10%. However, while increasing the NE to 50,000 significantly improved overall performance, it also resulted in considerable overfitting.

Impact of the numbers of coils

The three methods were applied to dataset from different coils arrangement. Two metrics were compared: the MAE on the training and test dataset as well as the Score defined as the ratio of points of the test dataset for which the accuracy is better than 10 mm.
For the KNN method, the MAE decreased by an average of 25% when increasing from three to four coils (Table A.4. While adding more coils improved accuracy along the Z-axis, it had little effect on the X- and Y-axis. Additionally, accuracy diminished as the number of neighbors increased.
For the RF method, increasing the number of coils slightly reduces the MAE on the X- and

Y-axis, with a more pronounced improvement on the Z axis. Increasing the NE from 50 to 500 has a minimal impact on the results. Reducing the MSL from 15 to 5 enhances performance but also increases overfitting. With MSL set to 5, the effect of increasing the number of estimators becomes more significant. The combination of MSL = 3 and NE = 500 yields the best results on the test dataset (Table A.5), but overfitting becomes notable, with the MAE increasing by more than 50% between the training and test datasets.
Using MSL = 1 and NE = 500 produces even better results, but overfitting is severe, as the MAE rises by 200% between the training and test datasets.

Table A.4: Results obtained on different coil configurations with KNN method for N=3.

Coils	$X_{training}$	$Y_{training}$	$Z_{training}$	X_{test}	Y_{test}	Z_{test}	Score (%)
3	5.98	5.33	5.91	9.04	7.93	9.23	33.10
4	4.87	4.83	3.57	7.37	7.20	5.74	44.25
5	4.32	4.74	2.48	6.97	7.34	4.37	49.98
6	3.99	4.34	1.88	6.16	6.54	3.34	57.47
7	3.75	4.15	1.33	5.20	5.83	2.24	64.16
8	4.04	3.97	0.49	5.97	6.03	0.81	56.83
9	3.51	3.49	0.16	5.00	5.13	0.35	64.78

Table A.5: Results obtained on different coil configurations with RF method for NE=50 and MSL=15.

Coils	$X_{training}$	$Y_{training}$	$Z_{training}$	X_{test}	Y_{test}	Z_{test}	Score (%)
3	2.60	2.65	3.58	3.89	3.93	5.75	71.03
4	2.07	2.07	2.82	3.14	3.07	4.55	75.96
5	2.26	2.81	2.96	3.20	4.64	4.97	69.80
6	2.45	2.70	2.85	3.55	4.30	4.77	69.18
7	2.17	2.21	2.55	3.25	3.37	4.15	75.38
8	2.09	2.08	2.36	2.95	2.96	3.68	76.49
9	2.09	2.09	2.30	2.98	2.97	3.55	76.64

For the GB method, using four coils instead of three improves accuracy by approximately 30% (Table A.6). While accuracy generally increases with the number of coils, this improvement is primarily observed along the Z-axis. For the X- and Y-axis, accuracy remains similar between 4 and 7 coils but improves again when the number of coils exceeds eight. Interestingly, the results for the Y-axis with five coils are somewhat unexpected. Given the symmetry of the system with five coils, comparable performance on the X- and Y-axis would be anticipated, but this is not reflected in the results.
Increasing the NE from 5,000 to 50,000 enhances accuracy by approximately 30%. Reducing the MSL from 15 to 5 does not significantly affect the results. Similarly, increasing the LR from 10% to 30% yields no substantial change in performance.

Table A.6: Results obtained on different coil configurations with GB method for NE=5000, MSL=15 and LR=0.3.

Coils	$X_{training}$	$Y_{training}$	$Z_{training}$	X_{test}	Y_{test}	Z_{test}	Score (%)
3	1.42	1.37	1.46	2.93	3.12	4.02	83.30
4	0.84	0.86	0.83	2.34	2.39	2.82	94.27
5	0.86	1.21	0.74	2.75	3.84	2.84	85.89
6	0.80	0.91	0.59	2.89	3.30	2.79	89.21
7	0.78	0.42	0.51	3.00	1.71	2.50	94.08
8	0.56	0.55	0.44	2.09	2.05	2.20	97.29
9	0.41	0.41	0.36	1.91	1.92	2.19	97.44

Impact of the noise

Noise was added to the simulated data to reflect rms noise of the sensor, and quantization was applied based on the sensor's specifications. The values for noise and quantization were derived from the MMC5306NJ datasheet, which specifies a resolution of 6.25 nT/LSB and a rms noise of approximately 250 nT.
It is important to note that in practice the magnetic field for each data point represents the difference between the magnetic field measured with one coil activated and the background field measured with all coils deactivated. As a result, the effective noise value corresponds to the sensor's noise multiplied by the square root of 2.

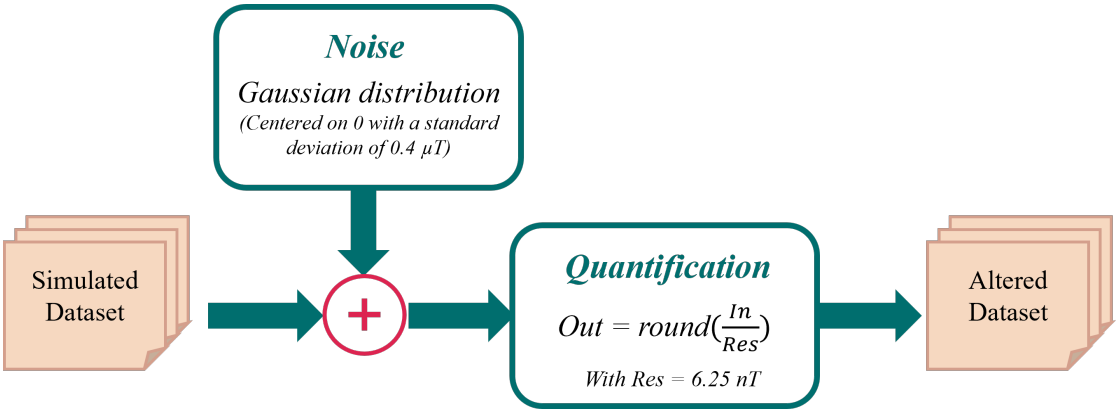

Figure A.2: Alteration methods applied on the simulated dataset including noise generation and quantification.

With the 20-bit AMR sensor, its high resolution and low noise result in a reduced impact from alterations. For example, using the KNN method, results show only about a 5% degradation. Similarly, the RF method (NE = 500, MSL = 5) and the GB method (NE = 5000, MSL = 15, LR = 0.1) exhibit approximately a 10% degradation, but this effect diminishes as the number of coils increases.

Using the GB method, increasing the NE improved performance on simulated data. However, with altered data, a higher NE amplified overfitting without improving prediction. Noise had a significantly greater impact, reducing accuracy by 30% compared to results from simulated data. To mitigate overfitting with the GB method, we reduced the LR. The configuration of NE = 50000, MSL = 15, and LR = 0.01 struck a good balance between accuracy and overfitting (Table A.7).
Increasing the number of coils from three to four resulted in an average accuracy gain of 10% across all three axes. From four to five coils, accuracy improved by 20% along the X-axis but worsened along the X- and Z-axis, leading to a lower overall score. This raises questions about the asymmetry in our results, given that the problem itself is symmetric, and whether the order of X, Y, and Z processing influences outcomes.

Table A.7: Results obtained on different coil configurations with GB method for NE=50000, MSL=15 and LR=0.01 on altered dataset.

Coils	$X_{training}$	$Y_{training}$	$Z_{training}$	X_{test}	Y_{test}	Z_{test}	Score (%)
3	1.46	1.51	2.16	2.85	3.04	4.33	83.51
4	1.10	1.11	1.18	2.46	2.50	2.63	93.47

Impact of the data reduction

By reducing the number of input data, we aimed to identify any potential decrease in performance. This approach helps determine the minimum amount of information required, particularly when planning to acquire experimental data.
Five data reductions were tested and summarized in Table A.8. The name of each dataset consists of three numbers, each representing the reduction applied along one spatial direction. For example, "112" indicates that every other data point is selected along the Z-axis, while all available data points are included in the X-Y plane.

Table A.8: Data reduction along each axis for the simulated data.

Dataset	Points along X	Points along Y	Points along Z	Numbers of points
*Simulated dataset	26	26	16	10816
112	26	26	8	5408
211	13	26	16	5408
221	13	13	16	2704
222	13	13	8	1352

⋆ *ABC : reduction of A along X-axis, B along Y-axis and C along Z-axis*

For the RF method, efficiency drops from 63% to 35% or 32% when the number of points is halved and further declines to 10% when the number of points is reduced to a quarter.
For the GB method, the efficiency decrease is moderate when using 50% or 25% of the points. However, below this threshold, the reduction in efficiency becomes substantial.

Validation on experimental data

Experimental data were acquired using a MFC employing a magnetoresistive sensors, LIS3MDL from ST electronics. These magnetometers exhibit a sensitivity of 14.6 nT and a rms noise of about 400 nT. A volume of 24 cm x 10.2 cm x 14.4 cm was mapped with a pitch of 4 mm along X- and Y-axis, and 3 mm along Z-axis. For each position 25 sensors readings were average. The mapping counted 146462 positions and associated magnetic fields. The FG employed for the mapping was the FG presented in **Publication I** with a configuration of three-coil.

Two algorithms have been tested including the RF method with a NE=500 and MSL=5 and a GB method with NE=5000, MSL=15 and LR=0.1. Results are presented in Table A.9. The algorithms are performing effectively and do not show any signs of overfitting.

Table A.9: Validation of the RF (NE=500,MSL=5) and GB (NE=5000, MSL=15,LR=0.1) methods on experimental data.

Method	$X_{training}$	$Y_{training}$	$Z_{training}$	X_{test}	Y_{test}	Z_{test}	Score (%)
RF	1.6	1.3	2.6	2.1	1.6	3.6	99.72
GB	1.9	1.4	4.0	2.1	1.5	4.5	87.90

Data reduction was also investigated using experimental data. Seven data reductions were tested and summarized in Table A.10. Results show that a mapping with about 20000-point mapping is enough to obtain acceptable results. for both Rf and GB methods. The results using RF methods were presented in Table A.11.

Table A.10: Data reduction along each axis for the experimental data.

Dataset	Points along X	Points along Y	Points along Z	Numbers of points
Simulated dataset	61	49	49	146461
211	31	49	49	74431
112	61	49	25	74725
221	31	25	49	37975
222	31	25	25	19375
333	21	17	17	6069
444	16	13	13	2704
666	11	9	9	891

Table A.11: Data reduction impact on experimental data.

Reduction	$X_{training}$	$Y_{training}$	$Z_{training}$	X_{test}	Y_{test}	Z_{test}	Score (%)
112	1.5	1.4	2.9	2.1	1.8	4.1	99.79
211	1.6	1.4	2.7	2.2	1.9	3.8	99.59
221	1.9	1.8	3.1	2.5	2.3	4.4	99.17
222	2.2	2.1	3.8	2.8	2.7	5.1	98.54
333	2.8	3.0	5.2	3.6	3.7	6.8	93.57
444	3.9	4.4	6.9	5.1	5.4	8.6	77.68
666	6.5	8.0	1.0	8.1	9.7	15.2	44.57

Discussion

This study highlights the potential of the GB method for improving the performance of a quasi-static electromagnetic tracking system. By tuning key parameters such as the NE, MSL, and LR, it is possible to achieve notable improvements in accuracy. However, these adjustments come at the cost of increased overfitting. For example, using 50,000 estimators and reducing the learning rate to 1% yields the best results, with a MAE of 2.5–3 mm for noisy data when employing three coils. Despite the increase in overfitting, the accuracy gains justify these parameter optimizations for specific use cases.
The findings also confirm that increasing the number of coils positively impacts accuracy, with the most significant improvement observed when transitioning from three to four coils. Beyond five coils, the improvement becomes marginal. This suggests that while additional coils contribute to greater accuracy, there is a point of diminishing returns that should be considered during system design.

Regarding sensor selection, the algorithm is evident that Hall effect sensors lack the precision required for effective mapping, making high-sensitivity magnetometers essential for this application (data not presented). The computational demands of the GB method are manageable, even with a large number of estimators (data not presented). The training phase takes several minutes, but prediction for a single point is achieved within approximately one millisecond, meeting the real-time requirements of this application.

The study also reveals that reducing the dataset size decreases accuracy and exacerbates overfitting, particularly in sparse datasets. Fine-tuning algorithm parameters becomes essential in such scenarios to balance accuracy and overfitting. However, some results remain difficult to explain, such as the inconsistent MAE observed on the X- and Y-axis, despite the problem's inherent symmetry. This discrepancy persists across both training and verification datasets and requires further investigation. Potential causes could include coding errors or the algorithm's sequential handling of the X-, Y-, and Z-axis predictions. Future work will involve verifying data symmetry in the input files and systematically testing potential sources of these anomalies.

Experimental mapping results corroborate the trends observed in simulation. A dataset comprising a minimum of 20,000 points is sufficient to achieve an accuracy of approximately 3 mm for the X- and Y-axis and 5 mm for the Z-axis, with fewer than 2% of points exhibiting an error exceeding 10 mm. Additionally, the experimental results show slight differences in performance along the axes, with the Y-axis displaying slightly higher accuracy than the X-axis, unlike in simulation. This discrepancy could be attributed to the lack of symmetry in the experimental setup.
In general, the Z-axis consistently shows greater inaccuracies compared to the X- and Y-axis, with error margins roughly twice as large. This can be partially explained by the smaller pitch between consecutive Z-planes in the dataset, which likely contributes to reduced accuracy. Future efforts should focus on optimizing Z-axis performance, as it represents the primary limitation in achieving uniform accuracy across all dimensions.

Conclusion

The study assessed the performance of machine learning algorithms, the impact of coil configurations, and the effect of dataset depletion on the localization accuracy in an electromagnetic tracking (EMT) system.

- **Best Machine Learning Algorithm:** Among the evaluated algorithms, GB demonstrated the most promising results, particularly when parameters such as the number of estimators, learning rate, and minimum samples per leaf were fine-tuned. Although GB provided the best accuracy, increasing the number of estimators beyond a certain point led to overfitting, highlighting the need for careful parameter optimization.

- **Optimal Number of Coils:** The number of coils in the field generator significantly influenced the tracking performance. The transition from three to four coils yielded the most substantial improvement in accuracy, while additional coils beyond four provided limited improvements. This suggests that four coils offer an optimal balance between performance and complexity.

- **Impact of Dataset Depletion:** Reducing the dataset size negatively affected both accuracy and overfitting across all machine learning models. Algorithms struggled to maintain robust performance with sparse data, emphasizing the importance of comprehensive datasets for training and validation to achieve reliable tracking accuracy. A dataset comprising a minimum of 20,000 points seems sufficient to achieve an accuracy of approximately 3 mm.

These findings offer valuable insights for improving EMT system design and performance, guiding future efforts to enhance localization accuracy and robustness in real-world applications. However, continued efforts are necessary to address challenges such as overfitting, axis-specific discrepancies, and Z-axis inaccuracies.

APPENDIX B

Evaluation of the EMT systems compatibility to DBS surgical tools

Foreword and Overview

This appendix examines the performance accuracy of EMT systems in the presence of various distortion sources. These sources were selected based on observations and feedback from clinical teams involved in DBS surgery. The study compares the performance of the ManaDBS system and a commercial system (ND Aurora) under these distortion conditions. This study is complementary to **Publication III**.

Contribution: The candidate was overall responsible for the design of the study. The candidate performed the measurement and analysis.

Introduction

Despite its potential, EMT technology has limitations that affect its clinical application. One inherent limitation arises from the technology's sensitivity to electromagnetic (EM) distortions caused by the proximity of medical diagnostic devices like CT or MRI scanners [5], as well as ferromagnetic objects [6]. These issues accentuate the need for ongoing advancements to enhance EMT's robustness and adaptability in clinical settings. Typical EMT systems consist of a FG producing an alternating magnetic field and specific magnetic sensors, called miniaturized coils. The EMT systems based on miniaturized coils provide high-accuracy localization and have been used in many clinical applications. However, the use of alternating magnetic fields leads to additional EM distortions. Indeed, in addition to the main sources of distortions – i.e., ferromagnetic and/or metallic materials and electronic devices – the Eddy currents induced by alternating magnetic fields in conductors lead to a secondary EM field disturbing the primary magnetic field. To assess the significance of induced distortions, factors such as the size, composition, proximity, and shape of objects must be taken into account. Therefore, it is essential to identify distortion sources relevant to DBS surgery and evaluate their impact on the performance of EMT tracking systems.

Materials

The source of distortions were chosen in accordance with observations and feedback provided by the clinical teams from the University Hospital of Basel (Switzerland) and the University Hospital of Clermont-Ferrand (France). The following surgical instruments were included in the study (Fig. B.1): Needle holder, Skin retractor, Scalpel, MicroTargeting Drive system (FHC, Bowdoin, USA), DBS electrode (Model 3389 ,Medtronic Inc., Minneapolis, USA), Insertion stylet for the DBS electrode (Medtronic Inc.), Guide tube for the DBS electrode (Medtronic Inc.), and a MER electrode (LeadPoint, Medtronic Inc.).

Magnetic footprints of the surgical tools

The intrinsic magnetic field of each instrument was measured with a magnetic field camera, HallinSight magnetic field camera (from Metrolab Technology SA, Plan-les-Ouates, Switzerland). This magnetic field camera consists of a 2D arrays of 32 × 32 sensors measuring the magnetic field from several microteslas (μT) up to two teslas (T). The sensing area of 8 x 8 cm^2 captures the magnetic footprint of the selected instruments. For longer instruments, two to three acquisitions were combined. Initially, a baseline acquisition without the instrument on the sensing area was conducted. This baseline acquisition was then subtracted from the acquisition with the instrument, effectively eliminating the magnetic field from the environment, including the Earth's magnetic field. The sensing elements of the MFC are located 2.5 mm beneath the surface of the MFC package, where the tools were positioned. The insertion stylet, guide tube, and DBS electrode were not detected by the HallinSight camera, suggesting that they either do not generate any magnetic fields or generate magnetic fields of less than 5 μT. The magnetic footprints of the other objects are depicted in Figure B.2. The

MicroTargeting drive produces the strongest magnetic field, peaking at approximately 1.1 mT. Notably, the microelectrode generates a moderate magnetic field of around 150 μT at its tip.

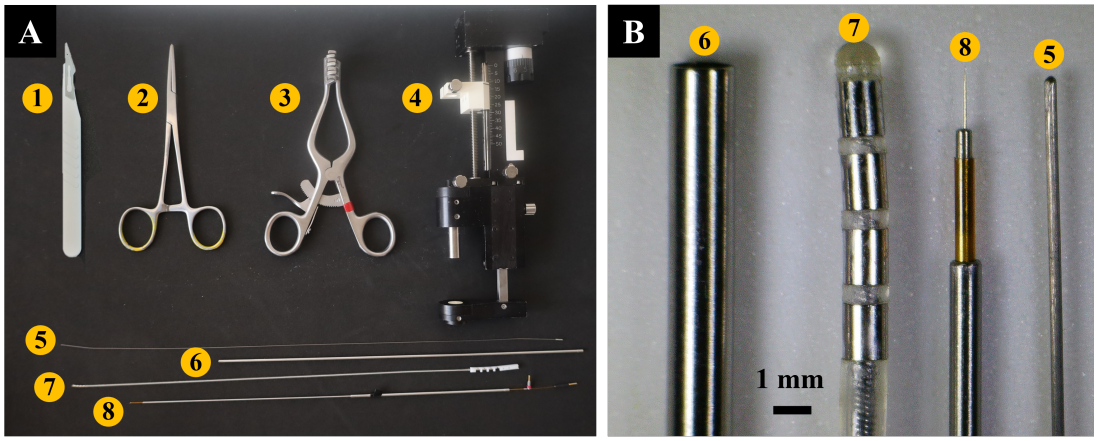

Figure B.1: Surgical tools used as source of distortions: A) Picture of the different sources of distortions tested: (1) Scalpel, (2) Needle holder, (3) Skin retractor, (4) MicroTargeting Drive, (5) Insertion stylet for the DBS electrode, (6) Guide tube for the DBS electrode, (7) DBS electrode and (8) Microelectrode within its cannula.
Zoom on the small surgical instruments such as the MER electrode, DBS electrode and its associated guide and stylet.

Electromagnetic tracking systems

❉ **NDI Aurora:** The commercial EMT system considered in this paper is the Aurora V2 Planar Field Generator (FG) from Northern Digital Inc.(Waterloo, Canada). The FG, with dimensions of 20 × 20 × 7 cm, generates an alternating magnetic field within a tracking volume of 50 × 50 × 50 cm^3. NDI reports localization errors of 0.5 mm and 0.3° at the center of the tracking volume with an update rate of 40 Hz. A flextube of 1.3 mm diameter, containing a standard six degrees-of-freedom (DOF) sensor (610060 from NDI) was used as the tracking tool in the two evaluative studies. All tracking data (positions and orientations) were recorded and managed via the NDI ToolBox software.

❉ **ManaDBS:** Our system sequentially generates four static magnetic fields using four identical coils. The position and orientation information are extracted from this sequence, resulting in an update rate of 0.4 Hz. A 4mm-carbon tube integrating a magnetic sensor at its tip was used in this study. The magnetometer is an anisotropic magnetoresistive three-axis sensor (MMC5603NJ, Memsic Semiconductor Co.). The technological principle of the ManaDBS system and its characterization are presented in **Publication II**, which reported an average error of 1.72 mm and 0.89° within a tracking volume of 15 × 15 × 30 cm^3.

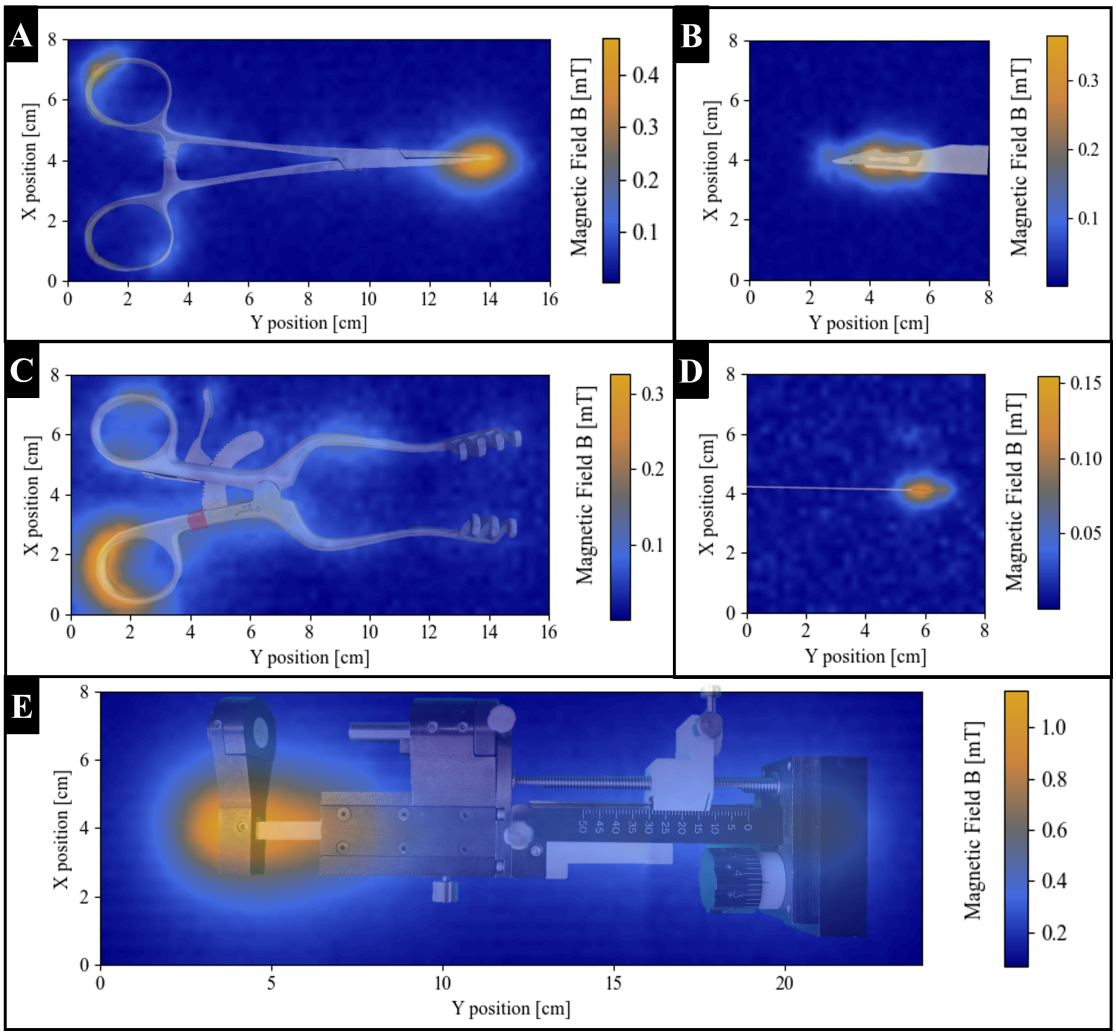

Figure B.2: Magnetic footprints of different sources of distortions measured with the commercial MFC, HallinSight: (A) Skin retractor, (B) Scalpel, (c) Needle holder, (D) MER electrode and (E) MicroTargeting Drive.

Methods

Each sensor was positioned at a fixed location in the center of the MV. Localization was performed twice: initially without any instrument and then with the instrument placed at varying distances from 80 mm to 2 mm from the sensor (Fig. B.3). For each position, 25 measurements were recorded. The part of the instrument generating the strongest magnetic field or the most likely to be in close proximity to the sensor during clinical conditions was oriented toward it.
The MicroTargeting Drive was excluded from this study because the loan agreement with the University Hospital of Basel concluded before its use could be initiated.
Data were evaluated with Python 3.8 using custom-made scripts. Position errors were defined

as the Euclidean distance between the measured position and the ground-truth position. The orientation error was also defined as the Euclidean distance (in the angular space) between the measured orientation and the ground-truth orientation. The latter were defined as the position and orientation obtained without the surgical instruments.

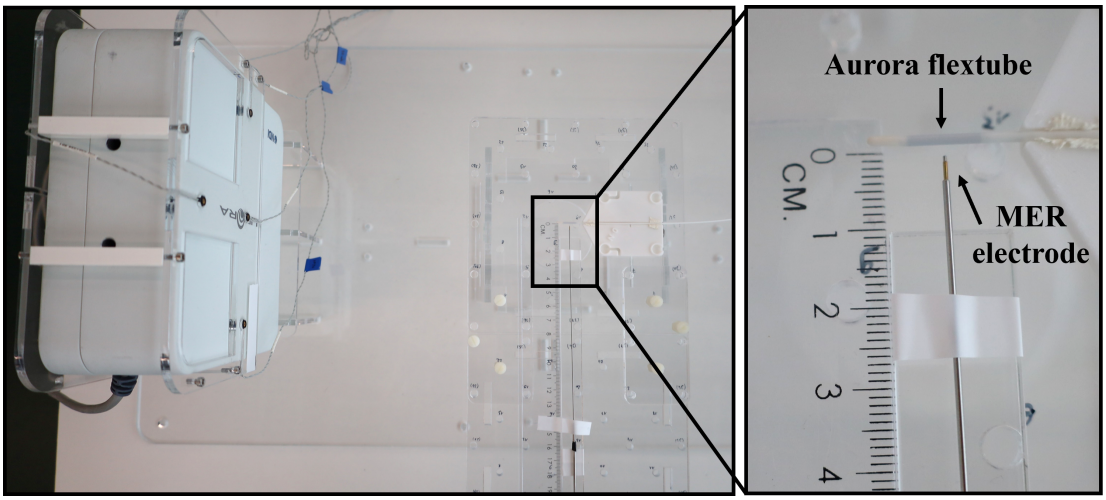

Figure B.3: Experimental setup for the evaluation of EM distortions impact. MER electrode placed at 2 mm of the Aurora flextube in the center of the MV.

Results

The graphs in Figure B.4 compare the positional error performance of the Aurora and ManaDBS systems across varying distances between the object and the sensor, evaluated for multiple surgical instruments. Similarly, the graphs in Figure B.5 compare the orientation error performance.

Using the Aurora (Fig. B.4(A)), positional errors remained consistently low across all tested distances (5 mm, 20 mm, and 80 mm) and instruments. Errors were generally below 0.2 mm, indicating high precision and negligible variability between instruments. Using the ManaDBS (Fig. B.4(B)), the positional error showed greater variation across distances. While error levels were minimal at 80 mm and 20 mm, they exceeded 0.8 mm for specific instruments (e.g., needle holder and retractor) at 5 mm, indicating reduced accuracy at closer distances.

Figure B.4(C) presents a finer resolution of positional error trends for Aurora. Errors remained stable and consistently below 0.35 mm across distances ranging from 80 mm to 2 mm, with minor variations for instruments like the retractor. In contrast, positional errors for ManaDBS increased substantially as the object moved closer to the sensor (Fig. B.4(D)). Errors exceeded 1 mm at distances below 5 mm, particularly for instruments such as the needle holder and retractor, highlighting limitations in close-proximity tracking.

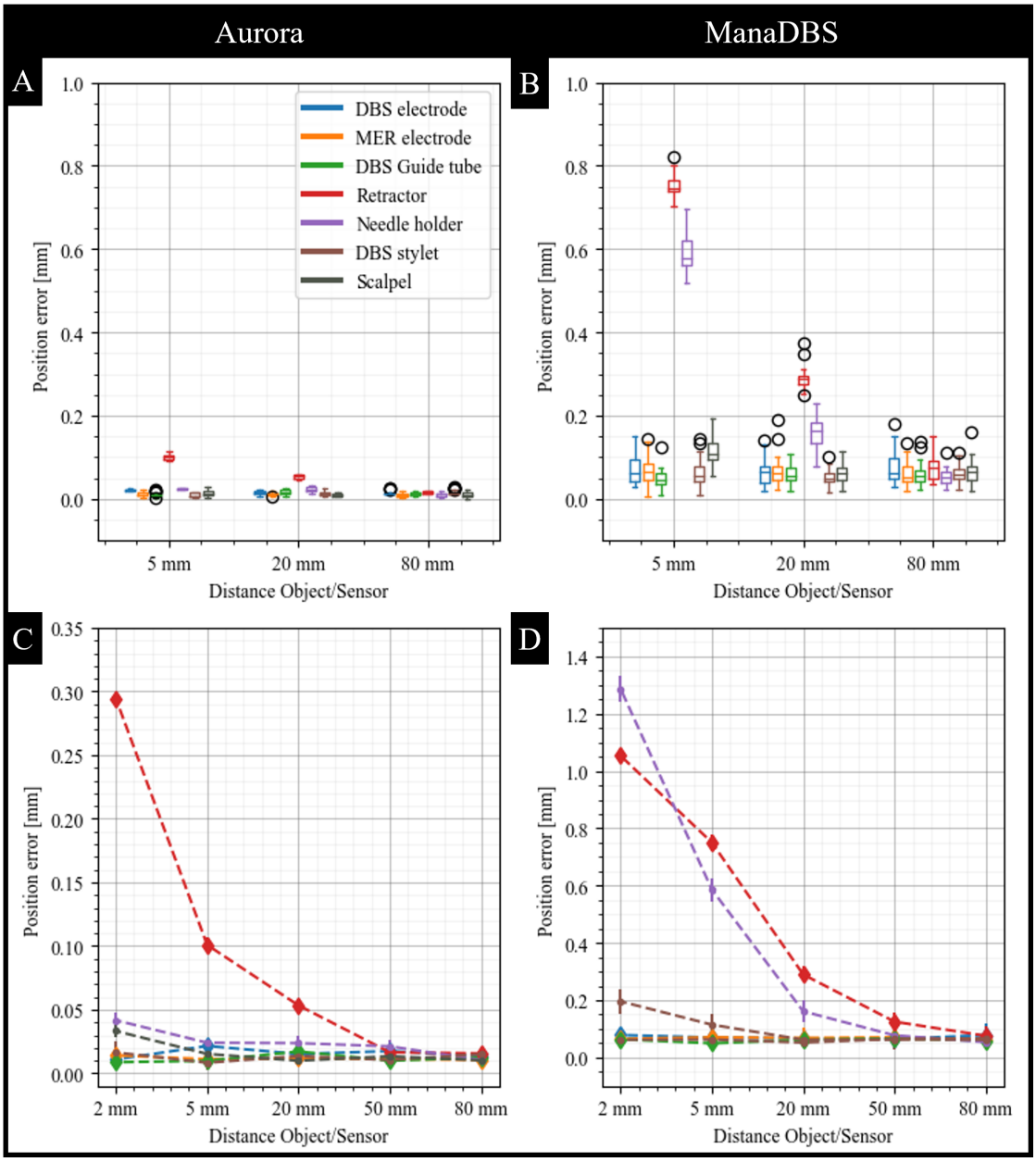

Figure B.4: Impact on the position error for the different sources of distortion: (A) Boxplot of the position error for the Aurora, (B) Boxplot of the position error for the ManaDBS, (C) Plot of the position error for the Aurora (D) Plot of the position error for the ManaDBS; at different distance from the sources of distortion.

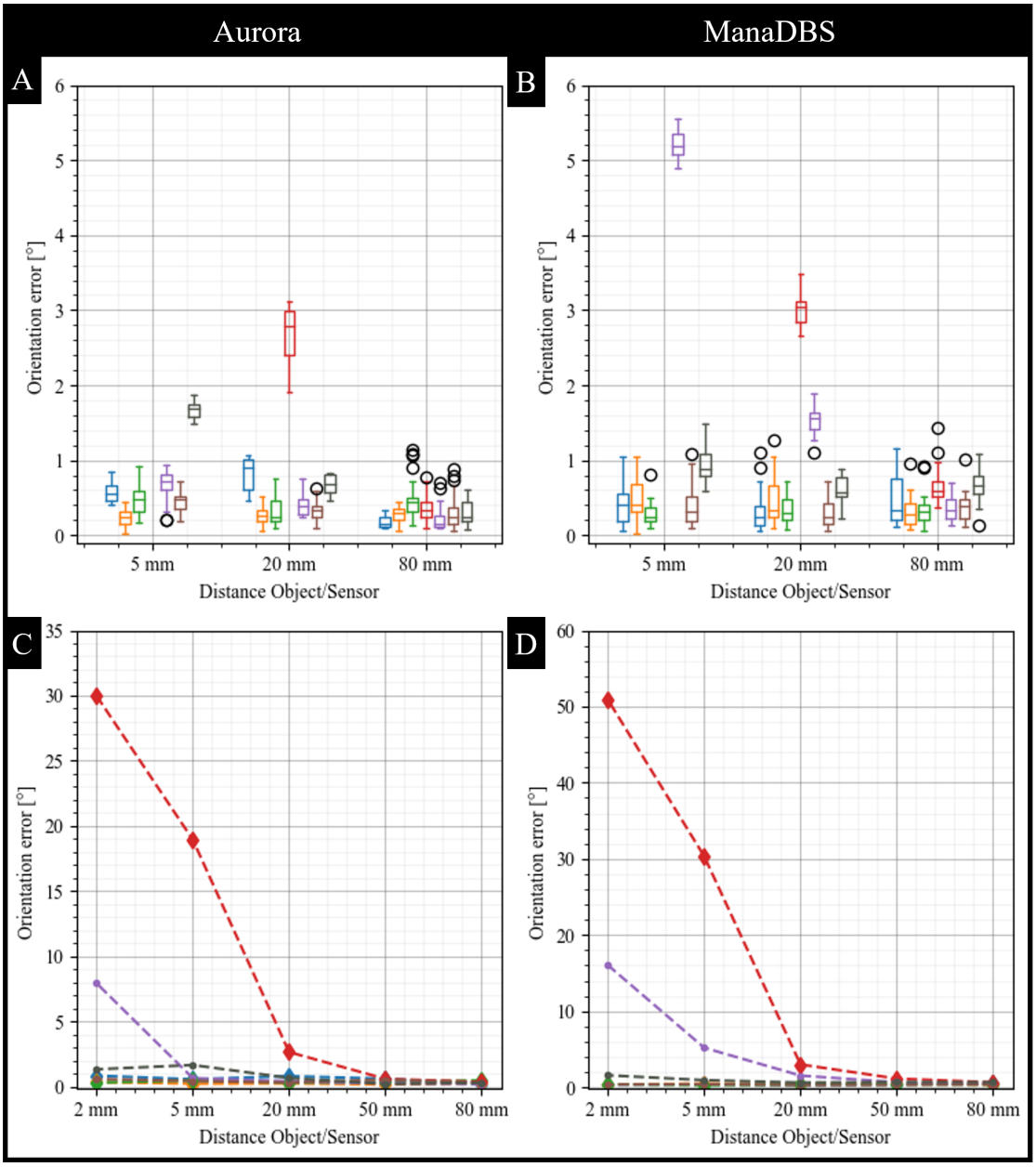

Figure B.5: Impact on the orientation error for the different sources of distortion: (A) Boxplot of the orientation error for the Aurora, (B) Boxplot of the orientation error for the ManaDBS, (C) Plot of the orientation error for the Aurora (D) Plot of the orientation error for the ManaDBS; at different distance from the sources of distortion.

Using the Aurora (Fig. B.5(A)), orientation errors were generally low, with most instruments maintaining errors below 1° across all distances (5 mm, 20 mm, and 80 mm). A notable exception was the retractor below 20 mm distance, which exhibited an increased error, indicating a specific sensitivity for this instrument. Using the ManaDBS (Fig. B.5(B)), the orientation errors were more pronounced compared to Aurora, with certain instruments, such as the retractor and needle holder, displaying errors up to 30° at 5 mm. However, errors were relatively stable at 80 mm, suggesting that distance impacts the orientation accuracy of this system.
At finer distances (ranging from 80 mm to 2 mm), orientation errors increased significantly as the distance between the object and sensor decreased for both Aurora and ManaDBS system. Errors for specific instruments, such as the retractor and needle holder, exceeded 5° at 2 mm, underscoring the system's challenges in maintaining accuracy at short distances. Moreover, the scalpel caused a slight increase in error, remaining below 2° even at a 2 mm distance.

Discussion

Aurora demonstrated superior accuracy and precision, with errors remaining below 0.35 mm across all instruments and distances. ManaDBS, on the other hand, exhibited higher positional errors, which can be explained by the intrinsic lower performance of the system if compared to the Aurora. Aurora's performance was largely unaffected by object-sensor distance, whereas ManaDBS displayed a clear distance-dependent trend, with position error magnitudes increasing significantly at short distances for some instruments. These specific instruments, i.e. the needle holder and retractor, consistently exhibited higher errors, suggesting variability in system performance based on instrument type. These instruments, being the largest made of steel, generated magnetic fields over a large volume, making them highly prone to distorting the FG's magnetic field with the greatest impact.
The Aurora and ManaDBS displayed greater variability and significantly higher orientation errors, particularly at shorter distances. The systems exhibited clear distance-related trends. Again, the retractor and needle holder were more prone to orientation inaccuracies, especially at shorter distances.
The Aurora system demonstrates strong position detection with minimal sensitivity to distance or instrument type, making it well-suited for surgical applications requiring high precision. In contrast, the ManaDBS system shows error trends that suggest potential challenges in maintaining consistent tracking accuracy when in close proximity (<20 mm) to specific surgical tools. Both systems exhibited significant orientation errors at short distances (<20 mm), which could compromise their reliability in scenarios requiring high angular precision. The instruments causing the largest errors were the retractor and needle holder, both of which are typically positioned near the burr hole and used to keep the surgical site open. At the start of the implantation process, the EMT sensor may be within one to a few centimeters of these instruments. Conversely, instruments expected to be a few millimeters from the sensor, such as the DBS guide tube or MER electrode, had no measurable impact on the performance of either system. The most challenging distortion sources are magnetic or ferromagnetic instruments with volumes of several hundred cubic millimeters. Therefore, tools like the microtargeting

drive or other similar drive systems must be carefully considered and thoroughly evaluated to ensure compatibility with EMT systems.
The resilience of the Aurora system can be attributed to the relatively small dimensions of the instrument compared to the stereotactic system. As a result, conductive distortions are likely negligible, leaving the static magnetic field generated by the instrument as the primary source of distortions. Given that the Aurora system operates based on inductive principle and alternating magnetic fields, static distortions have a reduced impact on its tracking performance compared to the ManaDBS system. However, this does not account for the significant errors observed in orientation detection.

To improve the ManaDBS systems, distortions detection and compensation methods are required. Potential solutions include hardware improvements, such as modifying the activation sequence to low-frequency sinusoidal or ramped signals. Another approach for the compensation of EM distortions involves leveraging generative adversarial neural networks (GANs) to identify and compensate for distortions caused by specific surgical instruments [122].

Conclusion

This study evaluated the tracking performance of the Aurora and ManaDBS systems in the presence of various surgical instruments commonly used during DBS procedures. Larger ferromagnetic tools, such as the retractor and needle holder, significantly impacted the tracking performance of both systems, when placed within 20 mm of the EMT sensors. These issues may be critical for DBS surgery and highlight the necessity of developing compensation methods to mitigate such distortions.
Encouragingly, objects expected to be in closest proximity to the EMT sensor (< 5 mm), such as the DBS guide tube and MER electrode, did not adversely affect tracking performance, suggesting that these systems can handle the most immediate surgical challenges effectively.

APPENDIX C

Investigation on the resilience of AMR magnetometers to strong magnetic fields

Foreword and Overview

This appendix investigates the resilience of the AMR magnetometers used in the ManaDBS system to strong magnetic fields. Preliminary findings suggest that AMR sensors show promising potential for integration into long-term implants. Notably, the sensors remained unaffected by the strong magnetic fields present in MRI machines, indicating that the EMT system could be a viable option for post-operative electrode localization.

Contribution: The candidate was overall responsible for the design of the study. The MFC used in this study was already developed by the research laboratory (Sensors lab, FHNW-HLS). The candidate received support from the different imaging facilities (Zentrum für Bilddiagnostik AG, Basel and IRIS platform, Strasbourg). The candidate performed the measurement and analysis. The candidate was overall responsible for the writing of the manuscript. The supervisors and co-authors supported the process and reviewed the paper.

Abstract

On-chip magnetometers are already integrated within long-term implants such as cardiac implantable electronic devices. They are also good candidates to be integrated within the next generations of brain stimulation electrodes to provide their position and orientation. In all cases, long-term implants are expected to be at least certified as MRI conditional. We investigated the resilience to the exposure to 3 T and 7 T of an AMR sensor integrating a set/reset function. The sensitivity, non-linearity, and offset of a batch of 63 identical sensors were not affected by the exposure. These preliminary results provide new insights on the usability of magnetoresistive sensors for biomedical applications requiring MRI conditionality.

Introduction

Magnetic field sensors are used in a large range of applications including biomedical systems for which they are particularly promising for the development of EMT systems. EMT systems are generally based on pick-up coils integrated within surgical tools [180]. With the new generation of on-chip magnetometers, the gap in terms of miniaturization and signal-to-noise ratio between integrated magnetometers and pick-up coils is getting narrower. These improvements have opened the way to the design of various medical tools and devices integrating magnetometers such as long-term implants. For instance, the instrumentation of prosthetics or brain stimulation electrodes would allow their localization post-operatively without relying on medical imaging. However, for such devices, constraints such as safety, conditionality, or compatibility with MRI need to be addressed. Three categories of integrated magnetometers are of interest to long-term implants. Sensors based on Hall effect, AMR, and MEMS combine sub-millimeter dimensions for their integrability, as well as range, linearity, and resolutions that are sufficient for EMT [185]. AMR technology offers the best resolution and miniaturization. However, to our knowledge, among the commercially available sensor chips, the maximal exposed field reaches only 1 T [175]. This is below the field strength of a clinical MRI, and the degradation of the sensors' performances after exposure to stronger magnetic fields needs to be investigated. AMR sensors are made of a nickel-iron (permalloy) thin film deposited on a silicon wafer and patterned as a resistive strip. The permalloy thin film is magnetized during the fabrication process. Its coercivity is low enough so that an on-chip circuitry called Set/Reset can restore its initial magnetization after an exposure to a strong magnetic field [4]]. This circuitry typically injects a current pulse into an integrated strap or planar coil to generate the necessary magnetic fields [4,[265]]. This paper investigates the impact of exposure to 3 T or 7 T MRI for an AMR sensor featuring a set/reset function. Section II describes the materials and methods used for the calibration of the sensor as well as the exposure protocol. Section III details and discusses the experimental results.

Materials & Methods

Anisotropic magnetoresistive sensor

The sensor investigated is a 3D AMR sensor (MMC5603NJ, MEMSIC Semiconductor Co., Ltd., China) with a resolution of 6.25 nT/LSB and a rms noise of 200 nT.
In this study, the configuration chosen for the sensor provides the highest resolution at the expense of the output data rate. The chip is encapsulated in a wafer-level chip-scale package of 0.8 mm x 0.8 mm x 0.4 mm. The small dimension of the chip allows the integration into surgical tools or implants, as well as the design of a high-density MFC consisting in an array of 8 x 8 sensors (Fig. C.1) with spacing of 2 mm along the X- and Y-axis.

MFC allows us to perform tests on a larger set of sensors and under the same experimental conditions. Out of the 64 sensors, one of them was damaged during the assembly of the printed circuit board, the study was then performed on 63 sensors. According to the datasheet of the manufacturer, the maximal exposure field is 1 T [4].

Exposure to strong magnetic fields

The MFC was consecutively exposed to the static field of a 3 T MRI and then, 7 T MRI (Fig. C.2). For the 3 T exposure the total duration of exposure was 30 min (10 min per sensor's axis). For the 7 T exposure, only the Y-axis was exposed during 2 min due to the MFC's dimension and the restricted diameter of the MRI.

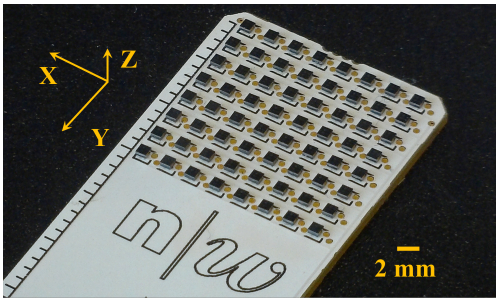

Figure C.1: Magnetoresistive based MFC with spacing of 2 mm in between sensor chips with a configuration of an 8 x 8 array.

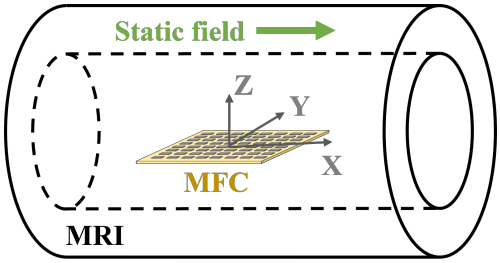

Figure C.2: MFC position within the MRI scanner with the X-axis aligned along the static field.

Calibration methods

The MFC has been calibrated within a one-axis Helmholtz coil supplied by an operational amplifier (KEPCO bipolar operational power supply) and driven by a function generator (GW Instek MFG-2230M) for ac measurements. This experimental setup provides a high accuracy current to the coils (maximal error of 0.2%). To calibrate independently the X, Y and Z channels of the MFC, a low-frequency sinusoidal magnetic field has been applied. The misalignment of the MFC during the calibration of each sensor's axis was detected and compensated through the measurement of the residual sinusoidal signals on the two other axis, which were quantified

through a Fast Fourier Transform (FFT) analysis. Static magnetic field measurements have been conducted to obtain the relationship between the known magnetic field and the magnetic field measured by the sensors. Seven static magnetic fields values were measured from -1 mT to 1 mT. A linear regression provides the sensitivity and offset correction coefficients for each axis of the sensors composing the MFC. However, the offset extracted does not correspond to the intrinsic offset of the sensors as it also contains the static magnetic field present in the environment. The mean static field obtained for the 63 offsets was subtracted to each offset value to only observe the distribution centered around zero.

Parameters of interest

To evaluate the degradation of the sensor's performances, three parameters were extracted and compared before and after exposure to each MRI. These three parameters are of primary importance in EMT systems. First, the sensitivity, as the slope of the linear regression corresponds to the ratio of the sensor's output data and the actual magnetic field. The sensitivity here is dimensionless. Second, the offset was extracted from the linear regression. Third, linearity is the expression of the extent to which the actual measured curve of a sensor departs from the ideal linear curve. In this study, linearity is specified in terms of percentage of nonlinearity, which is defined as: $NonLinearity(\%) = \frac{D_{\text{in(max)}}}{FSO} * 100$, with $D_{\text{in(max)}}$ being the maximum input deviation and FSO as the full-scale output.

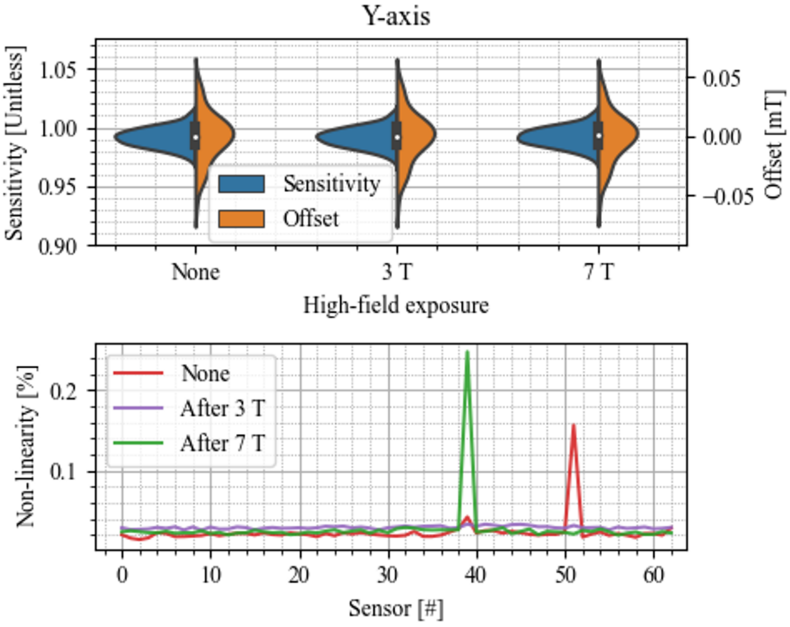

Figure C.3: Violin plot of the sensitivities and offsets along the Y-axis which was exposed to 3 T then 7 T static field (Top graph). Non-linearity values along Y-axis for the 63 sensors investigated (Bottom graph).

Results & Discussion

No degradation of the performances of the AMR sensors was observed after each exposure. Along the three axes, the absolute variation of maximum 0.53 % was observed on the sensitivity with an average variation of 0.032 % and 0.24 % after 3 T and 7 T exposure respectively. The maximal difference in the offset was about 8 μT and an average difference of 0.93 μT and 1.38 μT after 3 T and 7 T exposure respectively. The non-linearities were smaller than the range specified by the datasheet [0.5 %, 0.75 %] with a maximum at 0.24 %. Figure C.3 shows the distributions of the three parameters along the Y-axis. Results of the same order of magnitude were observed along the X- and Z-axis.
The distribution of the sensitivities and offsets remained consistent. The extracted value for the sensitivity and non-linearity parameters stays in the range provided in the datasheet of the AMR sensor. Furthermore, no significant differences were found between the three parameters before and after exposure. These results suggest that the Set/Reset function succeeds in realigning the magnetic domains of the permalloy thin film. No calibration procedure should be required to guarantee the performance of the sensor after exposure.

Conclusion

The exposure to high-field such as in clinical MRI does not impact the performance of the tested AMR sensor integrating a Set/Reset function. Its safe integration into medical implants can now be further investigated.

APPENDIX D

Safety assessment of the ManaDBS system

Foreword and Overview

This appendix provides an experimental evaluation of the ManaDBS safety in accordance with official guidelines on electromagnetic exposure. Using a custom-made MFC, multiple activation sequences of the ManaDBS system were measured and analyzed.

Contribution: The candidate was overall responsible for the design of the study. The MFC was already developed by the research laboratory (Sensors lab, FHNW-HLS). The candidate performed the measurement and analysis.

Introduction

Unlike other technologies for intra-operative localization, static magnetic fields (up to a few Teslas) have negligible attenuation when passing through the human body and are unaffected by tissue type [14]-[15]. However, the safety of EMT systems must be carefully assessed. Relevant standards include the "Guidelines for Limiting exposure to time-varying electric and magnetic fields (1 Hz to 100 kHz)" [266] from the International Commission on Non-Ionizing Radiation Protection (ICNIRP) guideline and IEEE C95 Standards (C95.6-2002 for 0 Hz to 3 kHz) [212] from the International Committee on Electromagnetic safety (ICES). These guidelines aim to prevent adverse effects, with reference levels for magnetic fields differing between them [267]. For quasi-static magnetic fields (< 8 Hz), the ICNIRP and ICES guidelines recommend magnetic flux density limits of $40/f^2$ and $18.1/f$, respectively, for head exposure, where f is the frequency in Hz. Preliminary investigations, as detailed in **Publication II**, determined that the magnetic flux generated by the system poses no risk due to its low amplitude. Similarly, the low gradient within the MV does not present a risk of peripheral nerve stimulation. One final verification, not included in **Publication II**, was addressed in this appendix. Both guidelines specify an additional requirement for non-sinusoidal exposures: a multi-frequency analysis to ensure compliance with safety standards (Eq. (D.1)). This evaluation was conducted as part of the safety assessment presented here. The guidelines followed for the multi-frequency analysis are based on the IEEE Standard. However, the analysis is similar to the ICNIRP guidelines, which use a comparable equation for the exposure coefficient but with slightly different values for the maximum permissible exposure.

$$\sum_{i=0Hz}^{3kHz} \frac{A_\mathrm{i}}{ME_\mathrm{i}} \leq 1 \tag{D.1}$$

With A_i magnitude of the ith Fourier component of the exposure waveform, ME_i is the maximum permissible exposure in milliteslas with a single sinusoidal waveform at a frequency f_i.

The values for the magnetic maximum permissible exposure ME_i for the head and torso, are described in the following Table D.1. Similarly, the values for the magnetic maximum permissible exposure ME_i for the arms and legs, are described in the following Table D.2.
While the first case pertains to patient exposure, the second case concerns the exposure of surgeons and medical teams.

In our case, we are following to the requirements for a controlled environment, as the system will be used exclusively in a clinical setting by trained personnel. Additionally, we are following the maximum exposure limits for the head, as these values will also serve to validate the exposure levels for other body parts.

Table D.1: Magnetic maximum permissible exposure levels: Exposure of head and torso (IEEE C95.6-2002 Standards [212]).

Frequency range (Hz)	General public (B[mT])	Controlled environment (B[mT])
< 0.153	118	353
$0.153 - 20$	$18.1/f$	$54.3/f$
$20 - 759$	0.904	2.71
$759 - 3000$	$687/f$	$2060/f$

***Controlled environment**: An area that is accessible to those who are aware of the potential for exposure as a concomitant of employment or where the environment is not accessible to the general public and those individuals having access are aware of the potential for adverse effects*
***General public**: All individuals who may experience exposure, except those in controlled environments. It includes individuals of all ages, and of varying health status, and this will include particularly vulnerable groups or individuals such as the frail, elderly, pregnant workers, babies and young children*

Table D.2: Magnetic maximum permissible exposure levels: Exposure of arms and legs (IEEE C95.6-2002 Standards [212]).

Frequency range (Hz)	General public (B[mT])	Controlled environment (B[mT])
< 10.7	353	353
$10.7 - 3000$	$3790/f$	$3790/f$

Materials & Methods

Instead of only relying on simulated data, the induced magnetic field from the FG was directly measured. For high-speed magnetic field measurements, a custom magnetic camera was developed using commercially available components and a custom-designed PCB (Fig. D.1) [268]. The MFC features a Field Programmable Gate Arrays (FPGA) interfaced with an array of 7 × 7 monolithic integrated three-axis Hall effect magnetic sensor (Texas Instrument, TMAG5273). These 49 sensors are connected via independent Inter-Integrated Circuit (I2C) buses. The sensors were arranged in a square grid measuring 56 × 56 mm^2, with an 8 mm separation between adjacent sensors in both horizontal directions. Each sensor operated in continuous measurement mode at a conversion rate of 7 kHz. Synchronous readings of all 49 sensors were performed regularly, triggered by an external signal.
However, it is important to account for high-frequency noise originating from the magnetic field sensors, which is unrelated to the activation sequence and does not pose any risk of exposure. This noise, introduced by the measurement tool itself, artificially increase the calculated exposure coefficient. To correct for this error, the MFC was placed inside a zero-gauss chamber, and the magnetic fields were recorded for the same duration as the ManaDBS activation sequence. The zero-gauss chamber helps eliminate any influence from the surrounding magnetic field. The exposure coefficient calculated from this signal reflects the additional impact of the MFC noise. These values, which range from 9 to 11.5, were then subtracted from the exposure coefficient calculated later.

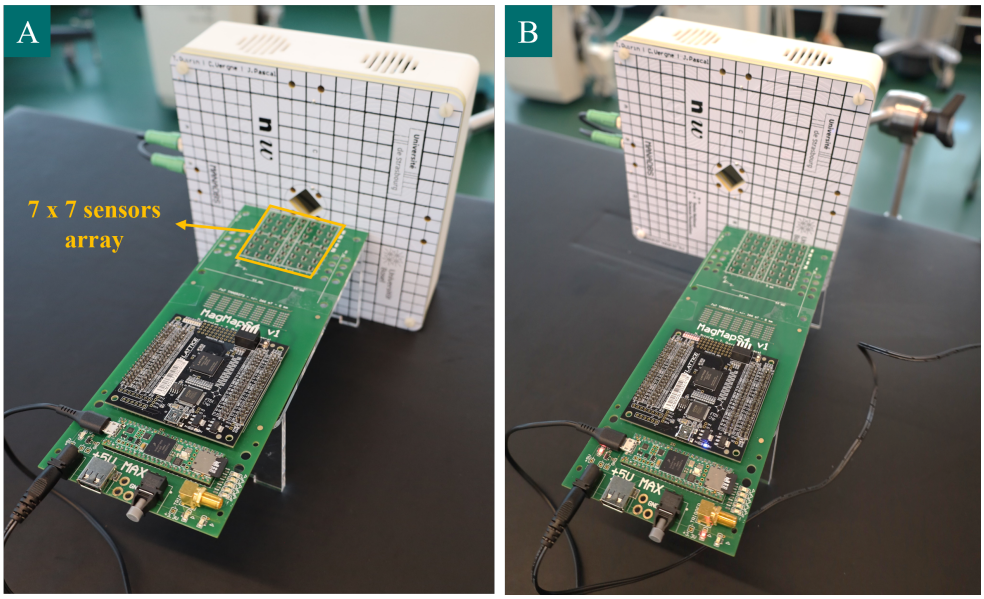

Figure D.1: Experimental setup for the non-ionizing radiation evaluation: the FPGA-magnetic field camera being placed at (A) the center of the FG or at (B) the center of one coil.

The magnetic field was measured at two distinct positions near the FG to simulate worst-case scenarios. The first measurement was taken at the center of the FG (Fig. D.1(A)), while the second was conducted at the center of one of the coils (Fig. D.1(B)). The distance from the surface of the FG and the first sensors of the MFC was 5 mm.

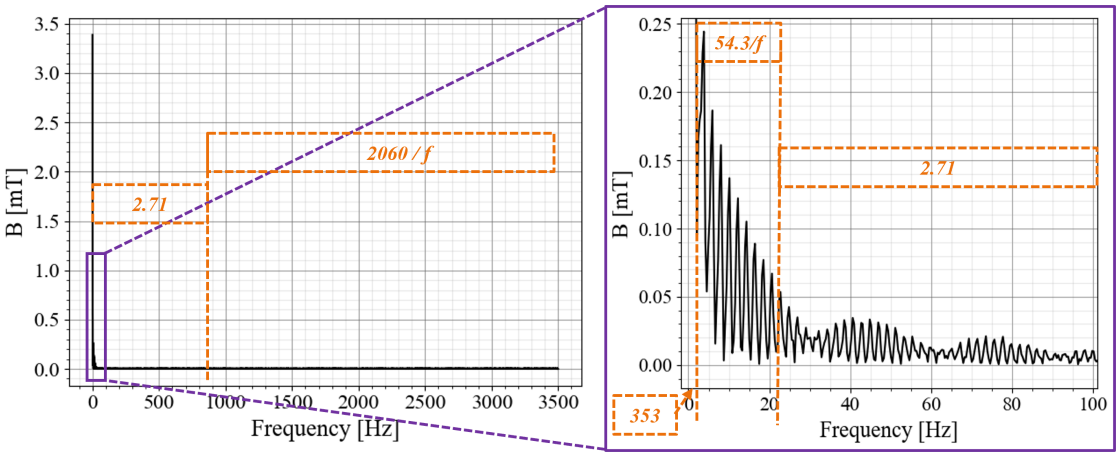

Figure D.2: Fast Fourier Transform of the magnetic field signal and the associated maximum permissible exposure levels for each frequency range. The FFT signal was obtained from a rectangular activation sequence using the MFC located at the center of the FG and selected a sensor positioned closest to the FG.

A Fast Fourier Transform (FFT) was performed on a single magnetic field signal (Fig. D.2), analyzing harmonics from 0 Hz to 3 kHz. Equation (D.1) was then applied to the FFT signal. Here is the coefficient calculation associated to this signal:

$$\begin{aligned} Coeff &= \sum_{i=0Hz}^{0.153Hz} \frac{A_{\mathrm{i}}}{353} + \sum_{i=0.153Hz}^{20Hz} \frac{A_{\mathrm{i}}}{54.3/f_{\mathrm{i}}} + \sum_{i=20Hz}^{759Hz} \frac{A_{\mathrm{i}}}{2.71} + \sum_{i=759Hz}^{3kHz} \frac{A_{\mathrm{i}}}{2060/f_{\mathrm{i}}} \\ &= 0.01 + 0.68 + 2.55 + 9.30 \ = 12.54 \quad (with\ measurement\ noise) \\ &= 0.01 + 0.66 + 1.32 + 0.23 \ = 2.22 \quad (without\ measurement\ noise) \end{aligned} \tag{D.2}$$

Figure D.3(A) illustrates the magnetic field signal generated during the activation sequence, which was primarily based on rectangular waveform.

Results

Depending on the position of the MFC, the calculated exposure coefficient varies from 1 to 15. The maximum values were observed at closer proximity to the coil (Fig. D.4(A)). The exposure coefficient significantly exceeds the maximum permissible levels under the conditions tested. However, this study focused on a worst-case scenario. In practical applications, the FG is typically positioned at least 15 cm away from the patient's head. Taking into account the 5 mm distance between the first sensors and the FG surface, measurements from sensors placed farther away (approximately 45 mm) showed a notable decrease in the exposure coefficient.
Potential solutions to reduce the exposure coefficient include implementing a ramped activation sequence for each coil. This approach is feasible with the existing control electronics, as it already incorporate a digital-to-analog converter. The ramped activation will help minimize harmonics in the signal. Another solution is to apply a simple low-pass filter to the activation currents of the coils, effectively suppressing high-frequency harmonics.
The first solution was implemented, and the activation sequence was subsequently modified to incorporate a 30-ms ramp (Fig. D.3(B)), and measurements were repeated at both MFC positions. The resulting exposure coefficient was found to range between 0.1 and 6 (Fig. D.4(B)). This modification significantly reduced the exposure coefficient, but it was still insufficient to reach the recommended limit of 1.
In addition to modifying the activation sequence, a Butterworth low-pass filter (cut-off at 25 Hz) was applied to the measured magnetic field (Fig. D.3(C)). This filter was used to simulate the potential effect of applying a similar low-pass filter to the activation currents of the coils. The resulting exposure coefficient was found to range between 0.1 and 4 (Fig. D.4(C)).

Conclusion

This study evaluated the electromagnetic exposure of the ManaDBS system, testing two activation sequences for the FG. The ramped sequence showed a reduction in the exposure coefficient. With this modification, the simulated exposure coefficient was reduced to below the recommended threshold at a distance of four centimeters from the FG.

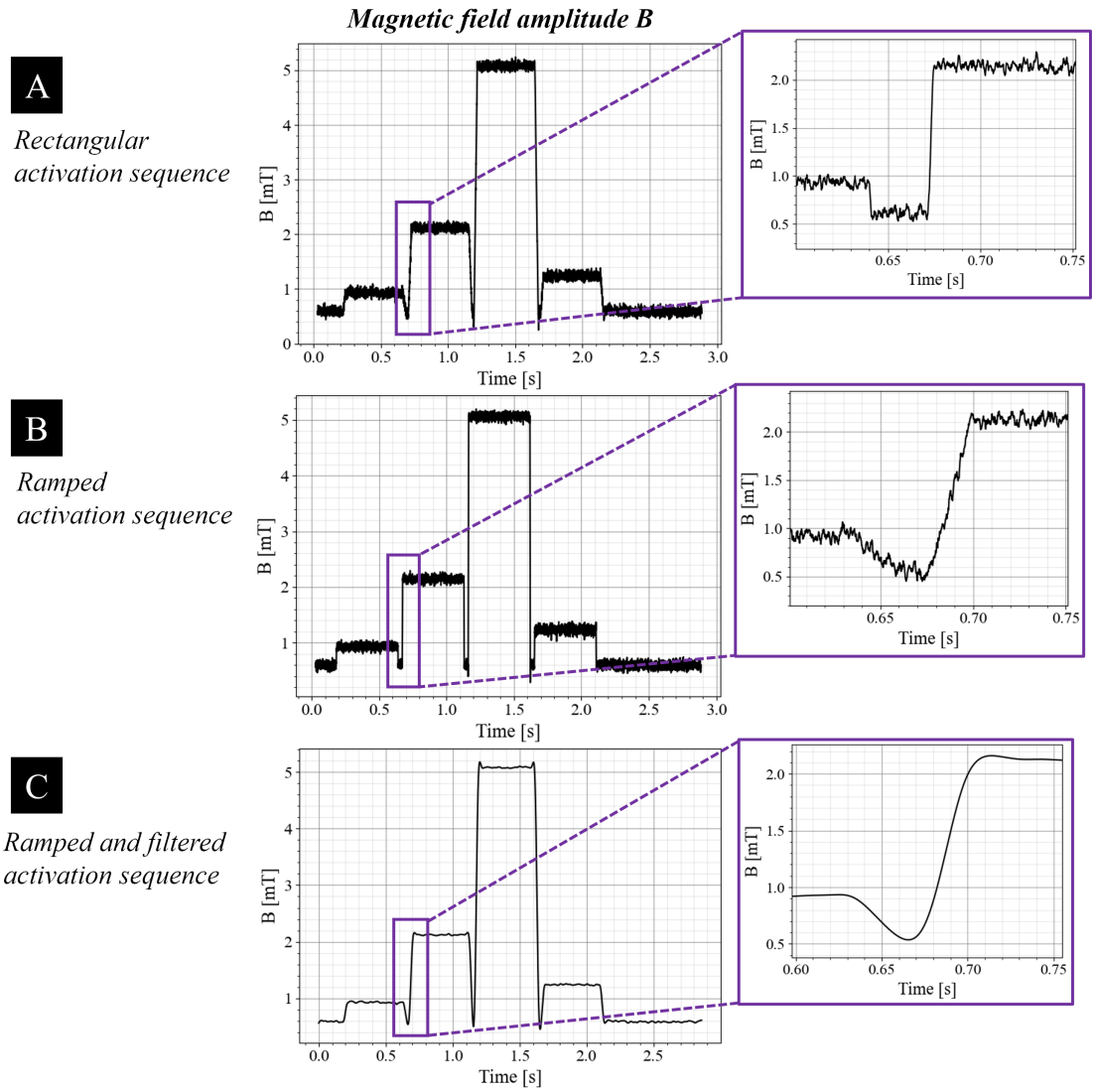

Figure D.3: Amplitude the magnetic field signal: from (A) rectangular activation sequence, (B) Ramped activation sequence and (C) Ramped activation sequence after low-pass filtering. A moving average was applied to the MFC sensors' data to reduce noise for improved visualization.

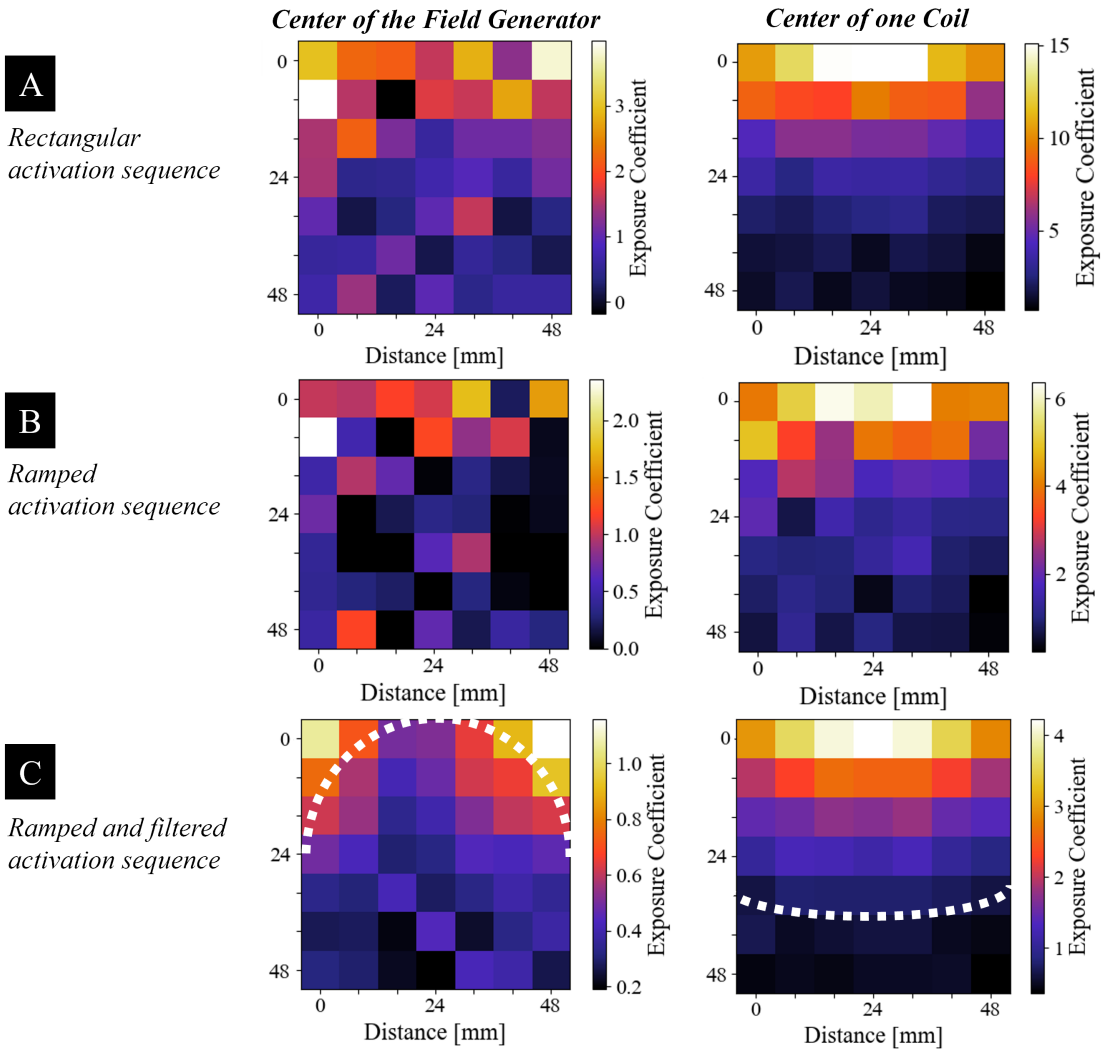

Figure D.4: Exposure coefficient calculated for two MFC positions and different activation sequences: from (A) rectangular activation sequence, (B) Ramped activation sequence and (C) Ramped activation sequence after low-pass filtering.
The white dashed line demarcates the exposure coefficient of less than 1. These results reflect the system's exposure coefficients after eliminating the amplitude caused by measurement noise.

APPENDIX E

Preliminary demonstration of a novel EMT technique based on quantum sensing

Foreword and Overview

This appendix presents a novel EMT technique based on low-intensity and low-frequency ac magnetic field, detected by high-resolution magnetometers. The localization method was demonstrated in 2D and involves small flexible PCB coil with the potential to be integrated into medical instruments.

Contribution: The candidate was overall responsible for the design of the study. The candidate received technical support from members of the research laboratory (Sensors lab, FHNW-HLS) concerning the development of flexible PCBs. The candidate performed the measurement and analysis. The candidate was overall responsible for the writing of the manuscript. The supervisors and co-authors supported the process and reviewed the paper.

Abstract

Optically pumped magnetometers represent a breakthrough in magnetic measurements, enabling new applications across various fields including medicine. In this paper, we propose a novel electromagnetic tracking approach using optically pumped magnetometers to detect ac magnetic fields generated by small, thin, and flexible coils with sub-nanotesla noise levels. This approach could facilitate tasks such as catheter localization, monitoring of endoscopic capsules, and capturing object shapes without a line of sight. This first proof-of-concept demonstrates a position error of less than 3 mm in two dimensions. In addition, we investigated the impact of coil bending on tracking error, which is crucial for applications where the coil deforms during tracking. While similar tracking performance was observed up to 60° of bending, larger curvatures resulted in a significant rise in the tracking error.

Introduction

Catheter localization in minimally invasive surgery represents a well-recognized technological and medical challenge addressed by various techniques. Optical tracking, the gold standard in surgical environments, is often unsuitable due to the requirement of a line of sight. EMT system is the second most commonly used technique [180], followed by ultrasound approach, which is mostly effective for soft tissues and at a small distance to the target. We propose a novel electromagnetic tracking method, which competes with the three main localization techniques described in the literature and detailed in Fig. E.1. For the sake of simplicity, Fig. E.1 does not include the recently introduced method using miniature magneto-mechanical resonators [127]. The most common method involves induction principle, where an ac electromagnetic field generated by transmitter coils induces a voltage in receiver coils, integrated into the target device [198, 269]. The induced voltage depends on the electromagnetic field strength, as well as on the distance between the transmitter and receiver coils, and their relative orientation. Commercialized for over two decades, this method is nowadays available for surgical procedures. Recently, a second method involving integrated magnetometers and quasi-static magnetic fields has been explored [135, 200]. External coils, sequentially activated, generate dc magnetic fields, which are acquired by an integrated magnetometer placed in the target device. These magnetic fields uniquely encode a spatial position within the tracking volume. While this method provides similar performance to the first, its limited tracking volume and sampling rate are balanced by greater robustness to electromagnetic interference. The third method relies on an array of integrated magnetic sensors, also known as MFC [131, 132, 208]. A permanent magnet in the target device is detected by the sensors on the MFC. This approach enables significant miniaturization, with magnets ranging from millimeter to micrometer scale, but it is limited by an even smaller tracking volume.

In this paper, we introduce a new method based on high-resolution magnetic field sensors and flexible coils. Inspired by the Global Positioning System (GPS) principle, this approach was previously impractical in biomedical applications due to the lack of high-resolution magnetic sensors operating at room temperature and with very low noise. Our method is based on a small

coil, either rigid or flexible, which generates a low ac magnetic field measured by Optically Pumped Magnetometers (OPM) [270]. The magnetic field magnitude measured by these OPMs varies with the distance to the coil, allowing for multilateration approach to localize the coil. OPMs offer best in class noise level, about few femtoteslas. Additional advantages include room-temperature operating range, compactness, and immunity to electromagnetic interference. Compared to SQUID-based systems, OPMs offer enhanced portability, reduced operational complexity, and improved signal-to-noise ratios, ideal for wearable or bedside monitoring.

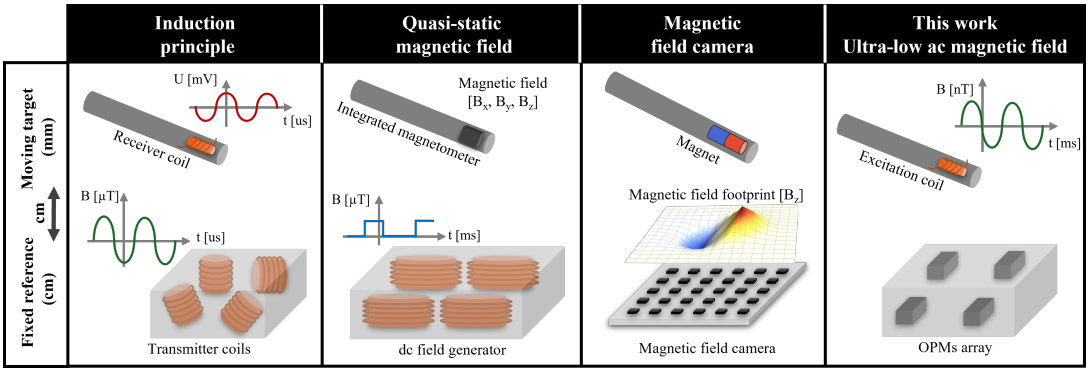

Figure E.1: Schematic describing the basic principle of the three existing EMT methods in addition to the method proposed in this work, based on ultra-low ac magnetic field.

By taking advantage of these properties, the localization of a catheter, integrating small coils, by detecting ultra-low-intensity ac magnetic fields with multiple OPMs is achievable. As the human body is mostly transparent to magnetic fields, the maximum tracking distance should not be affected by human tissues. However, at such ultra-low magnetic field, intrinsic magnetic biosignals might be detectable. To avoid interferences, the magnetic field must oscillate at a frequency where no biosignal can be observed. Multiple coils could be simultaneously detected by assigning individual frequencies to each coil. The use of flexible coils paves the way for additional biomedical applications, including endoscopic capsule monitoring or limb shape capture in the design process of orthoses and prostheses. Flexible coils can easily conform to various shapes and surfaces, increasing the patient comfort while enhancing signal quality and reliability, as illustrated for MRI applications [271]. This paper demonstrates a new electromagnetic tracking technique based on OPMs. Section II outlines the tracking system's components and principles. Section III demonstrates the method in 2-D, while Section IV discusses its advantages, limitations, and prospectives.

Materials & Methods

Optically pumped magnetometer and flexible coils

In this paper, we used the OPM QTFM Gen-2 (QuSpin Inc., USA) [12]. This OPM is known as a total-field OPM as it can operate within Earth's magnetic field and measures the

magnetic field magnitude (Fig. E.3(A)). OPMs rely on atoms trapped into a vapor cell, which have a well-defined precession frequency directly proportional to the magnitude of the magnetic field ($6.998 Hz/nT$) [272]. For this reason, the QTFM-Gen 2 is a scalar magnetometer, and not a vector magnetometer such as Hall effect sensors. The QTFM-Gen 2 exhibits a dynamic range of ± 150 μT, and a noise of $3pT/\sqrt{Hz}$. For this study, the OPM sampling rate was set to 125 Hz. The second part of the system is the excitation coil. We used small coils with a diameter of 9 mm (18 turns, resistance of 0.2 Ω), on a 0.1 mm-thick flexible PCB (Fig. E.3(B)).

Tracking principle

For cost reasons, we used a single OPM instead of three OPMs, which was successively placed at three positions on a Lego board (Fig. E.4). For each position, an ac current (sine wave) of $0.8A$ at 10 Hz was injected through the flexible coil while the magnetic field generated was recorded during 20 seconds by the OPM. At this frequency, no magnetic perturbations are observed in our experimental environment. A fast Fourier transform (FFT) was performed on each magnetic field signal to extract the peak amplitude at 10 Hz (Fig. E.2). The resulting peak at 10 Hz was clearly identified, along with the peak at 50 Hz, from the electricity network, and 16.7 Hz, the latter related to the power supply of the near railway. Each spatial position in the tracking volume is encoded by a vector of three magnetic field amplitudes, extracted from the frequency space. The principle of multilateration (i.e., the determination of a point's location by measuring the difference in distance between that point and multiple known reference points) is then applied. The multilateration resolution was achieved through the minimization function of the Python library, Scipy.optimize. The proposed tracking principle was evaluated for different coil curvatures (0°, 30°, 60° and 90°) as shown in Fig. E.4.

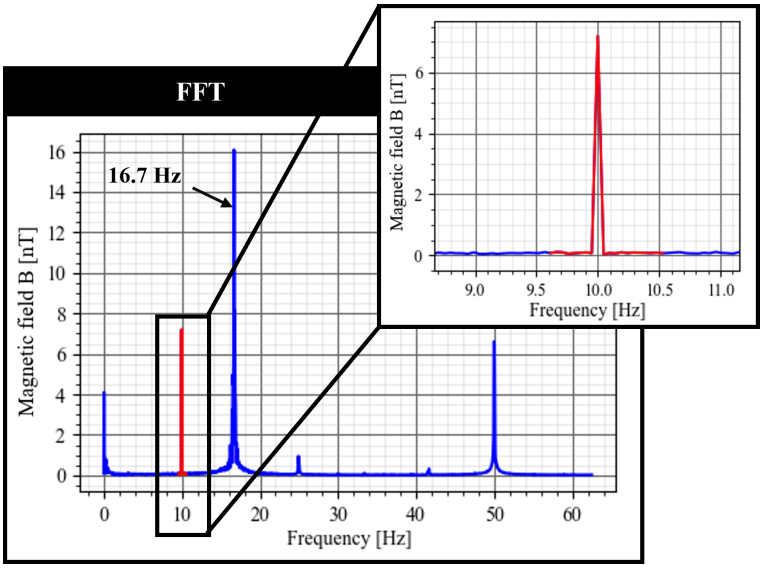

Figure E.2: FFT from a 20 seconds magnetic field measurement (blue) at a sampling rate of 125 Hz. The maximum amplitude within the red window represents the amplitude of the 10 Hz ac magnetic field.

Prior to the evaluation of the tracking performance, the characteristic curve between the magnetic field amplitude and the distance was obtained experimentally (Fig. E.3(C)). This characteristic is compared to the dipolar approximation describing the magnetic field strength of a magnetic dipole as a function of the distance.

Results

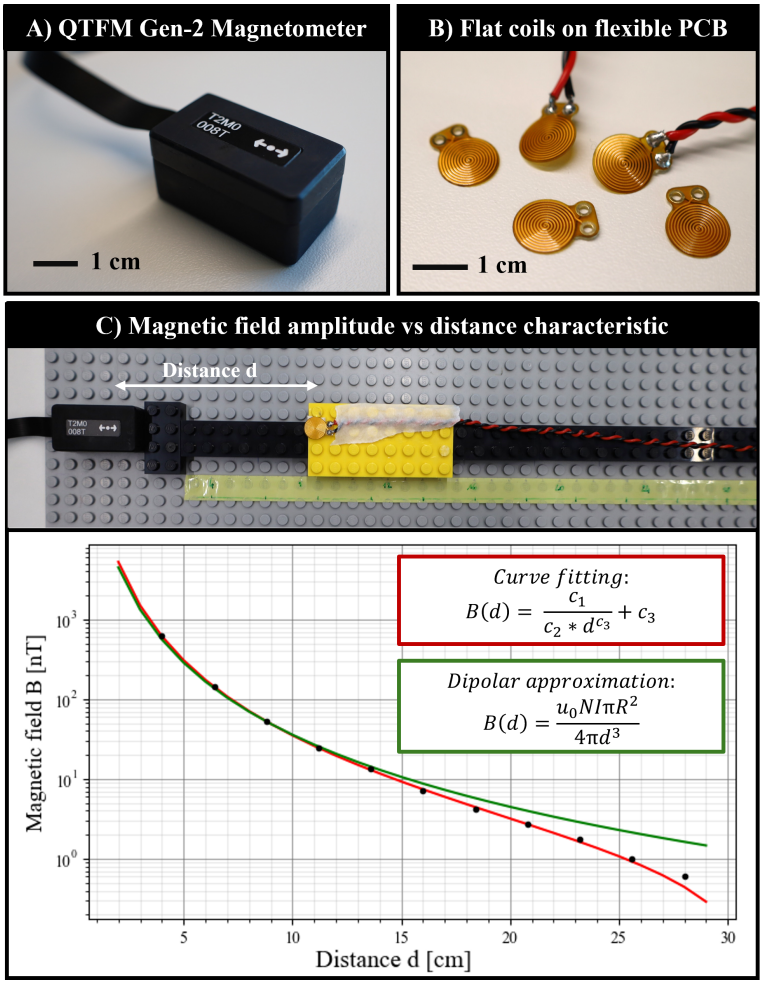

Figure E.3: (A) Pictures of the QTFM-Gen 2 OPM and (B) flexible PCB coils. (C) Magnetic field characteristic as a function of the distance d between the sensor and the coil.

Characteristic of the magnetic field amplitude B vs the distance d

The characteristic curve of the flexible coil was obtained by measuring the magnetic field magnitude at distances ranging from 4 cm to 28 cm (every 2.4 cm) between the coil and the

OPM, with an averaging of five measurements for each location. The analytical formula used for the curve fitting is shown in Fig. E.3(C). We compared this curve fitting to the dipolar approximation, after correcting the offset distance, as the exact position of the OPM sensing unit within the package is unknown and had to be determined. Experimental data matched with analytical data up to a distance of 14 cm (Fig. E.3(C)). Above 14 cm, the experimental characteristic provided a better fit and was therefore chosen for the multilateration tracking algorithm.

Performance assessment

The first study evaluated the tracking performance of the system. The coil was positioned at six different locations on a Lego 2-D board, at distances from the OPM ranging from 5 cm to 16 cm. The error was defined as the Euclidean distance between the known position on the Lego board and the position obtained after the multilateration resolution. The tracking error was evaluated at 2.8 ± 1.2 mm (Euclidean distance ± STD).

Table E.1: Coil curvatures and associated tracking performance.

Bendings	0°	30°	60°	90°
$Error \pm STD[mm]$	2.8 ± 1.2	2.6 ± 1.4	2.9 ± 1.1	9.2 ± 6.7

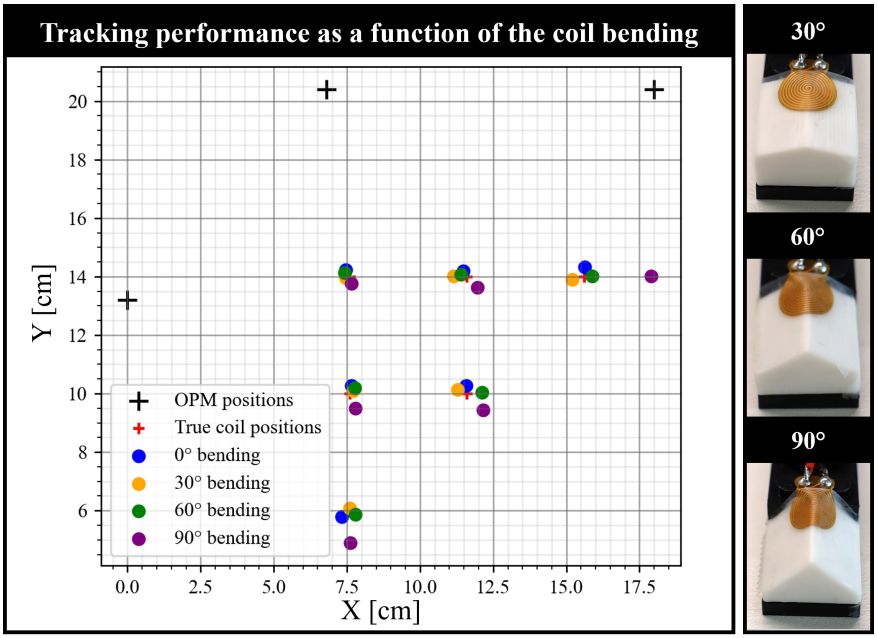

Figure E.4: True positions (red crosses) vs tracked positions for different coil bendings (colored dots). The OPM positions are represented by black crosses. Pictures of the coil for different bendings are shown on the right.

A second study assessed the tracking performance for different coil curvatures. Measurements were performed with flexible coils taped to 3D-printed supports at angles of 30°, 60°, and 90° (Fig. E.4). The coil bending negatively impacted the tracking error for curvatures above 60°, as shown in Table E.1. For a 90° angle, a position error of 9.2 mm was observed (Fig. E.4). The detected positions were farther from the true coil positions, suggesting a decrease in the magnetic field magnitude generated by the coil.

Discussion

Recent progress in magnetic sensors, particularly OPMs, have enabled the development of a new tracking system based on ultra-low-intensity magnetic fields, in the range of few nanoteslas, described in this paper as a first proof-of-concept using flexible coils. Tracking small coils represents significant interests for biomedical applications such as catheter localization or monitoring endoscopic capsules. In the standard configuration, the coil was localized in 2–D with a position error of less than 3 mm. The tracking performance was also assessed in the case of bent flexible coils. Flat flexible coils offers the advantage of their easy integration on various surfaces such as medical devices or directly on limbs. Hence, this evaluation showed steady performance up to an angle of 60°. However, larger bending impacted the magnetic field generated, and consequently the tracking performance significantly. For larger curvature, compensation could be applied by knowing the coil's deformation angle.
Future works will include the extension of these results to 3-D localization as well as adding a fourth OPM position for improved accuracy, especially at greater distances. Therefore, the magnetic field characteristic obtained in 1-D should be extended in 3-D, with, for instance, the simulation of the 3-D magnetic field generated by the flexible coil with multiphysics software (e.g., Comsol Multiphysics). Vector output (i.e., B_x, B_y and B_z) can also be retrieved from scalar measurements using a three-axis coil attachment provided by the OPM manufacturer. With the three magnetic field components, two orientation angles can be extracted, which is highly valuable for biomedical applications. However, OPM technology has a major drawback: a drop in the sensor sensitivity in certain configurations, known as dead-zones. According to the QTFM Gen-2 datasheet, this sensor enters a dead-zone when aligned within a 7° cone in the direction of the Earth's magnetic field. However, this limitation is also being investigated with potential solutions such as the assembly of two vapor cells [273].

Conclusion

The proposed EMT system, based on cutting-edge OPM technology and flexible coils generating ultra-low intensity ac magnetic fields, offers an innovative approach to biomedical devices localization. We demonstrated a position error of less than 3 mm in 2-D. In addition, the tracking of bent flexible coils was explored and confirmed, extending to potential applications involving mechanical constraints.

Additional publications

Below is a list of publications produced during the PhD project. This list includes side projects and collaborative research.

First author peer-reviewed publications in international scientific journals

1. Badertscher P* , **Vergne C*** , Féry C, Mannhart D, Quirin T, Osswald S, Kühne M, Sticherling C, Knecht S* and Pascal J*. 'Magnetic field interactions of smartwatches and portable electronic devices with CIEDs – Did we open a Pandora's box?'. IJC Heart & Vasculature, 43, 101122. Sept 2022.
2. **Vergne C**, Inácio J, Quirin T, Sargent D, Madec M, and Pascal J (2023). 'Tracking of a magnetically navigated millirobot with a magnetic field camera'. IEEE Sensors Journal, vol. 24, no. 6, pp. 7336-7344. March 2024.

* These two first and two last authors contributed equally.

Co-author peer-reviewed publications in international scientific journals

1. Meier Y, Duhr P, Mordarski M, **Vergne C**, Poloni E, Studart A, Pascal J, Demirörs A. 'Magnetic Hair Tactile Sensor for Directional Pressure Detection', Adv. Intell. Syst. 2400106. June 2024.

Peer-reviewed conference proceedings

Oral presentation

1. Badertscher P, **Vergne C**, Fery C, Spies F, Schlageter V, Mannhart D, Quirin T, Kuehne M, Sticherling C, Pascal J and Knecht S. Magnetic field interactions of smartwatches and portable electronic devices with cardiovascular implantable electronic devices. EP Europace, Volume 24, Issue Supplement_1, May 2022, euac053.576.
2. Quirin T, **Vergne C**, Féry C, Badertscher P, Nicolas H, Mannhart D, Osswald S, Kuhne M, Sticherling C, Madec M, Hébrard L, Knecht S and Pascal J. A magnetic camera to assess the risk of magnetic interaction between portable electronics and cardiac implantable electronic devic-es, 2022 IEEE International Symposium on Medical Measurements and Applications (Me-MeA), Messina, Italy, 2022, pp. 1-6.
3. **Vergne C**, Inacio J, Quirin T, Sargent D, and Pascal J. 'Millirobot magnetic manipulation for ocular drug delivery with sub millimeter precision'. 2022 IEEE Sensors Conference, Dallas, TX, USA, 2022, pp. 1-4.
   ⋆ *IEEE Sensors 2022 Best Student Paper Award*

4. Quirin T, Féry C, **Vergne C**, Madec M, Hébrard L and Pascal J. A Magnetic Tracking System Featuring Calibrated Three-Axis AMR Sensors. Proceedings. 2024; 97(1):31.
5. Filipozzi M, **Vergne C**, Rauter G and Cattin P. 'Ultra Miniaturized Absolute Rotary Encoder Integrated into Hinge Joint'. 2024 IEEE Sensors Conference, Kobe, Japan, 2024.
https://doi.org/10.1109/SENSORS60989.2024.10784533

Poster presentation

1. Nicolas H, **Vergne C** and Pascal J. 'Iron detection method based on high-resolution magnetic field camera'. 2024 IEEE Sensors Conference, Kobe, Japan, 2024.
https://doi.org/10.1109/SENSORS60989.2024.10784707

International conferences; refereed without associated proceedings

Poster presentation

1. Nicolas H, **Vergne C**, Quirin T and Pascal J. 'Application specific magnetic field cameras for biomedical engineering'. International Symposium on Integrated Magnetics 2023, Sendai, Japan, May 14-15, 2023

Version résumé
(in french)

Système de tracking électromagnétique pour l'implantation d'électrodes de stimulation cérébrale profonde utilisant des capteurs magnétiques intégrés

Céline Vergne, Basel, April 2025

Préface

Le projet de recherche est le fruit d'une collaboration entre la Haute école des sciences appliquées et des arts du nord-ouest de la Suisse (FHNW), l'Université de Bâle et l'Université de Strasbourg. Cette thèse de doctorat a été développée dans le cadre de la bourse du Fonds national suisse de la recherche scientifique (204448), intitulée « Development of an Electromagnetic Tracking System for the Implantation of Deep Brain Stimulation Electrodes ». Dans ce contexte, mon projet de recherche a été mené dans un environnement international et multidisciplinaire. Ce cadre a été très gratifiant, offrant de riches possibilités d'apprentissage, mais il a également présenté de nombreux défis.

Résumé

La stimulation cérébrale profonde (DBS) est devenue un traitement essentiel des troubles neurologiques et psychiatriques. Malgré son succès, la chirurgie de stimulation cérébrale profonde est confrontée à des défis majeurs, notamment le placement et l'orientation précis des électrodes et l'optimisation des paramètres de stimulation. Les méthodes traditionnelles s'appuient fortement sur l'imagerie stéréotaxique et les enregistrements physiologiques intra-opératoires, mais ne disposent pas d'un tracking temps réel. Cette limitation met en évidence le besoin de solutions innovantes pour améliorer à la fois la précision chirurgicale et les résultats thérapeutiques.

Cette thèse se concentre sur le développement d'un démonstrateur de système de tracking électromagnétique (EMT) pour relever le défi de la localisation DBS. Le système proposé combine des champs magnétiques quasi-statiques avec des capteurs magnétiques intégrés. Une évaluation complète des performances du système EMT et de son applicabilité à la chirurgie DBS a été réalisée. Les résultats expérimentaux ont démontré des performances de tracking fiables avec respectivement, une erreur spatiale et angulaire de 1,7 mm et 0,9°. En outre, le système a prouvé sa robustesse lorsqu'il est utilisé avec des systèmes stéréotaxiques. Outre la localisation en temps réel, cette recherche met l'accent sur l'intégration du nouveau système EMT dans la procédure chirurgicale DBS. Une nouvelle méthode de recalage, utilisant les mêmes capteurs magnétiques, a été mise au point pour simplifier le processus chirurgical. Cette approche réduit la charge de travail des équipes médicales tout en garantissant une localisation précise lors de la visualisation des positions des électrodes par rapport aux structures cérébrales.

En relevant les défis techniques et cliniques associés à la DBS, cette recherche souligne le potentiel des systèmes EMT pour améliorer la précision chirurgicale, réduire les risques procéduraux et, à long terme, améliorer les résultats thérapeutiques, marquant ainsi un pas en avant dans l'intégration des technologies de pointe dans la pratique neurochirurgicale.

Mots clés: DBS, neurochirurgie stéréotaxique, système EMT, capteur magnétique, procédure chirurgicale.

1. Introduction

La stimulation cérébrale profonde (DBS) s'est imposée comme une intervention neurochirurgicale transformatrice pour la prise en charge des troubles du mouvement tels que la maladie de Parkinson, les tremblements essentiels et la dystonie. En délivrant une stimulation électrique à des structures cérébrales ciblées (Fig. R.1), la DBS soulage efficacement les symptômes et améliore la qualité de vie des patients. Malgré son efficacité reconnue, plusieurs aspects de la procédure, en particulier le placement et la programmation de la stimulation, présentent encore des défis [2, 3]. L'une des étapes critiques de la chirurgie DBS est le positionnement précis de l'électrode par rapport à la cible anatomique. Traditionnellement, ce positionnement est réalisé à l'aide de systèmes stéréotaxiques guidés par l'imagerie pré-opératoire. Toutefois, ces approches ne permettent pas d'obtenir un retour d'information en temps réel sur la position et l'orientation de l'électrode pendant l'implantation.

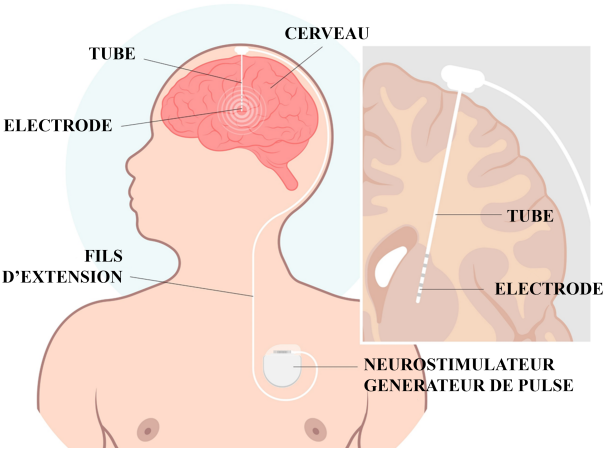

Figure R.1: Système de stimulation cérébrale profonde.

Motivation

Les progrès récents de la technologie DBS ont permis l'utilisation d'électrodes directionnelles qui permettent un meilleur contrôle des régions cérébrales stimulées. Dans ce contexte, la connaissance de la position et de l'orientation de l'électrode par rapport à l'anatomie du cerveau est cruciale. Cependant, les méthodes actuelles fournissent un retour d'information per-opératoire limité. Une solution potentielle est le développement de systèmes de tracking complémentaires, la technique de tracking électromagnétique (EMT) apparaissant comme une option prometteuse. Malgré les progrès réalisés dans les systèmes EMT, les solutions existantes sont confrontées à des problèmes tels que les interférences causées par les objets métalliques dans la salle d'opération. De nouvelles approches combinant des champs magnétiques quasi-statiques et des capteurs magnétiques miniaturisés présentent un grand potentiel pour relever ces défis. Le développement d'un système de localisation robuste pourrait combler les lacunes existantes et améliorer la sécurité et l'efficacité de la chirurgie DBS.

Intention

Cette thèse propose un nouveau système EMT et évalue ses performances et son potentiel pour fournir en temps réel, le positionnement des électrodes DBS pendant la chirurgie. Le système vise à surpasser les systèmes EMT existants en proposant:

- ❉ **Localisation précise des électrodes:** Erreur spatiale et angulaire inférieure à 1 mm et 1°, satisfaisant ou dépassant les normes basées sur l'imagerie.
- ❉ **Intégration & Adaptabilité:** Compatibilité avec les procédures chirurgicales existantes, y compris les techniques stéréotaxiques et les techniques d'enregistrement per-opératoire.

En répondant à ces objectifs, le système proposé ouvre la voie à l'amélioration de la précision des procédures DBS et à l'optimisation des paramètres de stimulation. En outre, ce travail contribue à l'adoption clinique plus large des technologies de tracking avancées.

2. Contexte médical & technique

2.1. Stimulation cérébrale profonde (DBS)

La DBS est une procédure neurochirurgicale moderne qui implique l'implantation d'électrodes dans des régions spécifiques du cerveau. Ces électrodes délivrent des impulsions électriques permettant de moduler l'activité neuronale anormale dans les zones cérébrales ciblées. La DBS est l'une des interventions chirurgicales les plus avancées sur le plan technologique, résultant de la convergence de multiples contributeurs et innovations. Après des années de recherche et d'innovations technologiques, la DBS a démontré son efficacité en améliorant significativement le contrôle moteur et la qualité de vie des patients atteints de troubles du mouvement. Son utilisation s'est également élargie à des pathologies comme l'épilepsie et certains troubles psychiatriques [40]. L'implantation chirurgicale du système DBS est une procédure complexe, avec des différences significatives entre les centres en ce qui concerne les techniques, les outils et le temps consacré à chaque étape de la procédure [41, 42]. Étant donné que la DBS implique l'implantation d'une électrode dans des structures cérébrales de l'ordre du millimètre, il est essentiel de relier avec précision l'anatomie du patient à l'espace de référence utilisé pendant l'intervention. Le système stéréotaxique joue ce rôle en définissant un référentiel 3D et en servant de guide mécanique pour un ciblage précis. Bien que de nouvelles approches aient été proposées pour la mise en œuvre de la DBS, la majorité des centres privilégient encore les méthodes basées sur le cadre stéréotaxique, bénéficiant de leur fiabilité éprouvée et de leur longue expérience. Une vue d'ensemble simplifiée du déroulement de l'intervention chirurgicale pour la DBS est illustrée dans la Figure R.2. Cette vue d'ensemble est basée sur l'utilisation d'un système stéréotaxique et incorpore des tests per-opératoires.

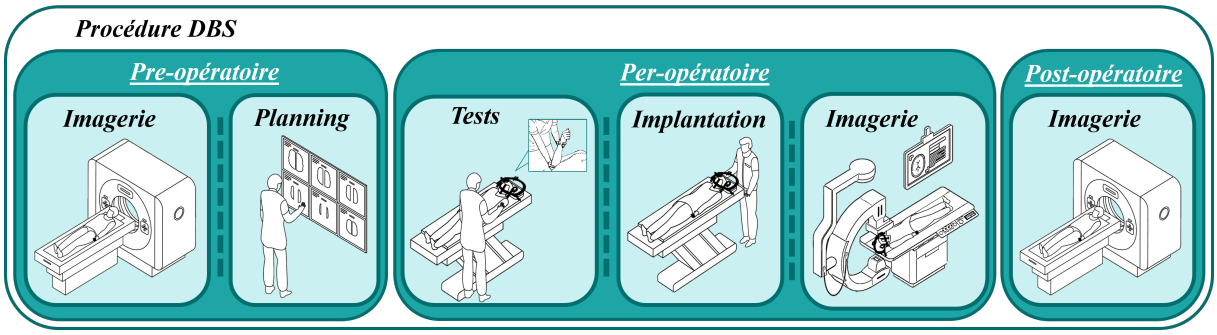

Figure R.2: Vue d'ensemble simplifié du déroulement de la chirurgie DBS, comprenant les étapes pré-opératoires, per-opératoires et post-opératoires.

❊ **Etape pré-opératoire : Imagerie & Planning chirurgical**
Avant l'opération, une imagerie cérébrale détaillée (généralement IRM ou CT scan) est réalisée pour cartographier le cerveau du patient, identifier les zones cibles pour le placement des électrodes ainsi que les marqueurs pour l'espace de référence stéréotaxique. Ces structures cibles étant très petites, généralement quelques millimètres, cela les rend difficiles à imager et à visualiser.

❊ **Etape per-opératoire: Test, Implantation & Validation**
Compte tenu des difficultés liées au ciblage précis des structures cérébrales profondes lors de l'implantation d'un DBS, des tests per-opératoires sont couramment utilisés pour optimiser le placement des électrodes. Une fois que la position finale de l'électrode DBS a été définie, l'imagerie est réalisée pour valider sa position par rapport à la cible pré-opératoire. Selon les centres cliniques, différentes modalités telles que la radiographie 2D, la fluoroscopie, IRM ou CT per-opératoires, peuvent être utilisées. Cette étape d'imagerie fournit une première confirmation visuelle, plus ou moins détaillée, de la position de l'électrode.

❊ **Etape post-opératoire: Imagerie & Suivi**
Après l'ancrage de l'électrode DBS sur le crâne du patient et la suture du cuir chevelu, une imagerie 3D supplémentaire est réalisée pour obtenir la position et l'orientation de l'électrode ainsi que vérifier l'absence d'hémorragie.

La procédure est très individualisée, avec des étapes chirurgicales, y compris les tests per-opératoires et les techniques d'imagerie, qui varient selon les préférences du neurochirurgien et les équipements disponibles. Ces dernières années, d'importants progrès ont été réalisés notamment dans les techniques opératoires et la conception des électrodes. Toutefois, des défis persistent et de nouveaux enjeux émergent. Ces éléments mettent en évidence l'importance du tracking en temps réel du positionnement des électrodes afin d'améliorer la précision et d'optimiser les résultats thérapeutiques.

- ➥ **Défis liés au positionnement des électrodes DBS:** L'imagerie per-opératoire améliore à la fois le confort du patient et l'efficacité de la chirurgie en réduisant la nécessité de déplacer le patient et en rationalisant les étapes de la procédure. Cependant, l'imagerie n'est disponible qu'avant et après l'implantation de l'électrode DBS. Les neurochirurgiens ne disposent donc pas d'un retour d'information en temps réel sur la position et l'orientation de l'électrode au cours de la procédure. Ce retour d'information est crucial car il permettrait de valider le processus d'implantation, signaler les déviations de trajectoire et fournir un positionnement précis de l'électrode pendant les enregistrements per-opératoires. Malgré son potentiel, ce défi n'est toujours pas relevé, car aucun système disponible en clinique n'y répond actuellement.
- ➥ **Défis de la programmation DBS:** Les électrodes DBS conventionnelles possèdent entre quatre et huit contacts cylindriques permettant de stimuler les tissus environnants. Cependant, en raison de la forme irrégulière des structures anatomiques, une seule électrode peut difficilement cibler précisément une zone sans affecter involontairement les régions adjacentes. Pour pallier ce problème, des électrodes directionnelles ont été développées, offrant un contrôle plus précis de la stimulation électrique. Elles améliorent la précision du ciblage, réduisent les effets secondaires et optimisent les résultats cliniques. Toutefois, leur conception plus complexe rend la programmation plus difficile, reposant encore sur une approche manuelle par essais et erreurs. Les récents progrès des outils d'aide à la programmation, tant académiques que commerciaux, permettent de visualiser les structures anatomiques, de simuler les zones d'activation et d'optimiser les paramètres. Cependant, leur efficacité dépend de la connaissance précise de la position et de l'orientation de l'électrode dans le cerveau.

2.2. Systèmes de localisation et de navigation pour DBS

Plusieurs technologies non invasives, telles que l'échographie transcrânienne [4, 101], ou l'électroencéphalographie [102] ont également été étudiées pour leur potentiel à localiser les électrodes DBS en per-opératoire. Bien que prometteuses, ces méthodes exploratoires ne sont pas compatibles avec l'utilisation per-opératoire et les procédures stéréotaxiques DBS. La technologie la plus prometteuse repose sur la technique EMT.

Systèmes de tracking électromagnétique existants et leurs limites

Les systèmes EMT sont traditionnellement utilisés pour la navigation chirurgicale lors d'interventions guidées par image, sans ligne de vue. Les applications cliniques actuelles exploitant l'EMT pour la localisation des instruments incluent la bronchoscopie [109], la neurochirurgie [110] et la chirurgie de l'oreille, du nez et de la gorge [111]. Dans le contexte de DBS, la localisation à l'aide d'un système EMT pour la navigation chirurgicale a déjà été démontrée cliniquement par Burchiel [108] en 2020. L'étude a été réalisée en utilisant une approche sans cadre stéréotaxique et fait état de

performances comparables à celles de l'imagerie CT. Cependant, les systèmes EMT actuels sont très sensibles à la présence d'objets métalliques ou magnétiques dans le volume de tracking, ce qui limite leur application dans les chirurgies impliquant de nombreux équipements. Ces systèmes reposent sur un champ magnétique alternatif de faible intensité généré par un ensemble de bobines positionnées à proximité de la zone chirurgicale. Leur technologie de détection est basée sur des micro-bobines et sur le principe de tracking (Figure R.3(A)). De faibles tensions sont induites dans la micro-bobine par le champ électromagnétique alternatif. Ces tensions sont ensuite traduites en données de position en temps réel. Outre le générateur de champ (FG) et les capteurs, les systèmes EMT comprennent également un contrôleur, un logiciel de visualisation et un système de recalage. Le système de recalage permet d'aligner la position de l'outil chirurgical sur l'imagerie pré-opératoire du patient. Ce processus de recalage est généralement réalisé en se référant à des marqueurs externes ou à des repères anatomiques visibles dans les données d'imagerie et détectables par le système EMT. Enfin, le logiciel de visualisation intègre généralement les données d'imagerie pré-opératoire, ce qui permet au chirurgien de visualiser la position en temps réel de l'instrument par rapport aux structures anatomiques.
Bien que les systèmes EMT présentent plusieurs avantages, tels que le guidage sans rayonnement X et le tracking en temps réel avec une précision spatiale submillimétrique, ils font face à des défis techniques. La principale limitation étant les interférences électromagnétiques. La précision des systèmes EMT, qui repose sur la géométrie connue du champ électromagnétique généré, est fortement influencée par les distorsions du champ. Ces distorsions peuvent notamment être causées par des champs électromagnétiques externes, induits par des matériaux ferromagnétiques ou des appareils électroniques. Ce phénomène se manifeste par des déviations dans les lignes de champ magnétique produites par FG. Le deuxième type d'interférences est appelé distorsions conductrices. Les champs électromagnétiques alternatifs produits par le FG induisent des courants de Foucault dans les matériaux conducteurs. Ces courants génèrent un champ secondaire qui interfère avec le champ primaire.

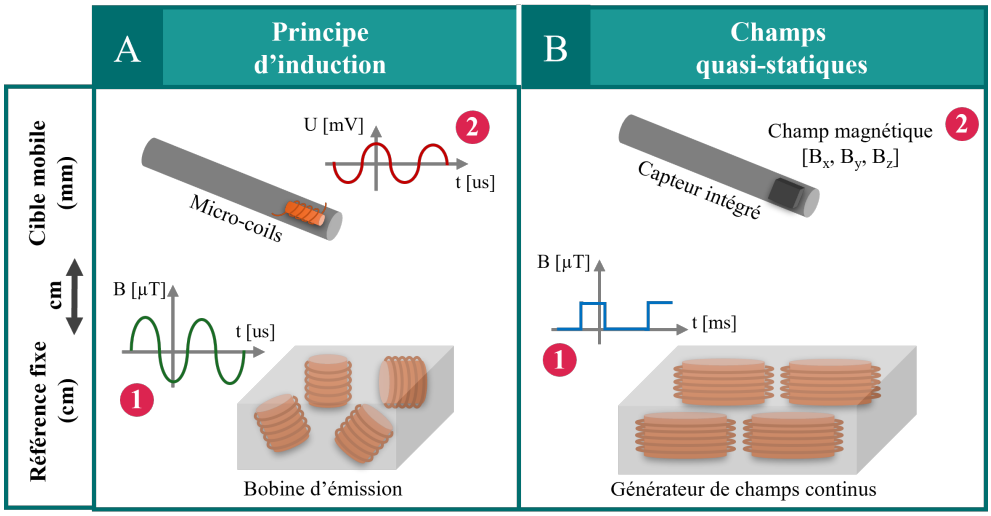

Figure R.3: Schéma décrivant les deux principes de tracking électromagnétique : (A) Principe d'induction sur lequel sont basés la plupart des systèmes électromagnétiques existants, (B) Principe basé sur des champs magnétiques quasi-statiques.
Les chiffres représentent la séquence étape par étape de la technique EMT.

Nouveaux systèmes de tracking électromagnétique

La recherche dans ce domaine s'est largement concentrée sur deux approches principales: l'amélioration des technologies existantes et la proposition de nouveaux principes EMT pour surmonter les limitations actuelles. Une approche innovante et prometteuse repose sur l'utilisation de capteurs

magnétiques monolithiques intégrés et de champs magnétiques quasi-statiques (Figure R.3(B)). Dans cette approche, les bobines du FG sont activées séquentiellement pour générer des champs magnétiques continus, qui sont ensuite détectés par les magnétomètres intégrés dans l'outil chirurgical. Cette configuration fournit un système d'encodage spatial unique dans le volume de tracking, offrant des performances comparables aux méthodes traditionnelles. En 2021, Sharma et al. [135] ont fait la démonstration d'un système basé sur des capteurs magnétiques à effet Hall à trois axes permettant d'obtenir des performances de tracking inférieures à 100 μm d'erreur. Le principal avantage de cette technique réside dans sa robustesse face aux interférences électromagnétiques, en particulier les distorsions conductrices. Les premières études ont montré que les systèmes EMT quasi-statiques sont compatibles avec certains outils chirurgicaux et équipements médicaux. Cependant, ces systèmes sont confrontés à plusieurs défis. Un problème important est la nécessité d'une caractérisation précise du champ magnétique généré, pour assurer de bonnes performances de tracking. Une autre limitation est la forte décroissance du champ magnétique à mesure que l'on s'éloigne du FG. L'augmentation de l'intensité du champ magnétique et l'utilisation de capteurs à haute résolution permettent de trouver un compromis entre des performances adéquates, la minimisation de la consommation d'énergie et de l'échauffement de la bobine. La dernière limite est la fréquence d'échantillonnage du système EMT, qui est limité par la fréquence des capteurs magnétiques et par le temps d'activation pour chaque bobine.

Malgré les avancées prometteuses des systèmes EMT, plusieurs défis subsistent. L'un des principaux obstacles demeure leur sensibilité aux interférences, notamment celles générées par les objets métalliques ou ferromagnétiques, fréquemment présents en salle d'opération. Grâce aux progrès en miniaturisation et en sensibilité des capteurs magnétiques, de nouveaux systèmes EMT peuvent être développés. L'approche reposant sur les champs magnétiques quasi-statiques et les capteurs magnétiques intégrés démontre un fort potentiel. Ces systèmes offrent une solution prometteuse pour localiser avec précision les électrodes DBS tout en garantissant leur compatibilité avec les procédures stéréotaxiques.

2.3. Magnetic sensing technologies

Les capteurs magnétiques jouent un rôle clé dans de nombreuses applications [136]. Ils se déclinent en plusieurs catégories selon leur principe de fonctionnement, chacune ayant des caractéristiques spécifiques adaptées à différentes utilisations [137]. Ces dernières années, leur technologie a considérablement évolué, répondant à une demande croissante en haute résolution, miniaturisation et performances optimisées dans des environnements complexes. Malgré ces progrès, plusieurs défis persistent dans le développement des capteurs magnétiques. L'un d'entre eux est le compromis entre la sensibilité et la taille. La miniaturisation est cruciale pour de nombreuses applications, mais la réduction de la dimension du capteur se traduit souvent par une augmentation du bruit. Les progrès en cours dans le domaine des nanomatériaux et de la conception de capteurs innovants devraient permettre de résoudre ce problème et de créer des capteurs magnétiques miniatures mais conservant leur sensibilité.
Certaines technologies permettent de mesurer l'intensité et la direction des champs magnétiques sur les trois axes spatiaux (X, Y, Z), une capacité essentielle pour le suivi précis de l'orientation, le positionnement 3D et les systèmes de navigation avancés. Parmi les technologies de détection existantes, peu d'entre elles sont disponibles sous forme monolithique et en trois axes. Le conditionnement sur puce (monolithique) offre de nombreux avantages en plus de la miniaturisation : haute fiabilité, grande robustesse et durée de vie prolongée. Par conséquent, les capteurs magnétiques monolithiques à haute-résolution, sont de bons candidats pour leur combinaison au sein d'un système EMT basé sur des champs magnétiques quasi-statiques.

3. Objectifs

Ce travail se concentre sur le développement d'un système EMT innovant qui combine des champs magnétiques quasi-statiques avec des capteurs magnétiques intégrés. L'objectif principal de cette thèse est de concevoir un démonstrateur basé sur cette nouvelle méthode pour les applications DBS. Cette recherche constitue une première étape vers la localisation en temps réel de la position et de l'orientation de l'électrode DBS pendant la chirurgie, avec pour but d'améliorer les pratiques actuelles de DBS et les résultats thérapeutiques à long terme. Pour répondre aux exigences DBS, le système vise une surveillance en temps réel avec une erreur spatiale inférieure à 1 mm et une erreur angulaire d'environ 1 degré. Bien que la résolution temporelle requise pour le système soit moins stricte que pour d'autres applications chirurgicales, une résolution de 500 ms est jugée suffisante pour la chirurgie DBS. De plus, le système doit intégrer une méthode de recalage permettant de visualiser les électrodes DBS par rapport aux structures anatomiques du cerveau. Le système global doit être soigneusement conçu pour garantir la compatibilité avec les procédures et outils chirurgicaux existants.
Cette intention générale a été divisée en objectifs spécifiques abordés dans les quatre publications qui constituent cette thèse :

➥ Proposer une nouvelle méthode de localisation 3D basée sur des capteurs magnétiques monolithiques à haute résolution et des champs magnétiques quasi-statiques. Conclure sur les exigences et les meilleures technologies de détection actuelles pour cette approche.
➥ Concevoir un démonstrateur EMT pour la chirurgie DBS en tenant compte des spécifications de l'environnement chirurgical. Étendre la méthode de localisation à la détection de l'orientation.
➥ Valider l'adéquation du système EMT développé avec le cadre de la chirurgie DBS et plus particulièrement avec le système stéréotaxique. Comparer les performances du système EMT développé aux systèmes existants pour la chirurgie DBS.
➥ Fournir une méthode de recalage pour l'intégration du système EMT dans la procédure chirurgicale.

4. Resultats

4.1. Publication I - Concept

Publication I présente une nouvelle technique de localisation des électrodes DBS utilisant un champ magnétique quasi-statique et des capteurs magnétiques intégrés. Ce travail examine et discute les exigences relatives à la sensibilité des capteurs magnétiques ainsi que les gradients du champ magnétique généré par le FG. Ces deux aspects sont les principales caractéristiques de cette nouvelle technique EMT. En visant la génération d'un champ magnétique de faible intensité et en tenant compte du gradient minimal du champ magnétique dans le volume de mesure, des capteurs de type magnétorésistance anisotrope ont été sélectionnés pour leur résolution exceptionnelle et leur faible bruit rms. Ces capteurs de taille millimétrique peuvent être intégrés dans des outils chirurgicaux, tels que les électrodes DBS. La technique de localisation utilisée dans ce travail est basée sur la multilatération, une méthode qui détermine la position d'un objet en analysant les signaux émis par plusieurs émetteurs. La multilatération fonctionne en calculant les distances entre le récepteur et les émetteurs, permettant ainsi la création de sphéroïdes centrés sur chaque émetteur. La position de l'objet est déterminée mathématiquement en identifiant l'intersection de ces sphéroïdes. Dans le contexte des champs électromagnétiques, les émetteurs sont des générateurs de champ, représentés ici par trois bobines de cuivre, tandis que le récepteur est un capteur intégré dans l'électrode DBS. Les signaux utilisés sont les composants du champ magnétique générés par chaque bobine. Cette technique est avantageuse en raison de sa simplicité tant dans la génération que dans la détection des champs magnétiques.

Cependant, son efficacité dépend fortement de la précision des processus de génération et de détection du champ magnétique. Cette première version a conduit à un encodage spatial sans ambiguïté et avec une erreur absolue moyenne de 3 mm à 42 cm du FG.

4.2. Publication II - Développement & Performance

Publication II prolonge cette étude initiale en proposant une version améliorée capable de déterminer l'orientation du capteur ainsi que d'évaluer les performances du système dans le cadre de la chirurgie DBS. Cette version inclut un générateur de champ optimisé, conçu pour garantir des gradients de champ magnétique adéquats dans le volume de mesure, tout en restant compatible avec les installations chirurgicales DBS (Figure R.4). Le nombre de bobines du générateur de champ a été porté à quatre pour améliorer les performances. Ces bobines ont été fabriqué sur circuits imprimés assurant une grande reproductibilité et des champs magnétiques précis.

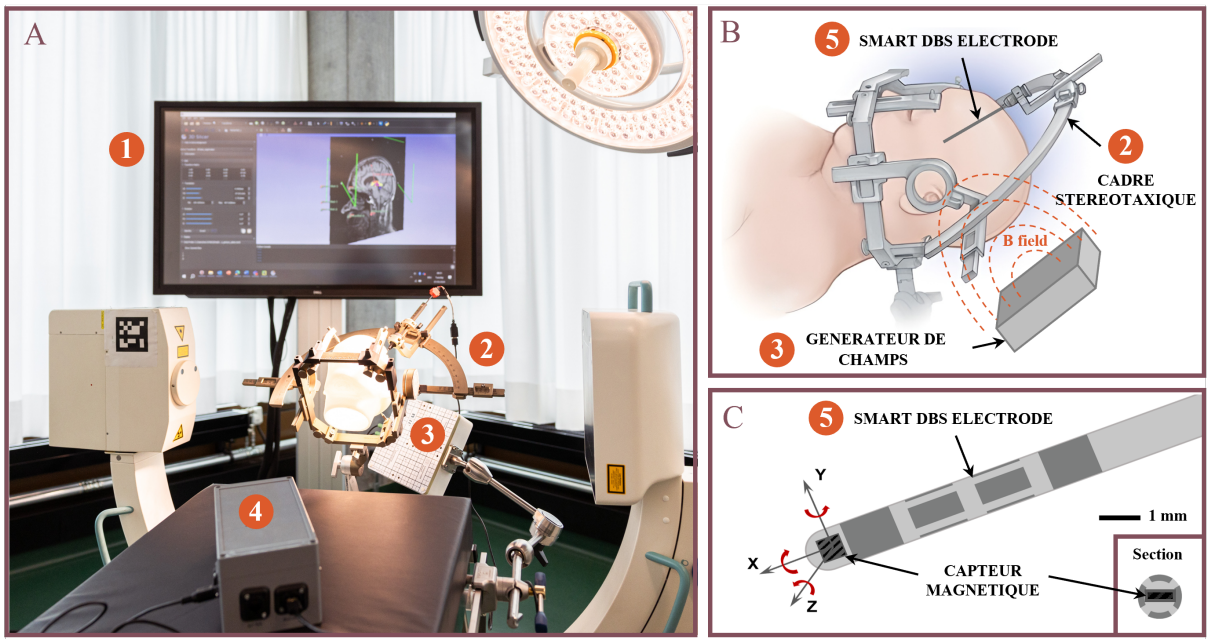

Figure R.4: (A) Photo du système EMT et de son intégration dans l'environnement chirurgical DBS ; 1) Logiciel de visualisation montrant la localisation de l'électrode DBS par rapport à l'imagerie du patient, 2) Cadre stéréotaxique fixé à la table d'opération, 3) FG fixé à la table d'opération et placé près de la tête du patient, 4) Unité de contrôle du système EMT. (B) Image conceptuelle du système EMT. (V) Image conceptuelle de 5) l'électrode DBS intégrant le capteur à son extrémité.

En utilisant la même séquence d'activation, l'algorithme de tracking a été étendu pour déterminer l'orientation en utilisant les trois composants du champ magnétique, tandis que la position est dérivée du vecteur de champ magnétique. Cela souligne la nécessité de capteurs de champ magnétique à trois axes. La localisation des positions a été évaluée à l'aide d'une caméra de champ magnétique placée à diverses positions dans le volume de mesure (Figure R.5), tandis que l'orientation a été évaluée à l'aide d'un système stéréotaxique utilisé dans la chirurgie DBS. Enfin, des implantations DBS ont été simulées pour conclure sur la validité du système de tracking pour la chirurgie DBS (Figure R.6). Les résultats démontrent l'efficacité du système, avec une erreur de localisation moyenne de 1,72 mm et une erreur angulaire de 0,89°. Ces performances ont été obtenues dans un volume de 15 x 15 x 15 cm^3, et à une distance de 18 cm par rapport au FG.

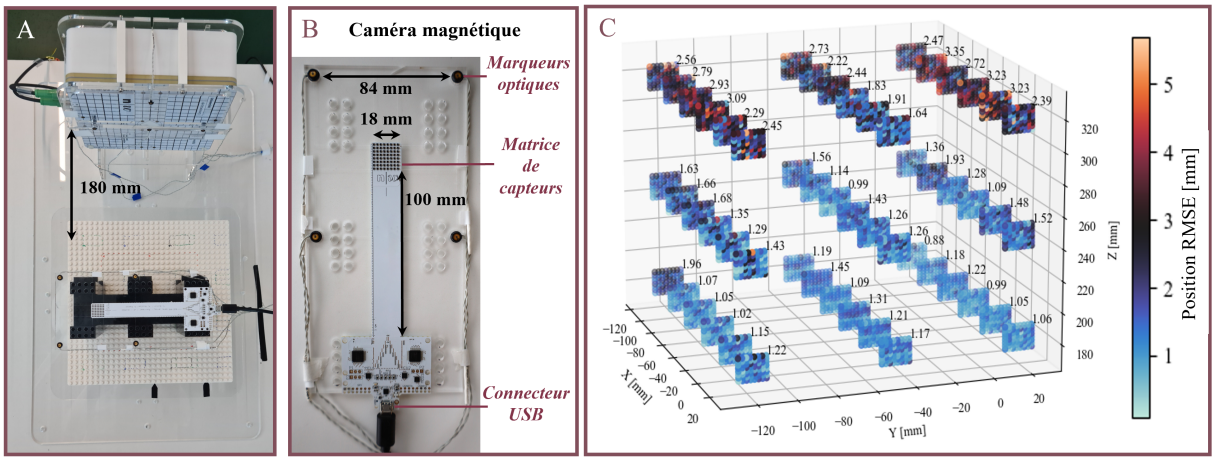

Figure R.5: (A) Banc expérimental comprenant le FG et la caméra magnétique placée à 18 cm. (B) Plaque intégrant les marqueurs optiques et la caméra magnétique. (C) Visualisation 3D de l'erreur de position dans le volume de mesure.

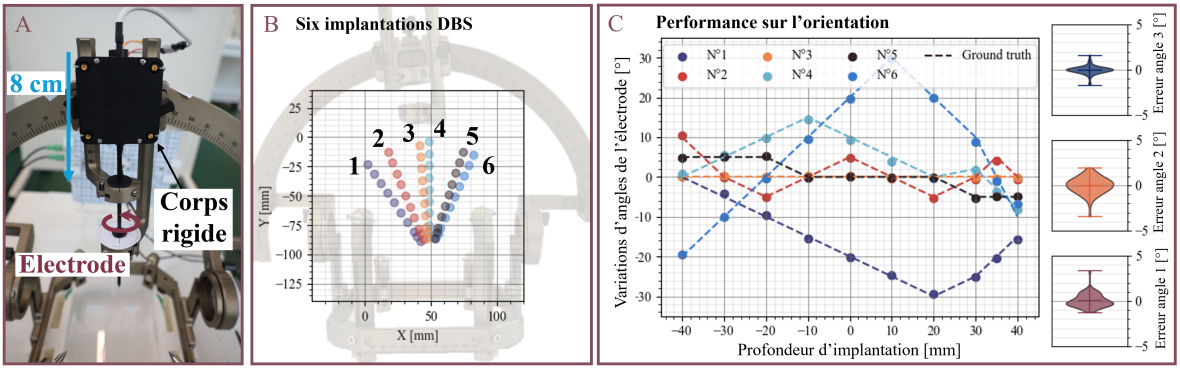

Figure R.6: (A) Corps rigide intégrant les marqueurs optiques sur le prototype d'électrode DBS. (B) Visualisation 3D des six implantations DBS avec le cadre stéréotaxique en transparence. (C) Variations de l'angle des électrodes pour chaque implantation. Les marqueurs circulaires indiquent l'angle obtenu à partir du système EMT; la ligne pointillée représente les angles obtenus à partir du tracking optique.

Le système a cependant montré des performances non uniformes en fonction de la position des capteurs par rapport au FG. De plus, la fréquence d'échantillonnage du système est relativement faible (0,4 Hz). Bien que cette fréquence puisse potentiellement être augmenté à quelques Hz, il reste limité par l'activation séquentielle des bobines et par le nombre de mesures des capteurs nécessaires pour maintenir la précision du tracking. Le système DBS est destiné à être utilisé pendant la phase d'implantation des électrodes, comme DBS implique l'insertion lente et progressive d'électrodes dans le cerveau du patient, cette fréquence est considérée suffisante, surtout si on le compare à la résolution temporelle des systèmes d'imagerie.

4.3. Publication III - Compatibilité avec l'environnement chirurgical

Plutôt que d'optimiser le système, la thèse se concentre sur l'adéquation du système EMT à l'application chirurgicale. **Publication III** met en évidence la robustesse du système lorsqu'il est intégré avec des cadres stéréotaxiques, surpassant les systèmes commerciaux en limitant les erreurs

supplémentaires dues aux distorsions conductrices. Cet article vise à évaluer et comparer les performances de localisation (position et orientation) du nouveau système EMT par rapport à un système EMT commercialement disponible (Figure R.7). Deux études ont été menées pour évaluer l'adéquation de chaque système EMT pour la chirurgie stéréotaxique DBS. La première étude a évalué la précision des performances dans le volume de mesure en présence de deux systèmes stéréotaxiques différents (Frame G et Vantage, Elekta AG).

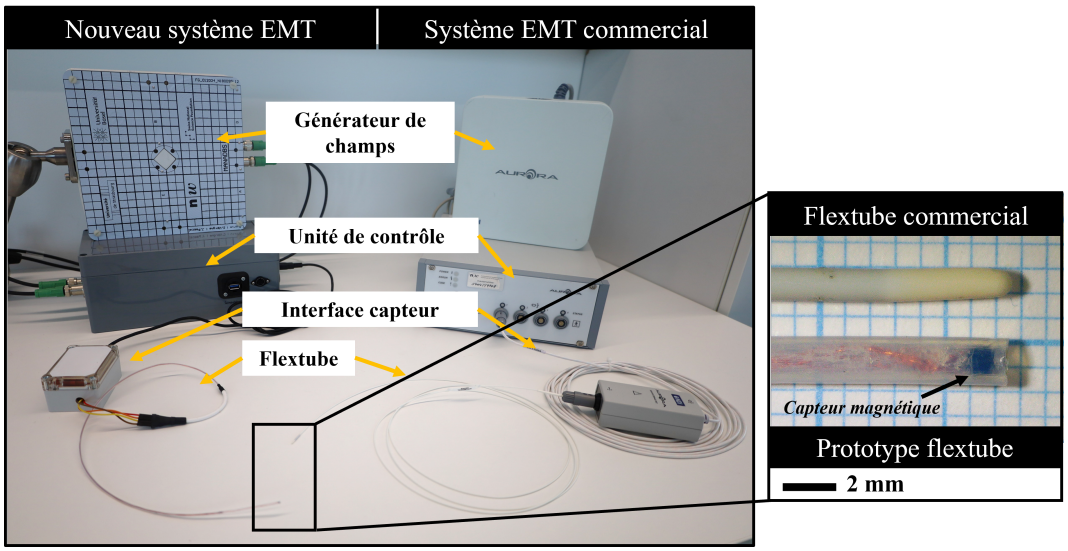

Figure R.7: Les deux systèmes de tracking : commercial (à droite) et le nouveau système que nous avons développé (à gauche), tous deux avec un FG de 20 × 20 × 7 cm et les flextubes associés d'un diamètre de 1,3 mm et 1,8 mm, respectivement.

La deuxième étude a simulé un théâtre chirurgical DBS, réalisant des procédures d'implantation avec chaque système EMT et évaluant la précision de position du capteur EMT. Les erreurs de localisation du système commercial (0,66 mm et 0,89°) étaient inférieures à celles du nouveau système (1,57 mm et 1,01°). Cependant, en présence d'un système stéréotaxique, le système commercial a montré une dégradation notable (2,34 mm et 1,03°), tandis que le second est resté inchangé. Ce schéma a persisté lors de la simulation d'implantation dans un environnement chirurgical DBS, où des fluctuations d'erreur significatives le long du chemin d'implantation ont été observées avec le système commercial (Figure R.8). Les distorsions significatives du champ électromagnétique rendent le système commercial incompatible pour la chirurgie stéréotaxique DBS. Cependant, le nouveau système EMT n'a montré aucun impact de ces distorsions, suggérant son adéquation potentielle pour la chirurgie DBS et d'autres applications potentielles en neurochirurgie stéréotaxique.

4.4. Publication IV - Intégration dans la procédure chirurgicale DBS

Publication IV introduit une méthode de recalage personnalisée adaptée à la neurochirurgie stéréotaxique, en mettant l'accent sur l'automatisation, la dépendance minimale à l'utilisateur et le caractère non invasif. L'intégration d'un système de navigation dans un flux de travail chirurgical introduit inévitablement des étapes et des erreurs supplémentaires. Pour minimiser ce phénomène, un système d'enregistrement a été mis au point, basé sur des marqueurs électroniques souples et sans fil, fixés au cadre stéréotaxique pendant la phase préopératoire (Figure R.9(C)). Ces marqueurs sont automatiquement segmentés sur les images CT préopératoires (Figure R.9(D)) et sauvegardés en tant que repères. Cette méthode de recalage a démontré des performances robustes avec une segmentation

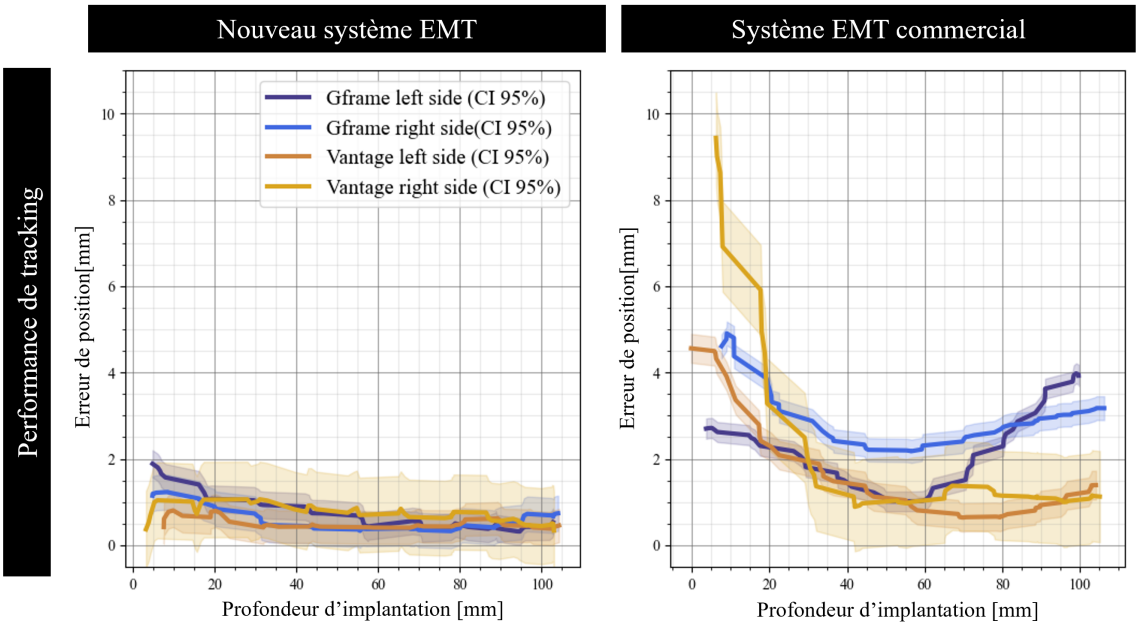

Figure R.8: Erreurs de position avec intervalles de confiance à 95% en fonction de la profondeur d'implantation pour le nouveau système et le système commercial. Données provenant des deux configurations stéréotaxiques (Gframe et Vantage) et des deux côtés d'implantation différents (gauche et droite).

automatique des marqueurs sur les images CT, atteignant une erreur moyenne de correspondance des points de 1,51 mm (Figure R.10(A)).
Pendant l'opération, le FG du système EMT est positionné derrière la tête du patient et fixé au rail latéral de la table d'opération. Le système EMT acquiert ensuite les positions des marqueurs stéréotaxiques et les recalent sur les positions obtenues par CT. Cela permet d'obtenir la matrice de transformation, qui est ensuite appliquée aux positions EMT suivantes, ce qui permet de visualiser l'électrode DBS par rapport au cerveau du patient à partir de l'imagerie préopératoire.
Développée comme une extension du système EMT, cette approche a atteint une erreur de localisation de 2,54 ± 0,92 mm, bien que la validation de l'orientation n'ait pas encore été confirmée (Figure R.10(B)). Le développement du système a été guidé par les exigences de la salle d'opération. Ces exigences ont été discutées avec les neurochirurgiens qui ont collaboré au projet. Les principaux objectifs de conception étaient la compacité et l'intégration transparente aux procédures DBS existantes dans différents centres cliniques. Cette méthode d'enregistrement, présentée comme une preuve de concept dans **Publication IV**, est prometteuse en raison de sa nature indépendante de l'utilisateur et entièrement automatisée. Cependant, son erreur de localisation actuelle est insuffisante pour la chirurgie DBS et doit être améliorée. Par exemple, des améliorations peuvent être obtenues en optimisant la conception et le placement des marqueurs sur le cadre stéréotaxique.

5. Discussion & Perspectives

5.1 Discussion

Cette thèse se concentre sur le développement d'un prototype initial d'un système EMT utilisant des champs quasi-statiques et des magnétomètres intégrés. Le système EMT développé permet une localisation régulière de la position et de l'orientation de l'électrode pour la chirurgie stéréotaxique

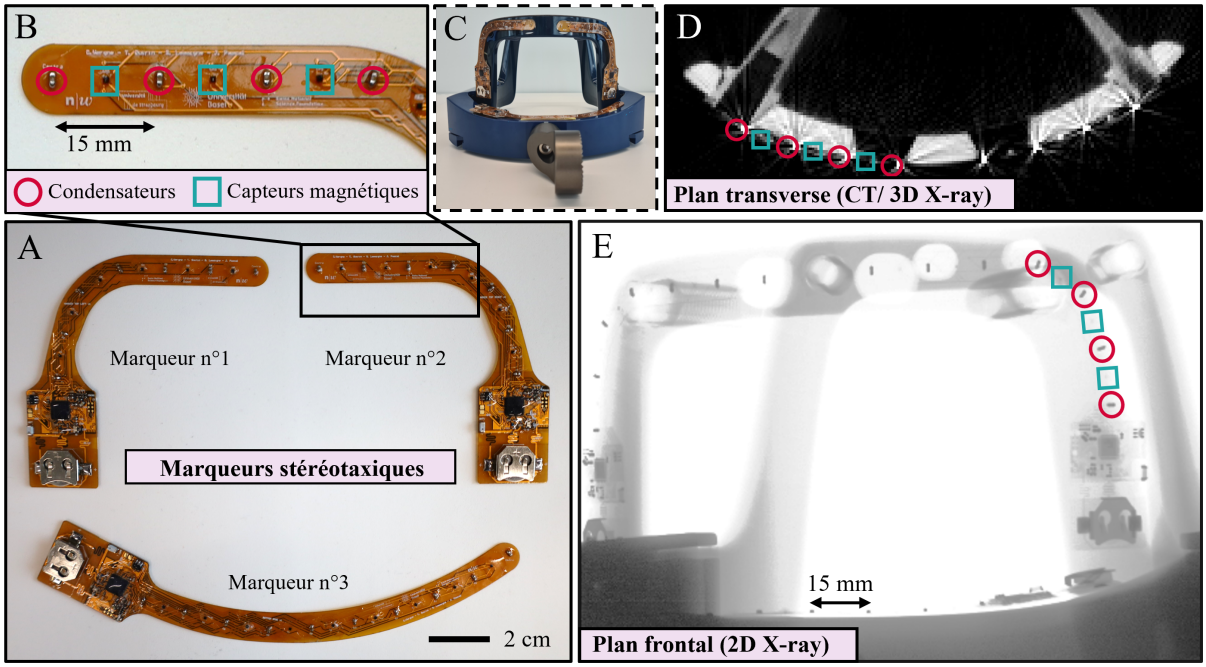

Figure R.9: (A) Marqueurs stéréotaxiques : Trois versions différentes pour une meilleure conformation au cadre stéréotaxique (total de 21 capteurs magnétiques). (B) Zoom sur le marqueur n°2 avec les capteurs magnétiques et les condensateurs. (C) Placement des trois marqueurs sur le cadre stéréotaxique. (D) Plan transversal d'un CT scans et (E) Plan frontal d'une radiographie 2D du cadre stéréotaxique et des marqueurs stéréotaxiques associés.

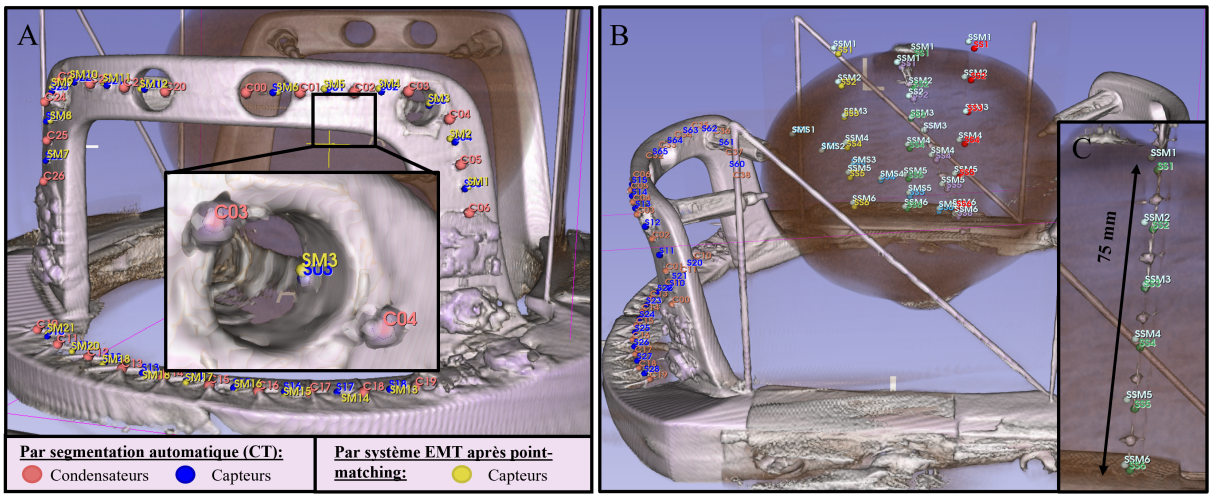

Figure R.10: (A) Visualisation de la partie postérieure du cadre stéréotaxique avec les condensateurs segmentés (en rose : C00:26) et les positions des capteurs résultantes (en bleu : S00:20) obtenues à partir de l'imagerie CT ainsi que les positions des capteurs (en jaune : SM1:21) obtenues à partir du système EMT. (B) Visualisation des cinq implantations. (C) Zoom sur une d'implantation, montrant les positions extraites manuellement du scanner (en vert, SS1 à SS6) ainsi que les positions EMT après recalage (en blanc, SSM1 à SSM6).

DBS, et fait le lien entre le développement technique du système et son intégration pratique dans les procédures chirurgicales.

Technique de tracking

Idéalement, les générateurs de champ devraient entourer le volume de mesure pour améliorer la précision de détection. Cependant, cette configuration est impraticable dans un environnement de salle d'opération. En guise de solution, une configuration planaire du FG a été adoptée, offrant compacité mais introduisant de nouveaux défis. Un défi majeur est la performance de localisation inégale. La performance est nettement meilleure au centre de la disposition plane, tandis qu'elle diminue vers la périphérie. Ce phénomène a été démontré dans la **Publication I**, où une précision de tracking submillimétrique a été atteinte au centre du FG. La **Publication II** a confirmé cette observation lors d'une évaluation complète de l'ensemble du volume de mesure, mettant en évidence la disparité de résolution entre le centre (environ 1 mm d'erreur de position) et les régions périphériques (environ 3 mm d'erreur de position). Puisque l'orientation est dérivée des composants du champ magnétique mesurés et de la position calculée, toute augmentation de l'erreur de détection de position aura un impact négatif sur la précision de la détermination de l'orientation.

Performance du système

Le système EMT offre des résolutions spatiales et angulaires comparables aux technologies d'imagerie, mais évite les longs temps d'acquisition et l'exposition aux radiations. Conçu pour aider les neurochirurgiens à prendre des décisions, il se concentre sur la localisation plutôt que sur le guidage actif de l'électrode. Comparé aux systèmes EMT existants, ce nouveau système présente des performances légèrement inférieures et un volume de mesure plus petit. Cependant, il reste bien adapté et prometteur pour les applications DBS. Les performances pourraient être améliorées en augmentant le rapport signal/bruit du système. Cela impliquerait de générer des champs magnétiques plus puissants ou d'utiliser des capteurs moins bruyants.

Il convient de noter que les performances du système ont été principalement évaluées avec des capteurs placés dans tout le volume, tous maintenant une orientation cohérente. Cette limitation provient de la configuration expérimentale, qui nécessitait une connaissance précise du placement des capteurs, se basant sur une caméra magnétique [**Publication I** et **II**] ou sur un banc expérimental [**Publication III**]. Dans la **Publication IV**, les performances du système ont été évaluées en utilisant l'imagerie CT, permettant une plus grande flexibilité dans le placement et l'orientation des capteurs. Au cours de cette expérience, une erreur systématique allant de 1 mm à 6 mm a été observée, en fonction de l'orientation du capteur et de sa proximité avec le FG. Une analyse préliminaire a indiqué que la sensibilité croisée des capteurs était probablement la principale source de cette erreur. Selon la fiche technique des capteurs utilisés dans cette recherche, pour un champ magnétique de 100 µT le long de l'axe X, jusqu'à 5 µT de champ magnétique supplémentaire peuvent observer le long des axes Y et Z. Ce phénomène peut être atténué en caractérisant et en compensant les sensibilités croisées des capteurs. Alternativement, générer des gradients magnétiques plus forts pourrait réduire l'impact des sensibilités croisées, ou adopter différentes technologies de détection pourrait fournir une solution plus robuste. Cette thèse, en tant que preuve de concept, établit les exigences pour la génération de champ magnétique et les unités de capteurs. Bien que divers capteurs soient actuellement disponibles et que de nouveaux modèles soient fréquemment introduits, une solution immédiate prometteuse pourrait consister à utiliser des capteurs à effet Hall, tels que l'AK09919C [174], qui partagent des dimensions similaires avec les capteurs utilisés dans cette recherche. Les capteurs à effet Hall présentent intrinsèquement des sensibilités croisées plus faibles, ce qui en fait une option intéressante pour les futures itérations du système.

Finalement, les performances du système montrent un équilibre entre les capacités de détection, les

dimensions du FG et la consommation énergétique. Le défi de cette thèse était de concevoir un système répondant aux exigences environnementales et de performance spécifique aux procédures DBS. À cet égard, l'objectif a été atteint avec ce nouveau système EMT.

Intégrabilité

Si la compatibilité avec le système stéréotaxique a été confirmée, les instruments chirurgicaux plus petits, tels que les microprocesseurs, les écarteurs ou les électrodes MER, n'ont pas fait l'objet d'une évaluation complète. Ces instruments peuvent introduire des distorsions localisées et statiques affectant le champ généré, qui sert de référence pour le tracking. Cette sensibilité a été étudiée dans une étude complémentaire, soulignant que le système EMT est vulnérable aux larges instruments ferromagnétiques, tels qu'un écarteur en acier ou un porte-aiguille. Ces distorsions entraînent des erreurs de tracking, avec des imprécisions de position de quelques millimètres et des écarts d'orientation de dizaines de degrés lorsque les instruments se trouvaient à moins de 2 cm du capteur. Les systèmes EMT existants ne présentaient des dégradations que sur les composantes angulaires d'environ quelques dizaines de degrés lorsque les mêmes instruments se trouvaient à moins de 2 cm du capteur. Toutefois, dans la pratique, le porte-aiguille et l'écarteur ne sont pas placés à proximité de l'électrode DBS intégrant les capteurs magnétiques. En revanche, les instruments placés à quelques millimètres de l'électrode DBS, comme l'électrode MER, n'ont pas affecté les performances de tracking. Les progrès futurs devraient se concentrer sur le développement de méthodes de compensation pour résoudre ce problème.
D'autre part, il est aussi crucial de vérifier si les capteurs conservent leurs performances après exposition à des champs magnétiques puissants, comme ceux des outils chirurgicaux ou des IRM. Les capteurs utilisés sont sensibles aux champs magnétiques forts et peuvent être involontairement magnétisés ou démagnétisés, affectant leurs performances. Dans une étude complémentaire, nous avons démontré expérimentalement que les performances de ces capteurs sont maintenues même après une exposition à 7T. Cela permet de garantir que leur intégration et possible exposition à des champs non contrôlés n'affectera pas les performances du système.

Fabrication & Miniaturisation

La conception de chaque composant du système EMT a été guidée par des exigences spécifiques et un objectif d'amélioration des performances. Initialement basé sur des bobines en cuivre traditionnelles, le système a évolué vers l'intégration de bobines sur un circuit imprimé en raison des imperfections de bobinage et des inhomogénéités des champs magnétiques. La fabrication de circuits imprimés, avec sa précision micrométrique et sa capacité de production en série, a permis d'améliorer les performances, la robustesse et de faciliter la transition vers une production industrielle du système. De plus, les marqueurs stéréotaxiques utilisés pour le recalage peuvent être produits en série à faible coût facilitant encore la mise en œuvre pratique du système.
D'autre part, l'électrode DBS a présenté le plus grand défi. Pour maintenir les mêmes dimensions que les électrodes DBS traditionnelles (environ 1,2 mm de diamètre), des capteurs submillimétriques ont été préférés. Le premier prototype incorporait un petit circuit imprimé sur lequel le capteur magnétique AMR était soudé. Nous avons progressivement réduit la taille du PCB et finalement l'avons supprimé pour intégrer les capteurs directement dans l'électrode DBS. Les fils étaient soudés directement sur les pads du capteur et encapsulé dans de la résine à la pointe de l'électrode. Bien que cette méthode se soit avérée fonctionnelle, elle n'est pas pratique pour la production en série. En conséquence, des solutions techniques doivent être développées pour intégrer les capteurs et le câblage associé tout en assurant un alignement correct avec l'axe de l'électrode. Ces solutions restent inexplorées et présentent un défi ouvert pour les développements futurs.

5.2 Perspectives

Vers les essais cliniques

Avant de déployer le système EMT pour des essais cliniques, plusieurs considérations de sécurité doivent être abordées. La sécurité initiale a été évaluée et le système semble peu susceptible de stimuler les nerfs périphériques. Cependant, des évaluations supplémentaires sont nécessaires pour garantir la conformité aux normes de sécurité, notamment celles de la Commission Internationale de Protection contre les Rayonnements Non Ionisants et les normes IEEE C95. Des modifications du système, comme une séquence d'activation progressive des bobines, pourraient être nécessaires. Il est également crucial de considérer la sécurité des patients tout au long de leur vie, notamment lors de procédures d'imagerie comme les radiographies et les IRM. Bien que les capteurs intégrés dans l'électrode DBS ne posent pas de risque pour les rayons X, la compatibilité IRM reste un défi. Les électrodes DBS doivent être compatibles avec les systèmes IRM pour une acceptation clinique généralisée.

Utilisation post-opératoire du système EMT

Cette thèse se concentre sur le développement d'un système de navigation pour la chirurgie DBS, avec des applications potentielles pour le tracking post-opératoire des électrodes DBS. Le capteur intégré dans l'électrode pourrait permettre de localiser l'électrode après l'opération sans exposition supplémentaire aux radiations, ce qui est utile pour l'optimisation de la programmation DBS et le suivi des patients. Cependant, des modifications significatives des systèmes DBS actuels seraient nécessaires, notamment dans la conception d'un neurostimulateur capable de contrôler le capteur magnétique. De plus, une méthode pour aligner l'espace de référence du système EMT avec l'espace anatomique du patient doit être développée. L'application post-opératoire du système EMT doit être soigneusement évaluée et discutée avec les neurochirurgiens et les neurologues pour déterminer sa valeur clinique.

6. Conclusion

Ce travail fait progresser la neurochirurgie en développant un système EMT pour améliorer la localisation en temps réel et le retour d'information sur l'orientation pendant les procédures stéréotaxiques DBS. Une nouvelle approche utilisant des champs magnétiques quasi-statiques et des capteurs intégrés a été présentée, avec un premier démonstrateur montrant une précision prometteuse dans le tracking de la position et de l'orientation. Le système a démontré sa robustesse dans les environnements chirurgicaux et sa compatibilité avec les systèmes stéréotaxiques, ce qui a conduit au développement d'une méthode d'enregistrement innovante.

D'autres améliorations sont nécessaires, notamment pour atteindre une précision submillimétrique. Bien que conçu pour la DBS, le système est adaptable à d'autres procédures nécessitant un placement précis des électrodes. La validation par des simulations chirurgicales a confirmé son potentiel d'intégration clinique, bien que des défis subsistent, notamment les interférences électromagnétiques provenant des outils chirurgicaux.

Le système a été évalué dans des conditions simplifiées, démontrant sa faisabilité, mais nécessitant des tests supplémentaires dans une procédure chirurgicale complète pour évaluer les interactions avec d'autres systèmes tels que l'imagerie peropératoire et les appareils électroniques.

L'intégration du système EMT dans les procédures DBS est un processus itératif, dans le cadre duquel des perfectionnements continus permettront d'améliorer sa conception et ses performances. Cette première itération permet de relever avec succès les principaux défis de la chirurgie DBS, jetant ainsi les bases de futures améliorations et d'une adoption clinique plus large.